Optimal Methodologies for Ultrasonic Guided-Wave Based Structural Health Monitoring

A Thesis Submitted to The University of Nottingham
for the Degree of Doctor of Philosophy

Sergio Cantero Chinchilla, MSc, BSc

August 2020

Abstract

The assessment of structural integrity is a key issue for many industries due to its important implications in safety, maintenance cost reduction, and improved asset availability. In this context, structural health monitoring (SHM) systems using ultrasonic guided-waves are being explored for an efficient diagnosis of damage and prognosis of the remaining useful life of the monitored structure. Nonetheless, addressing this monitoring scenario is a challenge given the inherent complexities associated to each of the diagnosis steps, which encompass the optimal SHM design, the detection of damage, its localisation, and its identification. Among these complexities, uncertainties stemming from several sources such as equipment noise, manufacturing defects, and the lack of conclusive knowledge about wave propagation introduce a high variability in the response of the SHM system. The main objective of this thesis is to provide probabilistic Bayesian and fuzzy logic methodologies to manage global uncertainties for each step in the SHM process.

The accuracy and reliability of an ultrasonic guided-wave based SHM system are dependent on the chosen number and location of sensors and actuators. A general framework for optimal sensor configuration based on value of information is proposed in this thesis, which trades-off information gain and cost. This approach optimally chooses the sensor position so that they render the largest information gain when inferring the damage location. The methodology is tested using different case studies in the context of ultrasonic guided waves and piezoelectric (PZT) sensors. However, although this framework is mathematically rigorous, it is computationally expensive should the actuators be considered in the optimisation problem. To overcome this issue, a cost-benefit analysis is also proposed using both the Shannon's information entropy and a cost function associated to the number of sensors and actua-

tors. The objective function is based on binary decision variables, which are relaxed into continuous variables, hence convexifying the objective function. This optimisation methodology is illustrated in several case studies considering plate-like structures with irregular geometries and different materials, providing a high computational efficiency.

The first diagnosis stage requires a robust and computationally efficient damage detection approach in real-life engineering scenarios. To this end, a novel damage index for ultrasonic guided-wave measurements based on fuzzy-logic principles is proposed in this thesis. This approach assesses the time of flight (ToF) mismatch between signals acquired in undamaged and non-pristine states using fuzzy sets for its evaluation. The robustness partially builds on the use of a large amount of signals stemming from two experimental procedures: the round robin configuration and the transmission beamforming technique. This new damage index is validated in several scenarios with sudden and progressive damage.

Once a damage area has been detected, the next diagnosis stage requires a reliable damage localisation. To address this SHM step, a robust methodology is proposed based on two hierarchical levels: (1) a Bayesian time-frequency (TF) model class selection to obtain the ToF of damage scattered waves; and (2) a Bayesian inverse problem (BIP) of damage localisation that considers as input data the outcome of the first level. The effectiveness and robustness of the proposed methodology is illustrated using two cases studies with one and two areas of damage.

Lastly, to provide a complete diagnosis of damage using ultrasonic guided-waves, the identification of damage needs to be addressed. A multi-level hybrid wave and finite element (WFE) model-based Bayesian approach is proposed to identify the type of damage in composite beams based on posterior probabilities, hence accounting for different sources of uncertainty. In addition to the type of damage, this approach allows the inference of damage-related parameters and the damage location. A carbon fibre beam with two damage modes, i.e. a crack and a delamination, is used to illustrate the methodology.

List of Publications

Journal publications:

- **S. Cantero-Chinchilla**, J.L. Beck, M. Chiachío, J. Chiachío, D. Chronopoulos, and A. Jones. Optimal sensor and actuator placement for structural health monitoring via an efficient convex cost-benefit optimization. *Mechanical Systems and Signal Processing*, 144:106901, 2020.

- W.J. Yan, D. Chronopoulos, **S. Cantero-Chinchilla**, K.V. Yuen, and C. Papadimitriou. A Fast Bayesian Learning Scheme for Identification of Local Structural Properties of Layered Composites based on Wave and Finite Element-assisted Metamodeling Strategy and Ultrasound Measurements. *Mechanical Systems and Signal Processing*, 143:106802, 2020.

- **S. Cantero-Chinchilla**, G. Aranguren, M.K. Malik, J. Etxaniz, and F. Martín De La Escalera. An Empirical Study on Transmission Beamforming for Ultrasonic Guided-Wave Based Structural Health Monitoring. *Sensors*, 20(5):1445, 2020.

- **S. Cantero-Chinchilla**, J. Chiachío, M. Chiachío, D. Chronopoulos, and A. Jones. Optimal sensor configuration for ultrasonic guided-wave inspection based on value of information. *Mechanical Systems and Signal Processing*, 135:106377, 2020.

- W.J. Yan, D. Chronopoulos, C. Papadimitriou, **S. Cantero-Chinchilla**, and G.S. Zhu. Bayesian inference for damage identification based on analytical probabilistic model of scattering coefficient estimators and ultrafast wave scattering simulation scheme. *Journal of Sound and Vibration*, 468:115083, 2020.

- **S. Cantero-Chinchilla**, J. Chiachío, M. Chiachío, D. Chronopoulos, and A. Jones. A robust Bayesian methodology for damage localization in plate-like structures using ultrasonic guided-waves. *Mechanical Systems and Signal Processing*, 122:192–205, 2019.

- R.K. Apalowo, D. Chronopoulos, and **S. Cantero-Chinchilla**. Wave interaction with nonlinear damage and generation of harmonics in composite structures. *Composite Structures*, 230:111495, 2019.

- J. Chiachío, N. Bochud, M. Chiachío, **S. Cantero**, and G. Rus. A multilevel Bayesian method for ultrasound-based damage identification in composite laminates. *Mechanical Systems and Signal Processing*, 88:462-477, 2017.

Conference proceedings:

- **S. Cantero-Chinchilla**, J. Chiachío, M. Chiachío, D. Chronopoulos, A. Jones, Y. Essa, and F. Martín De La Escalera. Optimal Ultrasonic Sensor Configuration for Plate-Like Structures Using the Value of Information. In *Structural Health Monitoring 2019: Enabling Intelligent Life-Cycle Health Management for Industry Internet of Things (IIOT) - Proceedings of the 12th International Workshop on Structural Health Monitoring*, volume 1, pages 1455-1462, 2019.

- **S. Cantero-Chinchilla**, J. Chiachío, and M. Chiachío. Optimal Ultrasonic Sensor Configuration Based on Value of Information. In *Proceedings of the 29th European Safety and Reliability Conference*, 2019.

- **S. Cantero-Chinchilla**, J. Chiachío, M. Chiachío, D. Chronopoulos, A. Jones, Y. Essa, and F. Martín De La Escalera. Uncertainty quantification in ultrasonic guided-waves based damage localization. In *COMPDYN 2019: Proceedings of the 7th International Conference on Computational Methods in Structural Dynamics and Earthquake Engineering*. Volume 2, 2019.

- M.K. Malik, **S. Cantero-Chinchilla**, D. Chronopoulos, J. Chiachío, and Y. Essa. Ultrasonic guided-wave based system identification for beams.

In *Structural Health Monitoring 2019: Enabling Intelligent Life-Cycle Health Management for Industry Internet of Things (IIOT) - Proceedings of the 12th International Workshop on Structural Health Monitoring*, volume 2, pages 2313-2320, 2019.

- W.J. Yan, D. Chronopoulos, C. Papadimitriou, **S. Cantero-Chinchilla**, and G.S. Zhu. Bayesian damage characterization based on probabilistic model of scattering coefficients and hybrid wave finite element model scheme. In *COMPDYN 2019: Proceedings of the 7th International Conference on Computational Methods in Structural Dynamics and Earthquake Engineering*. Volume 2, 2019.

- **S. Cantero-Chinchilla**, J. Chiachío-Ruano, M. Chiachío-Ruano, J. Etxaniz, G. Aranguren, A. Jones, Y. Essa, and F. Martín De La Escalera. Lamb wave-based damage indicator for plate-like structures. In *European Conference of the PHM Society*, volume 4, 2018.

- **S. Cantero-Chinchilla**, J. Chiachío, M. Chiachío, A. Jones, Y. Essa, and F. Martín De La Escalera. A Bayesian time-of-flight estimation for ultrasonic damage detection. In *9th European Workshop on Structural Health Monitoring, EWSHM*, 2018.

- G. Aranguren, J. Etxaniz, **S. Cantero**, M.K. Malik, F. Martín De La Escalera, and Y. Essa. Proposal for an industrial structural health monitoring system based in ultrasonic signal. In *9th European Workshop on Structural Health Monitoring, EWSHM*, 2018.

Acknowledgements

First of all, I want to express my gratitude to my academic supervisors, Prof Arthur Jones, Dr Juan Chiachío, and Dr Dimitrios Chronopoulos for their kind support and guidance throughout this thesis. They have always shown enthusiasm in my research interests and helped me incredibly to develop my own ideas. I also wish to thank my internal examiner Dr Luis Neves for his constructive comments and advice during our review meetings. Furthermore, I acknowledge my industrial supervisors from Aernnova Engineering Division S.A., Dr Yasser Essa and Dr Federico Martín de la Escalera for sharing their valuable industrial experience with me.

I would like to thank Prof Gerardo Aranguren from the University of the Basque Country for his kind support during my industrial secondments. A special mention goes to Prof James L. Beck from the California Institute of Technology for sharing his invaluable expertise in Bayesian methods along my academic secondment. It has been a real pleasure working along with such a brilliant professional and wonderful person.

I acknowledge the European Commission for funding both my PhD thesis and the SAFE-FLY EID project via the Horizon 2020 research and innovation programme under the Marie Skłodowska-Curie grant agreement No. 721455. I express my gratitude to the University of Nottingham for this experience.

Also I want to thank Dr Manuel Chiachío from the University of Granada, for his productive and friendly advice, and my SAFE-FLY colleagues for their support and the pleasant moments shared together during these years.

Finally, I thank my splendid family, for being supportive and understanding during this time, and my beloved fiancée, for always being there. I would be lost without all of you.

Contents

List of Acronyms

AGF   averaged goodness-of-fit

AIMS   asymptotic independent Markov sampling

ASD   active sensing diagnostics

BEIG   benefit of the expected information gain

BIP   Bayesian inverse problem

CFRP   carbon fibre reinforced polymer

CVI   conditional value of information

CWT   continuous wavelet transform

DAS   delay-and-sum

DoH   degree of health

EIG   expected information gain

ESS   essential sampling size

EVI   expected value of information

FEM   finite element modelling

GA   genetic algorithms

HHT   Hilbert-Huang transform

IMF   intrinsic mode functions

KL   Kullback-Leibler

MAP   maximum a posteriori

MC   Monte Carlo

MCMC   Markov chain Monte Carlo

M-H   Metropolis-Hastings

NDT   non-destructive testing

PAMELA   phased array monitoring for enhanced life assessment

PDF   probability density function

PEB   posterior expected benefit

PMIE   principle of maximum information entropy

PSD	passive sensing diagnostics
PZT	piezoelectric
QoI	quantity of interest
RCI	relative cost of implementation
RUL	remaining useful life
SHM	structural health monitoring
SHMUS	structural health monitoring ultrasonic system
SMF	S-shaped membership function
SNR	signal-to-noise ratio
STFT	short-time Fourier transform
TF	time-frequency
ToF	time of flight
WFE	wave and finite element
WVD	Wigner-Ville distribution
ZMF	Z-shaped membership function

List of Symbols

Latin symbols

a, b main axes of the wave propagation velocity ellipse for composite structures; scaling and time-shift factors

$\mathbf{a}$ guided-wave amplitudes

$b(\cdot)$ benefit function

B' maximum prior expected benefit

B'' maximum posterior expected benefit

c normalising constant in Bayes' theorem

$\mathbf{C}^b$ damping matrix of a beam section

$\mathfrak{C}$ vector of optimal spatial sensor configuration

$\mathcal{C}^n_{opt}$ optimal spatial configuration of n sensors

$\mathbf{D}$ dataset used in the Bayesian inverse problem

$\mathbf{D}^b$ frequency dependent dynamic matrix of a beam section

$\hat{\mathbf{d}}^{(k)}$ set of $\hat{d}_j$ in the k-th sensor

$\mathfrak{D}$ space of datasets

$\hat{d}_j^{(k)}$ first energy peak provided by j-th TF model in the k-th sensor

$\mathfrak{d}_{ik}$ distance from the i-th transducer to the k-th point of interest

$D^{(k)}$ time of flight data acquired at the k-th sensor

$\mathfrak{d}_{0k}$ distance from the origin of coordinates to the k-th point of interest

$\mathcal{D}$ ultrasonic measurement data

$\tilde{d}^{(k)}$ first energy peak in the k-th sensor

E Young's modulus

$e, \mathbf{e}$ prediction error term

$e_i^j(t)$ uncertain prediction error at time n at the i-th sensor, considering the j-th actuator

$\mathbb{E}[\cdot]$ mathematical expectation

$\mathfrak{f}$	vector of internal forces
$f(\cdot)$	inverse of cost function
f	frequency
G	shear stiffness
$g_j(\cdot)$	j-th TF model
$\mathfrak{h}(t)$	window function
$h(w,z)$	entropy-based convex objective function
$h^*(w,z,n)$	cost-benefit entropy-based convex objective function
$h(\boldsymbol{\psi}_a, \boldsymbol{\psi}_s)$	entropy-based objective function for optimal discrete sensor and actuator placement
$\mathbf{H_k}$	matrix of μ_m values
$J(\mathcal{C})$	mean estimator of the expected value of information
$\mathcal{J}(\cdot)$	goodness-of-fit function
$\mathbf{K}^b$	stiffness matrix of a beam section
k	wave-number
$\mathrm{KL}(\cdot\|\cdot)$	Kullback-Leibler divergence
l_x	length of the a waveguide
$\mathbf{M}^b$	mass matrix of a beam section
$\mathbf{M}$	set of model classes $\mathcal{M}_j$
$\mathcal{M}_j$	j-th model class
n	number of sensors
N_a	number of possible actuator locations
N_a^g	number of actuators installed in a structure
$\mathfrak{N}$	set of sensor configurations (number and position)
$\mathcal{N}(\cdot)$	Gaussian probability distribution
N_m	number of model classes
N_{pk}	number of maximum and minimum peaks of a signal
n'_{opt}	optimal sensor configuration under prior information
n''_{opt}	optimal sensor configuration under posterior information
N_q	number of samples in an ultrasonic signal
N_s	number of possible sensor locations

N_s^g	number of sensors installed in a structure
N_i^A	number of samples in i-th annealing level
N_t	number of times that a experimental test is repeated
N^θ	number of uncertain model parameters
$\mathcal{N}(\cdot)$	Gaussian probability distribution
$p(\cdot)$	probability density function
$P(\cdot)$	probability
$\mathbf{q}_\mathcal{D}$	ultrasonic signal data
$q(\cdot)$	proposal PDF in MCMC sampling algorithms
$\mathbf{q}_\theta$	ultrasonic wave propagation model
r	acceptance rate for the M-H algorithm
$\mathbf{R}$	rotation matrix
r_{bb}	bending-to-bending reflection coefficient
r_{bp}	bending-to-pressure reflection coefficient
r_{pb}	pressure-to-bending reflection coefficient
r_{pp}	pressure-to-pressure reflection coefficient
$\mathbf{S}$	scattering matrix
$s(\cdot)$	monotonically increasing dimensionless cost function
$\vec{s}_i$	vector from the origin of coordinates to the i-th transducer
$\mathbf{T}$	transfer matrix
T_s	number of samples generated in M-H algorithm
t	discrete instant of time
$\mathrm{ToF}^{(a-s)}$	time of flight of a wave emitted at the actuator a and received at the sensor s
$\mathrm{ToF}_\mathcal{D}^{(a-s)}$	measured time of flight
$\mathrm{ToF}_M^{(a-s)}$	modelled time of flight
$\mathbf{u}$	vector of degrees of freedom
$\mathcal{U}(\cdot)$	uniform probability distribution
V	wave propagation velocity
v	mean of prior PDF of the velocity in isotropic materials
V_{a-d}, V_{d-s}	wave propagation velocity in paths a-d and d-s, respectively

w_j	continuous activation variable of the j-th actuator
$\mathfrak{w}_j^{(k)}$	weight of the j-th TF model class in the k-th sensor used in the hyper-robust model
$X(t)$	time series of the signal
X_a^j, Y_a^j	j-th actuator position coordinates
X_d, Y_d	damage position coordinates
$x_i^j(t, \theta)$	deterministic model prediction at time n for parameters θ at the i-th sensor, considering the j-th actuator
X_s^j, Y_s^j	i-th sensor position coordinates
$y_i^j(t)$	observation of a quantity of interest at time n at the i-th sensor, considering the j-th actuator
z_i	continuous activation variable of the i-th sensor

Greek symbols

α	trade-off constant between cost and information used to obtain the value of information
β_a, β_s	angle of the actuator-damage and damage-sensor paths
γ	threshold parameter for AIMS algorithm
δ	time delay
ϵ	error term in TF model
ζ	number of state of the chain in M-H
η	trade-off variable between information gain and cost
Θ	space of model parameters
θ	set of uncertain model parameters
$\hat{\theta}$	maximum a posteriori value of the posterior distribution
$\kappa_j(t)$	magnitude of an analytic signal
λ	wave propagation constant
μ_ℓ	membership value for the evaluation of the S-shaped membership function
μ_m	minimum membership value of an entire signal

$\mu_{\{max\}}$	membership value of the maximum peaks of a signal
$\mu_{\{min\}}$	membership value of the minimum peaks of a signal
μ_r	membership value for the evaluation of the Z-shaped membership function
ν	Poisson's ratio
$\vec{\xi}$	beam direction
$\pi(\cdot)$	probability density function of the current state of information: either prior or posterior
ρ	density
σ_e	standard deviation of the prediction error term e
σ_ϵ	standard deviation of ϵ
σ_M	MAP value of σ_ϵ
$\hat{\sigma}$	maximum a posteriori value of the standard deviation of the prediction error e
σ_v	standard deviation of prior PDF of the velocity
ϕ	parameter angle
$\boldsymbol{\phi}$	wavemodes of the beam model
$\boldsymbol{\psi}_a$	vector of binary decision variables of the activation of actuator
$\psi_a^{(j)}$	binary activation variable of the j-th actuator
$\boldsymbol{\psi}_s$	vector of binary decision variables of the activation of sensors
$\psi_s^{(i)}$	binary activation variable of the i-th sensor
$\Psi(t)$	analysing wavelet
ω	angular frequency

List of Tables

List of Figures

List of Algorithms

Part I

INTRODUCTION

1

Introduction

The assessment of structural integrity is a key issue for many industries due to its important implications in safety, maintenance cost reduction, and improved asset availability. This chapter introduces the context and motivation of this work on SHM and ultrasonic guided-waves. It also provides the main research objectives and the subsequent contributions made throughout this Ph.D. thesis.

1.1 Context and motivation

The evaluation of the structural health condition has been typically carried out using well-established non-destructive testing (NDT) techniques such as visual inspection, radiography, or ultrasound [1, 2]. Despite being highly accurate, these methods may require the temporary suspension of the operation of a specific industrial asset, e.g. a bridge or an aeroplane. The costs associated with these inspection actions are intrinsically related to the number of hours required for each test [3], given that little or no service is provided during the inspection time. Besides, the amount of required maintenance operations tends to increase with the requested level of safety imposed by the norms and standards for each industry, thus leading to a high impact in safety-critical industries. Note that these industries (e.g. nuclear or aerospace) require high

levels of safety-integrity, given that failures could lead to catastrophic consequences [4].

In this context, the benefits and drawbacks of real-time or on-board SHM systems are being explored by a range of industries. These systems are typically regarded as diagnosis tools that have the potential to mitigate the side-effects of scheduled maintenance actions by reducing unnecessary costs while providing a higher safety level. By using a particular on-board SHM system, a structure is continuously monitored through time until an anomaly is detected. When this happens, a more profound assessment of its location and severity is typically carried out, and decisions on best operation and maintenance actions and when to optimally implement them are taken. This is typically regarded as *condition-based* maintenance [5, 6], whereby maintenance actions are undertaken based on the actual condition of the asset. When the SHM system enables predictions of the future stages of damage propagation and the remaining useful life of the monitored structure, then a *predictive maintenance* approach can be adopted [7]. Note that the detection, localisation, and identification of damage can be enclosed within the *diagnosis* stage, while damage prediction and remaining useful life (RUL) estimation fall into the *prognosis* stage. An overview of the condition-based maintenance elements is provided in Figure 1.1.

The accuracy of the SHM systems may rely on the type of technique adopted to actively or passively interrogate the structural condition. Among the most well-known approaches, it is worth mentioning the use of vibration analysis [8, 9] and fibre Bragg grating [10]. These SHM methods stand out due to their efficiency in monitoring very large structures such as buildings or bridges, although generally lack of sensitivity to small and local damage. In this sense, a promising technique is the use of ultrasonic guided-waves, which are mechanical waves that have the property to travel and explore very large thin-walled structural components with a relatively small attenuation [11]. Moreover, these ultrasonic waves are particularly sensitive to small damage forms in the early stage of growth, such as the initiation of a fatigue crack.
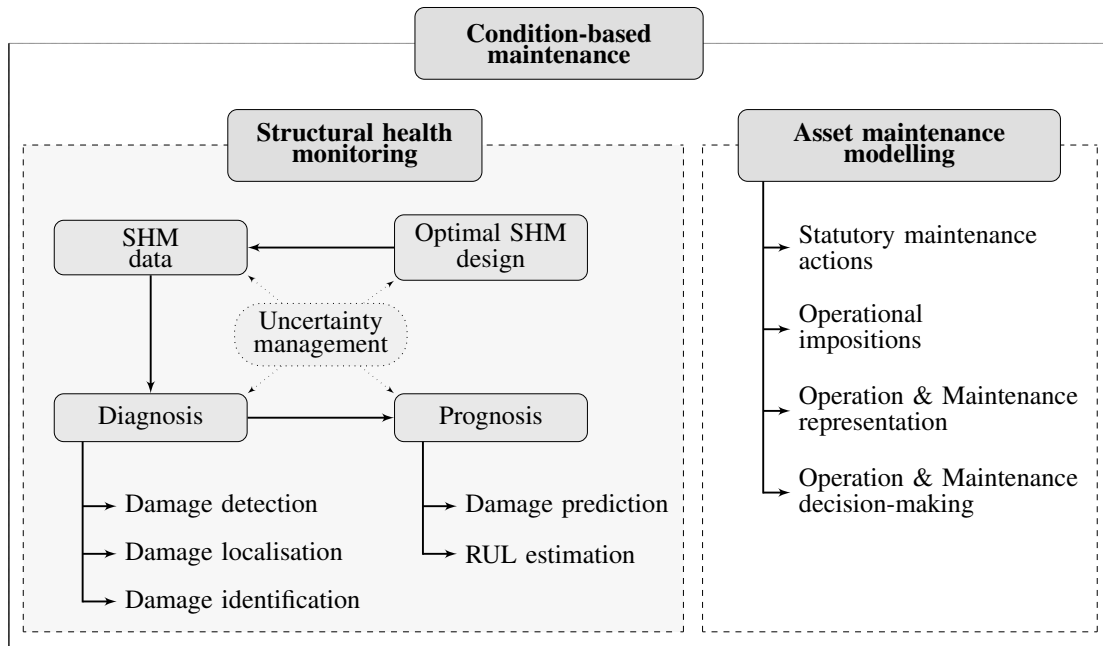
Figure 1.1: Hierarchical structure of condition-based maintenance.

These remarkable characteristics have led industries, such as the aerospace industry, to focus on this diagnosis technology. One noticeable example of this development is the phased array monitoring for enhanced life assessment (PAMELA)® SHM system developed by Aernnova Engineering S.A. [12–14], consisting of an integrated hardware and software system, including sensors and actuators, able to perform ultrasonic guided-wave based experiments in thin-walled structures.

1.1.1 Optimal SHM design

The effectiveness and reliability of a suitable ultrasonic guided-wave based SHM system depend heavily on the configuration (number and location) of the sensors and actuators. Inaccurate and biased diagnosis may lead to an erroneous diagnosis such as false positive or false negative alerts [15], which depending on the case, may have negative impact on safety and cost, particularly in safety-critical structures. In order to provide a reliable, yet efficient, configuration for a SHM system, the adoption of an optimal sensor and actuator configuration is a key aspect in any SHM system, since it enables a

balance to be struck between the performance of the SHM system and its related cost [16]. Theoretically, an infinitely reliable system would require an infinite amount of information; however such a theoretical rule finds an exception in practice when features related to the complexity of the monitoring system, such as the cost or the weight, are taken into consideration. The latter suggests a trade-off between reliability and complexity for SHM design that needs to be assessed rigorously for optimal SHM functionality. Authors have investigated these aspects and the most relevant approaches can be broadly categorised into two groups, namely, approaches using the *value of information* as an optimality criterion [17, 18] and those using *cost-benefit* analysis [19]. The first approach provides the sensor and/or actuator configuration that holds the best balance between cost of the SHM system and the amount of information gain by the system. Alternatively, the second one typically uses performance indices (such as the probability of detection [16] or the Lindley information measure [20]) and cost-related features associated within the layout of sensors of the SHM system, which are simultaneously maximised and minimised respectively using a multi-objective type of optimisation algorithm. In this thesis, original contributions have been done in both approaches using a rigorous probabilistic Bayesian framework.

1.1.2 Damage detection

Damage detection in structural assets is carried out by monitoring health-related features, such as vibration modes, deformations, or ultrasonic signatures, throughout their design lifespan. The main advantage of using real-time SHM techniques instead of other NDT methods, such as visual inspection or radiography, is that a structure can be interrogated continuously and autonomously over time, especially when it is out of reach, such as inside an aeroplane wing. Therefore sudden events that might compromise its integrity can be immediately identified. One possible output of this continuous monitoring is a binary indicator that provides Boolean information on whether or not a structure is damaged. However, a damage index taking values within

a numerical interval is often preferred since it provides not only information about the presence of damage, but also information related to the degree of damage so that inspection and maintenance actions can be planned according to its severity. In the context of ultrasonic testing, the most common methods for providing damage indices typically rely on time or energy-related features from the ultrasonic signals acquired by the SHM system [21]. Additionally, there are a number of complexities that need to be addressed in order for this technology to be implemented in real-world engineering scenarios. For instance, factors such as environmental noise that contaminates the measurements or inaccurate measurement systems may compromise the effectiveness and accuracy of the SHM system. Therefore, accurate damage detection for structural applications demands a fast and highly reliable approach to avoid biased diagnosis such as false positives and false negatives. In addition, a suitable experimental procedure needs to be established to collect the required amount of information for an accurate damage detection. In this sense, the contributions of this thesis on optimal number and position of sensors support the definition of the previously mentioned experimental procedure by suggesting optimal configurations. Once a damaged area is detected, proper operational decisions can be taken, e.g. to carry on to the next stage of damage localisation.

1.1.3   Damage localisation

The localisation of damage is particularly relevant for the industries such as the aerospace and the wind power industries, given that some of the structures used in aircraft or wind turbines are very large, and some of them are out of range for other NDT techniques such as visual inspection. To address such a challenging scenario, the damage localisation stage can be addressed using guided-wave based SHM along with post-processing techniques applied to ultrasonic measurements [22]. Two general approaches are typically adopted at this stage for damage assessment: (1) model-based inverse problems [23], whereby complete damage information can be obtained

at a considerable computational cost; and (2) inverse problems based on post-processed signal features, whereby other relevant information can be obtained more efficiently. In regard to the model-based inverse problem type of identification, a physics-based wave propagation model is required, which needs to be parametrised and whose outputs are compared to the available experimental dataset. Alternatively, the second approach uses simpler models (such as the time-of-flight) whose outcomes are comparable with the ones provided by post-processing techniques (e.g. time-frequency transforms) instead of raw experimental data [24]. Note that an excessively high level of information is not usually required at the damage localisation stage, given that depending on the location of the damage, this might have different levels of relevance.

1.1.4 Damage identification

If a localised damage site falls within a critically stressed area of a structure, a more detailed level of information is required, which involves the identification of the type of damage. In this regard, it is well-known that different damage modes have unequal implications in the serviceability of the damaged structures, for example impact damage may be more critical in terms of safety than initial corrosion damage. These damage modes also differ between materials, e.g. fatigue cracks in metallic plates [25] or impact delaminations in carbon fibre reinforced polymer (CFRP) sheets [26]. Moreover, depending on the size and severity of the damage, the asset manager might decide to suspend the service of a specific asset in order to carry out maintenance actions, which may include preventing an aeroplane from flying. In this context, the use of real-time ultrasonic guided-waves for damage identification establishes a challenging, yet promising, scenario. It involves the use of model-based inverse approaches that allows the inference of the complete damage features, including damage-type identification, from ultrasonic measurements. As explained before, these wave propagation models have typically been computationally challenging, thus preventing them from being used on-board for real-time damage identification. There are, however, some developments available

in the literature aimed at alleviating this computational complexity consisting of the surrogacy of physics-based models [27]. The resulting tools can be regarded as efficient meta-models that approximate the input-output behaviour of the physics-based models.

1.1.5 Uncertainty management

In addition to the aforementioned complexities, several sources of *uncertainty*, e.g. unknown material properties, measurement errors stemming from equipment or sensor noise, manufacturing defects, environmental changes, and epistemic uncertainty (i.e. lack of conclusive knowledge about wave propagation in heterogeneous media), also introduce a high variability. If these uncertainties are not rigorously considered, a biased and potentially erroneous diagnosis might be provided. To overcome these challenges, robust, rigorous, and efficient methodologies are proposed in this thesis at each stage of the diagnosis process (see Figure 1.2). Thus, the three main approaches used herein: (1) information theory [28] and *Bayesian* analysis for the design stage; (2) *fuzzy logic* [29, 30] for the damage detection; and (3) BIPs [31–33] for damage localisation and identification. Note that for the Bayesian approaches, which have been scarcely used in the literature in the context of ultrasonic guided-wave based SHM, parameters or information inferred from measurements are not treated as deterministic values, but instead as probability density functions. These probabilities are understood here as a *degree of belief* [32, 34] given a proposition, e.g. the degree of belief on a particular theoretical model given a particular SHM dataset. The use of these rigorous methodologies in the previous context entails a powerful tool that results in a more efficient and reliable SHM, and therefore their applications to the different stages of ultrasonic guided-wave based SHM represent the main contribution of this doctoral thesis.
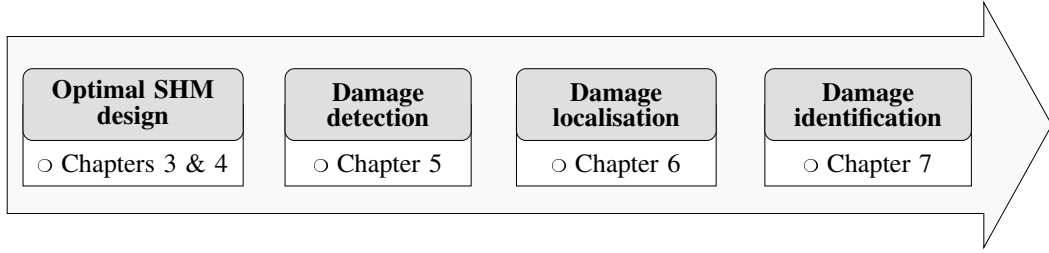
Figure 1.2: SHM stages addressed in this thesis and outline of the contributions.

1.2 Research objectives and contributions

Several ultrasound-based SHM methodologies have been proposed in the literature to tackle the different monitoring stages, namely optimal SHM design, damage detection, localisation, and identification, mainly based on deterministic formulations to solve the corresponding inverse problems [34]. Overall, these methods neglect modelling and accounting uncertainties stemming from (1) unknown model parameter given a particular model class and (2) the choice of a specific model class among a set of candidates. In this context, the use of Bayesian and fuzzy-logic based approaches provides rational ways of managing global uncertainties for each step in the SHM process. This is the central research objective of this thesis, which has been approached by establishing several specific objectives on the basis of the following research hypotheses.

1.2.1 Research hypothesis 1

The accuracy and performance of any SHM system is influenced by several design variables. In particular, the number and position of sensors are typically regarded as two of the most relevant variables, with important implications in cost and reliability [15, 16]. Numerous approaches for optimal sensor placement have been proposed in the context of ultrasonic guided-wave based inspection which use deterministic methodologies that neglect inherent modelling uncertainties [35–38]. Some Bayesian probabilistic approaches have also been proposed for applications different from ultrasonic guided-waves by using, in general, the quantification of information gain as optimality crite-

rion [39, 40], and neglecting the cost associated with the SHM configuration. This could lead to uneconomical system configurations.

> **Hypothesis 1.** An optimised and cost-efficient sensor configuration (number and position) can be obtained by trading-off the information gain and the cost of the configuration using the *value of information* instead of the amount of information.

Research Objective 1. *Propose a general framework for optimal sensor configuration based on value of information by trading-off information and cost, which can be then specialised to the particularities of ultrasonic guided-wave based inspection.*

Contribution. To explore this research objective, a novel methodology based on the value of information is proposed. This approach is based on a rigorous Bayesian damage localisation framework for optimal sensor placement, whereby the sensor locations are optimally chosen such that they render the largest information gain when inferring the damage localisation. The optimal number of sensors is obtained by assessing the value of information, and hence the cost of the SHM system is taken into consideration. In general, uncertainties coming from data measurements, unknown model parameters, and even a partially unknown diagnosis model itself are rigorously addressed. The mathematical description of the proposed methodology, several case studies, and a discussion on the results obtained and the potential extensibility of the method are provided in **Chapter 3**.

1.2.2   Research hypothesis 2

The design of active SHM systems also involves the optimisation of the actuators as well as the sensors. Besides, adaptive sensing SHM systems, which use a subset of sensors that are the optimal ones to assess a potential damage, require efficient methods to address the sensor and actuator optimisation as soon as a potential damage is detected [41, 42]. In this regard, the adoption of

classical and rigorous methodologies based on information gain entails a significant limitation when addressing real-world engineering scenarios, where a large number of sensors and actuators are required. To alleviate this burden, several methodologies have been provided in the literature which transform the objective function of the optimisation problem from being defined over binary variables (sensor→1, no sensor→0) to continuous variables [43]. This transformation is known as a *convex relaxation* [44], and it provides a considerable improvement in the computational cost under certain conditions [45]. However, none of these methodologies have focused on the optimisation of both the sensors and actuators. Furthermore, none of them have been applied on active ultrasonic guided-wave based SHM which could benefit from the use of these efficient approaches.

> **Hypothesis 2.** Optimal configurations for both sensors and actuators can be obtained simultaneously and very efficiently by using the Shannon's information entropy along with the cost of the system.

Research Objective 2. *Provide a methodology for simultaneous optimal actuator and sensor configuration based on (1) a rigorous quantification of modelling uncertainties and (2) a description of the cost of the system using convexification strategies to address the objective function in a highly efficient manner.*

Contribution. To address this twofold objective, an entropy-based optimisation method for both actuators and sensors is proposed. The objective function is convexified based on [43, 45], which implies that the optimisation problem has a global minimum within the interval where the variables are defined, and therefore simple methods can be used, such as the interior-point algorithm. In addition to the optimal location of sensors and actuators, the proposed method is able to provide the optimal number of sensors by introducing a cost function, which depends on the number of sensors and actuators. This novel cost-benefit methodology along with the proposed case studies that illustrate its capabilities are provided in **Chapter 4**.

1.2.3 Research hypothesis 3

The detection of damage in real engineering scenarios require robust, reliable, and fast methods. Ultrasonic guided-wave based SHM provides a relatively inexpensive and effective tool to assess the integrity of engineering structures [46]. In this context, several methods can be found in the literature for damage detection which are based on the energy content or the ToF characteristics of the guided-waves [47, 48]. However, they are usually based on deterministic modelling hypotheses that neglect the assessment and quantification of measurement uncertainties. These uncertainties are particularly relevant when considering industrial environments, as a biased assumption can introduce false negative or positive alerts. The adoption of Bayesian approaches is a rigorous yet powerful tool to account for these uncertainties, but they are computationally very expensive.

> **Hypothesis 3.** An efficient on-board SHM system for damage detection requires a fast and robust damage index that can be obtained using computationally simple fuzzy logic methods.

Research Objective 3. *Provide an efficient damage detection approach based on fuzzy logic theory, whereby measurement-related uncertainty can be quantified and damage severity information can be obtained as a by-product.*

Contribution. To investigate this research objective, a novel methodology based on fuzzy logic is proposed. This approach considers a measurement of data uncertainty to create fuzzy sets, which are subsequently used to evaluate the *degree of membership* [29] of new ultrasonic data within the healthy state. A significant variation of this degree of membership is deemed to belong to the presence of damage. Besides, the fuzzy sets enable the determination of a damage index defined in the interval $[0,1] \in \mathbb{R}$, whereby the damage detection and severity are assessed. The mathematical and procedural descriptions of this novel approach are provided in **Chapter 5**. Additionally, the application of this method in real plate-like structures is illustrated in Chapter 5 using

aluminium and CFRP sheets with different modes of damage, ranging from impact to fatigue damage. The ability to detect and monitor in real-time the degradation of structural performance is also investigated.

1.2.4 Research hypothesis 4

The localisation of damage in plate-like structures using ultrasonic guided-wave based SHM has been addressed in the literature using deterministic and probabilistic approaches [11, 49, 50]. The ToF obtained from a damage-scattered wave has been extensively used as a signal feature that provides information about the damage location. In this context, the few probabilistic Bayesian approaches proposed in the literature usually focus on quantifying the uncertainties associated with the unknown model parameters, such as the position of the damage or the group velocity of the guided-waves [50]. However, an important source of uncertainty comes from the assumption of a particular post-processing model, in the form of a TF transform, whereby the ToF information is obtained. This epistemic uncertainty stemming from the adoption of one particular model among a set of candidates may lead to a biased localisation of damage.

> **Hypothesis 4.** Bayesian theory can be adopted to rigorously assess both the damage localisation and the best TF model simultaneously with quantified uncertainty.

Research Objective 4. *Propose a multi-level BIP for (1) TF model class selection and (2) damage localisation along with an efficient algorithm that facilitates the identification of multiple locations of damage within a structure.*

Contribution. To deal with this twofold research objective, a set of TF candidate models is firstly proposed. These models are able to provide ToF measurements from damage-scattered guided-waves. The problem of model class selection is addressed by means of *posterior probabilities*, which provides infor-

mation about the relative degree of belief of the candidate models. These posterior probabilities are used to obtain a hyper-robust TF model. Next, the damage localisation is computed by considering the ToF estimation of the hyper-robust TF model using a BIP framework [24]. The asymptotic independent Markov sampling (AIMS) [51, 52] algorithm is adopted to obtain the posterior probability density function (PDF) of the model parameters, which is particularly efficient and accurate when dealing with multiple damage scenarios, i.e. several damage instances in the same structure, for example, via different mechanisms. The proposed methodology, along with their corresponding case studies and discussion are provided in **Chapter 6**.

1.2.5   Research hypothesis 5

Finally, the identification of damage using ultrasonic guided-waves needs to be also addressed in order to provide a complete diagnosis of a structure. In the literature, some Bayesian methods have been proposed which use signal features obtained from measurements in isotropic beams in order to quantify the damage [53, 54]. However, a natural step forward would be to address layered materials, such as composite materials, that are closer to the ones used in the aerospace industry. In this context, and given the complex nature of such materials, Bayesian methodologies provide a powerful tool to handle the associated uncertainties [32]. Additionally, the identification of the type of damage mode provides valuable information for the maintenance operator in order to prepare a proper maintenance plan and to carry out further studies on the remaining useful life of the component.

> **Hypothesis 5.** Measurements from ultrasonic guided-waves can provide useful information about not only the presence and location of damage, but also the severity and type of damage within a composite structure.

Research Objective 5. *Propose a multi-level Bayesian approach in order to quantify and identify the type of damage based on posterior probabilities, which measure the*

degree of belief of different damage hypotheses.

Contribution. To address this research objective, a multi-level model-based BIP framework is developed. An ultrasonic guided-wave propagation model based on the hybrid WFE method [55] is used to infer damage-related information represented by a number of model parameters, e.g. damage location and transmission and reflection coefficients, while accounting for different sources of uncertainty. These parameters can be grouped and categorised depending on the damage nature, e.g. cracks or delaminations. Thus, different model parametrisations, hence different model hypotheses, related to different damage types are formulated in order to address the identification problem. Additionally, the model parameter inference problem allows the localisation of damage and the estimation of its extent. The methodology, which is limited here to one-dimensional beam structures, is shown in **Chapter 7**. Several case studies are also presented to show the capabilities of the proposed multi-level Bayesian framework in identifying and quantifying the damage modelled for composite structures.

2
Literature review

The process of SHM consists of the following stages: (1) design of the optimal strategies and configurations of a SHM system; (2) damage detection of a structure or structural system that is in operation; (3) localisation of a damaged structure or damaged area within a structure; (4) identification and quantification of the previously localised damage; and (5) prediction of the remaining useful life of the structure so that maintenance decisions can be made. The emphasis throughout this review is on the first four stages pertaining to the diagnosis part, and hence the state-of-the-art in these fields is presented.

The literature review is organised as follows: Section 2.1 introduces the context and state-of-the-art of the most used SHM techniques in engineering applications; Section 2.2 provides an overview on optimal sensor placement approaches; Section 2.3 summarises the methods that address the optimisation of actuators as well as sensors; Section 2.4 depicts the state-of-the-art of damage detection techniques as well as an overview of experimental techniques; Section 2.5 describes the latest methods used for damage localisation; damage identification techniques are briefly presented in Section 2.6. Finally, an overview of types of uncertainty, probability logic and sampling-based methods is provided in Section 2.7. It is worth mentioning that the focus throughout this review lies in two specific parts: (1) ultrasonic guided-wave related techniques and (2) uncertainty quantification methods.

2.1 Overview of NDT and SHM techniques

The assessment of the structural health condition can be addressed by adopting one of the following approaches: (1) NDT techniques and (2) SHM methods. The first group of techniques are usually adopted in scheduled maintenance policies, where they provide a sufficiently accurate level of information about the damage mechanism and the extension of the damage. Alternatively, SHM methods can be regarded as tools that enable an online and continuous monitoring of the complete structure by using permanently mounted sensors at the cost of a lower degree of precision.

Many NDT techniques are published in the scientific literature and they are commercially available given the high level of standardisation that they have reached (see Figure 2.1). For instance, *radiographic inspection* [56] can be used to obtain the discontinuities in the material caused by manufacturing errors or damage [57]. The resulting image is dependent on the absorption properties of the structure being tested. *Infrared thermography* [58] is another NDT imaging tool that is based on the detection of thermal radiation properties of the specimen. It typically requires a heating source and an infrared camera, in addition to a processing unit that is able to interpret the recorded heat patterns as possible damage sources [59]. *Eddy current* [60] NDT is used in electrically conductive materials and it is able to detect damage (e.g. corrosion or cracks) by measuring impedance changes [61]. Alternatively, ultrasound-based NDT techniques provide with information through-the-thickness of thin and thick structures. The most commonly adopted ultrasonic techniques are the *pulse-echo* [62] and *through-transmission* [63]. They use a transducer for the emission and acquisition and an emitter and a receiver, respectively. The main strength of this technique is that the signals contain all the information coming from inhomogeneities inside the structure, although at the cost of complex post-processing techniques. Overall, the applicability of the previously described NDT techniques is limited to a localised area of the structure and to an offline-type of inspection [64].
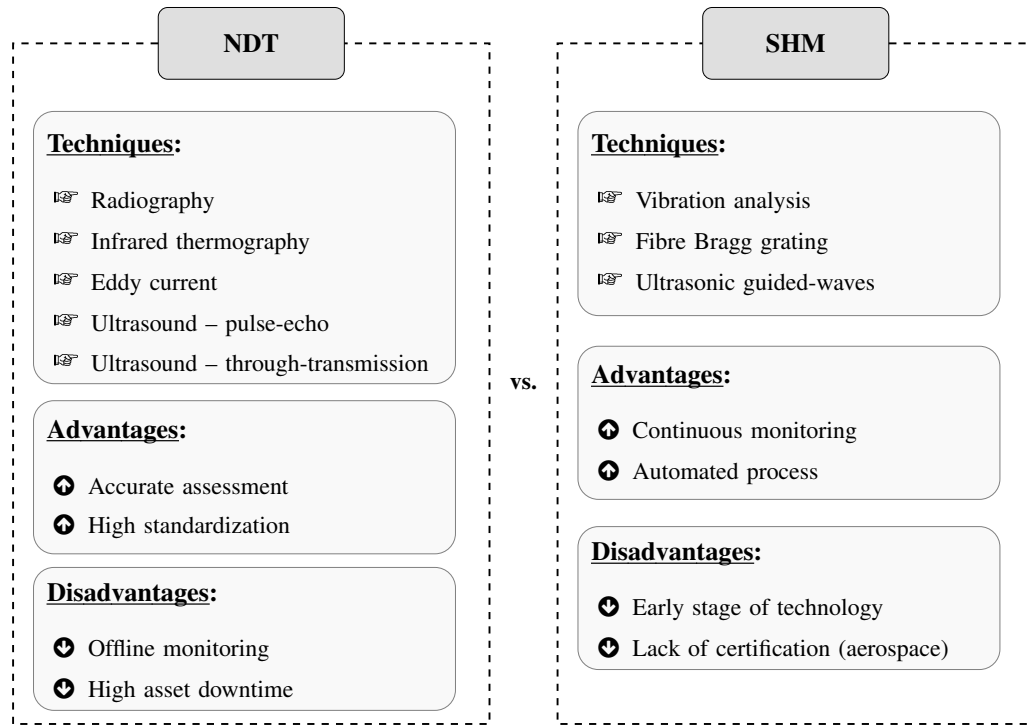
Figure 2.1: Comparison between NDT and SHM.

A significant amount of SHM methods have been developed during recent decades, driven by the interest of industries in adopting condition-based maintenance plans. For instance, *vibration*-based monitoring methods [9] (e.g. using accelerometers) are used to detect, localise [65], and identify defects in very large structures, such as bridges or buildings [66]. However, this relatively mature technology is limited to a large scale, and the assessment of localised damage entails the use of high-order modes which may be difficult to excite and post-process [67]. *Fibre Bragg grating* sensing systems [68] have also been widely applied to civil structures, whereby the deformation of a structure can be monitored and an anomaly may be inferred from the measurements [69]. This technology is mainly limited by the lack of engineering experience and the high cost of the interrogation system [70]. Ultrasound-based techniques have also been investigated for SHM in aircraft structures. In this context, ultrasonic guided-waves stand out, given their ability to actively interrogate a relatively large two-dimensional structure [71] (see Figure 2.2), in contrast to the ultrasonic NDT techniques mentioned above. In this case, ultrasonic waves bounce back and forth inside the monitored structure, causing interference

phenomena that ultimately lead to the creation of guided-waves [72]. Note that the use of ultrasonic guided-waves is usually limited to thin-walled structures, as the plate thickness needs to be smaller or on the order of magnitude of the wavelength (i.e. wave velocity divided by frequency) for guided-waves to exist. Besides, a high excitation energy is required to excite guided-waves in relatively thick plates, which establishes an additional limitation of this technique for thicker structures. Their main advantage over vibration analysis and the use of fibre Bragg gratings is that they are able to interact with small damage forms in their initial stages of growth [73]. This is particularly relevant in structural applications using composite materials, due to their susceptibility to sudden and non-visible damage. Additionally, this type of SHM is relatively cost-effective, as long as the correct number and positions of sensors are used, given that they are low-weight and relatively inexpensive compared to the cost of the structure itself. These advantages have attracted the aerospace industry, which seeks to benefit from the early detection of small and localised damage enabling a cost-effective and safe transition from scheduled to condition-based maintenance.
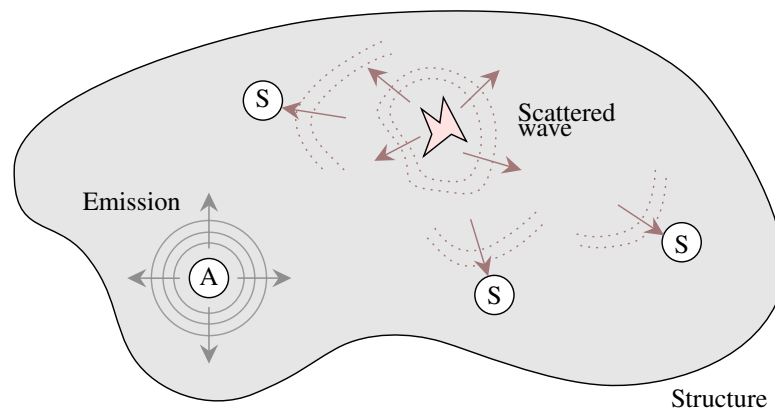
Figure 2.2: Schematic of guided-waves based inspection in an arbitrary structure. An actuator (A) emits guided-waves, which interact with damage and creates a damage-scatter that is read by the sensors (S).

2.2   Optimal sensor configuration

The first stage in SHM usually consists of the optimal design of a SHM system. In particular, the placement of sensors in a structure is one of the most important parameters to be optimised that have been extensively studied in the literature. The number and position of sensors play a key role on the quantity and quality of the information collected, hence on the damage assessment. Here, a review on different deterministic and probabilistic approaches to address the optimal sensor placement in structural applications is presented.

In the context of ultrasonic guided-wave based SHM system design, several approaches have been proposed in the literature to optimise the number of PZT sensors and/or their locations in plate-like structures in both active sensing diagnostics (ASD) and passive sensing diagnostics (PSD) [74]. PSD techniques consider an arbitrary number of sensors in listening-mode (e.g., receiving signals from an acoustic emission source) which capture sudden changes in the structure, such as impacts or crack growth. These techniques have been widely used in the literature for impact localisation. For instance, in [75], a deterministic method to localise impacts by using the time of arrival measured at several PZT sensors was proposed. A structural model-free approach was proposed in [76], which allowed not only the localisation of the impact, but also the reconstruction of the force time history by using transfer functions. Alternatively, impact localisation has also been addressed by a hybrid reasoning based methodology using analogy in a learning database, and wavelet transforms to extract damage position-related signal features in [77]. More recently, the efficiency of impact localisation in PSD has been enhanced by using kernel extreme learning machine, which was compared to other computational techniques in [78]. Alternatively, ultrasonic ASD techniques consider the interaction of the transducers with the structure by means of emission and reception of guided waves [46]. Sparse or phased-array sensor layouts are placed so that a structure is actively interrogated on demand, which confers higher accuracy and reliability [79]. In both cases, several attempts have been

proposed to optimise the SHM performance (number and location of sensors) through optimisation methods such as (1) artificial neural networks combined with genetic algorithms [80–83], whose efficiency has been improved by using the trilateration technique [84] and whose convergence has been enhanced by modifying the crossover stage in [85]; (2) simulated annealing to achieve complete coverage and discrimination whereby every point in a structure is covered by at least one sensor [86]; and (3) particle swarm optimisation to maximise the damage localisation accuracy of a SHM system based on beamforming imaging [87]. Alternatively, sensor placement optimisation has been addressed by the use of performance indices such as the probability of detection in [35, 36], damage-related PDFs derived from the weights of an artificial neural network in [88], and the area of coverage, whereby guided-wave propagation properties and geometrical complexities such as openings are taken into account [37, 38, 89]. The influence of faulty sensors in the area of coverage of the entire network [90] and the use of a more efficient mixed integer nonlinear algorithm [91] have also been investigated in order to improve its robustness and performance, respectively. The vast majority of these approaches rely on deterministic assumptions, and hence do not account for the inherent uncertainties associated with ultrasound-based SHM, such as signal noise and uncertain material and ultrasonic parameters. These uncertainties propagate across different models leading to uncertainty in the damage reconstruction, which needs to be quantified for a rigorous optimal sensor location assessment.

Several Bayesian probabilistic approaches for optimal sensor configuration have been proposed in the literature, but for applications other than guided-wave based SHM. For example, the position and/or the number of sensors in structural systems have been optimised by making use of model-based BIPs and probabilistic metrics. Additionally, *Shannon's information entropy* of the pre-posterior distribution was considered in [92, 93] by assuming asymptotic approximations to reduce its associated computational cost. Forward and backward sequential sensor placement algorithms are typically used to place sensors optimally in this context [94, 95]. However, the issue of sensor clus-

tering could appear using the previous approaches due to the lack of spatial correlation in the prediction error between sensor locations, which was tackled in [96]. The *Kullback-Leibler (KL) divergence* between the prior and posterior distributions, which accounts for the information gained after measurements have been acquired, has also been considered for optimal sensor placement [97]. It is worth mentioning that the maximisation of the KL divergence has been found to be equivalent to the minimisation of the information entropy [40]. The computation of such information-related features establishes again a challenging scenario, which has been alleviated in the literature by using polynomial chaos expansion approximation techniques combined with Monte Carlo (MC) sampling [39] to reduce the computational burden of the model evaluations, stochastic optimisation [98], and principal component analysis [99]. Additionally, the *mutual information* between data and model parameters has been considered as feature to be maximised depending on the sensor positions [100], although it can be considered equivalent to the minimisation of the information entropy as long as asymptotic approximations are taken into account [45, 101]. In analogous structural applications, Bayesian experimental design framework has been proposed, which provides a case-specific utility function, such as the KL divergence [102], whereby the maximisation of its probabilistic expectation provides the optimal experimental design [103]. As a general comment, these methods provide rigorous criteria for optimal sensor configuration from an information-theoretic point of view, so that the more sensors are used, the more information is gained and the better is the damage identification [94]. Note that some of these approaches, which focus on the selection of the correlated prediction error models, not only make it possible to account for the uncertainties but also provide indications of the optimal number of sensors [96]. However, in practice, decision-theoretic instead of information-theoretic criteria would be preferred, where important variables such as the cost of the monitoring system can be rigorously taken into consideration for optimal SHM system design.

Given that the performance and reliability of a SHM system heavily relies on the number and position of sensors, an infinite number of sensors would

be required to achieve the maximum level of information. Such rule finds a limitation in reality, whereby the amount of resources is restricted, and therefore a trade-off is necessary. In the particular case of ultrasonic guided-wave based SHM, the aforementioned trade-off is especially relevant since uncertainty factors such as sensor noise, material property uncertainties, and variations in the acquisition and generation equipment, are well-known sources of complexity which limit the monitoring functionality. For this reason, several authors have recently adopted the concept of *value of information* [17, 18] to investigate optimal SHM designs based on a healthy and principled balance between the amount and the benefit of the monitoring information. For example, the value of information has been adopted to address the maintenance decision optimisation in [104, 105] by using SHM results [106, 107], reliability methods [108], and influence diagrams [109]. Besides, it has also been used to assess the value of SHM systems based on structural risks, integrity management, service life costs, pre-posterior analysis, and Bayesian decision theory [110–113]. In the context of optimal sensor placement, the value of information has been adopted to optimise spatially distributed systems, which allow for information propagation [114], although with known submodularity issues whereby the benefit of adding new measurements to a smaller set is comparatively higher than adding them to a greater set. This is particularly relevant when using greedy optimisation strategies along with different sets of information, as it might lead to suboptimal solutions far from the optimal one [115]. However, none of these contributions to date has focused on ultrasonic guided-wave based SHM, precisely where the benefits of this decision-theoretic concept can be fully exploited due to the high dependence of ultrasonic information on both the number and position of PZT sensors. Therefore, a rigorous approach that trades-off cost of the SHM system and information gain in ultrasonic guided-wave based inspection would still be necessary.

2.3   Optimal actuator and sensor configuration

The performance of SHM systems is also related to the number and location of actuators as well as sensors depending on the application field. When measurements of a structure are acquired during an external action (e.g. earthquakes or wind), the SHM system only demands sensors to measure the response of such structure. However, when SHM is actively carried out, i.e. a controlled action is induced into the structure, the optimisation of the actuators plays an important role. In this context, the optimal joint positioning of actuators and sensors has been studied in structural applications other than ultrasonic guided-wave based SHM by heuristically maximising the controllability of global vibrations [116–119]. Further vibration-related features such as the observability of modal shapes and the spillover effect of residual modes have also been introduced as performance indicators to optimise the location of both actuators and sensors in [120, 121]. Note that most of the previous works used genetic algorithms (GA) as optimisation approach in order to search for a global optimum. These types of algorithms, however, might find a limitation if the objective function is especially heavy to compute and a relatively high number of variables are required to be optimised.

In contrast to evolutionary algorithms, convex optimisation [43] techniques can be used to provide optimal configurations of sensors and/or actuators in a highly efficient manner, as reported in the literature. These optimisation techniques require that the objective function is convex within the interval in which the variables are defined, which might be achieved by relaxing binary decision variables into continuous ones [44]. Convex mixed-integer semidefinite algorithms have also been proposed in structural dynamics applications to address the optimisation of sensors and actuators to minimise the dynamic cost and state estimation error [122]. More recently, a non-smooth convex algorithm using proximal methods was employed for optimal sensor and actuator location based on the controllability of dynamic systems [123]. In general, one of the advantages of using convex objective functions is that they can be min-

imised using conventional algorithms for function minimisation such as the interior point algorithm [124, 125], which is highly efficient in terms of computational cost. However, none of the previous methods has considered the uncertainty present in the data as well as in the model, thus limiting its robustness against noise or modelling uncertainty. Note that the only Bayesian attempts for optimising jointly actuators and sensors for SHM systems have been presented in Section 2.2, which focus on the optimisation of sensors only. In addition, it is worth mentioning that the main limitation of Bayesian methods lies in the prohibitively high computational cost for relatively large search spaces; specifically, when the actuators are added to the optimisation problem such search space increases significantly. Therefore, a rigorous and highly efficient approach able to address the joint optimisation of actuators and sensors by considering different sources of uncertainty, which can be used for active ultrasonic guided-wave based SHM, is still missing in the literature.

2.4   Damage detection

The second stage in SHM consists of the detection of damage either in a structural system or in a particular structure. In this stage, the data acquired by experimental methods are post-processed in order to obtain an index-based damage estimator. Based on the value of such index, a decision on whether or not there is damage can be taken.

Ultrasonic guided-waves can be actively excited in structures using different methods that can be broadly categorised into: (1) pitch-catch, i.e. a PZT transducer emits guided-waves while other transducers act as receivers only, and (2) pulse-echo where the emission and reception are carried out using the same transducers. Due to manufacturing and cable track limitations, PZT transducers are typically placed in phased-array types of geometry. These arrays of PZT can be used by test methods that only utilise one emitter PZT for each test, while the rest act as receivers, such as the round-robin method [126]. However, signal post-processing techniques are needed in order to obtain damage-

related information out of the measurements. One of the most used methods is receiver beamforming [127], where the signals acquired in a round-robin test are summed up (e.g. using delay-and-sum (DAS) imaging algorithm [128]) at different points of the structure using the ToF from the centre of phased-array to the point of interest as delay [129], thus creating a virtual representation of the beamforming technique based on superposition. Note that both round-robin and receiver beamforming can be carried out using different geometrical layouts of PZT transducers. In contrast, transmission beamforming is the only technique that can use multiple PZT transducers simultaneously as emitters [127], which is particularly difficult to implement in practice due to complexities in the hardware. The transmission beamforming technique is able to create physically a wave-front with a significantly greater amplitude by using a whole array of PZT simultaneously in generation [126, 130]. It creates a beam from the constructive interference of different wave packets by introducing a phase difference between ultrasonic signals. By modifying such phase, the main beam can be steered in different directions to sweep a large area [131]. Transmission beamforming has been scarcely used in practice, while receiver beamforming has been widely studied in the literature due to the ease of experimental implementation [132]. Unfortunately, receiver beamforming still has all the limitations of the round-robin method due to the presence of only a single emitter at a time, e.g. lower amplitude and signal-to-noise ratio (SNR). In contrast, transmission beamforming overcomes these issues providing a higher amplitude and therefore an information with higher quality. A more in-depth review of the different beamforming techniques is provided in the following subsections.

2.4.1   Beamforming techniques

Receiver beamforming

The receiver or virtual beamforming technique has been developed and investigated over the years. For instance, the performance of 1D and 2D geometries

of arrays of PZT transducers has been comparatively studied in order to obtain the configuration that provided lower side-lobe effects by Yu and Giurgiutiu [133]. The experiments were carried out using a data acquisition system, a signal generator and a multiplexer unit that controlled PZT transducers in order to perform round-robin tests. The resulting ultrasonic signals were then used for an imaging algorithm. Other geometries of PZT arrays have also been explored. This includes circular arrays with a single actuator in the centre [134] or a comparison of uniform and circular arrays for localising acoustic emission sources, i.e. using the PZT transducers in passive mode [135]. Additionally, the performance of receiver beamforming has been assessed in composite structures using a laser vibrometer for acquiring ultrasonic signals. The specific guided-wave parameters and the energy skew effects are also taken into account for anisotropic materials by Yu and Tian [136]. The use of receiver beamforming and laser Doppler vibrometer have been further explored in damage detection and quantification in composite structures [137]. Also in an improved damage identification in aluminium plates by a modified DAS algorithm by Tian *et al.* [138].

Nevertheless, receiver beamforming suffers from side-lobe effects in the reconstructed image. This issue has been typically addressed by using adaptive methods, which apply weighting coefficients to the signals received in the array of PZT transducers in order to reduce the side-lobe effects [139, 140]. For example, the adaptive technique has been used for the development of an improved imaging algorithm using distributed arrays of PZT and a multipath approach in both aluminium and composite plates, without the need of material information [141, 142]. Furthermore, this beamforming mode has been applied to laser vibrometer measurements along with a baseline-free imaging algorithm [143]. Alternatively, the adaptive method has been recently applied for transmission beamforming, whereby a recursive approach has been used for the generation of the main beam in two directions [144]. However, most of the receiver beamforming based approaches show a limitation for real-world SHM applications, which typically require a light-weight and integrated de-

vice. Such a device should be able to both excite and acquire PZT transducers with a relatively low post-processing burden and have the ability to work in a noisy environment.

Transmission beamforming

To provide comparatively higher amplitude in the acquired signals, in order to be suitable for noisy working environments, transmission beamforming may be used. However, this technique has typically required a more complex signal generation system, comprising external function generators and data acquisition systems (e.g. oscilloscopes) [145, 146], thus limiting its applicability to real-world engineering scenarios, i.e. to out-of-lab environments. In addition, the number of actuators emitting synchronously is limited to the number of channels available in the function generator [147], given that the use of more channels entails more advanced equipment, which is prohibitively expensive for most of the engineering cases. Thus, the use of this technique have focused mainly on the development of the proof-of-concept with conventional equipment (e.g. using waveform generator cards) [127]. For example, the performance of compact triangular phased arrays was investigated by Senyurek *et al.* [148], where two PZT transducers were used as actuators with a third one acting as sensor. Compared to receiver beamforming, the transmission beamforming technique has the advantage to generate different geometries of beams, such as the bottle shaped beam and the vortex beam. These geometries may be helpful for NDT and SHM given that they provide greater amplitudes, and therefore a higher SNR can be obtained [149]. Nevertheless, there is still an evident need for a dedicated hardware able to perform transmission beamforming using a higher number of PZT actuators in order to achieve enhanced ultrasonic guided-wave based SHM.

2.4.2   Post-processing for damage detection

Efficient damage detection methods are typically based on signal features such as energy content and ToF, which can be obtained straightforwardly from the time-amplitude guided-wave representation. Alternatively, model-based inverse problems methodologies can be applied to extract a higher level of information from the signal [23], at the cost of a significant increase in computational time. To avoid such computational complexity while providing a high level of information, some authors have looked at signal features, which can be obtained from TF transforms. These signal features are commonly monitored to obtain a better understanding of the guided-wave behaviour when it interacts with damage. Then, the correlation of those signal features with physical damage features such as the length of fatigue crack or the area of delamination has been explored by many authors. In particular, the correlation between energy-based indices and crack growth in aluminium plates by using TF transforms has been explored in [47, 150]. On the other hand, the use of time-amplitude signal features has been reported in the literature to be a useful feature to monitor damage in aluminium plates [151, 152]. Other damage indicators have been also reported in the literature. Among them, both the energy density and the ToF have been related to the diameter of delamination in composite laminates in [48]. Likewise, energy-based probability damage indices have been explored and empirically correlated with crack growth in a full-scale aircraft structure by Qiu *et al.* [153]. Lastly, a mixed model based on phase and amplitude changes was developed to monitor crack length, and was experimentally validated in aluminium plates by Yang *et al.* [154].

The aforementioned damage-related features are normally used to classify structures into several health states. Thus, key information about the relevance of the damage is facilitated to the operator of the structural system. In this context, fuzzy logic provides a powerful tool that accounts for: (1) the structural damage classification in predefined importance levels and (2) the classification uncertainty, i.e. providing with the degree of membership of a damage into

some predefined importance levels [155]. The damage monitoring of structures by using fuzzy techniques has been explored by many authors in the literature. Particularly, fuzzy sets have been used as the basis of the inference system for bridge damage diagnosis [156]. A Bayesian updating framework has also been proposed to define structural health patterns (i.e. damage levels) by Taha and Lucero [157]. The dynamic behaviour of a structure was established by a wavelet norm index, which was then used to classify the health state according to the patterns. Mojtahedi *et al.* [158] proposed the use of a model updating approach to define damage levels using a finite element model. Fuzzy logic was then used to classify the damage among the previously defined levels in an efficient manner. More recently, Pragalath *et al.* [159] developed a fuzzy logic-based framework which supported the quantification of damage using image processing algorithms. However, a highly efficient yet robust method designed to work under real-world engineering scenarios is still missing in the literature in the context of ultrasonic guided-wave based SHM. This method will be able to provide a damage assessment by means of a damage index using ultrasonic guided-waves obtained by transmission beamforming tests.

2.5   Damage localisation

The third stage of SHM focuses on the localisation of damage within either a structural system, i.e. the localisation of a structure among a whole system such as an aeroplane, or a structure whereby a bounded region of damage is to be localised. The latter is particularly relevant for industries such as the aerospace industry, where some structures are relatively large, i.e. in the order of magnitude of metres. The use of traditional inspection techniques (e.g. visual inspection) for such a maintenance task involves a high cost for the operator with limited accuracy. In the context of ultrasonic guided-waves and damage localisation, several model-based inverse techniques have been reported in the literature [11], for instance, the time-reversal technique [49] or imaging algorithms based on differences of ToF between guided-waves [160] and cross-

correlation between signals [161]. Among them, the ToF has been extensively used as a signal feature for its efficiency in obtaining information about material properties along with damage localisation using post-processing scattered signals.

TF representation techniques have been intensively used for the extraction of ToF as a signal feature. By TF representation, a frequency domain spectrum can be obtained at each instant of time [162], however the results slightly differ from each other depending on the adoption of the various approaches available in the literature. Among them, the Hilbert-Huang transform (HHT), the continuous wavelet transform (CWT), the short-time Fourier transform (STFT) and the Wigner-Ville distribution (WVD) [162–165], are some of the most commonly used techniques in ultrasonic guided-waves based SHM applications. For instance, CWT was used in [50] to extract the time of flight from damage-scattered waves in order to carry out damage localisation in plates. Additionally, the Hilbert transform, which is closely related to the HHT, was also used for damage localisation in [166, 167]. Typically, the selection of one among the available options has been based on the modeller's experience or based on specific TF resolution characteristics. However, the selection of an inappropriate model may result in a biased damage identification [168, 169] due to the disparate model assumptions and hypotheses adopted for each of them. In other words, the choice of a particular TF approach instead of another one is subject to *epistemic* uncertainty (i.e., lack of knowledge). Moreover, ultrasound-based damage localisation conveys other sources of uncertainty which are mostly related with the measurement system and physical properties of the material. They might produce unreliable damage predictions should these uncertainties not be properly considered and quantified within the calculations.

To partially address this modelling issue, a number of researchers have proposed the use of probability-based methods, e.g. maximum-likelihood estimation [170], kernel density estimation [171], extended Kalman filter [172], and BIP [50]. Among them, the BIP applied to ultrasound based damage localisation is getting increasing attention within the SHM community due to

its ability to handle and quantify large uncertainties in a rigorous manner, although it is still in its early stage. For instance, in [50], the BIP was successfully demonstrated in localising damage areas in aluminium plates. More recently, a BIP methodology to account for the anisotropy in the *group velocity* was proposed in [166] for composite laminates. Notwithstanding this, there is still an evident need for a rigorous treatment of the uncertainty in modelling the damage localisation using ultrasonic guided-wave based methods, especially when multiple damage locations are expected in the monitored structure.

2.6   Damage identification

Lastly, the fourth stage of SHM involves the identification of damage, i.e. the specification of the type of damage so that a concrete type of maintenance action can be taken. Over the years, different methodologies for identification and quantification of damage have been developed to overcome the drawbacks derived from classical modelling approaches for ultrasonic guided-waves (e.g. finite element modelling (FEM)). One such example is the semi-analytical finite element method [173, 174] which is very time efficient when modelling structures that are discontinuous in their thickness but continuous in the direction of propagation. This method, however, experiences serious limitations in case of structures that are periodic in the direction of propagation [175]. Another guided-wave modelling approach is the scaled boundary finite element method [176], which allows a reduction of the degrees of freedom in two or three orders of magnitude when compared with the FEM. This is achieved due to the use of an analytic formulation to scale the exterior domain [177]. Additionally, the Rayleigh-Lamb wave equations [178] have been used to obtain analytically the dispersion characteristics of guided-waves through different materials. All of these approaches provide more efficient, yet accurate, tools for ultrasonic guided-wave modelling compared to FEM. More recently, the hybrid WFE method [55] was proposed to facilitate the post-processing of the eigenproblem solutions. It is based on a combined analytical and numerical

framework to reduce computational complexity. The efficiency of the hybrid WFE method encourages its use with model-based inverse approaches for primarily identifying damage, whereby a measured ultrasonic guided-wave can be used to identify and quantify the damage in a plate-like structure. However, this method is still in its early stage in the context of ultrasonic guided-waves at a relatively high frequency range, and consequently only 1D structures, e.g. beams, can still be properly modelled [179].

Damage identification and quantification using guided-waves can be difficult given the associated modelling complexities and uncertainties stemming from several sources, e.g. material properties, modelling assumptions, and measurement noise. To address this challenging scenario, some Bayesian approaches [32] have been proposed in the literature. For instance, a Bayesian multi-level approach for identifying damage patterns from impact damage in CFRP laminates using through-the-thickness ultrasonic measurements was proposed in [23]. In the field of guided-waves, a Bayesian framework for quantifying and localising damage in isotropic structures was proposed in [54]. A spectral finite element model [180] was used to simulate a semi-infinite beam whereby the damage was modelled by reducing the cross-sectional area of the beam. A Bayesian framework was applied to infer the model parameters, i.e. position and damage size. A Bayesian model class selection approach for the localisation and quantification of a number of cracks in isotropic beam-like structures has been proposed by He and Ng [53]. The method uses posterior plausibilities to assess the degree of belief of different model classes, which represent different numbers of cracks, in order to obtain the most probable damage scenario. More recently, Yan *et al.* [181] introduced a new Bayesian framework for damage identification based on an analytical probabilistic model of the scattering coefficient and a computationally efficient wave scattering simulation scheme. Notwithstanding the previous approaches, there still an evident need for a computationally efficient method in order to obtain damage information from guided-wave measurements in layered and orthotropic materials, using the time-domain signal directly measured in experiments.

2.7 Uncertainty quantification

As described in the previous sections of this literature review, uncertainty constitutes a critical aspect for making unbiased and principled maintenance decisions in each of the diagnosis stages. Different interpretations of the uncertainty nature can be found in engineering, i.e. *aleatory* and *epistemic* uncertainty. Aleatory or *irreducible* uncertainty refers to the inherent randomness caused by the stochasticity of some processes, e.g. wind or an earthquake [32]. Epistemic or *reducible* uncertainty refers to the lack of information about the process itself (e.g. manifested by an approximate numerical model), which could be reduced or even completely removed by collecting additional new data [182, 183]. However, scarce data are typically available in most engineering scenarios; hence, both aleatory and epistemic types of uncertainties are present and need to be quantified. To this end, several methods arise such as probability theory [184], fuzzy logic [185], and imprecise probability [186].

Within the probability theory, which has gained attention from engineering applications over the last decades, two methods can be differentiated: the *frequentist* and the *Bayesian* approaches. The frequentist method enables the quantification of aleatory uncertainty alone by assuming independent repetitions of a random experiment, but without the consideration of prior knowledge [31]. It is also based on *ad-hoc* mathematical estimators that are not effective in all situations, such as extreme cases. Alternatively, Bayesian techniques overcome the previous limitations and quantify both aleatory and epistemic uncertainty by considering prior information and determining the optimal estimators in an automatic and principled manner [31]. These methods are based on *probability logic*, whereby probability is viewed as a multi-value conditional logic that accounts for the case of incomplete information, and therefore it extends the Boolean logic (0 or 1) [32]. In this context, a conditional probability $P(a|b)$ represents the subjective probability or degree of belief in the proposition a, given the (possibly incomplete) information b.

Bayesian methods for inverse problems usually involves the use of stochas-

tic methods to obtain the posterior distribution of model parameters, whereby a model is updated based on the available data. This is as a result of the lack of analytical solutions for generic non-linear relations between quantity of interest (QoI) and the model parameters. In this context, many Markov chain Monte Carlo (MCMC) methods [187] have been developed for sampling the posterior distribution without the need for calculating the normalising constant of the Bayes' theorem. In particular, two properties need to be satisfied to ensure that the samples are properly extracted from the target distribution: (1) *ergodicity*, whereby it is ensured that the areas of high probability density are explored; and (2) *stationarity*, whereby all samples are equally distributed as per the posterior PDF.

The Metropolis algorithm is one of the first MCMC algorithms reported in the literature, which was initially developed by Metropolis *et al.* in [188], and later generalised by Hastings in [189]. Its versatility and simplicity of implementation make the Metropolis-Hastings (M-H) algorithm one of the most used in the literature. It generates samples from a specially constructed Markov chain whose stationary distribution is the posterior PDF. Its main drawback is the slow convergence in parameter spaces with high dimensionality, especially when some parameters are highly correlated [190]. The Gibbs sampler [191] partially overcomes these issues by making it possible to sample marginal distributions, without the need to sample the complete multivariate distribution [192]. Alternatively, slice samplers, which sample uniformly from the target distribution and consider the horizontal coordinate only, may provide faster convergence than M-H and Gibbs sampler with less tuning effort [193]. The reversible jump MCMC algorithm allows jumping between different subspaces of different dimensionality [194]. This method is particularly useful when the dimensionality of the model parameters vector is variable, and hence such a dimensionality is an unknown parameter *per se*. Sampling difficult posterior PDFs can also be addressed with adaptive methods, such as the transitional MCMC algorithm [195] and the AIMS [51, 52], whereby intermediate PDFs are constructed until they converge to the target PDF. The main

difference between these adaptive methods lies in the sampling procedure of the intermediate steps: while the AIMS method samples are generated from a proposal distribution based on the previous step, the transitional MCMC approach provides the Markov chains by resampling at each level. This difference leads to an overall better performance of the AIMS method, especially for high dimensional and multimodal scenarios [51].

2.8 Conclusions about the state-of-the-art

Once the literature has been extensively reviewed, the main gaps and challenges can be identified for each of the processes in SHM, and the main contributions of this thesis, outlined in Chapter 1, can be put in context. In the following points, the main conclusions along with the proposed contributions are described:

☞ For ultrasonic guided-wave based optimal sensor placement (see Section 2.2), a framework that trades-off information gained and cost of the SHM system is missing in the literature and it is proposed and fully developed by using the concept of value of information in Chapter 3.

☞ However, a more efficient methodology that considers both actuators and sensors is crucial for active SHM systems, as can be extracted from Section 2.3. To overcome such an issue, a convex entropy-based objective function is proposed for optimal sensor and actuator configuration in Chapter 4.

☞ For damage detection, a fast and efficient method to detect and monitor damage, which can use information coming from an on-board type of device that generates and acquires guided-waves, is still missing in the literature (refer to Section 2.4). Hence, a fuzzy-logic based damage detection methodology that is based on ToF differences is proposed and experimentally tested using aluminium and composite structures in Chapter 5.

☞ The review on the damage localisation stage has revealed a lack of rigorous approaches to deal with modelling and measurement-related uncertainties altogether (see Section 2.5). Therefore, a unified methodology to handle uncertainties from the post-processing stage of the signal using TF transforms and an ellipse-based model for the reconstruction of multiple damage locations is proposed in Chapter 6.

☞ Finally, the identification of damage in layered structures using Bayesian methods and ultrasonic guided-waves has shown to be in its infancy, as observed in Section 2.6. Thus, the use of an efficient wave propagation model along with a multi-level Bayesian framework is proposed in Chapter 7 to tackle the challenging scenario that the damage identification stage entails.

Part II

CONTRIBUTIONS

3

Optimal sensor configuration based on value of information

A novel and generic methodology for optimal sensor configuration in ultrasonic guided-wave based SHM is provided in this chapter. To take rigorously into account both information gain and cost-related benefits while accounting for the underlying uncertainties, the expected value of information is proposed as an optimality criterion. The value of information is defined as the difference between the maximum prior and posterior expected benefits [107], and here it is proposed to be used as an objective function for obtaining the optimal number of sensors. In particular, different sensor configurations with an increasing number of sensors are proposed according to a forward sequential sensor placement algorithm [94]. Then, the optimal sensor position for each of these configurations is determined by maximising the information gained between the prior and the posterior PDFs of the damage identification parameters (e.g., damage position). The computation of the information gain is carried out using a damage localisation model based on a robust Bayesian methodology proposed in Chapter 6 (published in [24]). Next, the expected value of information for each of the optimally-located sensor configurations is obtained, so that the optimal configuration is chosen as the one which maximises the value of information. The methodology is illustrated using two

case studies for two different plate-like structures, namely (1) a flat aluminium panel and (2) an aeronautical hat-type stiffened aluminium plate. The optimal sensor configuration is obtained considering the prior information about the possible damage occurrence within a particular bounded area, whereby the data is simulated by using a time of flight model [170]. Then, the effectiveness of the optimal sensor configuration is tested in a particular damage scenario by simulating the structures in Abaqus$^{®}$ [196] and inferring the position of the damage using the robust Bayesian methodology provided in [24] and Chapter 6 of this thesis. In general, the results show the efficiency of the proposed methodology in obtaining the optimal number and position of sensors in contrast to pure information based approaches. In particular, the results reveal that non geometrically constrained configurations are preferred from a value of information point of view, since they provide the best trade-off between amount of information and benefit of such information.

The remainder of this chapter is organised as follows: Section 3.1 describes the proposed optimisation methodology based on the value of information and the fundamentals of Bayesian damage localisation; Section 3.2 illustrates the methodology through two case studies for two different plate-like structures; a discussion is provided in Section 3.3 to investigate the influence of the parameters involved in the optimisation result and to provide insight on the extensibility of the proposed approach; and finally, Section 3.4 provides concluding remarks.

3.1   Methodology

3.1.1   Optimal sensor configuration based on value of information

In general terms, the value of information quantifies the increment of benefit as a consequence of the information gain about a set of uncertain model parameters θ (e.g. damage location parameters) when ultrasound data $\mathbf{D}$ are

taken into account.

In mathematical terms, let $\mathfrak{N} = \{1, \ldots, n, \ldots\}$ denote a set of potential sensor configurations and $b(n, \boldsymbol{\theta}) : \mathbb{N} \times \mathbb{R}^{n_\theta} \to \mathbb{R}$ a benefit function for the n-th sensor configuration, given a set of updatable model parameters $\boldsymbol{\theta} \in \boldsymbol{\Theta} \subset \mathbb{R}^{n_\theta}$. Note that the n-th sensor configuration implies a layout of n sensors. Let $p(\boldsymbol{\theta})$ and $p(\boldsymbol{\theta}|\mathbf{D})$ also denote the prior and posterior PDFs of the parameters $\boldsymbol{\theta}$, respectively, with $\mathbf{D}$ being the dataset. In this chapter, $b(n, \boldsymbol{\theta})$ is defined as the product of a normalised inverse cost function (e.g. from economic or manufacturing cost sources) $f(n) : \mathbb{N} \to [0, 1]$ and the information gain between the current and prior PDF of model parameters, as follows:

$$b(n, \boldsymbol{\theta}) = f(n) \left(\alpha + \log_2 \left[\frac{\pi(\boldsymbol{\theta}, \mathbf{D})}{p(\boldsymbol{\theta})} \right] \right) \tag{3.1}$$

where $p(\boldsymbol{\theta})$ is the prior PDF of model parameters $\boldsymbol{\theta}$, $\pi(\boldsymbol{\theta}, \mathbf{D})$ is used to denote the current PDF of $\boldsymbol{\theta}$, which could be either the prior or the posterior PDFs depending on the availability of the dataset $\mathbf{D}$, and $\log_2[\pi(\boldsymbol{\theta}|\mathbf{D})/p(\boldsymbol{\theta})]$ is the information gain between the aforementioned PDFs in terms of bits. In Equation (3.1), the inverse cost function $f(n)$ can be defined as a generally decreasing and dimensionless function, which gives a measure on how much benefit in terms of cost savings a particular configuration of n sensors provides. The constant $\alpha > 0$ introduced in Equation (3.1) represents the basic state of information assumed in the system such that it makes $b(n, \boldsymbol{\theta}) = \alpha f(n)$ when $\pi(\boldsymbol{\theta}, \mathbf{D}) = p(\boldsymbol{\theta})$, which happens when there is no learning about $\boldsymbol{\theta}$ from data $\mathbf{D}$ and therefore the benefit directly equals the cost savings.

Next, the concept of *maximum prior expected benefit B'*, obtained from the adoption of the optimal configuration $n'_{opt} \in \mathfrak{N}$, is defined as follows [107]:

$$B' = \mathbb{E}_{p(\boldsymbol{\theta})} \left[b(n'_{opt}, \boldsymbol{\theta}) \right] \quad \leftarrow \quad n'_{opt} = \arg \max_{n \in \mathfrak{N}} \int b(n, \boldsymbol{\theta}) p(\boldsymbol{\theta}) d\boldsymbol{\theta} \tag{3.2}$$

Analogously, the *maximum posterior expected benefit (PEB) $B''(\mathbf{D})$* can be ob-

tained as [107]:

$$B''(\mathbf{D}) = \mathbb{E}_{p(\boldsymbol{\theta}|\mathbf{D})}\left[b(n''_{opt}, \boldsymbol{\theta})\right] \quad \leftarrow \quad n''_{opt} = \arg\max_{n\in\mathfrak{N}} \int b(n, \boldsymbol{\theta})p(\boldsymbol{\theta}|\mathbf{D})d\boldsymbol{\theta} \quad (3.3)$$

where the conditioning on $\mathbf{D}$ is used to denote that B'' depends on the data obtained through the PZT sensors. Finally, by subtracting both mathematical expectations, the *conditional value of information (CVI)* given $\mathbf{D}$ is defined as:

$$\text{CVI}(\mathbf{D}) = B''(\mathbf{D}) - B' \tag{3.4}$$

Therefore, by substituting Equations (3.2), (3.3) and (3.1) into Equation (3.4), the CVI can be expressed as follows:

$$
\begin{aligned}
\text{CVI}(\mathbf{D}) &= \int b(n''_{opt}, \boldsymbol{\theta})p(\boldsymbol{\theta}|\mathbf{D})d\boldsymbol{\theta} - \int b(n'_{opt}, \boldsymbol{\theta})p(\boldsymbol{\theta})d\boldsymbol{\theta} \\
&= \int f(n''_{opt})\left(\alpha + \log_2\left[\frac{p(\boldsymbol{\theta}|\mathbf{D})}{p(\boldsymbol{\theta})}\right]\right)p(\boldsymbol{\theta}|\mathbf{D})d\boldsymbol{\theta} \\
&\quad - \int f(n'_{opt})\left(\alpha + \log_2\left[\underbrace{\frac{p(\boldsymbol{\theta})}{p(\boldsymbol{\theta})}}_{=1}\right]\right)p(\boldsymbol{\theta})d\boldsymbol{\theta} \\
&= \alpha \int f(n''_{opt})p(\boldsymbol{\theta}|\mathbf{D})d\boldsymbol{\theta} \\
&\quad + \int f(n''_{opt})\log_2\left[\frac{p(\boldsymbol{\theta}|\mathbf{D})}{p(\boldsymbol{\theta})}\right]p(\boldsymbol{\theta}|\mathbf{D})d\boldsymbol{\theta} - \alpha \int f(n'_{opt})p(\boldsymbol{\theta})d\boldsymbol{\theta}
\end{aligned}
\tag{3.5}
$$

Note from the last equation that the inverse cost function is independent of the uncertain parameters $\boldsymbol{\theta}$, therefore Equation (3.5) can be reorganised as follows:

$$
\begin{aligned}
\text{CVI}(\mathbf{D}) &= \alpha f(n''_{opt})\underbrace{\int p(\boldsymbol{\theta}|\mathbf{D})d\boldsymbol{\theta}}_{=1} \\
&+ f(n''_{opt})\underbrace{\int \log_2\left[\frac{p(\boldsymbol{\theta}|\mathbf{D})}{p(\boldsymbol{\theta})}\right]p(\boldsymbol{\theta}|\mathbf{D})d\boldsymbol{\theta}}_{\text{KL}(p(\boldsymbol{\theta}|\mathbf{D})\|p(\boldsymbol{\theta}))} - \alpha f(n'_{opt})\underbrace{\int p(\boldsymbol{\theta})d\boldsymbol{\theta}}_{=1}
\end{aligned}
\tag{3.6}
$$

which finally leads to

$$\text{CVI}(\mathbf{D}) = \underbrace{f(n''_{opt})\text{KL}(p(\boldsymbol{\theta}|\mathbf{D})\|p(\boldsymbol{\theta}))}_{\text{BEIG}} - \underbrace{\alpha\left[f(n'_{opt}) - f(n''_{opt})\right]}_{\text{RCI}} \quad (3.7)$$

where $\text{KL}(p(\boldsymbol{\theta}|\mathbf{D})\|p(\boldsymbol{\theta}))$ denotes the KL divergence between the posterior and the prior PDFs of the uncertain model parameters $\boldsymbol{\theta}$. In the last equation, the term $f(n''_{opt})\text{KL}(p(\boldsymbol{\theta}|\mathbf{D})\|p(\boldsymbol{\theta}))$ can be understood as the benefit of the expected information gain (BEIG), which is always a non-negative value, i.e. $\text{BEIG} \in \mathbb{R}_0^+$. The second part of Equation (3.7) can be understood as the relative cost of implementation (RCI), since it accounts for the difference between the cost savings of implementing the optimal sensor configuration before and after considering the information from data $\mathbf{D}$. Note that, in practice, not adding any SHM system ($n = 0$) is cheaper than adding it by strictly considering economic factors, due to sensors and hardware costs savings, amongst others. Therefore, the RCI is positive under the assumption that $f(n)$ is decreasing, i.e. $n'_{opt} < n''_{opt}$ hence $f(n'_{opt}) > f(n''_{opt})$ as exemplified in Figure 3.1.
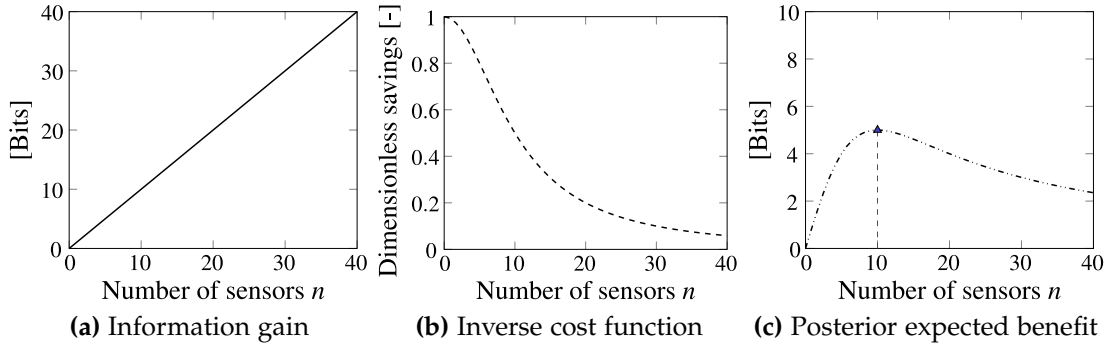
Figure 3.1: Example of functions of (a) information gain, (b) dimensionless inverse of cost, and (c) final combination of both functions.

Observe also that the non-negative constant α defined in Equation (3.1) avoids the prior expected benefit (Equation (3.2)) becoming zero, and therefore simpler configurations will be preferred under non-informative (i.e. prior equals posterior) scenarios. In addition, the value of α is defined so that both terms, i.e., BEIG and RCI, are comparable under all possible scenarios, even when the system is not very informative, so that neither one of the RCI nor the

BEIG terms individually drives the optimisation problem. This interpretation of Equation (3.7) suggests that the CVI conveys a trade-off between the global benefit of establishing a particular SHM configuration and the cost of actually implementing it. The CVI also provides a decision making index that ranks different strategies considering their suitability in performance and cost. The interpretation of Equation (3.7) is illustrated with two hypothetical examples below.

Example 1. Let us assume a non-informative SHM system where the posterior PDF is virtually equal to the prior PDF, such that the optimal number of sensors in prior and posterior states are the same, i.e. $n'_{opt} = n''_{opt}$ and thus $f(n'_{opt}) = f(n''_{opt})$, hence RCI = 0. Moreover, since the SHM system is non-informative, the expected information gain equals zero, and therefore the BEIG equals zero as well. In this extreme example, given that CVI = 0, no decision about adding or removing sensors could be made based on the current information, hence no change with respect to the prior configuration would be required. Figure 3.2a depicts this example.

Example 2. Let us assume a non-informative SHM system such that the optimal number of sensors when data are acquired are $n''_{opt} = n'_{opt}/2$. In this example, half of the sensor network in the prior or initial state, i.e., $n'_{opt}/2$, are placed opposite to each other in the plate, as depicted in Figure 3.2b. In this situation, let us assume that the posterior information captured by the system is equivalent to the prior information, hence the expected information gain (KL divergence) equals zero, thus BEIG also equals zero. Henceforth, the RCI term turns negative since $f(n'_{opt}) < f(n''_{opt})$, which leads to CVI > 0. This hypothetical example shows that the proposed formulation favours simpler and cheaper SHM systems under non-informative scenarios.

Expected value of information

The CVI criterion presented above formulates the optimisation problem for a particular set of data **D**, i.e., it implies that damage is located at a particular position. However, in practice, the optimal sensor configuration problem requires
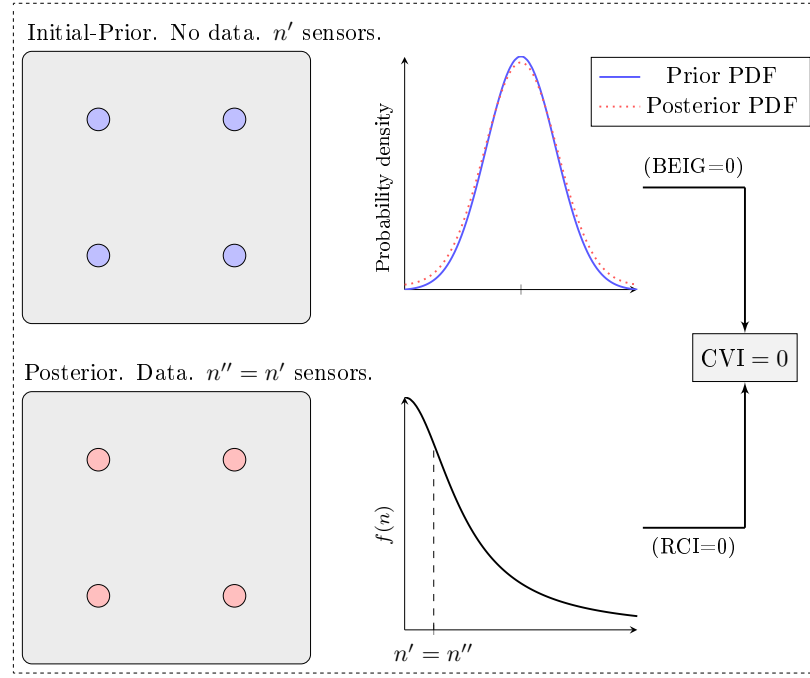
(a) Example 1
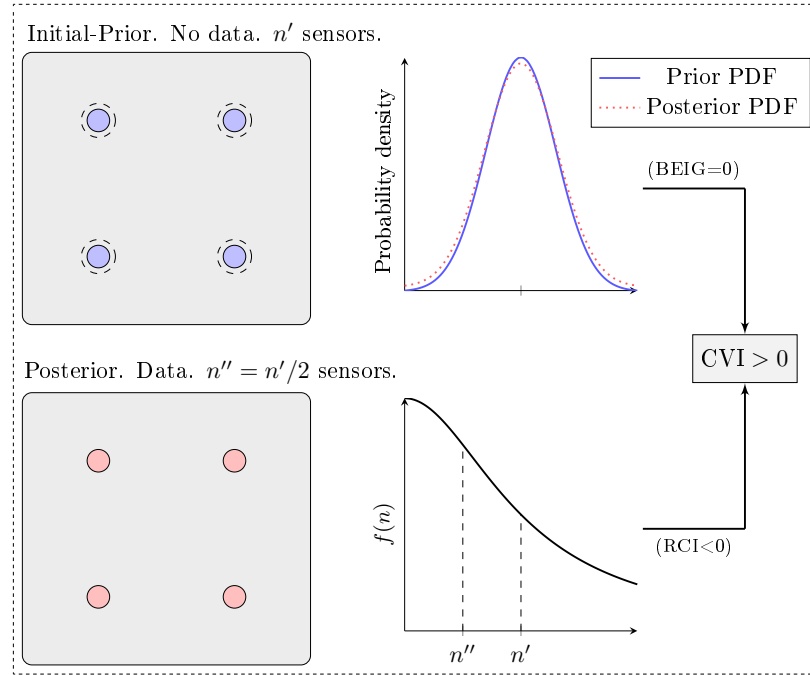
(b) Example 2

Figure 3.2: Graphical representation of Examples 1 and 2 about the influence of using the proposed CVI-based formulation in the decision of number of sensors. For Example 1, the prior distribution of sensors would be maintained. For Example 2, even when the BEIG= 0, the proposed formulation supports the configuration with less sensors. Dashed circles represent the sensors in the opposite side of the plate.

a sufficiently large set of damage scenarios to be addressed, hence a space of datasets $\mathfrak{D} \ni \mathbf{D}$ instead of a particular $\mathbf{D}$ needs to be considered. Note that,

at the design stage, experimental data are not typically available and therefore the data are simulated using a model and prior knowledge of the model parameters. Thus, a mathematical expectation is applied to Equation (3.7) to obtain the expected value of information (EVI) over the space of datasets $\mathfrak{D}$, as follows:

$$\text{EVI} = \int_{\mathfrak{D}} \left[f(n''_{opt}) \text{KL}(p(\boldsymbol{\theta}|\mathbf{D}) \| p(\boldsymbol{\theta})) \right] p(\mathbf{D}) d\mathbf{D} - \int_{\mathfrak{D}} \alpha [f(n'_{opt}) - f(n''_{opt})] p(\mathbf{D}) d\mathbf{D} \tag{3.8}$$

Observe that the first term of Equation (3.8) involves a double multidimensional integral that cannot be solved analytically in most cases. Therefore, it is numerically approximated using the MC method as follows [39, 97, 197]:

$$\text{EVI} \approx f(n''_{opt}) \frac{1}{N_{out}} \sum_{m=1}^{N_{out}} \left[\log_2 p(\mathbf{D}_{(m)}|\boldsymbol{\theta}_{(m)}) \right.$$
$$\left. - \log_2 \left(\frac{1}{N_{in}} \sum_{k=1}^{N_{in}} p(\mathbf{D}_{(m)}|\boldsymbol{\theta}_{(k)}) \right) \right] - \alpha [f(n'_{opt}) - f(n''_{opt})] \tag{3.9}$$

where $\boldsymbol{\theta}_{(m)}$ is a sample drawn from the prior distribution $p(\boldsymbol{\theta})$; $\mathbf{D}_{(m)}$ is a sample dataset drawn from the likelihood distribution $p(\mathbf{D}|\boldsymbol{\theta} = \boldsymbol{\theta}_{(m)})$ (refer to Equation (3.12) below); and N_{out} and N_{in} are the number of Monte Carlo samples used in the outer and inner summations, respectively. Thus, Equation (3.9) is adopted here as optimality criterion to obtain the optimal sensor configuration considering an area of possible damage locations. Further implementation details of the EVI criterion and the adopted search algorithm are provided hereinafter in Section 3.1.3.

3.1.2 Optimal sensor placement: Bayesian damage localisation

The previous section presented a rational fitness function to obtain the optimal number of sensors using the EVI, which requires updated information about the model parameters (e.g. damage coordinates) given a particular dataset $\mathbf{D}_{(m)} = \mathbf{D}$. This section describes the fundamentals of the Bayesian *inverse*

problem whereby model parameters are estimated.

The problem of damage localisation is addressed by a model-based BIP using an ellipse-based ToF model [170], which was previously published in [24] and is addressed in Chapter 6 of this thesis. The ToF is an ultrasonic signal feature widely adopted by both practitioners and researchers due to its efficiency in providing information about material properties and damage localisation in plate-like structures by post-processing scattered signals. Note that the use of guided-waves for SHM is typically restricted to two-dimensional thin-walled structures, as described in Section 2.1. To estimate the ToF from scattered signals, several TF representation techniques are available in the literature [162–165]. In particular, given a TF model, the ToF can be obtained as the difference between the time to receive the first energy peak of the excitation signal and the one from the scattered signal. From a theoretical point of view, the ToF information of the scattered signals can be obtained as follows [198]:

$$\text{ToF}^{(a-s)} = \frac{\sqrt{\left(X_d - X_a^j\right)^2 + \left(Y_d - Y_a^j\right)^2}}{V_{a-d}} + \frac{\sqrt{\left(X_d - X_s^i\right)^2 + \left(Y_d - Y_s^i\right)^2}}{V_{d-s}} \quad (3.10)$$

where $(X_d, Y_d) \in \mathbb{R}^2$ are the coordinates of the damage position, $(X_a^j, Y_a^j) \in \mathbb{R}^2$ are the coordinates of the *j*-th actuator transducer, $(X_s^i, Y_s^i) \in \mathbb{R}^2$ are the coordinates of the *i*-th sensor transducer, and V_{a-d} and V_{d-s} are the wave propagation velocities of the actuator-damage and damage-sensor paths, respectively. Note that these velocities are the same under the assumption of isotropic materials and damage concentrated within a bounded region, where $V = V_{a-d} = V_{d-s}$. Figure 3.3 depicts the wave propagation problem, where the elements of Equation (3.10) can be identified.

From this standpoint, the unknown model parameters of interest are $\theta = \{X_d, Y_d, V\}$ so, under the assumption of perfect sensor, if an exact value of θ^* is known, then the measured ToF and the modelled one using Equation (3.10) would be identical; mathematically: $\text{ToF}_{\mathcal{D}}^{(a-s)} \equiv \text{ToF}_M^{(a-s)}(\theta^*)$. However, in practice there are uncertainties due to signal measurement errors, partially un-
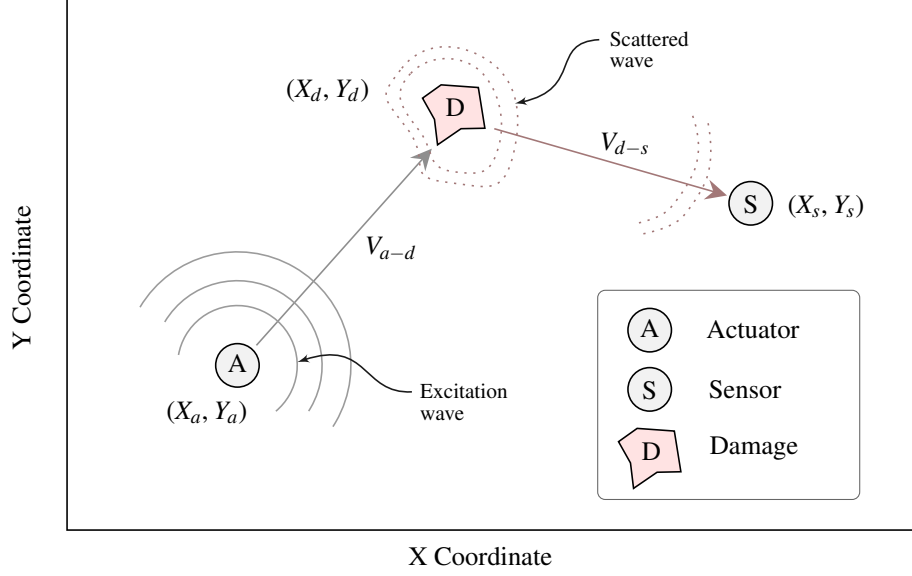
Figure 3.3: Schematic of ultrasonic guided-wave based damage (D) localisation using an actuator (A) and a sensor (S).

known material properties, and the uncertainty about the validity of the ToF model itself, which make the last identity seldom observed in real-world scenarios. Thus, a more appropriate and rigorous approach involves assuming the existence of these modelling uncertainties and quantifying them, as follows:

$$\text{ToF}_{\mathcal{D}}^{(a-s)} = \text{ToF}_{M}^{(a-s)}(\boldsymbol{\theta}) + e \tag{3.11}$$

where $e \in \mathbb{R}$ is an error term enclosing the uncertainty which accounts for the discrepancy between $\text{ToF}_{M}^{(a-s)}$ and $\text{ToF}_{\mathcal{D}}^{(a-s)}$. By the Principle of Maximum Information Entropy [28, 32], a probability model for e can be adopted so that it provides the largest uncertainty subject to some parametrised constraints. This assumption is considered to be conservative given that it produces the maximum entropy (i.e. largest uncertainty) in the prediction error of the ToF. For this entropy maximisation, a simple choice is to select the following constraints: a zero mean predictor and a parametrised error variance. The resulting PDF is a zero-mean Gaussian distribution with standard deviation $\sigma_e \in \mathbb{R}$. Thus,

Equation (3.11) can be rewritten probabilistically as:

$$p\left(\text{ToF}_{\mathcal{D}}^{(a-s)}|\boldsymbol{\theta}\right) = \left(2\pi\sigma_e^2\right)^{-\frac{1}{2}} \exp\left(-\frac{1}{2}\left(\frac{\text{ToF}_{\mathcal{D}}^{(a-s)} - \text{ToF}_{M}^{(a-s)}(\boldsymbol{\theta})}{\sigma_e}\right)^2\right) \quad (3.12)$$

which provides a probabilistic measure about the similarity between $\text{ToF}_{\mathcal{D}}^{(a-s)}$ and $\text{ToF}_{M}^{(a-s)}(\boldsymbol{\theta})$ for a particular value of $\boldsymbol{\theta}$. Recall that the last equation corresponds to the likelihood function of the inverse problem for model parameter $\boldsymbol{\theta}$.

Nevertheless, our interest lies precisely in the reciprocal information, i.e., to determine the values of $\boldsymbol{\theta}$ among the set of values $\boldsymbol{\Theta} \subset \mathbb{R}^{n_{\theta}}$ which lead to models that are more likely to satisfy the ideal identity $\text{ToF}_{\mathcal{D}}^{(a-s)} \equiv \text{ToF}_{M}^{(a-s)}(\boldsymbol{\theta})$. This inverse problem is formulated by Bayes' theorem [33, 34], as:

$$p(\boldsymbol{\theta}|\mathbf{D}) = \frac{p(\mathbf{D}|\boldsymbol{\theta})p(\boldsymbol{\theta})}{p(\mathbf{D})} \quad (3.13)$$

where $\mathbf{D} = \{D^{(1)}, \ldots, D^{(k)}, \ldots, D^{(n)}\}$ is the set of ToF data corresponding to the set of n sensors and a spatial configuration[1] $\mathcal{C}^n$, $p(\boldsymbol{\theta})$ is the prior PDF of the model parameters, and $p(\mathbf{D}|\boldsymbol{\theta})$ is the likelihood function for the set of data $\mathbf{D}$, as described in Equation (3.12).

Assuming stochastic independence of the measurements, the likelihood $p(\mathbf{D}|\boldsymbol{\theta})$ can be expressed probabilistically as $p(\mathbf{D}|\boldsymbol{\theta}) = \prod_{k=1}^{n} p(D^{(k)}|\boldsymbol{\theta})$, where each factor $p(D^{(k)}|\boldsymbol{\theta})$ is given by Equation (3.12). Finally, the term $p(\mathbf{D})$ refers to the evidence [32] of the data under the model specified by $\boldsymbol{\theta}$. This term, which acts as a normalising constant within Bayes' theorem, can be bypassed through sampling using MCMC methods [199]. Thus, Equation (3.13) can be rewritten as:

$$p(\boldsymbol{\theta}|\mathbf{D}) \propto \left(\prod_{k=1}^{n} p\left(D^{(k)}|\boldsymbol{\theta}\right)\right) p(\boldsymbol{\theta}) \quad (3.14)$$

---

[1]The conditioning on $\mathcal{C}^n$ has been omitted from $p(\boldsymbol{\theta}|\mathbf{D})$ given that it is intrinsically contained in $\mathbf{D}$, since a particular configuration implies a dataset, i.e., $\mathcal{C}^n \to \mathbf{D}$.

3.1.3 Algorithmic implementation

In this section, a forward sequential algorithm is used to solve the optimal sensor configuration problem over two main variables: (1) *number* and (2) *position* of the sensors, as proposed by [94, 96]. Therefore, the algorithm provides the optimal number of sensors n''_{opt} and their optimal spatial configuration $\mathcal{C}^n_{opt}$, whereby the EVI is finally obtained. In this algorithm, the optimal sensor placement problem is proposed to be solved through an exhaustive search methodology, which is performed by exploring all the possible sensor locations

---

Algorithm 3.1: Pseudo-code implementation of forward sequential search algorithm for geometrically unconstrained sensor configurations.

```
   /*          Preamble                                         */
 1 Define Ns ;                     // number of possible sensor locations
 2 Define ns,max ;                 // maximum number of sensors locations
                                      considered in the optimisation
   /*          Algorithm                                        */
 3 n'opt ← arg maxn f(n) ;         // Optimal number of sensors under
                                      prior information
 4 {{θ(m,h)}Nm=1}Nset h=1 ∼ p(θ) ;     // Nset sets of N = Nout = Nin samples
                                      drawn from the prior PDF
 5 {{D(m,h)}Nm=1}Nset h=1 ∼ p(D|θ(·,h)) ; // Nset sets of N = Nout = Nin samples
                                      drawn from the likelihood PDF
 6 ℭ ← ∅ ;                        // Initialise an empty vector of
                                      optimal sensors placement
   /* Forward sequential sensor for loop                        */
 7 for n = 1 to Ns do
     /* Exhaustive search for loop                              */
 8   for i = 1 to ns,max do
 9       Cn ← Cn−1 ∪ Ci ;          // Define Cn by concatenating the
                                      previous configuration to the i-th
                                      sensor
10       Obtain J(Cn) ;            // Evaluate the objective function
                                      according to Eq. (3.15)
11   end
12   Return: Cnopt and J(Cnopt) ;  // Optimal sensor layout and its
                                      corresponding objective function
                                      value
13   ℭ ← Cnopt ;                   // Store the n-th optimal sensor
                                      location for the next iteration
14 end
15 n''opt ← arg maxn J(ℭ) ;        // Optimal number of sensors under
                                      posterior information
```

within a discrete grid, given that a relatively small search space is considered. The objective function $J(\mathcal{C}^n) : \mathbb{N} \rightarrow \mathbb{R}$ for the optimisation problem is given by the average of the EVI (Equation (3.9)) for each spatial configuration $\mathcal{C}^n$, as follows:

$$J(\mathcal{C}^n) = f(n)\frac{1}{N_{set}}\sum_{h=1}^{N_{set}}\left\{\frac{1}{N_{out}}\sum_{m=1}^{N_{out}}\left[\log_2 p(\mathbf{D}_{(m,h)}|\boldsymbol{\theta}_{(m,h)},\mathcal{C}^n)\right.\right.$$
$$\left.\left. - \log_2\left(\frac{1}{N_{in}}\sum_{k=1}^{N_{in}} p(\mathbf{D}_{(m,h)}|\boldsymbol{\theta}_{(k,h)},\mathcal{C}^n)\right)\right]\right\} - \alpha[f(n'_{opt}) - f(n)]$$

(3.15)

where $\mathcal{C}^n$ is the sensor configuration variable that controls which sensors are active, their location, and therefore what ToF data $\mathbf{D}$ are used to calculate $J(\mathcal{C}^n)$. To efficiently address the expectation of the KL divergence (recall Eq. (3.9)), the $N_{out} = N_{in}$ prior samples are reused in both the inner and outer sums of Equation (3.15) at the cost of a small increment in the bias of the estimator [39, 97]. Nevertheless, the computation of the KL divergence implies a numerical error inversely proportional to the number of samples, leading to stochastic uncertainty in the value of the KL divergence. To reduce such stochasticity, the objective function is averaged over N_{set} sets of of $N_{out} = N_{in}$ samples for each configuration $\mathcal{C}^n$, as shown in Equation (3.15).

Furthermore, note that n'_{opt} in Equation (3.15) is obtained using Equation (3.2) and that the independence of the prior expected benefit on the sensor configuration makes it only dependent on the inverse cost function. Thus, n'_{opt} implies the most economically beneficial amount of sensors given that $f(n)$ is decreasing, regardless of their position.

Additionally, observe that the search of the optimal number of sensors implies a heavy computational problem involving $N_s!/n!(N_s - n)!$ potential configurations to be explored. For example, for $N_s = 40$ possible sensor locations and $n = 5$ sensors, the number of possible configurations would be $40!/5!35! = 658,008$. To avoid such computational complexity, several strategies can be applied to reduce the search space. Here, the *forward sequential search* approach [94] is adopted, as shown in Algorithm 3.1, consisting of run-

ning an exhaustive search for one individual sensor (e.g., n) having stored the optimal locations of the previous $n - 1$ sensors, thus limiting the search space. Following this methodology, the total number of configurations reduces to $n(2N_s - n + 1)/2$. Taking the same numerical example with $N_s = 40$ and $n = 5$, the number of possible configurations would be $5(80 - 5 + 1)/2 = 190$ instead of $658,008$ using the former method. Note that a suboptimal configuration is expected to be obtained, since the sequential search method does not necessarily provide the global optimal solution. However, the suboptimal configuration can be assumed to be effective and robust [200, 201].

From this standpoint, it is important to remark that Algorithm 3.1 provides a methodology to obtain geometrically unconstrained ("open") optimal sensor configurations. However, these may find a limitation in practice when installation issues such as the routing of the wires are taken into account. Therefore, more practical sensor configurations constrained to linear arrays of sensors [12, 14] are typically preferred for their ease of installation and maintenance. These sensor configurations using one or two arrays of sensors (see Figure 3.4) can be assessed by slightly modifying Algorithm 3.1 as follows: For one array of n sensors, only the n-th sensor (master) position is optimised,
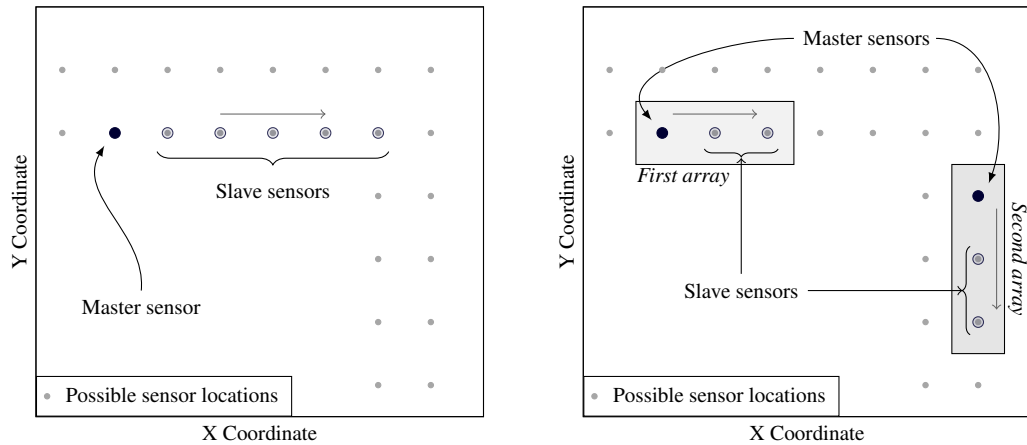
(a) Sensor distribution using 1 array and 6 sensors

(b) Sensor distribution using 2 arrays and 6 sensors

Figure 3.4: Illustration of sensor positioning strategies for 1 and 2 arrays. In panel (a), one-array configurations where one master sensor is optimally placed, while the slave sensors are placed next the master. Panel (b) for two arrays of sensors, where the first array is optimally placed and its position stored to start the search for the second one.

considering that the remaining $n - 1$ sensors (slave) are placed either on the left or right side of the master one, as depicted in Figure 3.4a. Note for this configuration the search space reduces as long as n increases. In case of two arrays of n sensors, the optimisation is carried out in two steps, (1) the first array of $n/2$ sensors is optimally placed, as explained before, and its position is stored, and (2) the optimal position of the second array of $n/2$ sensors is addressed considering the first one fixed, as shown in Figure 3.4b. The search space reduces even faster for two array configurations since only even numbers of sensors n are considered to form the two arrays.

3.2 Case studies

The proposed methodology to obtain the optimal sensor configuration based on EVI is exemplified herein using two case studies. Section 3.2.1 illustrates the methodology for a square aluminium plate. Finally, Section 3.2.2 provides a comparison between open and array configurations for an aeronautical hat-type stiffened plate.

3.2.1 Sensor optimisation in a square metallic plate

This case study deals with the problem of optimal sensor configuration for a 30cm $\times$ 30cm $\times$ 0.2cm aluminium 2024-T351 plate. The prior information of the model parameters $\boldsymbol{\theta}$ is represented as uniform distributions for the damage position parameters (X_d, Y_d) and as a Gaussian distribution for the velocity V, as follows: $p(X_d) = \mathcal{U}(-6,\ 6)$, $p(Y_d) = \mathcal{U}(-6,\ 6)$, and $p(V) = \mathcal{N}(5400,\ 60)$, with position and wave velocity units expressed in [cm] and [m/s] respectively. Note that the uniform PDFs depict a scenario where the damage is known to occur anywhere within a bounded region with the same probability. The Gaussian PDF of the velocity, however, represents the uncertainty around a known nominal value (e.g. by the guided-wave theory [72]) for the first symmetric guided-wave mode at a frequency 300 kHz and the considered

plate. To address the optimal sensor configuration, a grid of possible sensor locations is defined as two concentric squares of 12 cm and 18 cm of side respectively, resulting in a total of 40 possible locations. The area of possible damage occurrence is represented in blue colour in Figure 3.5b. The actuator is considered to be fixed at the origin of coordinates, i.e., the centre of the plate. The optimisation is addressed by using Algorithm 3.1 with $N_{set} = 1000$ and $N_{out} = N_{in} = 1000$ (recall Eq. (3.15)).

(a) Value of information

(b) Optimal sensor distribution
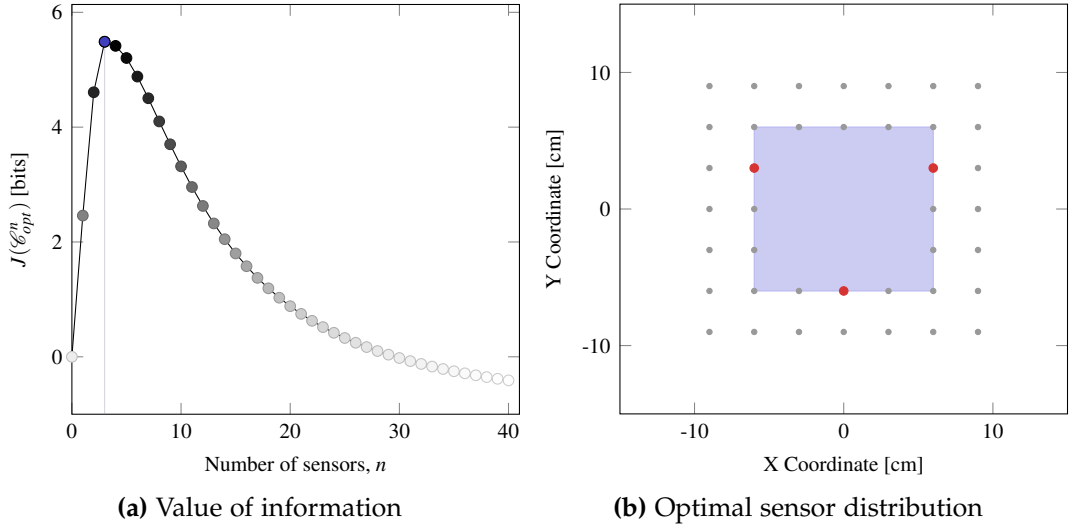
Figure 3.5: Estimator of the EVI (Eq. (3.15)) in panel (a) and the corresponding optimal sensor configuration with $n''_{opt} = 3$ sensors in (b), where the possible sensor locations (grey dots) and the optimal locations (red dots) are shown. The blue area denotes the area of possible damage occurrence.

The results for this case study are shown in Figure 3.5. As is evident from Figure 3.5a, $J(\mathcal{C}_{opt}^n)$ reaches a global maximum using a configuration of 3 sensors, provided an inverse cost function $f_0(n)$ given by:

$$f_0(n) = 100/(n^2 + 100) \tag{3.16}$$

The corresponding EVI value is 5.4875 [bits], adopting $\alpha = 1$ in Equation (3.9), i.e., assuming that both the RCI and the information members in Equation (3.15) are equally important. The optimal sensor distribution for this configuration is shown in Figure 3.5b. Note that the optimal sensor positions (in red) are found to be symmetrically placed with respect to the centre of the plate (where the actuator is located), and they are wholly contained within the inner square,

i.e. close to the area of possible damage occurrence. The symmetry of the optimal layout is highly influenced by the adopted prior distribution, which is symmetric as well with respect to the centre of the plate. Any other prior PDF, especially for the damage coordinates, will affect the optimal sensor placement.

Verification of the optimal sensor configuration

The performance of the optimal sensor configuration, as depicted in Figure 3.5b, is tested against simulated data for a specific damage within the area of possible damage occurrence. To this end, the plate is simulated in Abaqus® (Figure 3.6a) using C3D8R (8-node linear brick, reduced integration, hourglass control) solid elements [196] with mesh size 0.05 cm and mechanical properties $\rho = 2780$ kg/m^3, $E = 73.1$ GPa, and $\nu = 0.33$. Note that the optimisation of the sensor configuration was addressed with respect to the first symmetric guided-wave mode. Hence, solid elements are required as this mode implies a deformation of the plate thickness [72]. The mesh size is determined so that at least 10 nodes are contained per wavelength, and the chosen time step is obtained so that a disturbance cannot propagate through a grid spacing during one time step [11, 202]. The simulated damage is represented as a square 0.2 cm×0.2 cm hole, centred at (3.5, 2.5)cm, considering the centre of the plate as the origin of coordinates, as shown in Figure 3.6b. To simulate the wave propagation, an exciting force is applied at the centre of the plate in the perpendicular direction, consisting of a 5 cycle sine tone burst centred at a frequency 300 kHz.

The guided-waves are acquired at the three optimal sensor positions highlighted in red in Figure 3.5b and subtracted before and after damage to obtain the scattered signals. Then, the robust ToF estimation methodology previously developed in [24] is applied. The robust ToF data $\mathbf{D} = \{D^{(1)}, \cdots, D^{(n)}\}$ obtained for each of the optimal sensors are then used as input data for the Bayesian damage localisation problem described in Section 3.1.2, whereby the posterior PDFs of the model parameters $\boldsymbol{\theta} = \{X_d, Y_d, V\}$ are obtained. The prior knowledge of the model parameters is assumed to be equal to the one

(a) Abaqus® model

(b) Origin and damage coordinates in cm

(c) Damage position reconstruction

(d) Posterior velocity distribution
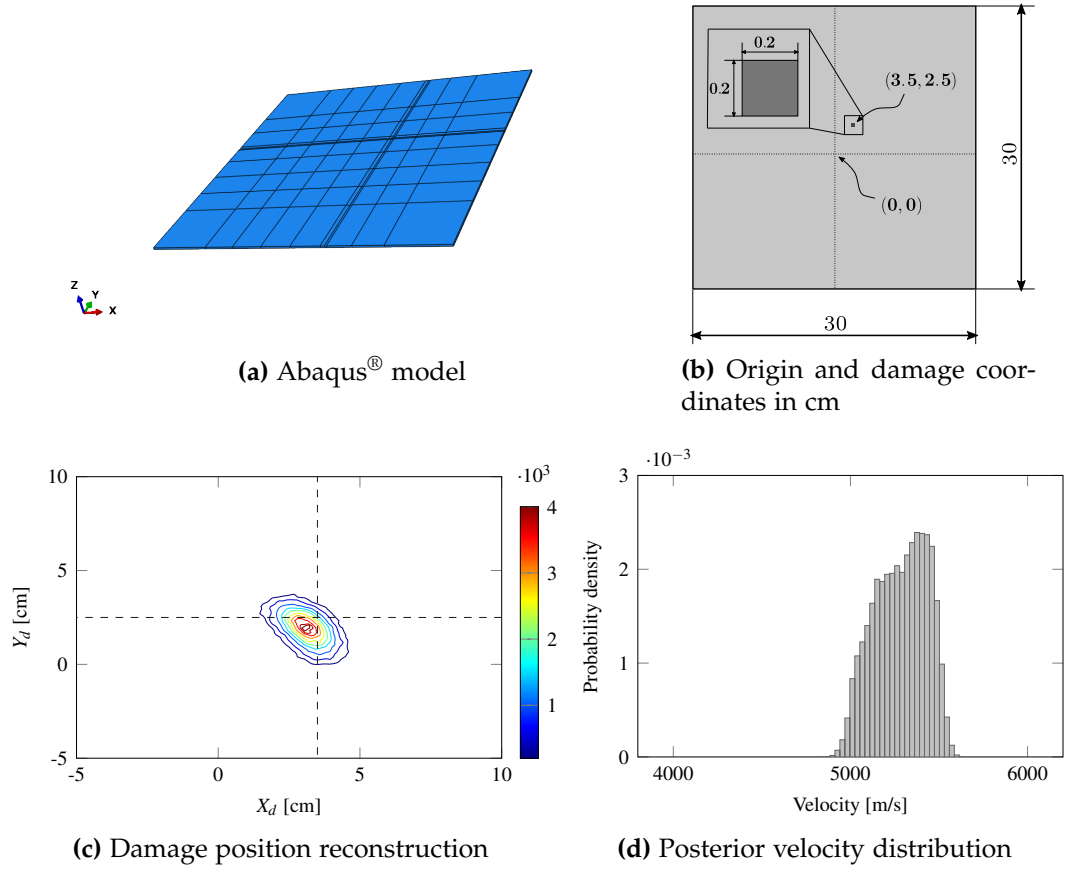
Figure 3.6: Abaqus® model in panel (a), dimensions of the plate and location of the simulated damage in panel (b), joint posterior distribution of the damage coordinates along with the centre of the real damage represented by the intersection of both dashed lines in panel (c), and velocity reconstruction in panel (d).

used for the optimisation process, described in the Section 3.2.1. To numerically solve the Bayesian inverse problem of damage localisation, the AIMS algorithm described in Section 6.3.1 is applied with a threshold value $\gamma = 1/2$, using $50,000$ samples per annealing level, using a Gaussian PDF as proposal distribution, i.e. $q(\theta'|\theta) = \mathcal{N}(\theta, \sigma)$, where σ is the standard deviation of the M-H random walk (see Appendix A). Implementation details of the AIMS algorithm can be found in Section 6.3.1 of this thesis. In this problem, σ is selected such that the acceptance rate lies within the suggested interval $[0.2, 0.4]$ [203–205].

The posterior information of the damage parameters $\theta = \{X_d, Y_d, V\}$ is illustrated in Figures 3.6c and 3.6d. It can be observed that the damage position is remarkably well reconstructed using the optimal sensor configuration.

In contrast, the uncertainty of the reconstructed wave propagation velocity is higher as shown in Figure 3.6d. A larger variability of the ToF data at the optimal sensors is identified as the reason for such relatively high uncertainty in the velocity, which may come from potential mode mixture issues between both anti-symmetric and symmetric 0 guided waves modes, namely A0 and S0 modes, respectively.

3.2.2   Sensor optimisation in aeronautical panel

The aim of this case study is to investigate the applicability of the proposed methodology using a more complex and realistic structure. In particular, a 50cm $\times$ 50cm $\times$ 0.2cm plate with top-hat section stiffeners, commonly used in aeronautical structures, is adopted for this case study. Here, the origin of the coordinates is located at the centre of the plate's left edge and the actuator is placed at the centre of the plate, i.e., $(25, 0)$ [cm]. An equivalent set of prior PDFs to those used in the previous case study (refer to Section 3.2.1 for their rationale) is adopted, so $p(X_d) = \mathcal{U}(5, \ 45)$, $p(Y_d) = \mathcal{U}(-10, \ 10)$, and $p(V) = \mathcal{N}(2800, \ 60)$, with position and wave velocity units expressed in [cm] and [m/s] respectively. Note that the velocity prior PDF is centred at 2800 m/s, which corresponds to the group velocity of the ultrasonic guided-wave mode A0 at a frequency 300 kHz. The search space is represented by eight rows of 39 possible sensor locations at $Y = \{20.81, 19.81, 10.19, 9.19, -9.19, -10.19, -19.81, -20.81\}$ [cm], separated by 1 [cm] in the X direction, as depicted in Figure 3.7c using grey dots. The optimisation is addressed considering Equation (3.15) with $N_{set} = 100$ sets of $N_{out} = N_{in} = 1000$ samples of the prior distribution.

For this case study, a comparison between different sensor placement strategies, i.e., (1) non geometrically constrained "open" configuration, (2) sensor positioning in 1 array, and (3) sensor positioning over 2 separated arrays, is carried out. Figure 3.7a depicts the adopted inverse cost function, whilst Figure 3.7b depicts the objective function output $J(\mathcal{C}_{opt}^n)$ (recall Eq. (3.15)) as

(a) Inverse cost function

(b) Value of information

(c) Optimal sensor distributions
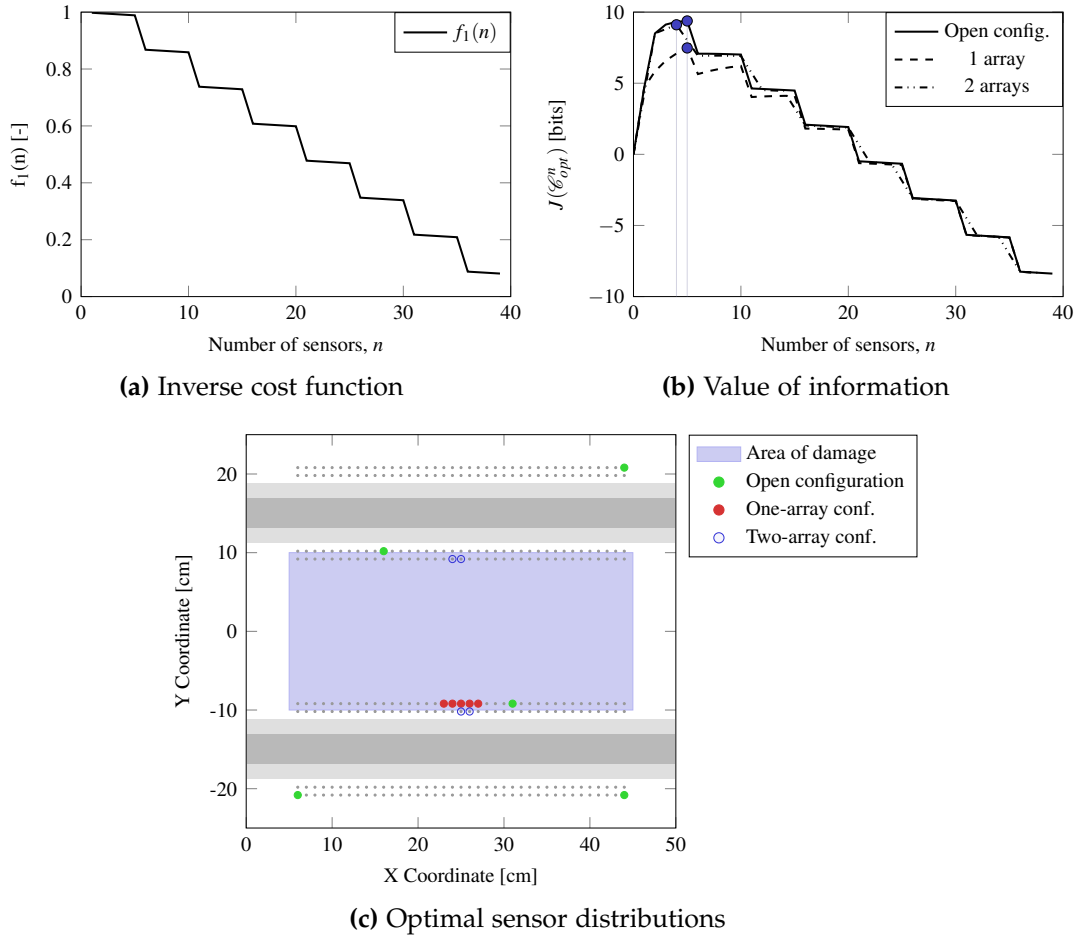
Figure 3.7: Inverse cost function $f_1(n)$ in panel (a). In (b), the estimator of the EVI (Eq. (3.15)) for the different positioning configurations is depicted. Panel (c) shows their corresponding optimal sensor layouts. The blue rectangle represents the area of possible damage occurrence with uniform probability.

a function of the number of sensors and their respective optimal number of sensors for each type of configuration. The optimal number of sensors is found to be $n''_{opt} = 5$ for both the open and the one-array configurations (EVI = 9.2874 [bits] and EVI = 7.3896 [bits], respectively), whereas the two-array configuration leads to 4 sensors (EVI = 9.0416 [bits]), assuming $\alpha = 10$ to emphasise the cost over the relative gain of information. In view of Figure 3.7b, both the open configuration and the one using 2 arrays are found to be the most valuable, and hence the preferred ones under the EVI criterion. This ranking is also supported by the robust BEIG and RCI terms (Eq. (3.7) and (3.9)) in Table 3.1. In particular, observe that even when the RCI for the open configuration is higher than the RCI of the two-array configuration, the

first one is preferred since it provides a relatively higher and more robust BEIG.

Table 3.1: Decomposition of EVI into the robust BEIG and RCI terms (Eq. (3.9)) for the three positioning strategies.

Configurations	BEIG [bits]	RCI [bits]	EVI [bits]	No sensors
Open config.	9.3774	0.0900	9.2874	5
One array	7.4796	0.0900	7.3896	5
Two arrays	9.1091	0.0675	9.0416	4

As a general comment, the open configuration is able to reconstruct the damage more accurately due to its flexibility. However, in real world engineering applications, factors such as the routing options of the cables introduce limitations and complexity that may prevent the use of sensor open configurations. Accordingly, the two-array configuration would be the preferred one based on the value of information criterion, as shown in Table 3.1. Finally, Figure 3.7c shows the optimal sensor layouts for each of the three positioning strategies.

Verification of the optimal sensor configuration

The resulting optimal sensor configurations in Section 3.2.2 are tested using a simulated damage scenario considering a hole in the metallic plate. To this end, an Abaqus® model, shown in Figure 3.8a, is developed to obtain the guided

(a) Abaqus® model

(b) Basic dimensions in cm
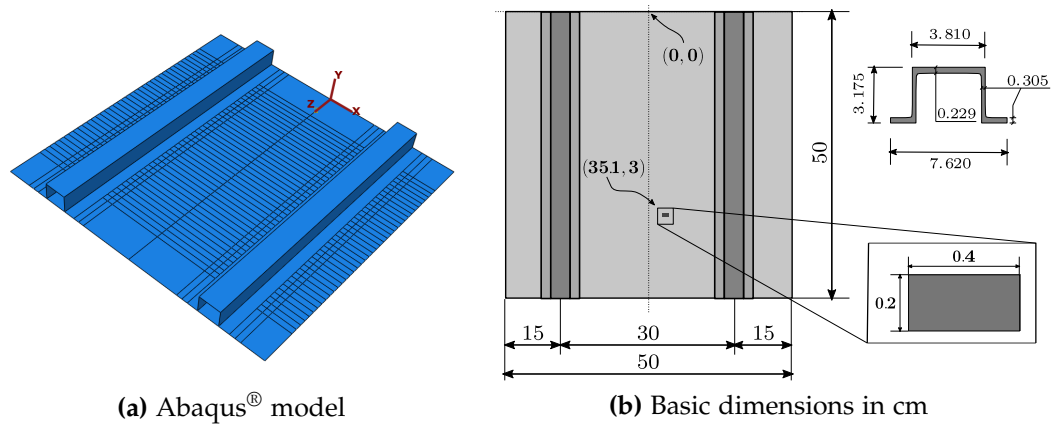
Figure 3.8: Abaqus® model in (a) and dimensions in (b) of the aerospace panel.

waves whereby the robust ToF is estimated and the Bayesian damage localisation is addressed. Here, the stiffeners are assumed to be perfectly bonded to the base plate whereas the damage is simulated as a 0.2cm × 0.4cm hole located at (35.1, 3) cm, considering the origin of coordinates at the centre of one plate's edges, as shown in Figure 3.8b. S4R (4-node doubly curved thin or thick shell, reduced integration, hourglass control, finite membrane strains) shell elements [196] are used with a mesh size of 0.05 cm. Note that shell elements capture only anti-symmetric wave modes, equivalent to bending modes, while solid elements may capture both symmetric and anti-symmetric modes. Therefore, and since the optimisation of the sensor configurations was addressed using the first anti-symmetric mode, the adoption of shell elements facilitates the robust ToF identification as no mode mixture (from both the symmetric and anti-symmetric modes) is expected to arise at a frequency 300 kHz.

The guided waves are generated with a 5 cycle sine tone burst centred at the aforementioned frequency applied in the perpendicular direction at the centre of the plate. The plate and stiffeners dimensions are depicted in Figure 3.8b. The material is aluminium 2024-T351, thus the mechanical properties (Young's modulus E and Poisson's ratio ν) are the values specified for the previous case study in Section 3.2.1. The prior knowledge of the model parameters remains the same as that specified in Section 3.2.2.

The damage localisation results of the optimal configurations are depicted by their corresponding posterior distributions in Figures 3.9a to 3.9c. As is evident from the damage localisation results, both the open configuration as well as the configuration with two arrays reconstruct the damage position remarkably well, while the configuration using one array provides higher uncertainty about the damage position. Note that the single array configuration would need comparatively more sensors than either the open or double array configurations to achieve the same level of preciseness. Such behaviour is also supported by the wave velocity reconstructions observed in Figure 3.9d, where the posterior PDFs provided by the open and two-array configurations are more precise (i.e. have less uncertainty) than the one with one-array configuration.

(a) Open configuration   **(b)** One array   **(c)** Two arrays

(d) Velocity reconstruction
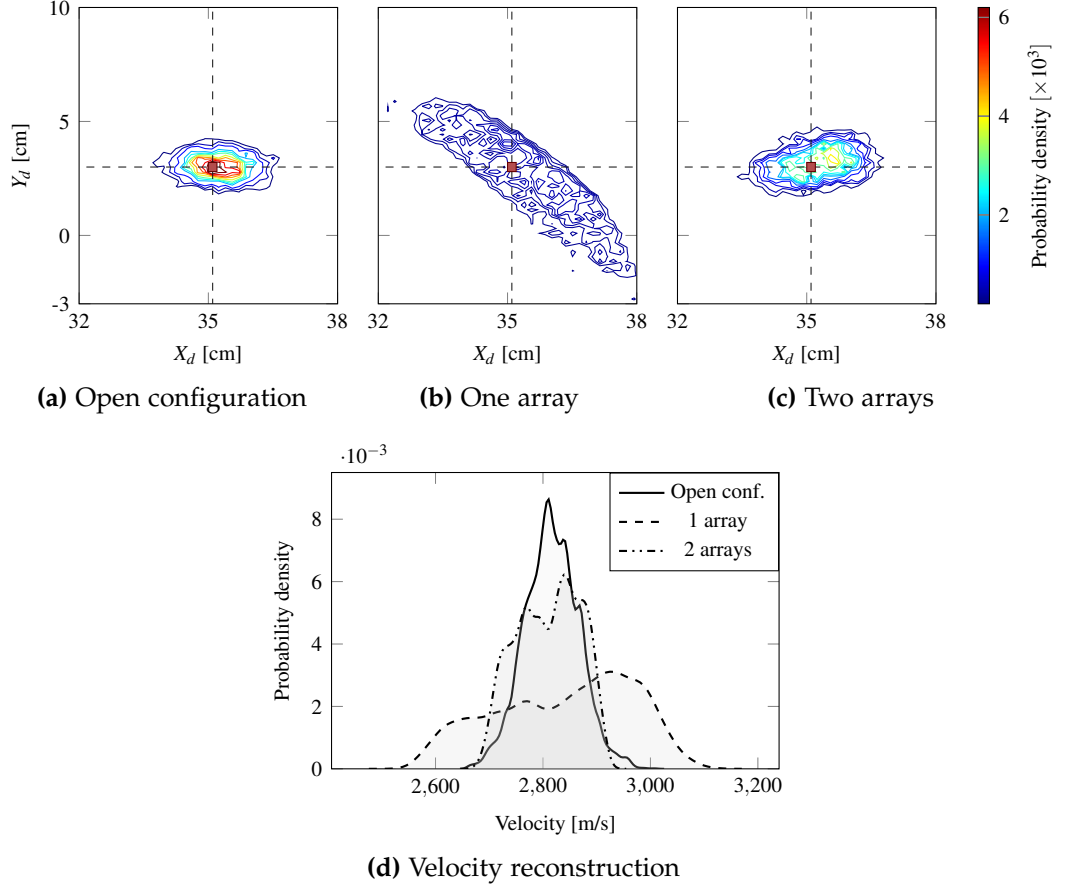
Figure 3.9: Damage position reconstruction corresponding to the optimal configurations using the open, one-array and two-array configurations in panels (a)-(c). The irregularities of contour lines could be improved using more AIMS samples at the cost of heavier computation. Wave propagation velocity reconstruction in panel (d).

3.3 Discussion

3.3.1 On the case studies results

The proposed methodology for optimal sensor configuration in ultrasonic guided-wave based SHM has been illustrated in Section 3.2 using two case studies. In particular, the optimal number and locations of sensors have been shown to be sensitive to the choice of the particular inverse cost function. Thus, a proper inverse cost definition is key for an accurate and efficient SHM design. This was an expected result as a consequence of using the *value* instead of the *amount* of information as the optimality criterion. Note that the definition of the inverse cost function depends on the manufacturing and mainte-

nance costs derived from the SHM system, and thus it is case specific. For instance, if the cost increases linearly with the number of sensors, a linearly decreasing inverse cost function could be assumed to be appropriate. To further explore the dependence of the optimisation results on the inverse cost function, the implications of using different inverse cost functions in the optimal number of sensors are discussed here. In particular, Figure 3.10 shows two different but similar numerical inverse cost functions, namely $f_1(n)$ and $f_2(n)$, and their influence in the value of information curve with respect to the number of sensors for case study 1. The first inverse cost function is defined as a step function $f_1(n) = m \cdot n + y_1$, where $m = \tan(\text{-}0.13°)$, $y_1 = 1 - 0.1188w$, $w = (n - (n \bmod d))/d$, $d = 5.01$, and $n = \{0, 1, 2, \dots\} \in \mathbb{N}^0$. The second inverse cost function $f_2(n)$ is given by interpolating monotonic cubic splines [206] with the following interpolating points: (0, 0), (10, 0.9), (30, 0.4), and (40, 0.05)

(a) Inverse cost function $f_1(n)$

(b) Value of information for different n

(c) Inverse cost function $f_2(n)$

(d) Value of information for different n
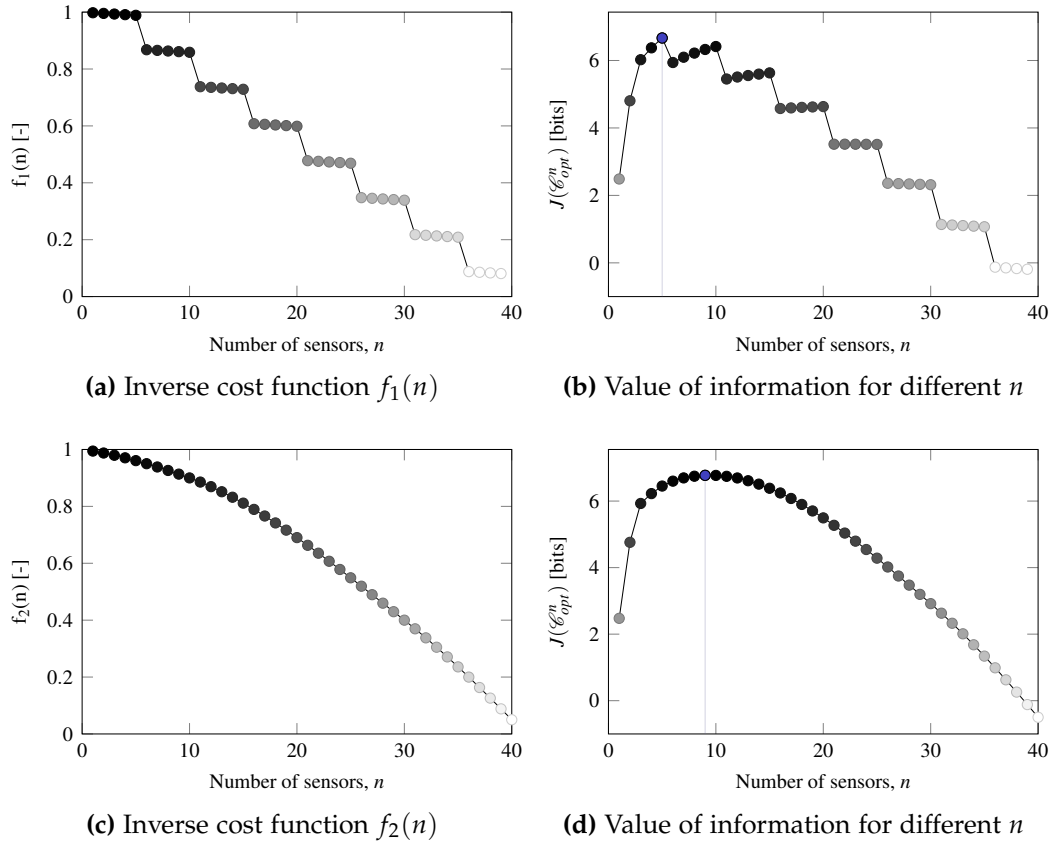
Figure 3.10: Alternative inverse cost functions accounting for SHM systems using slots of 5 sensors (a) along with the resulting influence in the optimal sensor configuration in (b). In (c), a different function which is continuous rather than discrete with a similar trend to (a) leads to a different optimal sensor configuration in (d).

in pairs of $(n, f_2(n))$. As is evident from the results in Figures 3.10b and 3.10d, the optimal number of sensors varies from 5 to 9 sensors just by changing the inverse cost function from $f_1(n)$ to $f_2(n)$, respectively. This simple example reveals the significance of the inverse cost function in the optimal sensor configuration under the proposed methodology based on value of information.

The importance of the definition of the inverse cost function $f(n)$ is also revealed in case study 2. Figure 3.11 summarises the EVI (recall Eq. (3.9)) for each of the optimal configurations under the consideration of both $f_0(n)$ (recall Eq. (3.16)) and $f_1(n)$. As observed, the optimal solution under $f_1(n)$ provides higher EVI values, which is in agreement with the more accurate and efficient (i.e. using fewer sensors) damage reconstructions observed in Figures 3.9a to 3.9c. Observe also that the EVI not only enables a rational criterion for optimal sensor configuration, but also establishes a measure to compare between several candidate inverse cost functions.
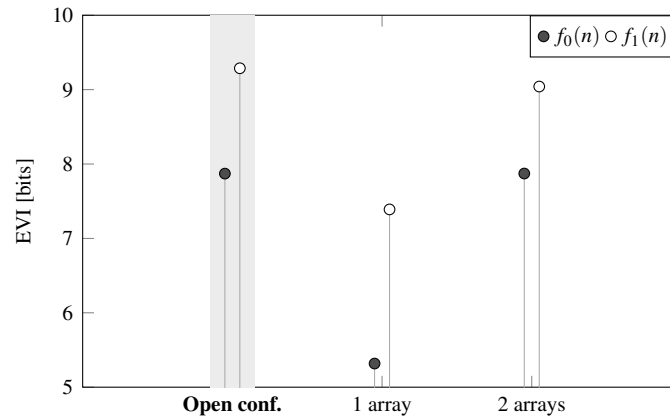
Figure 3.11: Results of the comparison in terms of EVI (circles) for the different sensor positioning strategies and inverse cost functions, namely $f_0(n)$ (grey symbols) and $f_1(n)$ (white symbols), for case study 2. Points on the upper part of the chart represent more informative alternatives.

Nevertheless, this dependence upon the inverse cost function may arguably be seen as an additional complexity, which may lead to suboptimal results depending on priorities, e.g. whether or not the cost is more important than the amount of information gained. However, it is shown here that adopting the value instead of the amount of information provides a better identifiability of the optimal design point. This is manifested in Figure 3.12, where the

KL divergence criterion is compared against the EVI criterion, taking the second case study using $f_0(n)$ and $\alpha = 10$ as an example. As shown in the results, an optimal SHM design point would be barely identifiable using the amount of information criterion (Figure 3.12a) in view of the asymptotic behaviour of the KL divergence. In contrast, the estimator of the EVI (i.e., $J(\mathcal{C}_{opt}^n)$) shown in Figure 3.12b reaches a globally identifiable optimum value, which greatly facilitates the optimisation process.

(a) Robust KL divergence criterion   **(b)** EVI criterion
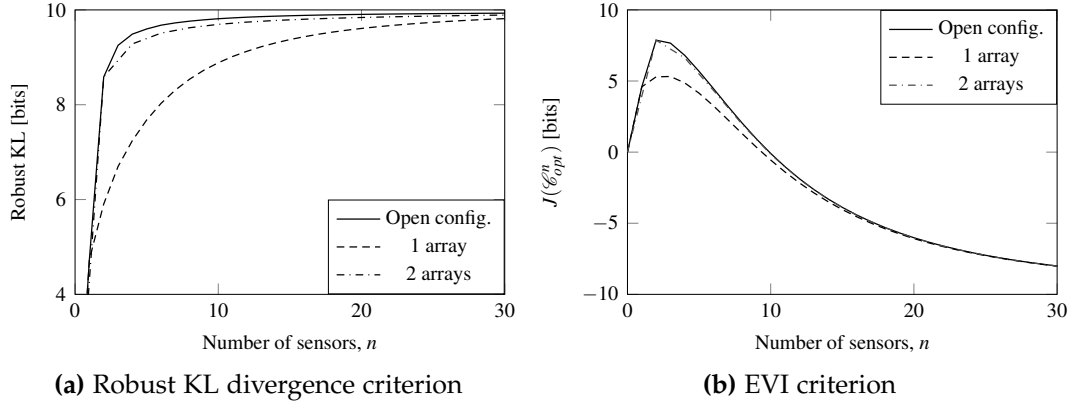
Figure 3.12: Comparison between the robust KL divergence over the area of possible damage occurrence and the EVI criterion using $f_0(n)$.

Note that the constant α included in Equation (3.1) plays an important role in modulating the EVI since it scales the relative cost component in Equation (3.9). However, in view of Figure 3.13a the rank between the candidate sensor positioning strategies is seen to be unaltered by this constant, where the EVI is calculated for $\alpha \in [0, 1000]$ using $f_1(n)$ and the data obtained in case study 2. Conversely, α is shown to influence the optimal number of sensors, as observed in Figure 3.13b. In particular, n_{opt}'' tends to decrease as long as α increases as a consequence of the increasing cost of sensors in the context of the trade-off between information and cost given by Equation (3.9).

3.3.2   On the extensibility of the method

The proposed methodology provides the optimal sensor configuration for a specific area of possible damage occurrence based on a ToF model, which takes into account the position of sensors, actuators, damage, and the wave propa-

(a) EVI for each configuration

(b) Optimal number of sensors
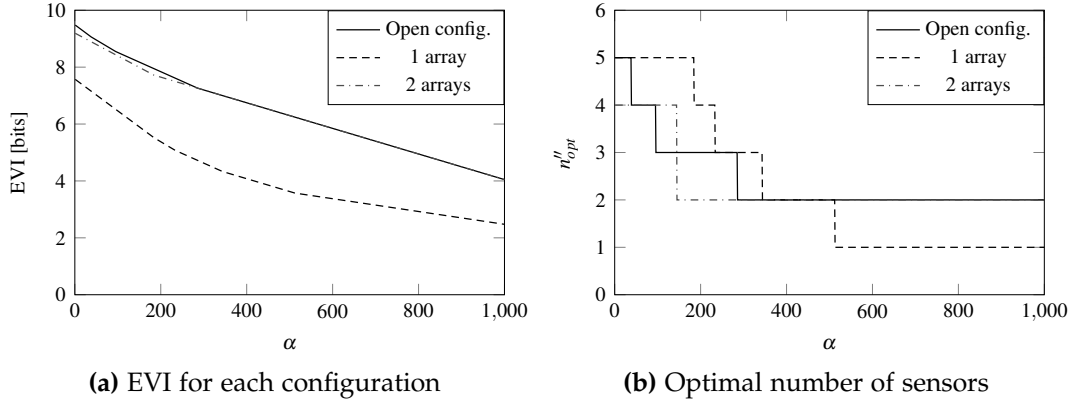
Figure 3.13: Effect of α values in the EVI of each sensor configuration in (a) and its effect in the optimal number of sensors in (b).

gation velocity. Further, the resulting optimal configurations have proven efficiency in reconstructing the damage position. However, the ToF model lacks of advanced physics-related information such as the interaction of the ultrasonic guided-wave with the damage or the effect of attenuation in the localisation of the damage. This prevents the proposed methodology from considering advanced damage features other than the position, such as damage mode and extent (e.g., delamination in composites), and from providing an optimal sensor configuration considering them. In order to consider these advanced damage features, a more complex and physics-based wave propagation model such as the hybrid wave and finite element methods [207] is required. The use of these models in the design of the optimal sensor configuration is still unfeasible due to their considerable computational cost. Therefore, the development of methods to alleviate such computational complexity, such as surrogate methods [27, 208–211], constitutes a desirable extension of this methodology.

Furthermore, note that the proposed method seeks the optimal sensor configuration, assuming that the actuators are fixed in the structure. However, the position and number of actuators play an important role in the optimisation problem. Besides, the sequential sensor placement algorithm using an exhaustive search may find a limitation in practice when considering very large areas of possible damage occurrence, which could lead to an intractable computational burden. In this context, a further and natural extension of the proposed

methodology is the consideration of both sensors and actuators in the optimisation problem considering large and complex structures (e.g. composite laminates). This computationally challenging problem is addressed in Chapter 4 of this dissertation.

3.4   Conclusions

A novel optimal sensor configuration approach based on value of information is presented in this chapter. The methodology is based on a Bayesian damage localisation framework for optimal sensor placement, while the optimal number of sensors is obtained by assessing the expected value of information; thus, uncertainties coming from several sources are taken into consideration. The effectiveness in providing an optimal design point has been illustrated using two case studies considering both flat and stiffened plate structures, respectively. The following conclusions are drawn from this chapter:

- The proposed approach provides a value of information-based framework that trades-off the amount of information and the cost of monitoring, giving a globally identifiable optimal design point.

- The open configuration provides the best damage reconstruction using the lower number of sensors due to its flexibility in positioning sensors over the structure;

- Based on the results, the two-array configuration provides more accurate damage reconstructions using less number of sensors than the one-array configuration.

- An accurate definition of the inverse cost function has been shown to be key for an unbiased optimal sensor configuration under the proposed methodology.

Further research work is needed to address (1) the extensibility of the proposed method using a physics-based model instead of the time of flight one

used here, (2) the efficiency of the method when considering the optimisation of both actuators and sensors in large plate-like structures, and (3) the optimality of the inverse cost function in different specific cases.

4

Entropy-based optimal sensor and actuator configuration

In this chapter, an efficient method is proposed to obtain both the optimal number and location of sensors and actuators for SHM systems by minimising a cost-benefit function in terms of Shannon's information entropy and a cost function. This approach extends the work previously developed in [45, 101], which addresses optimal placement of a fixed number of sensors by applying convexification and relaxation techniques to the entropy of the *pre-posterior* distribution, which is based on the model-predicted data. By performing a cost-benefit optimisation, the optimal number is found, as well as the optimal location of both sensors and actuators. Although the methodology presented here is generic and employable within any monitoring field involving actuators and sensors for obtaining information relating to a structural, chemical, or biological system, it is illustrated here using ultrasonic guided-wave based SHM. This application provides a challenging scenario involving the optimal configuration (number and location) of actuators and sensors over a two-dimensional space in isotropic and orthotropic materials. The chosen layout of the sensor and actuator grids and the area of possible damage occurrence are customisable, so that they can be adapted to any kind of structure and prior information. A high efficiency in obtaining the optimal configurations is observed

in comparison with existing information-based approaches regardless of the complexity of the material, which enhances the use of this methodology in complex, real-world applications.

The remainder of this chapter is organised as follows: Section 4.1 describes the proposed entropy-based convex optimisation methodology for the configuration of actuators and sensors configuration; Section 4.2 illustrates the methodology through two case studies using two different plate-like structures; Section 4.3 provides a discussion of the impact of the proposed method on ultrasonic guided-wave based SHM. Finally, Section 4.4 provides concluding remarks.

4.1 Methodology

4.1.1 Optimal placement for a given number of sensors and actuators

Let $x_i^j(t, \boldsymbol{\theta}) \in \mathbb{R}$ denote a deterministic model prediction for parameters $\boldsymbol{\theta}$ of an arbitrary QoI at discrete time t (e.g. time of flight of an ultrasonic wave or acceleration at a material point) at the i-th sensor, assuming that the input excitation is provided by the j-th actuator. It is assumed that T observations will be available for this QoI, denoted by $\mathbf{D}_T = \{y_i^j(t) \in \mathbb{R}, t = 1, \dots, T\}$, when the sensors are installed. These observations could come from an experiment or simulation that is repeated T times, or t could be interpreted as an instant of time within a QoI time-history [92, 93]. The deterministic model prediction and the actual QoI are related by introducing a stochastic prediction-error term that accounts for the discrepancy between the model output and the actual observation [32], as follows:

$$y_i^j(t) = x_i^j(t, \boldsymbol{\theta}) + e_i^j(t) \tag{4.1}$$

The uncertain prediction error is conservatively assumed to be modelled as a

zero-mean Gaussian distribution with standard deviation $\sigma_e \in \mathbb{R}$, as explained in Section 3.1.2. If the actual number of sensors and actuators installed are denoted by N_s^g and N_a^g, respectively, then the predicted data for a specified sensor and actuator configuration is:

$$p(\mathbf{D}_\mathrm{T}|\boldsymbol{\theta}) = \prod_{j=1}^{N_a^g} \prod_{i=1}^{N_s^g} \prod_{t=1}^{\mathrm{T}} p(y_i^j(t)|\boldsymbol{\theta}) \tag{4.2}$$

where the prediction errors in Equation (4.1) are chosen to be independent stochastically, that is, if one prediction error is known, it provides no information about the others. Next, two grids of sensor and actuator positions of N_s and N_a points, respectively, are chosen to provide possible locations of these devices. The actual locations of the sensors and actuators are then selected by activating binary variables denoted by $\Psi_s^{(i)} \in \{0,1\}$ and $\Psi_a^{(j)} \in \{0,1\}$, respectively, where 0 and 1 correspond to the absence and presence of a sensor or actuator at the i-th and j-th locations of their respective sets of grid points. Thus, Equation (4.1) can be rewritten as:

$$p(\mathbf{D}_\mathrm{T}|\boldsymbol{\theta}) = \prod_{j=1}^{N_a} \Psi_a^{(j)} \prod_{i=1}^{N_s} \Psi_s^{(i)} \prod_{t=1}^{\mathrm{T}} p(y_i^j(t)|\boldsymbol{\theta}) \tag{4.3}$$

Assuming a large number of data points T [92, 93], the posterior PDF of the model parameters $\boldsymbol{\theta}$ given the data $\mathbf{D}_\mathrm{T}$ and a particular actuator and sensor configuration specified by $\boldsymbol{\Psi}_a$ and $\boldsymbol{\Psi}_s$ respectively, can be asymptotically approximated as [93]:

$$p(\boldsymbol{\theta}|\boldsymbol{\Psi}_a, \boldsymbol{\Psi}_s, \mathbf{D}_\mathrm{T}) \cong \frac{[\det Q(\boldsymbol{\Psi}_a, \boldsymbol{\Psi}_s, \boldsymbol{\theta})]^{\frac{1}{2}}}{(2\pi\hat{\sigma}_e)^{\frac{1}{2}N_a N_s}} \exp\left[-\frac{1}{2\hat{\sigma}_e^2}(\boldsymbol{\theta} - \hat{\boldsymbol{\theta}})^T Q(\boldsymbol{\Psi}_a, \boldsymbol{\Psi}_s, \boldsymbol{\theta})(\boldsymbol{\theta} - \hat{\boldsymbol{\theta}})\right] \tag{4.4}$$

where $\hat{\boldsymbol{\theta}}$ is the maximum a posteriori (MAP) value of the posterior distribution in Equation (4.4) and $Q(\boldsymbol{\Psi}_a, \boldsymbol{\Psi}_s, \boldsymbol{\theta}) \in \mathbb{R}^{N_\theta \times N_\theta}$ (N_θ: the number of uncertain model parameters considered in the predictive deterministic model $x_i^j(\boldsymbol{\theta})$) is

given by [212]:

$$Q(\mathbf{\Psi}_a, \mathbf{\Psi}_s, \boldsymbol{\theta}) \cong \sum_{j=1}^{N_a} \Psi_a^{(j)} \sum_{i=1}^{N_s} \Psi_s^{(i)} \left\{ \sum_{t=1}^{T} \left(\nabla_{\boldsymbol{\theta}} x_i^j(\boldsymbol{\theta}) \nabla_{\boldsymbol{\theta}}^T x_i^j(\boldsymbol{\theta}) \right) \right\}$$

$$= \sum_{j=1}^{N_a} \Psi_a^{(j)} \sum_{i=1}^{N_s} \Psi_s^{(i)} P_i^j(\boldsymbol{\theta}) \tag{4.5}$$

where matrix $P_i^j(\boldsymbol{\theta}) = \sum_{t=1}^{T} \nabla_{\boldsymbol{\theta}} x_i^j(\boldsymbol{\theta}) \nabla_{\boldsymbol{\theta}}^T x_i^j(\boldsymbol{\theta}) \in \mathbb{R}^{N_\theta \times N_\theta}$ and $\nabla_{\boldsymbol{\theta}} x_i^j(\boldsymbol{\theta})$ denotes the gradient vector of $x_i^j(\boldsymbol{\theta})$. Notice that in Equation (4.4), the dependence on data $\mathbf{D}_T$ is only through the MAP values $\hat{\boldsymbol{\theta}}$.

When the optimal sensor and actuator configuration is being determined, data $\mathbf{D}_T$ will not be available, so a *pre-posterior* analysis is necessary where an expectation of the information entropy of the posterior in Equation (4.4) is taken, which is a measure of the posterior parameter uncertainty that also accounts for it being conditional on unknown future data that will be collected by the sensor network. The expectation of the posterior entropy is with respect to the data $\mathbf{D}_T$ as predicted probabilistically by the model in Equation (4.1).

An approximation was introduced in [93] that avoids such computationally demanding Monte Carlo simulation of samples for $\mathbf{D}_T$, as follows. Assuming large T, the MAP values $\hat{\boldsymbol{\theta}}$ of the model parameters are replaced by the nominal values $\boldsymbol{\theta}_0$ of the model parameters defined by their prior distribution $p(\boldsymbol{\theta}_0)$, which describes the designers' uncertainty about appropriate values of the model parameters. The entropy-based objective function can then be expressed as [93]:

$$h(\mathbf{\Psi}_a, \mathbf{\Psi}_s) = -\mathbb{E}_{\boldsymbol{\theta}_0} \left[\log \det Q(\mathbf{\Psi}_a, \mathbf{\Psi}_s, \boldsymbol{\theta}_0) \right] \tag{4.6}$$

The problem of optimal sensor and actuator placement now becomes the minimisation of this pre-posterior measure of parameter uncertainty over discrete variables $\Psi_s^{(i)}$ and $\Psi_a^{(j)}$, where $\sum_{i=1}^{N_s} \Psi_s^{(i)} = N_s^g$ and $\sum_{i=1}^{N_a} \Psi_a^{(i)} = N_a^g$.

Next, based on the idea in [44, 45, 101], the variables $\Psi_s^{(i)}$ and $\Psi_a^{(j)}$ in

Equation (4.6) are relaxed into continuous variables z_i and w_j in the interval $[0, 1]$. Therefore, the function Q now can be expressed as $Q(w, z, \boldsymbol{\theta}_0) \cong \sum_{j=1}^{N_a} w_j \sum_{i=1}^{N_s} z_i P_i^j(\boldsymbol{\theta}_0)$ with $w_j \in [0, 1]$ and $z_i \in [0, 1]$. Equation (4.6) is then of the form of $f(X) = -\mathbb{E}_X[\log \det(X)]$, where X is a positive semidefinite matrix that is linear in the continuous variables, and therefore the function is convex in the domain of these variables [43]. Thus, the original combinatorial optimisation problem is transformed into a continuous convex optimisation problem with respect to $z \in [0, 1]^{N_s}$ and $w \in [0, 1]^{N_a}$ that is readily solved numerically using classical convex minimisation methods [44, 45] such as the interior-point algorithm:

$$
\begin{aligned}
\underset{w, z}{\text{minimise}} \quad & h(w, z) = -\mathbb{E}_{\boldsymbol{\theta}_0} \left[\log \det Q(w, z, \boldsymbol{\theta}_0) \right] \\
\text{subject to} \quad & 0 \le w_j \le 1, \ j = 1, \ldots, N_a \\
& 0 \le z_i \le 1, \ i = 1, \ldots, N_s \\
& \sum_{j=1}^{N_a} w_j = N_a^g \\
& \sum_{i=1}^{N_s} z_i = N_s^g
\end{aligned} \tag{4.7}
$$

Note that $h(w^*, z^*)$, corresponding to the optimal values in Equation (4.7) for each $w_j^* \in [0, 1]$ and $z_i^* \in [0, 1]$, provides a lower bound of the minimum of $h(\boldsymbol{\Psi}_a, \boldsymbol{\Psi}_s)$ in Equation (4.6). If any w_j^* or z_i^* is not at its boundary value of 0 or 1, then the solution to Equation (4.7) is not directly applicable in its continuous form in practice since the sensors or actuators can only be present or absent at each grid point, i.e., w_j and z_i need to be either 1 or 0. In this case, the variables can be rounded to their closest binary value while ensuring that the constraints $\sum_{j=1}^{N_a} w_j = N_a^g$ and $\sum_{i=1}^{N_s} z_i = N_s^g$ are still satisfied. This gives a binary solution $(\boldsymbol{\Psi}_a^*, \boldsymbol{\Psi}_s^*)$ where $h(\boldsymbol{\Psi}_a^*, \boldsymbol{\Psi}_s^*)$ is an upper bound of the exact minimum of $h(\boldsymbol{\Psi}_a, \boldsymbol{\Psi}_s)$. If these upper and lower bounds are close, then $(\boldsymbol{\Psi}_a^*, \boldsymbol{\Psi}_s^*)$ can be taken as a near-optimal placement solution.

4.1.2 Optimal actuator and sensor configuration: cost-benefit analysis

Building on the problem of optimal actuator and sensor placement formulated in the previous sub-section, the optimal number of sensors and actuators may also be addressed by introducing a monotonically increasing dimensionless cost function $s(n) : [1, (N_a + N_s)] \rightarrow [0, 1]$ that quantifies the cost of adding n devices into the SHM system. Note that the cost function includes both actuators and sensors in the same function, which is appropriate for the application of interest, ultrasonic guided-wave based SHM, where a PZT transducer can be used as either a receiver or emitter. However, $s(n)$ can be defined differently in other applications where sensors and actuators may have different costs. For efficient optimisation, the variable n is chosen to be real, lying in the interval $n \in [0, (N_a + N_s)]$. Since the objective function in Equation (4.7) is monotonically decreasing with respect to n [94], and $s(n)$ is monotonically increasing, a new convex minimisation problem can be defined as follows:

$$
\begin{aligned}
\underset{w,z,n}{\text{minimise}} \quad & h^*(w, z, n) = -\mathbb{E}_{\boldsymbol{\theta}_0} \left[\log \det Q(w, z, \boldsymbol{\theta}_0) \right] + \eta \cdot s(n) \\
\text{subject to} \quad & 0 \leq w_j \leq 1, \ j = 1, \ldots, N_a \\
& 0 \leq z_i \leq 1, \ i = 1, \ldots, N_s \\
& \sum_{j=1}^{N_a} w_j + \sum_{i=1}^{N_s} z_i = n
\end{aligned}
\tag{4.8}
$$

where $\eta > 0$ is used to establish a particular trade-off between information gain and cost. $s(n) : [1, (N_a + N_s)] \rightarrow [0, 1]$ is chosen as a dimensionless cost function formed using interpolating monotonic cubic splines [206] due to their ease of implementation and versatility in mimicking almost any monotonically increasing cost function. The function $s(n)$ takes a value of 0 when there is the specified minimum number of sensors and actuators, and the value of 1 for the specified maximum number of them. As for the minimisation in Equation (4.7), the convex optimisation problem in Equation (4.8) may be addressed
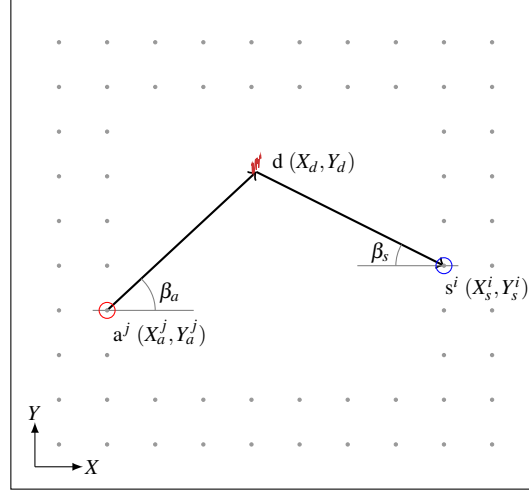
Figure 4.1: Graphical representation of the paths followed by the guided-waves emitted by the actuator a^j, which interact with the damage d and are acquired at the sensor s^i. The grey points represent the space of possible sensor/actuator positions.

with standard convex minimisation algorithms such as the interior-point algorithm. Hence, both the optimal placement and optimal number of actuators and sensors are simultaneously obtained in a very efficient, yet rigorous, manner.

4.1.3 Bayesian damage localisation using ultrasonic guided-waves

In this chapter, the proposed approach for optimal sensor and actuator configuration is utilised for ultrasonic guided-wave based damage localisation using the ellipse-based ToF model presented in Section 3.1.2 of this thesis. However, a more general expression that can be used for isotropic structures and composite laminates is adopted here, which is defined as:

$$x_i^j = \frac{\sqrt{\left(X_d - X_a^j\right)^2 + \left(Y_d - Y_a^j\right)^2}}{V_{a-d}(f, \beta)} + \frac{\sqrt{\left(X_d - X_s^i\right)^2 + \left(Y_d - Y_s^i\right)^2}}{V_{d-s}(f, \beta)} \quad (4.9)$$

where $(X_d, Y_d) \in \mathbb{R}^2$ are the coordinates of the damage position, $(X_a^j, Y_a^j) \in \mathbb{R}^2$ are the j-th actuator transducer coordinates, $(X_s^i, Y_s^i) \in \mathbb{R}^2$ are the coordinates of the i-th sensor transducer, and $V_{a-d}(f, \beta)$ and $V_{d-s}(f, \beta)$ are the wave prop-

agation velocities of the actuator-damage and damage-sensor paths defined by the angle β, respectively. Figure 4.1 depicts the geometrical characteristics of the paths from an arbitrary actuator to a sensor (selected from the possible sensor/actuator positions), passing through the damage position. In general, the velocities depend on the frequency of excitation f, the wave mode under investigation, and the direction of the path with respect to the material orientation. Assuming that the situation involves an orthotropic material, such as a composite laminate, these velocities can be approximated by modelling the velocity profile with respect to the angle for a given frequency. Here, the velocity is assumed to be distributed elliptically in space as in the case of angle-ply laminates, as follows [166]:

$$V(f,\beta) = \sqrt{V_x^2 + V_y^2} = \sqrt{(a \cdot \cos(\phi))^2 + (b \cdot \sin(\phi))^2} \qquad (4.10)$$

where the parameter angle ϕ relates to the physical angle β [166] as follows:

$$\phi = \arctan\left(\frac{a}{b}\tan\left(\beta\right)\right); \qquad (4.11)$$

where a and b denote the two main axes of the velocity ellipse and the angle β can be particularised for the actuator-damage and damage-sensor paths, namely β_a and β_s respectively, as follows:

$$\beta_a = \arctan\left(\frac{Y_d - Y_a^j}{X_d - X_a^j}\right), \quad \beta_s = \arctan\left(\frac{Y_s^i - Y_d}{X_s^i - X_d}\right) \qquad (4.12)$$

Therefore, the set of uncertain parameters of the ToF model for orthotropic materials are the damage coordinates in addition to a and b, so $\boldsymbol{\theta} = \{X_d, Y_d, a, b\}$. Alternatively, the set of parameters can be simplified if an isotropic structure (e.g. an aluminium plate) is considered, since both velocity terms would be identical. Then, the set of parameters would be $\boldsymbol{\theta} = \{X_d, Y_d, V\}$.

4.2 Case studies

In this section, the optimal actuator and sensor configuration methodology is applied to plate-like structures with irregular, but realistic, geometries motivated by the shape of wing skin panels of standard commercial aircraft, as suggested in Figure 4.2.
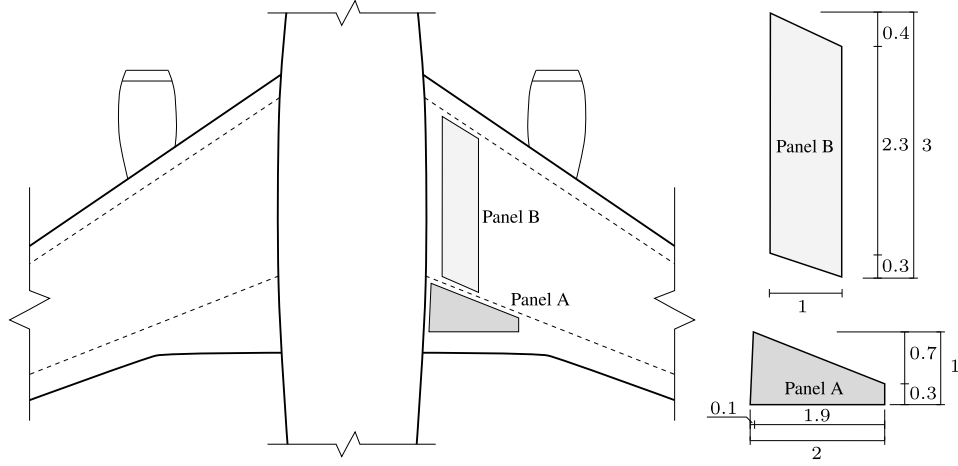
Figure 4.2: Top view of the central part of standard aircraft. Two typical skin panel geometries (A and B) with irregular geometries are highlighted in the right wing. Dimensions expressed in metres.

4.2.1 Description of structures and definition of problem

Two thin-walled structures, named panels A and B, as depicted in Figure 4.2, are considered in this case study. Additionally, it is assumed that there exist two possible panels for each geometry A and B, denoted as panels A1, A2, B1, and B2, where the number refers to different materials. Panels A1 and B1 are made of aluminium alloy 2024-T351 with 2 mm. On the other hand, panels A2 and B2 are made of a quasi-isotropic T800-M913 carbon fibre laminate with $[\text{-}45/90_2/45/0]_s$ stacking sequence and 1.5 mm thickness. The mechanical properties of both materials are shown in Table 4.1. Note that these properties are assumed to be deterministically known for all the examples in this case study.

The guided-wave mode assumed for health monitoring of the aluminium

Table 4.1: Nominal values of the mechanical properties of both the aluminium structure and one layer of the composite material.

Composite T800-M913	Longitudinal stiffness E_{11} [GPa] 152.14	Transverse stiffness E_{22} [GPa] 6.64	Shear stiffness G_{12} [GPa] 4.20
	Poisson's ratio ν_{12} [-] 0.25	Poisson's ratio ν_{23} [-] 0.54	Density ρ [kg/m^3] 1550
Aluminium 2024-T351	Young's modulus E [GPa] 73.1	Poisson's ratio ν [-] 0.33	Density ρ [kg/m^3] 2780

sheets (panels A1 and B1) is the A_0 mode at 300 kHz, whose group velocity is 3000 m/s. In case of the composite plates (panels A2 and B2), the S_0 mode is chosen at 150 kHz, whose group velocity is angle-dependent following an elliptical profile defined by its major axis $a = 7549$ m/s and its minor axis $b = 6030$ m/s, as shown in Figure 4.3a. Note that the global axis system is assumed to be coincident with the material axes. The wave propagation velocities for both aluminium and composite materials are related to their mechanical properties and obtained by computing their dispersion curves at different angles using Dispersion Calculator [213]. Note that also the only information needed to address the ToF-based actuator and sensor optimisation is the wave propagation velocity, either as a constant value for isotropic materials, or angle-dependent in case of orthotropic materials.

A cost function $s(n)$ is arbitrarily defined in order to address the proposed combined optimisation of the number and positions of PZT sensors and actuators (recall Eq. (4.8)) in the form of interpolating cubic splines with intermediate points that defined such a function, as shown in Figure 4.3b. The interpolating points are represented as circles in Figure 4.3b and are as follows: (0, 0), (30, 0.3), (50, 0.95), (60, 1), in pairs of $(n, s(n))$ where n is the number of transducers. Here, the same cost per unit is used for both sensors and actuators, arising from the nature of guided-wave based SHM, which uses PZT transducers for emitting and receiving ultrasonic signals. Additionally, the trade-off between information gain and cost, dictated by η in Equation (4.8), is

(a) Group velocity (S_0 mode) profile.
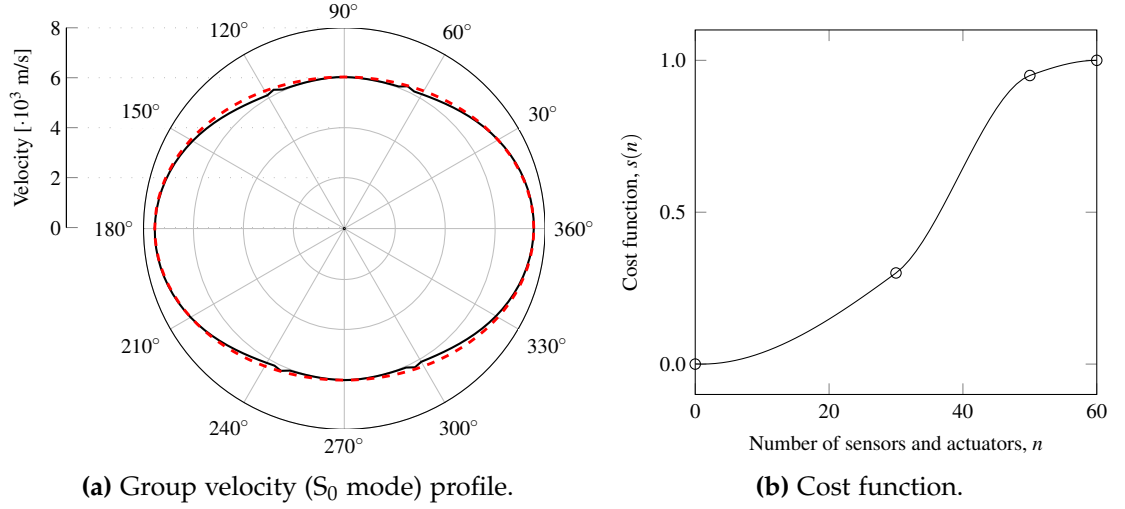
(b) Cost function.

Figure 4.3: In panel (a), angular dependence of the group velocity of the S_0 mode at 150 kHz (solid line) in the composite laminate and its approximation by an ellipse with major axis $a = 7549$ m/s and minor axis $b = 6030$ m/s (dashed line). In panel (b), the cost function $s(n)$ used for the optimisation of the number of sensors and actuators.

chosen to be $\eta = |h(w, z)|$ for the case studies presented hereinafter.

4.2.2 Optimal sensor and actuator configuration: panel A

Aluminium panel A1

The results for the isotropic plate (panel A1) are obtained using a uniform distribution of possible damage occurrence inside the grey area represented in Figure 4.4a. An estimation for the mean value of V can be obtained based on the guided-wave theory; hence, a normal distribution is adopted for its prior PDF with its mean centred at the theoretical V value and a specified standard deviation. Therefore, the prior uncertainty for the wave propagation velocity is quantified by a Gaussian PDF, $V \sim \mathcal{N}(3000, 40^2)$ in [m/s] units. Note that V intrinsically carries information about the material and manufacturing uncertainties as a byproduct.

The optimisation is addressed using 500 samples drawn from the prior distribution of the model parameters $\theta = \{X_d, Y_d, V\}$, along with the previously proposed cost function $s(n)$ in Figure 4.3b. Results from Figure 4.4a show that the optimal locations for the sensors and actuators are the same, generally at
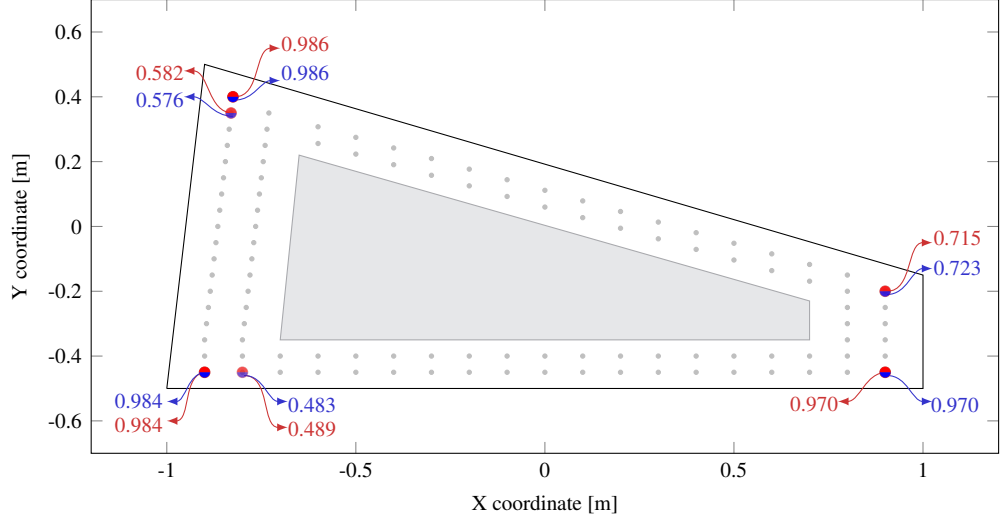
(a) Optimal actuator and sensor configuration for panel A1.
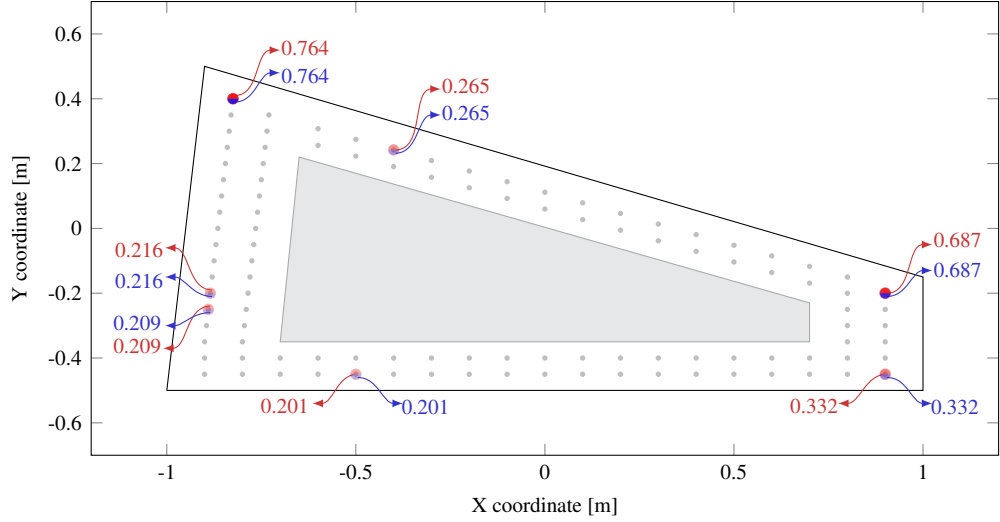
(b) Optimal actuator and sensor configuration for panel A2.

Figure 4.4: Optimal actuator and sensor configuration for the panel geometry A. (a) depicts the case for aluminium alloy 2024-T351 and a uniform prior over the grey inner polygon, and (b) shows the same geometry and prior uncertainty in case of the composite laminate of layup $[-45/90_2/45/0]_s$. Red and blue numbers represent the value of actuator and sensor decision variables (w_j and z_i), respectively.

the corners, with the same optimal number of $\sum_{j=1}^{N_a} w_j = \sum_{i=1}^{N_s} z_i = 6.30$ for each device type (i.e. $n = 12.60$, as in Eq. (4.8)). Note that the total number of sensors and actuators is a real number since the decision variables (w_j and z_i) are continuous in the interval $[0, 1]$. Note also that the results show only the sensor and actuator positions with $w_j \geq 0.2$ and $z_i \geq 0.2$ to better identify the optimal positions. These thresholds make the sum of decision variables $\sum_j w_j = 4.726$ and $\sum_i z_i = 4.722$ for actuators and sensors, respectively, which

are different from the optimal numbers of sensors and actuators given above as they consider all the values below the previous threshold.

In the left corners, both the upper and bottom ones, the results provide two sensors and actuators placed next to each other. This behaviour can be explained under the assumption of the stochastic independence of the data acquired by the sensors, which causes a sensor clustering effect. In this case, the optimal sensor and actuator configuration provides an objective function value (recall Eq. (4.8)) of $h^*(w, z, n) = 55.0237$. However, such optimal configuration cannot be applied in practice, and therefore, a Boolean approximation is selected by rounding off the number of sensors and actuators (e.g. $6.30 \rightarrow 6$) for each device type, and selecting the six positions with higher w_j and z_i (see Table 4.2). This Boolean approximation provides an objective function value of $h^*(\Psi_a, \Psi_s, n) = 55.0587$, which represents a remarkably close approximation to the optimal convex configuration. The coordinates of the positions above the specified threshold and the corresponding Boolean layout are given in Table 4.2.

Table 4.2: Sensors and actuators above the threshold $w_j \geq 0.2$ and $z_i \geq 0.2$ along with their coordinates and the approximate Boolean solution for the panel A1.

	PZT coordinates		Relaxed solution		Binary solution	
PZT No.	X [m]	Y [m]	w [-]	z [-]	Ψ_a	Ψ_s
1	-0.900	-0.450	0.984	0.984	1	1
2	-0.800	-0.450	0.489	0.483	1	1
3	0.900	-0.450	0.970	0.970	1	1
4	0.900	-0.200	0.715	0.723	1	1
5	-0.830	0.350	0.986	0.986	1	1
6	-0.825	0.400	0.582	0.576	1	1

Composite panel A2

In the case of the composite panel A2, the same number of samples and prior distribution of the damage coordinates (X_d, Y_d) used for the previous case (panel A1) are applied. The prior information of the parameters that define the elliptical model of the wave propagation velocity, a and b, are distributed using Gaussian PDFs as follows: $a \sim \mathcal{N}(6030, 40^2)$ and $b \sim \mathcal{N}(7549, 40^2)$,

with both expressed in [m/s] units. The normal probability models adopted for the prior distribution of the velocity-related parameters a and b are chosen following the rationale explained in the previous subsection.

Figure 4.4b shows the optimal actuator and sensor configuration using the $s(n)$ defined in Figure 4.3b, which gives an equal optimal number for sensors and actuators of 5.33. Note that the transducers are distributed differently from those in the isotropic case, appearing at intermediate zones of the structure. The angular-dependent wave propagation profile (see Figure 4.3a) drives the optimal positioning of the transducers, hence highlighting the importance of carrying out optimal sensor and actuator configuration studies for structures with different materials, even if they share the same geometry. The seven sensors that appear in Figure 4.4b are listed in Table 4.3 considering again the threshold values $w_j \geq 0.2$ and $z_i \geq 0.2$, and they lead to an objective function evaluation of $h^*(w, z, n) = 99.6435$, which is a lower bound. Given the stochastic nature of the objective function and that several PZTs have similar w and z values, the practical solution using a Boolean approximation is addressed by exploring the combinations of PZT 3 and 6 (i.e. the ones with highest w and z values) with the rest of transducers listed in Table 4.3. The best sub-optimal Boolean approximation corresponds to the six sensors and actuators specified in Table 4.3 and results in $h^*(\Psi_a, \Psi_s, n) = 100.2577$. Note also in Figure 4.4b that PZT 4 and 5 are close to each other and that with this approximation one of them is dropped, hence avoiding sensor clustering.

Table 4.3: Sensors and actuators above the threshold $w_j \geq 0.2$ and $z_i \geq 0.2$ along with their coordinates and the approximate Boolean solution for panel A2.

PZT No.	PZT coordinates		Relaxed solution		Binary solution	
	X [m]	Y [m]	w [-]	z [-]	Ψ_a	Ψ_s
1	-0.500	-0.450	0.201	0.201	1	1
2	0.900	-0.450	0.332	0.332	1	1
3	0.900	-0.200	0.687	0.687	1	1
4	-0.890	-0.240	0.209	0.209	0	0
5	-0.885	-0.190	0.216	0.216	1	1
6	-0.825	0.410	0.764	0.764	1	1
7	-0.400	0.242	0.265	0.265	1	1

4.2.3 Optimal sensor and actuator configuration: panel B

Aluminium panel B1

The results for the isotropic plate with the geometry B that are shown in Figure 4.5a are obtained in this case using a prior damage distribution of possible occurrence over the grey polygon with two concentrated areas. This example represents a plate that is stiffened in the centre and close to the lateral edges, and hence the centre of the spans between stiffeners are more likely to suffer damage. Thus, the a priori information of the X_d coordinate is represented as a bimodal Gaussian distribution consisting of the weighted summation of two Gaussian PDFs, $X_d \sim \{1/2\mathcal{N}(-0.6, 0.2^2) + 1/2\mathcal{N}(0.6, 0.2^2)\}$ with units expressed in metres, while the Y_d is uniformly distributed, both within the bounded area represented in Figure 4.5a. Furthermore, the wave propagation velocity V is equally distributed as specified in Section 4.2.2 using the same number of prior samples to evaluate the objective function.

As observed from the results shown in Figure 4.5a, the sensors and actuators above the previously specified thresholds ($w_j \geq 0.2$ and $z_i \geq 0.2$) are again coincident and concentrated at the corners of the plate, especially at the bottom left and upper right ones, with an optimal number of 6.35. Table 4.4 summarises the optimal positions along with their corresponding coordinates for the convex optimisation problem, which provides an objective function evaluation of $h^*(w, z, n) = 54.2611$. Correspondingly, the Boolean so-

Table 4.4: Sensors and actuators above the threshold $w_j \geq 0.2$ and $z_i \geq 0.2$ along with their coordinates and the approximated Boolean solution for the panel B1.

PZT No.	PZT coordinates		Relaxed solution		Binary solution	
	X [m]	Y [m]	w [-]	z [-]	Ψ_a	Ψ_s
1	-1.400	-0.400	0.412	0.408	1	1
2	-1.400	-0.450	0.997	0.997	1	1
3	0.900	-0.450	0.261	0.259	0	0
4	1.000	-0.450	0.991	0.991	1	1
5	-1.160	0.450	0.981	0.983	1	1
6	1.300	0.450	0.995	0.995	1	1
7	1.300	0.400	0.517	0.513	1	1
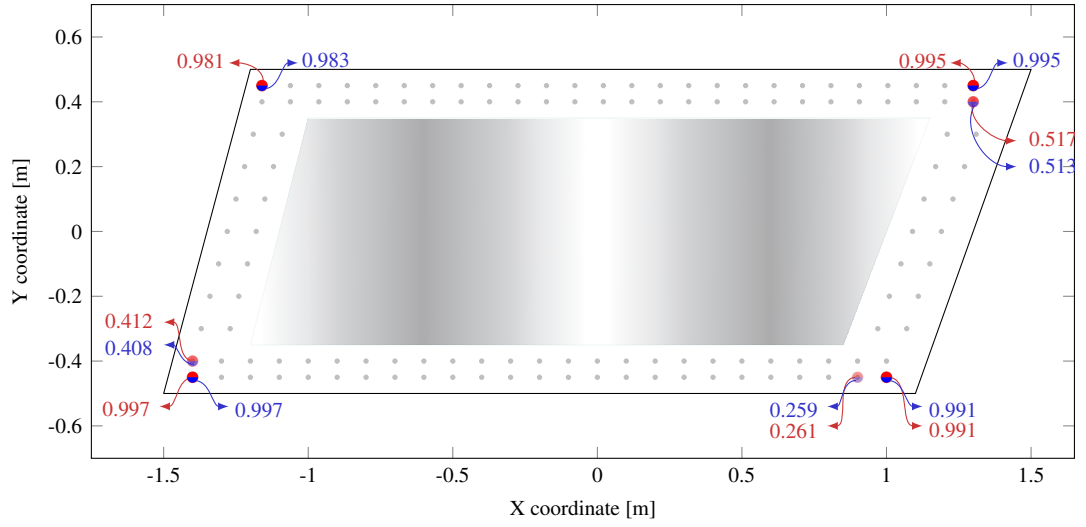
(a) Optimal actuator and sensor configuration for panel B1.
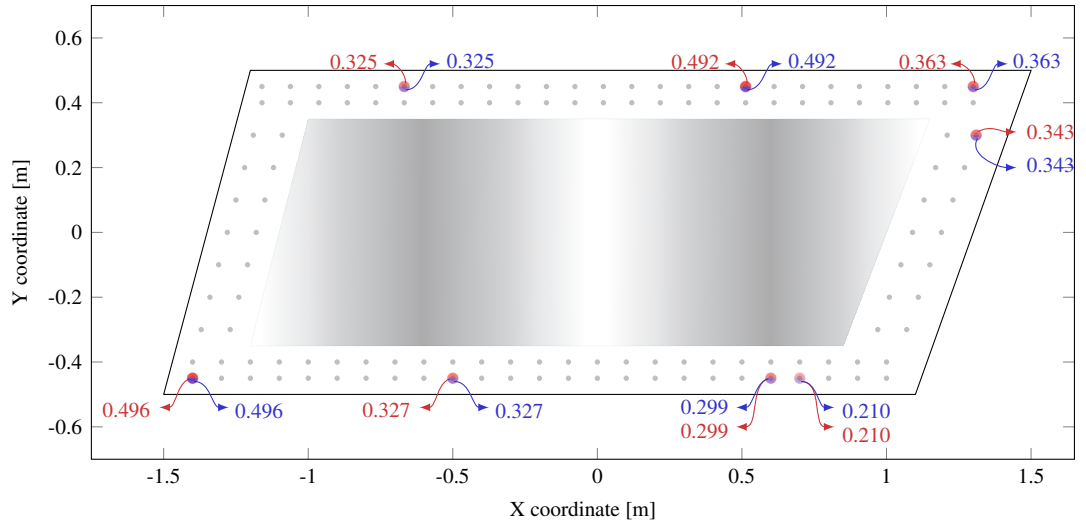
(b) Optimal actuator and sensor configuration for panel B2.

Figure 4.5: Optimal actuator and sensor configuration for the panel geometry B. Panel (a) depicts the case for aluminium alloy 2024-T351 and a bimodal prior distribution of damage occurrence within the grey areas, and (b) shows the case for the composite laminate of layup $[-45/90_2/45/0]_s$ and the same prior distribution. Red and blue numbers represent the value of actuator and sensor decision variables (w_j and z_i), respectively.

lution using the six actuators and six sensors shown in Table 4.4 results in $h^*(\Psi_a, \Psi_s, n) = 54.3951$, which again represents a remarkably close approximation to the convex solution.

Composite panel B2

Finally, the composite panel with the B geometry is assessed in order to iden-
tify the optimal positions for both sensors and actuators. The prior informa-
tion of the damage coordinates is the same as the one specified in Section 4.2.3,
while the wave propagation velocity related parameters a and b are defined as
in Section 4.2.2. Using 500 samples of the prior distribution for the evalua-
tion of the objective function, the optimal number of actuators and sensors is
$n = 10.75$, i.e., 5.37 actuators and 5.37 sensors. Figure 4.5b depicts the opti-
mal layout considering the threshold values of $w_j \geq 0.2$ and $z_i \geq 0.2$, which
distributes both coincident actuators and sensors around the most probable
damage occurrence areas. Their corresponding coordinates are also listed in
Table 4.5. In this case, the evaluation of the objective convex function with
the optimal solution provides a value of $h^*(w, z, n) = 98.2052$. Note that no
obvious choice can be made for the Boolean approximation in Table 4.5 given
the small w and z values. Therefore, the approximation is obtained by explor-
ing the combinations of PZT 1 and 6 (i.e. the ones with the largest w and
z values) with the rest of transducers. The best Boolean approximation re-
sults to have six sensors and six actuators (defined in Table 4.5) and leads to
$h^*(\Psi_a, \Psi_s, n) = 98.3123$, which is very close to the convex solution. Note also
in Figure 4.5b that this configuration avoids sensor clustering in PZT 7 and 8
and in PZT 3 and 4 by dropping PZT 3 and 7, respectively.

Table 4.5: Sensors and actuators above the threshold $w_j \geq 0.2$ and $z_i \geq 0.2$ along with
their coordinates and the approximated Boolean solution for the panel B2.

PZT No.	PZT coordinates		Relaxed solution		Binary solution	
	X [m]	Y [m]	w [-]	z [-]	Ψ_a	Ψ_s
1	−1.400	−0.450	0.496	0.496	1	1
2	−0.500	−0.450	0.327	0.327	1	1
3	0.600	−0.450	0.299	0.299	0	0
4	0.700	−0.450	0.210	0.210	1	1
5	−0.668	0.450	0.325	0.325	1	1
6	−0.513	0.450	0.492	0.492	1	1
7	1.300	0.450	0.363	0.363	0	0
8	1.310	0.300	0.343	0.343	1	1

4.3   Discussion

4.3.1   On the case study results

The proposed methodology for sensor and actuator entropy-based convex optimisation has been illustrated for ultrasonic guided-wave based inspection. This optimisation problem is addressed by relaxing the position-related decision variables (w_j and z_i) from binary $\{0,1\}$ to continuous $[0,1]$ values, thus transforming the combinatorial objective function into a convex one (recall Eq. (4.8)). This relaxation provides a lower bound for the original minimisation problem over the binary values. However, the obtained solution cannot be directly translated into an actual optimal sensor and actuator layout when any of these decision variables lie within the open interval $(0,1)$. However, an actual sensor and actuator configuration may be obtained by selecting the positions that have values close to 1, while avoiding sensor clustering as much as possible. This clustering effect is obtained due to the assumption of the stochastic independence of the predicted data, regardless of how close the positions of the sensor/actuators are [45]. When the optimal convex solution provides relatively low w and z values, the best Boolean approximation is not obvious and it arises from the evaluation of the objective function considering combinations of sensors and actuators with the largest w and z values.

It is also noticeable from the results that both the location and number of the sensors and actuators are coincident for the aluminium and composite plates and for the different geometries, because they have the same values of w_j and z_i. Since PZT transducers are able to both emit and receive ultrasonic guided-waves, they can act as both a sensor and an actuator and so only half of the PZTs would be needed for the inspection and monitoring of these plate-like structures. Furthermore, note that the resulting optimal PZTs in both aluminium plates are located at the corners of the plate, irrespective of the different prior distributions of damage considered in the case studies (see Figures 4.4a and 4.5a). Given that the aluminium plate provides a homo-

geneous medium for the guided-waves to travel and that attenuation is not taken into account, placing the PZTs at the corners allows a greater area to be monitored. In the case of the composite structures, the PZTs are spread along the plates with a certain preference for the predominant fibre directions due to the higher wave propagation velocity in such directions. Additionally, observe from the results for the composite panel B2 (Figure 4.5b) that the optimal PZTs are located around the most probable damage areas of the prior distribution in a triangular pattern.

The optimal number of sensors and actuators is influenced by the type of material, due to the different assumptions adopted in modelling the wave propagation velocity. In particular, the optimal configurations for the aluminium structures contain more sensors with a lower expected information entropy than those obtained for the composite plates. This behaviour can be explained by analysing the objective function in Equation (4.8), which directly multiplies the expected information entropy by the cost given the choice of the penalty term $\eta = |h(w, z, n)|$, as $h(w, z, n) + |h(w, z, n)| \times s(n)$. To further clarify this behaviour, the derivative of the objective function is set to zero so that the optimal number of sensors and actuators can be illustrated in cases where the entropy is different, as follows:

$$
\begin{aligned}
&\frac{\partial}{\partial n} \left\{ h(w, z, n) + |h(w, z, n)| \times s(n) \right\} = 0 \\
\Rightarrow &\underbrace{\frac{\partial h(w, z, n)}{\partial n} \times \left(1 + \frac{h(w, z, n)}{|h(w, z, n)|} s(n) \right)}_{\text{Variation of entropy}} = \underbrace{-\frac{\partial s(n)}{\partial n} \times |h(w, z, n)|}_{\text{Variation of cost}}
\end{aligned}
\tag{4.13}
$$

Thus, in case of two alternatives with similar $\partial h(w, z, n)/\partial n$ and equal cost $s(n)$, the optimal number of sensors is found to be smaller for structures providing lower variation of entropy. This is depicted in Figure 4.6, where the derivatives for the aluminium and composite results in panel A of the case studies are compared. This behaviour can be interpreted as a penalty for scenarios with higher uncertainty by reducing the amount of relatively unreliable information. Alternatively, in cases with lower uncertainty (entropy), the qual-

ity of such data is higher and more reliable, and hence the proposed approach allows it to use more sensors/actuators.

(a) Entropy

(b) Cost function

(c) Derivatives and intersection
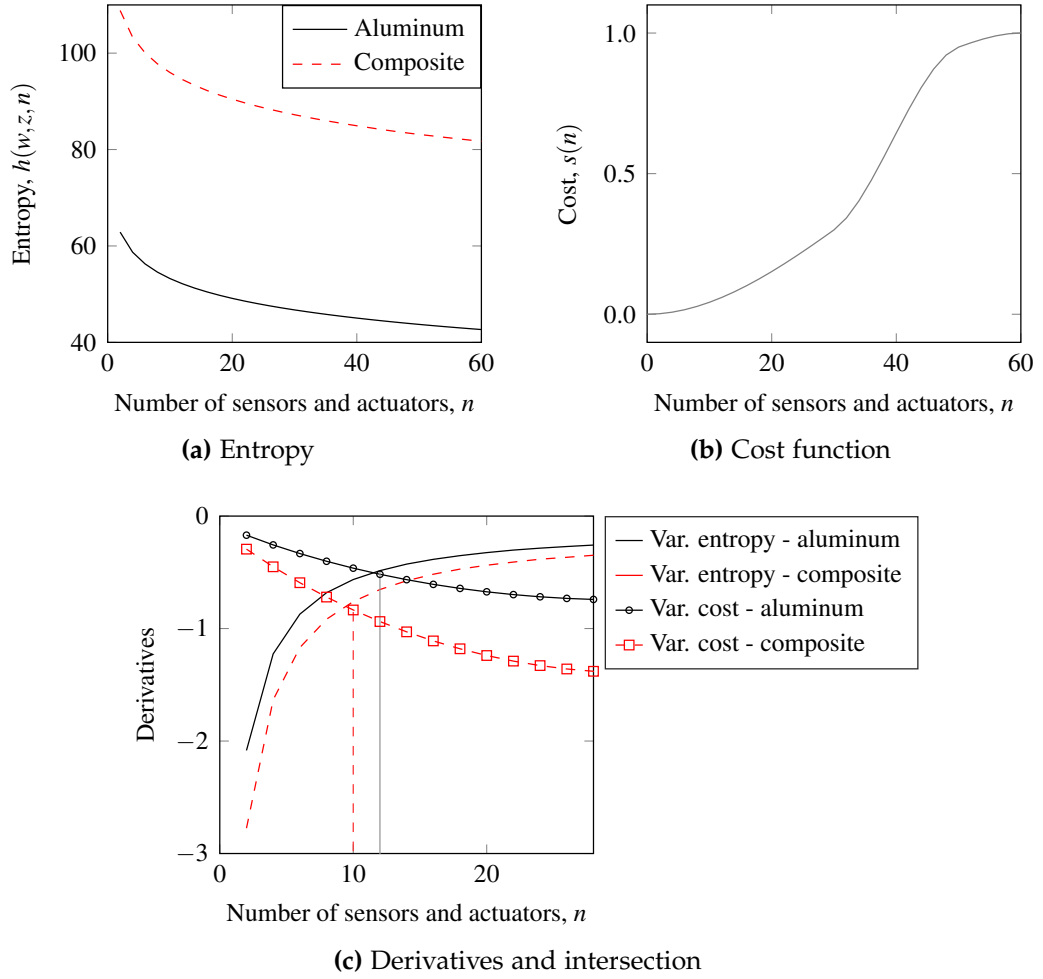
Figure 4.6: Behaviour of the objective function considering two entropy curves for optimal distributions of sensors for panel A of the case studies in (a), the same cost function in (b), and the intersection of the two members of Eq. (4.13) in (c).

4.3.2 On the ToF model and computational aspects

The ToF model used in this chapter allows the simulation of the time of flight of a scattered ultrasonic guided-wave to reach an arbitrary sensor without the need of a transient ultrasonic guided-wave simulation. This model has proven efficiency when dealing with complex materials and structures, providing the propagation characteristics are known. It is worth mentioning that the elliptical model of the wave propagation velocity used in this chapter is only valid for

anisotropic structures with quasi-elliptical slowness curves. However, the extension to more complex structures could be achieved by finding mathematical expressions that approximate such slowness curves. In addition, the optimisation framework does not account for the geometry of the structure other than the area of potential damage occurrence and its spatial prior distribution. An observation from the case studies is that the definition of such prior information is a key aspect, as it can drastically change the optimal sensor layout, at least in the composite structure. Despite its flexibility, the ToF model entails several limitations with regards to the physics of the guided-wave propagation as it does not account for attenuation or wave interaction with different types of damage. Therefore, it is desirable for future work to investigate a physics-based wave propagation model that is continuous and differentiable (e.g. by approximating a finite element model using a surrogate model such as a polynomial chaos expansion [214]), so that the gradients of Equation (4.5) can be applied.

Nevertheless, the computational efficiency of the proposed approach is remarkable when compared to other approaches in the literature that approximate the optimal binary solution. The optimal designs of the case studies in Section 3.2 have been obtained in approximately 300 - 400 seconds of runtime (equivalent to 75–120 objective function evaluations) in an Intel i3 2-core computer with 8 Gb of RAM, depending on the type of material and the prior distribution. In contrast, other approaches that use approximation methods such as the forward sequential sensor algorithm [215], take several hours to obtain a suboptimal sensor configuration, assuming a fixed distribution of actuators. Therefore, the runtime needed to address the joint search for sensors and actuators would be exponentially multiplied, thus highlighting the benefits of the proposed approach in practice. This high computational efficiency encourages the use of this method in complex scenarios, e.g. those involving intelligent SHM systems that adapt the utilisation of their sensors and actuators online based on some a priori information [41, 42]. This could be particularly relevant in the context of aerospace industry and edge/cloud computing [216], where

large transducer networks could be optimised online based on information provided by the SHM system itself while working in passive mode, and thus minimising the energy consumption.

Finally, note that the proposed method relies on the assumption of a large number of data $T \to \infty$, so that the posterior distribution can be approximated as Gaussian, ultimately justifying the use of the MAP parameter values [92, 93]. However, this hypothesis causes the model to lose some information about the model error and its uncertainty. Therefore, a more rigorous method would be to use the mutual information between data and model parameters as objective function given by [45, 101]:

$$I(\mathbf{D_T}, \boldsymbol{\theta}) = H(\mathbf{D_T}) - H(\mathbf{D_T}|\boldsymbol{\theta}) \tag{4.14}$$

where $H(\mathbf{D_T})$ is the entropy of the data and $H(\mathbf{D_T}|\boldsymbol{\theta})$ is the conditional entropy. Note that the first term involves a large number of evidence calculations $p(\mathbf{D_T})$, which is known to be computationally demanding [217] and could make the problem impractical.

4.4   Conclusions

An entropy-based approach for optimal sensor and actuator configuration (number of devices and their position) is proposed in this chapter. The methodology exploits the convexity of a relaxed optimisation problem, making it possible to be addressed with standard continuous-variable minimisation algorithms at relatively low computational cost. The efficiency and versatility of the optimisation method in addressing structures with arbitrary geometries and complex materials is illustrated using two case studies based on ultrasonic guided-wave based inspection. The following conclusions can be drawn:

- The proposed convex optimisation method produces a lower bound of the objective function using continuous optimisation variables, which are then approximated by Boolean variables to give a near-optimal sen-

sor/actuator configuration. The devices are placed at locations of the variables with higher values while avoiding sensor clustering.

- The optimal sensor and actuator layouts coincide, at least for the ultrasonic guided-wave based application, which suggests that the use of PZT transducers in pulse-echo mode is the most efficient test mode.

- The proposed objective function, which combines entropy and cost, recommends fewer sensors/actuators in cases with higher uncertainty (entropy), hence penalising scenarios with poor quality of data.

Further research work is under consideration on the following topics: (1) the computation of the mutual information between data and model parameters by addressing the calculation of the evidence; and (2) the use of a physics-based model, along with a surrogate of it for efficient calculations, so that the wave interaction with the damage type as well as wave attenuation are taken into account.

5

An efficient damage detection system for on-board applications

This chapter proposes a novel technique for damage detection based on ultrasonic guided-waves measurements. In particular, a novel damage index is proposed based on ToF differences of consecutive ultrasonic measurements acquired for an arbitrary plate-like structure. It relies on fuzzy logic fundamentals, which confer the proposed damage index with robustness against noise without compromising efficiency. The proposed approach is experimentally evaluated against the following structures and damage modes: (1) hole in an aluminium plate; (2) edge crack in an aluminium plate; (3) fall of a tool in a composite plate; (4) lightning strike in a composite plate; and (5) fatigue testing in an aluminium plate. The ultrasonic guided-waves are obtained using two experimental procedures, i.e. round-robin and transmission or physical beamforming. They are carried out using the latest version of PAMELA®, a dedicated structural health monitoring ultrasonic system (SHMUS) hardware developed by Aernnova Engineering S.A. (Spain) for the generation and acquisition of ultrasonic signals. This system relies on an integrated solution for the management of several input/output channels, which are able to emit and receive ultrasonic signals simultaneously and synchronously.

The outline of the remainder of this chapter is as follows: Section 5.1

presents the fuzzy logic based damage index; Section 5.2 details the experimental methods proposed for ultrasonic guided-wave based damage detection; Section 5.3 describes the experimental set-up as well as the specimens used for the experiments; the obtained damage detection and monitoring results are presented in Section 5.4; Section 5.5 discusses the potential practical implications of the proposed approach. Finally, Section 5.6 provides concluding remarks and future works.

5.1   Methodology

5.1.1   Hypotheses

The following hypotheses are assumed in order to develop a ToF and fuzzy logic based damage detection methodology for plate-like structures:

(1) Structures cannot self-heal, so they can only degrade over time;

(2) A difference in ToF of the guided-wave indicates structural deterioration;

(3) SHM data can be evenly acquired in time;

(4) SHM baseline data are available; and

(5) Noise introduces error in the ToF measurements and uncertainty in the damage assessment from those.

5.1.2   Fuzzy logic based damage detection

Considering the previous hypotheses, an algorithm based on the concept of fuzzy sets [29] is proposed to provide a damage index able to detect structural damage. The fuzzy sets are built from several measurements of the structure in the same health state. Since a non-perfect signal is expected, mainly due to measurement noise, different ToFs will be obtained for the same structure. The range of ToFs (i.e. the range of time values from minimum to maximum)
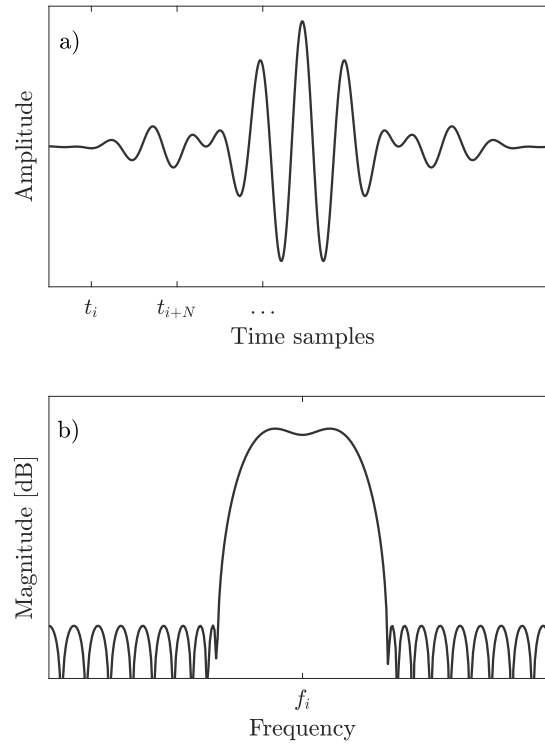
Figure 5.1: (a) Time-amplitude representation of band-pass filter. (b) Magnitude response of the filter. The same is designed so that the filter is centred in the frequency of interest (f_i).

for a particular peak in the signal is the basis for building the fuzzy sets for a particular structure.

First, a band-pass filter [2] is applied in order to reduce noise and obtain a signal containing the frequency of interest, i.e. the frequency of excitation. A time window representation of the band-pass filter in addition to the magnitude representation in frequency domain can be observed in Figure 5.1. Then, an algorithm specifically designed to obtain maximum (positive) and minimum (negative) points of the cycles of a signal is applied. An amplitude threshold is also applied to select only points with relatively high amplitude, thus avoiding further contamination by noise. As a result, an arbitrary number of peaks N_{pk} is obtained to build the fuzzy sets.

The test is then repeated an arbitrary number of times (N_t) in order to obtain a more robust information. These tests are performed in the same structural health state (e.g. in pristine state) and the ToFs of the N_{pk} peaks for each
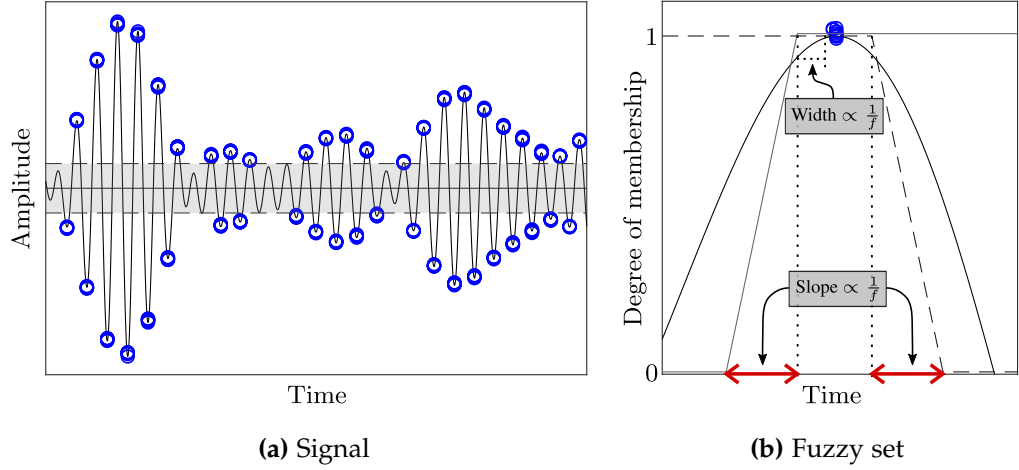
(a) Signal   **(b)** Fuzzy set

Figure 5.2: (a) Sample signal with identified maximum and minimum points in blue circles above the specified thresholds in dashed lines and grey area. (b) Fuzzy set created for one specific signal maximum set of points.

of the N_t ultrasonic guided-waves are stored. Given the noisy nature of the measurements, the ToF of the peaks are slightly different from each other and hence a range with a certain spread of ToFs is obtained, which is assumed to be a representative measurement of the irreducible uncertainty (explained in Section 2.7). Then, mimicking a fuzzy set, *membership* functions [29] are defined in the time domain around each peak using the ToF information from the N_t ultrasonic guided-waves acquired in pristine state. Details about the membership functions are provided below and in the Appendix B. The membership functions will then be used to evaluate the ToF mismatch (or degree of membership) of a new peak from an ultrasonic measurement acquired during operation with respect to the undamaged state.

Figure 5.2 depicts an example of an arbitrary ultrasonic signal with the selected peaks (in blue) above a certain threshold and the construction of one fuzzy set around a particular peak. Note that an additional width and slope (see Figure 5.2b) are introduced around the ToF range to take into account further variations unconsidered by the N_t tests. Both width and slope are defined based on the frequency of excitation so that there is no overlapping between membership functions of adjacent peaks (see Appendix B).

Several potential scenarios arise when a new peak is assessed using its

corresponding membership function: (1) the new peak lies within the limits of the sum of the *range* and the width, and the membership function assigns a maximum value of 1; (2) the new peak is within any zones of the *slope* (red interval in Figure 5.2b), where an arbitrary membership function assesses the degree of membership pertaining to the open interval $(0,1)$; and (3) the new peak lies outside the fuzzy zone and then a zero value (0) is assigned. As a result, the value of the membership function always lies within the closed interval $[0,1]$.

As aforementioned, the membership functions provide information about the signal mismatch, i.e. whether there has been a lag or a lead in the time-of-flight. This information is obtained from two subsequent functions that are used to define the fuzzy set [30], as demonstrated in Appendix B: (i) a S-shaped membership function (SMF), which evaluates the mismatch in the left-part of the range and (ii) a Z-shaped membership function (ZMF), which evaluates the right-part of the *range*. Figure 5.3 exemplifies the process of evaluating one peak over the two functions, i.e. the SMF and the ZMF. Observe that the new peak has a value of 1 in the ZMF, whereas the value in the SMF is lower than 1. These functions make it possible to distinguish if the new peak has a lead,
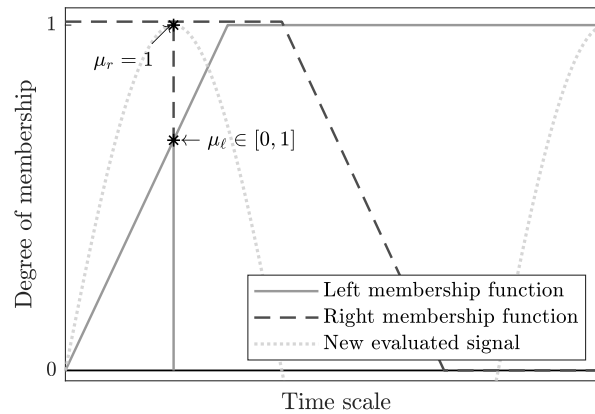
Figure 5.3: Fuzzy interval and membership function evaluation for both left and right-hand functions. The new signal is evaluated by selecting the maximum point of the cycle and simultaneously evaluating both membership functions. The membership value $\mu^i_{\{max\}}$ for the peak i would be the result of applying Eq. 5.2.

a lag, or if it is coincident with respect to the ToF information in pristine state. Then, the membership values for the maximum or minimum peak (denoted by superscripts j and i respectively) of SMF (e.g. μ_ℓ) and ZMF (e.g. μ_r) are then combined into a single value, by multiplying them as follows:

$$\mu^i_{\{min\}} = \mu^i_\ell \cdot \mu^i_r \tag{5.1}$$

$$\mu^j_{\{max\}} = \mu^j_\ell \cdot \mu^j_r \tag{5.2}$$

where $\mu^i_{\{min\}} \in [0,1]$ stands for the membership value of the i-th minimum peak and $\mu^j_{\{max\}} \in [0,1]$ for the j-th maximum peak. Finally, the minimum membership value of the total number of peaks (N_{pk}) is selected as follows:

$$\mu_m = \min\left(\mu^i_{\{min\}}, \mu^j_{\{max\}}\right); \quad \forall i,j \in \{1, 2, \ldots, N_{pk}\} \tag{5.3}$$

where $\mu_m \in [0,1]$ is the representative value of the signal m in terms of health assessing. This value is assumed to be an indicator of the degree of health of the structure. In this regard, $\mu_m = 1$ means that no change in the structure is observed, $\mu_m = 0$ means that the structure has significantly changed, and a value $\mu_m \in (0,1)$ indicates a certain degree of modification. Figure 5.4 summarises the proposed methodology in a flowchart. Two stages are differ-
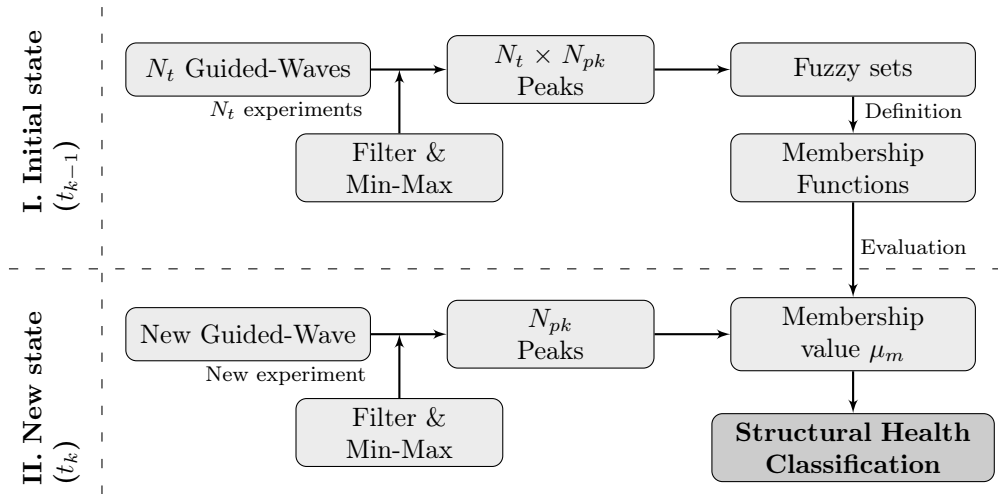
Figure 5.4: Flowchart of the proposed methodology for getting the health information of a structure by using guided-wave raw data.

entiated, one to define the fuzzy sets and membership functions, and other to evaluate a new signal and obtain the structural health assessment.

5.2   Experimental strategies

Once the method for obtaining the damage index out of a single signal has been proposed, the next step is to establish experimental strategies so that the structural health assessment can be tested. First, the classical round-robin approach is illustrated, and then, the newly implemented transmission beam-forming technique is detailed.

5.2.1   Round-robin configuration

The round-robin approach consists of emitting from the n-th actuator (A_n) and receiving with all the sensors (S). This procedure is typically repeated using different actuators and the same sensors. Thus, a greater area of the structure can be swept and more information about the structural health can be obtained. Using this method, not only a single membership value μ_m that stands for the degree of health (DoH) of the structure is obtained, but a matrix ($\mathbf{H_k}$) of $N_a^g \times N_s^g$ μ_m values can be provided, where N_a^g are the number of actuators and N_s^g the number of sensors given in a structure at a time t_k.

DoH matrices $\mathbf{H_k}$ obtained at time t_k need to be assessed in depth. This information is crucial for structural health assessment and further decision making. Different scenarios are likely to appear which correspond with either damage status or errors detection. Some damage status examples are shown

in Equations. (5.4-5.6).

$$
\mathbf{H_k} =
\begin{array}{c}
\begin{array}{ccccc} A_1 & A_2 & A_3 & \cdots & A_{N_a^g} \end{array} \\
\left[
\begin{array}{ccccc}
1 & 1 & 1 & \cdots & 1 \\
1 & 1 & 1 & \cdots & 1 \\
1 & 1 & 1 & \cdots & 1 \\
\vdots & \vdots & \vdots & \ddots & \vdots \\
1 & 1 & 1 & \cdots & 1
\end{array}
\right]
\begin{array}{c} S_1 \\ S_2 \\ S_3 \\ \\ S_{N_s^g} \end{array}
\end{array}
\tag{5.4}
$$

$$
\mathbf{H_k} =
\begin{array}{c}
\begin{array}{ccccc} A_1 & A_2 & A_3 & \cdots & A_{N_a^g} \end{array} \\
\left[
\begin{array}{ccccc}
0.7 & 0.2 & 0.4 & \cdots & 0.4 \\
0.3 & 0.5 & 0.5 & \cdots & 0.2 \\
0.4 & 0.3 & 0.2 & \cdots & 0.3 \\
\vdots & \vdots & \vdots & \ddots & \vdots \\
0.2 & 0.3 & 0.6 & \cdots & 0.9
\end{array}
\right]
\begin{array}{c} S_1 \\ S_2 \\ S_3 \\ \\ S_{N_s^g} \end{array}
\end{array}
\tag{5.5}
$$

$$
\mathbf{H_k} =
\begin{array}{c}
\begin{array}{ccccc} A_1 & A_2 & A_3 & \cdots & A_{N_a^g} \end{array} \\
\left[
\begin{array}{ccccc}
0 & 0 & 0 & \cdots & 0 \\
0 & 0 & 0 & \cdots & 0 \\
0 & 0 & 0 & \cdots & 0 \\
\vdots & \vdots & \vdots & \ddots & \vdots \\
0 & 0 & 0 & \cdots & 0
\end{array}
\right]
\begin{array}{c} S_1 \\ S_2 \\ S_3 \\ \\ S_{N_s^g} \end{array}
\end{array}
\tag{5.6}
$$

Equation (5.4) shows the example of a round robin test with no structural change detected. Equation (5.5) shows a certain level of mismatch in the signal which stands for a certain degree of damage. Lastly, Equation (5.6) shows the case of a round-robin test when the structure has changed significantly with respect to the baseline state. Note that in case of sensor malfunctioning, the row corresponding to such an erroneous sensor would appear full of zeros. Similarly, if the problem is in an actuator, a zero-value column would appear.

Note also that in case of carrying out the tests with a single array of PZTs (i.e. emitting and receiving from the same PZTs in a pulse-echo mode), a broken transducer would be evidenced by a column and a row full of zeros.

Decisions on whether the structure has changed or not can be made based on DoH matrices. Therefore, the detection of damage in plate-like structures is covered. Nevertheless, the coverage of the round-robin configuration is limited due to the use of a single emitter of ultrasonic guided-waves. In case of large structures a technique, which provides higher power and hence higher coverage, would be needed.

5.2.2 Transmission beamforming

Transmission beamforming is a suitable technique that meets this requirement. It is typically carried out by emitting multiple synchronised signals with a calculated phase difference in terms of time delay. Such signals go then to an array of PZT transducers, which propagate guided-waves by summing them up at either an arbitrary point or a certain direction in a thin-walled structure. A larger structure can then be inspected by sending a beam with significantly higher amplitude at several directions. Finally, a structural health assessment can be provided (see Section 5.1) in terms of DoH matrices, as explained below.

The time delays that control the directionality of this technique are calculated considering the following aspects: (i) the mechanical properties of the plate-like structure, which dictates the wave propagation velocity of the guided-wave mode of interest; (ii) the relative position of the PZT transducers in the phased array; and (iii) the mode in which transmission beamforming is performed to focus on one specific point or on a particular direction [218]. Considering an isotropic structure, the delay δ_i for the signal generated at the i-th transducer in the array for transmission beamforming in a direction $\vec{\zeta}$ is given by [219]:

$$\delta_i = -\frac{\vec{s}_i \cdot \vec{\zeta}}{V(f)} \tag{5.7}$$
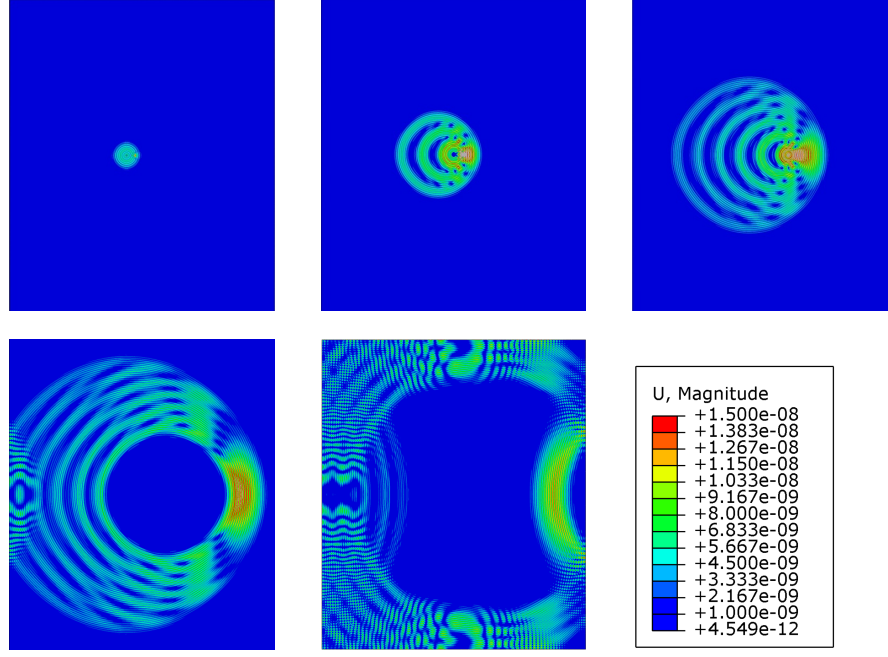
Figure 5.5: Transmission beamforming simulation using a linear phased array of 6 PZT focusing horizontally towards right of the plate.

where $\vec{s}_i$ is the vector from the origin of coordinates, which is normally assumed to be placed at the centre of the array, to the i-th transducer of the array. $\vec{\zeta}$ is the vector that defines the direction of the beam and $V(f)$ is the wave propagation velocity at a frequency f. Figure 5.5 illustrates a transmission beamforming simulation performed with a linear phased-array of 6 PZT transducers steering the beam towards the horizontal direction in an aluminium plate. The simulation is performed in Abaqus® [196] using the explicit dynamics solver. A four cycle Hanning-windowed sinusoid at 360 kHz is used as excitation. The main beam of the first antisymmetric mode is focused towards the right by introducing a delay between the excitation signals. On the other hand, it is possible to inspect specific points using the delays calculated as follows [219]:

$$\delta_i = -\frac{\eth_{0k} - \eth_{ik}}{V(f)} \tag{5.8}$$

where $\eth_{0k}$ is the distance between the origin of coordinates and the k-th point of interest and $\eth_{ik}$ is the distance between the i-th element of the phased-array and the point of interest. In this work, the beamforming approach to focus on a direction $\vec{\zeta}$ is used due to its generic character for monitoring a plate-like struc-

ture of different dimensions. Note that the use of this approach makes it possible to sweep an area without prior knowledge of its geometry, while focusing at specific points would require to establish a grid of monitoring points which are case specific. The wave propagation velocity is obtained through a preliminary experiment whereby one PZT is excited and two additional aligned sensors are used to acquire the ultrasonic signal. Once the signals are acquired, the ToFs between consecutive sensors are used to calculate the wave propagation velocity of the principal guided-wave mode of excitation at the frequency of excitation. These measurements are repeated several times so that an averaged and more reliable value is obtained.

As a result, the DoH matrices have columns for each direction $\vec{\zeta}$ investigated and every row contains the membership value μ_m obtained by each of the PZT in the phased-array. An example of these matrices is shown in Equation (5.9). Note that, similarly to the case of the round-robin configuration, a malfunctioning transducer would be spotted if a row full of zeros emerges in the DoH matrix.

$$
\mathbf{H_k} =
\begin{matrix}
\vec{\zeta}_1 & \vec{\zeta}_2 & \vec{\zeta}_3 & \cdots & \vec{\zeta} \\
\begin{bmatrix}
1 & 0.9 & 1 & \cdots & 0.8 \\
0.7 & 0.6 & 0.8 & \cdots & 0.9 \\
0 & 0 & 0 & \cdots & 0 \\
\vdots & \vdots & \vdots & \ddots & \vdots \\
1 & 0.8 & 0.9 & \cdots & 1
\end{bmatrix}
&
\begin{matrix}
S_1 \\
S_2 \\
S_3 \\
\\
S_{N_s^g}
\end{matrix}
\end{matrix}
\tag{5.9}
$$

5.3 Experimental set-up

The experimental set-up used in the experiments to validate the proposed fuzzy logic based damage detection algorithm is shown in Figure 5.6 and comprises the following: (1) hardware of the SHMUS, which is used to carry out round-robin and transmission beamforming experiments, (2) a control software, and (3) plate-like structures with an array of PZT transducers attached

to them.

(a) Schematic of the experimental setup.   **(b)** Actual experimental setup
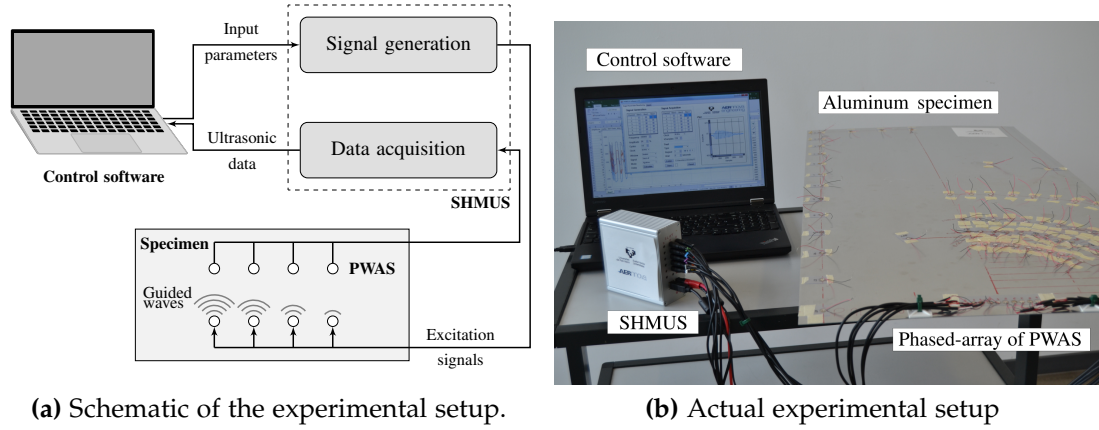
Figure 5.6: Experimental set-up used in the experiments for damage detection.

5.3.1   Hardware of the SHMUS

The execution of ultrasonic guided-wave tests for SHM requires an electronic system, which can be built from conventional or dedicated instrumentation. Conventional systems consist of a number of independent equipment such as an arbitrary signal generator, a data acquisition system, and a signal amplifier. However, factors such as their size or weight make them only applicable to laboratory-based activities, hence limiting their use in real-world engineering challenges, where the equipment needs to be efficient and portable. In addition, the delayed excitation of the actuators using such conventional equipment is limited with regard to the time precision of the necessary synchronisation. To overcome these limitations, a dedicated set of hardware for generation and acquisition of ultrasonic signals for the purpose of SHM is used here [220].

The SHMUS (including sensors and structure) is depicted in Figure 5.7. A control unit, which contains the processor and predefined internal communications, is used to command the rest of the elements in the experimental setup. Such a control unit internally generates n electrical signals using internal arbitrary waveform generators, which are then adjusted by introducing previously calculated delays $(\delta_1, \delta_2, \ldots, \delta_n)$. Note that each channel contains an independent waveform generator. The delays are calculated so that con-
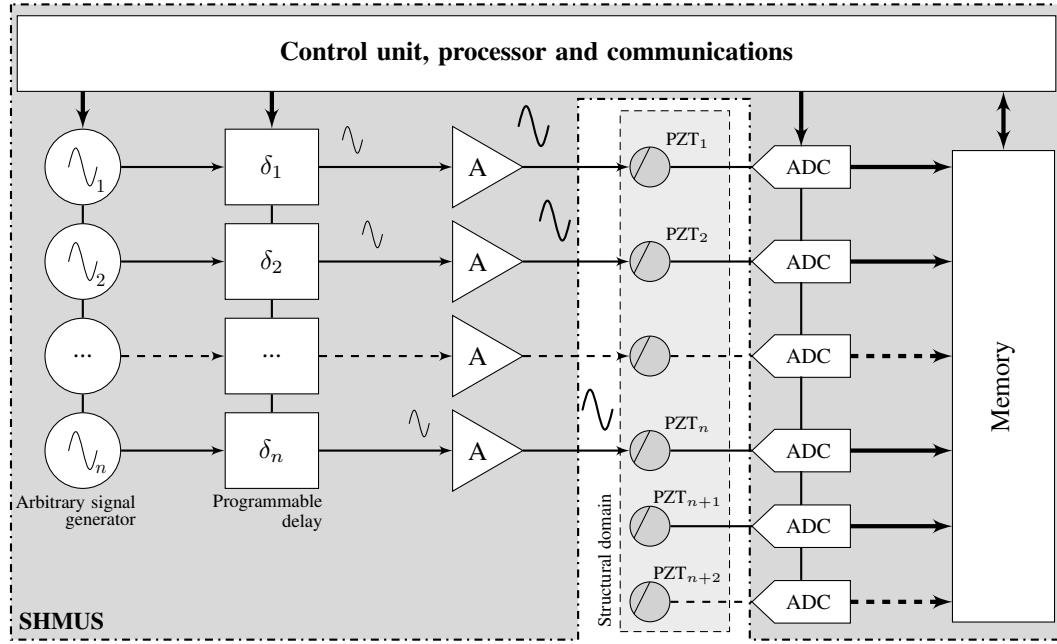
Figure 5.7: Generic scheme of the hardware needed to carry out transmission beam-forming. PZT $1, 2, \ldots, n$ are used in pulse-echo mode. Besides, PZT $n+1, n+2, \ldots$ are operated in pitch-catch mode.

structive interferences of the guided-waves are used to examine a plate-like structure in a similar way as a radar works [221], as shown in Section 5.2.2. The delayed signals are then amplified before reaching the PZT transducers that are attached to the plate-like structure. Finally, the electrical signals are transformed into mechanical displacements in the PZT transducers. The propagation characteristics of such guided-waves are defined according to both the plate's mechanical characteristics and the frequency of excitation.

At the same time that the PZT transducers excite the structure, they start acquiring the mechanical displacements. Such responses may vary depending on the test mode, which may typically be pulse-echo (e.g. PZT_1 to PZT_n in Figure 5.7) or pitch-catch (e.g. PZT_{n+1} and PZT_{n+2}). The acquired mechanical displacements are transformed into electrical signals by the PWAS transducers. These signals are then digitised by means of analogue-digital converters, and stored in the memory, which are managed by the control unit.

In the experiments, PAMELA® version 4 has been used as the SHMUS. It has 18 independent channels available for generation and acquisition, which

can be simultaneously operated. Sinusoidal signals can be generated with 30 kHz to 3 MHz frequency, up to 48 V_{pp} of amplitude, and up to 1 W per channel during the excitation of the PZT. The input channels have 1 V_{pp} of full scale and they are sampled at 60 MSPS with 12 bits of resolution. Here, PZT discs of 7 mm diameter and 0.2 mm thickness with radial mode vibration and a resonant frequency at 300 kHz supplied by STEMINC (part number SMD07T02R412WL) are used to both generate and acquire ultrasonic guided-waves.

5.3.2 Plate-like structures

Five different structures made of two different materials (aluminium and CFRP composite) are used to evaluate the performance of the proposed method for five different types of damage. The aluminium structure is made of an QQ-A-250/5 'O', a medium to high strength alloy with Young's modulus $E = 73$ GPa, density $\rho = 2740$ kg/m^3, and Poisson's ratio $\nu = 0.33$ and 1mm thickness. The CFRP composite laminate has a $[90_2, 0_4]_s$ stacking sequence and its layers were made up of SGL FT1021 unidirectional pre-impregnated composite material with TENAX®-E HTS45 12K carbon fibres.

The structures were manipulated to attach phased-arrays of PZT transducers close to one of the edges, as shown in Figure 5.8. Once identified the desired positions of the PZTs, the process to bond the transducers to the plate can be summarised as follows: (1) scratch the surface with medium grain sandpaper; (2) eliminate the particles and clean the surface with an alcohol-based solution; (3) apply the adhesive to the positions where the transducers are going to be attached; and (4) attach the PZTs and apply even pressure to ensure similar adhesive thickness under the PZT. After the adhesive is cured, the wires that are already attached to the PZT discs are tin-soldered to some thicker cables. These cables have 2.5mm jack plugs that are connected to PAMELA®, as can be observed in Figure 5.8b.

Five different forms of damage are applied to each structure, which are

(a) Sketch. Dimensions in mm **(b)** Aluminium plate
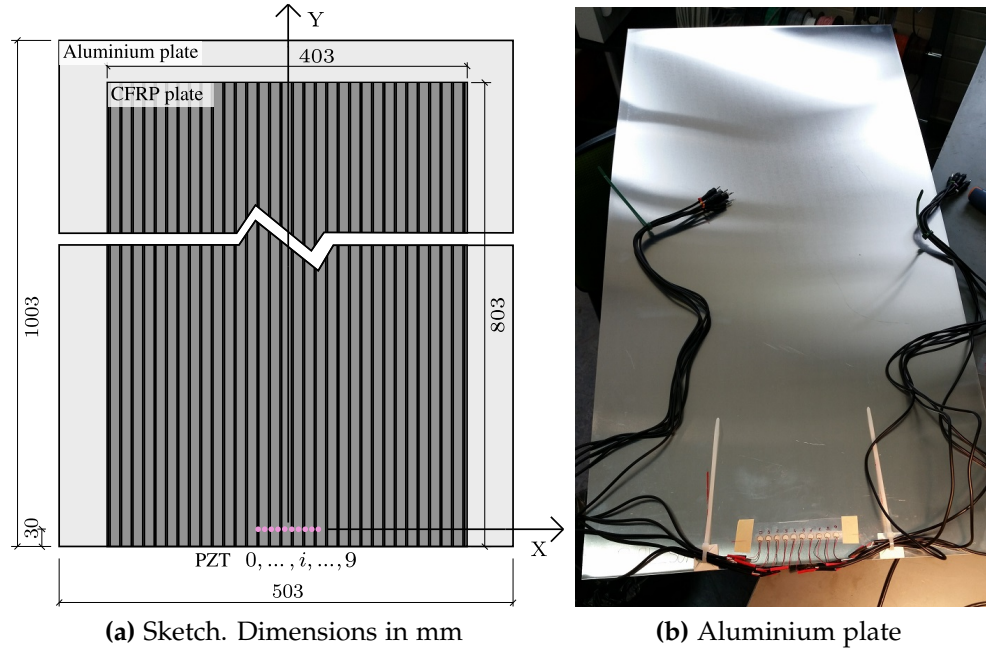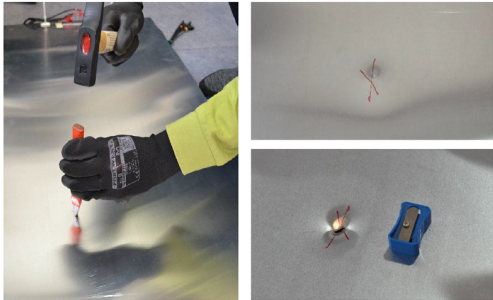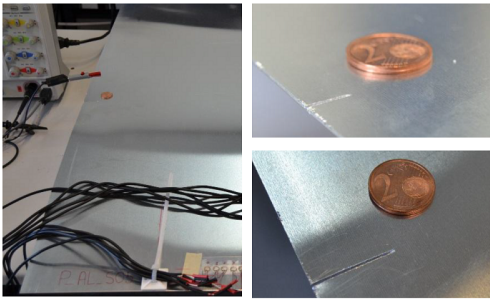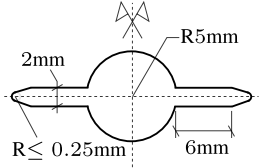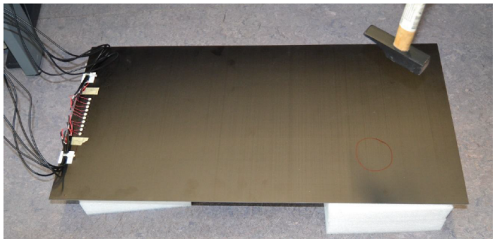
Figure 5.8: (a) Schematic dimensions of both the aluminium and composite plates for the experiments except the fatigue test. (b) One of these structures with the PZT attached and the cables already soldered.

listed in Table 5.1. Sudden damage scenarios in aluminium plates comprise: (1) a hole formed using a hammer and a chisel; and (2) an edge crack obtained by using a hacksaw. Note that both forms of damage are progressively applied in three and two stages, respectively. Similarly, instantaneous damage scenarios in composite plates are obtained by (1) dropping a tool (hammer) 40cm and 80cm above the plate; and (2) emulating a lightning strike in the lab with a 60V discharge using a 22mF capacitor. Finally, progressive damage is caused in an aluminium plate with a notch by means of a fatigue test, whose details are summarised in Table 5.1. Two cracks are assumed to grow symmetrically, one from each tip of the notch, and the proposed algorithm is tested to detect and monitor crack onset and growth, respectively. Note that all the experiments were carried out at the electronics lab of the University of the Basque Country (Spain), except for the fatigue test, which took place at ITAINNOVA in Zaragoza (Spain).

Table 5.1: Types of damage used to evaluate the proposed damage detection method for both aluminium and composite plate-like structures.

① Hole in aluminium plate	② Edge crack in aluminium plate	⑤ Fatigue test in aluminium plate
Dimensions: $1003 \times 503 \times 1$ mm^3	Dimensions: $1003 \times 503 \times 1$ mm^3	Dimensions: $500 \times 245 \times 1$ mm^3

③ Tool fall on composite plate	④ Lightning strike on composite plate	
		Fatigue test conditions: • Maximum load: 14 kN • Minimum load: 1.4 kN • Ratio: 0.1 • Number of cycles: 100 000 • Notch geometry:
Dimensions: $803 \times 403 \times 1.8$ mm^3	Dimensions: $803 \times 403 \times 1.8$ mm^3	

5.4 Experimental results

The results obtained from the proposed damage detection approach are shown in this Section for each damage scenario (refer to Table 5.1). All the experiments were carried out using the same configuration in PAMELA®, i.e., an excitation frequency of 300 kHz, approximately 48 V_{pp} of output amplitude, and 60 MSPS of sampling frequency.

5.4.1 Hole in aluminium plate

Damage was applied to a $1003 \times 503 \times 1$ mm^3 aluminium plate using a hammer and a chisel in three consecutive stages: (1) low level of damage resulting in a superficial scratch; (2) moderate level of damage resulting in a small indentation; and (3) severe level of damage leading to a hole in the plate. Pictures of this type of damage can be observed in Table 5.1. A 10 PZT phased array was used to carry out the guided-wave experiments in emission and reception. Note that in this material and damage scenario, both round-robin and beamforming experimental modes were used. Note also that beamforming was used by directing the main wave beam in several directions, which are noted here as: $\vec{\xi}_\ell$ where $\ell \in \{1, 2, \ldots, 37\} \equiv \{0°, 5°, \ldots, 180°\}$. As reference, the 0° direction is focused towards the right positive X axis, refer to Figure 5.8a. First, 10 experiments were carried out in pristine (undamaged) state to build fuzzy sets (Section 5.1), which assess the health condition of a structure. A threshold of 10% of the maximum amplitude (which minimises signal noise contamination), an additional width of the fuzzy set of 10% of half period, and a slope of 20% of half period are applied to obtain such fuzzy sets. Then, single experiments are carried out for each of the three aforementioned damage levels. It is worth mentioning that in the post-processing of the signals acquired with damage, a threshold of 15% of the maximum amplitude is considered to enhance the robustness of the measured maximum and minimum points.

The DoH matrices obtained for the round-robin experiments are shown

in Figure 5.9 as colour maps with a scale from 1 (i.e. no damage) to 0 (i.e. significantly damaged). It can be observed firstly for the case of the low damage level that the majority of the 10×10 matrix is full of ones, given that the structure was barely damaged. Secondly, for case of moderate damage, three

(a) Low level **(b)** Moderate level **(c)** Severe level

Figure 5.9: DoH matrices for round-robin data obtained for the aluminium plate with a hole as damage mode in three consecutive damage states.

(a) Low level

(b) Moderate level

(c) Severe level
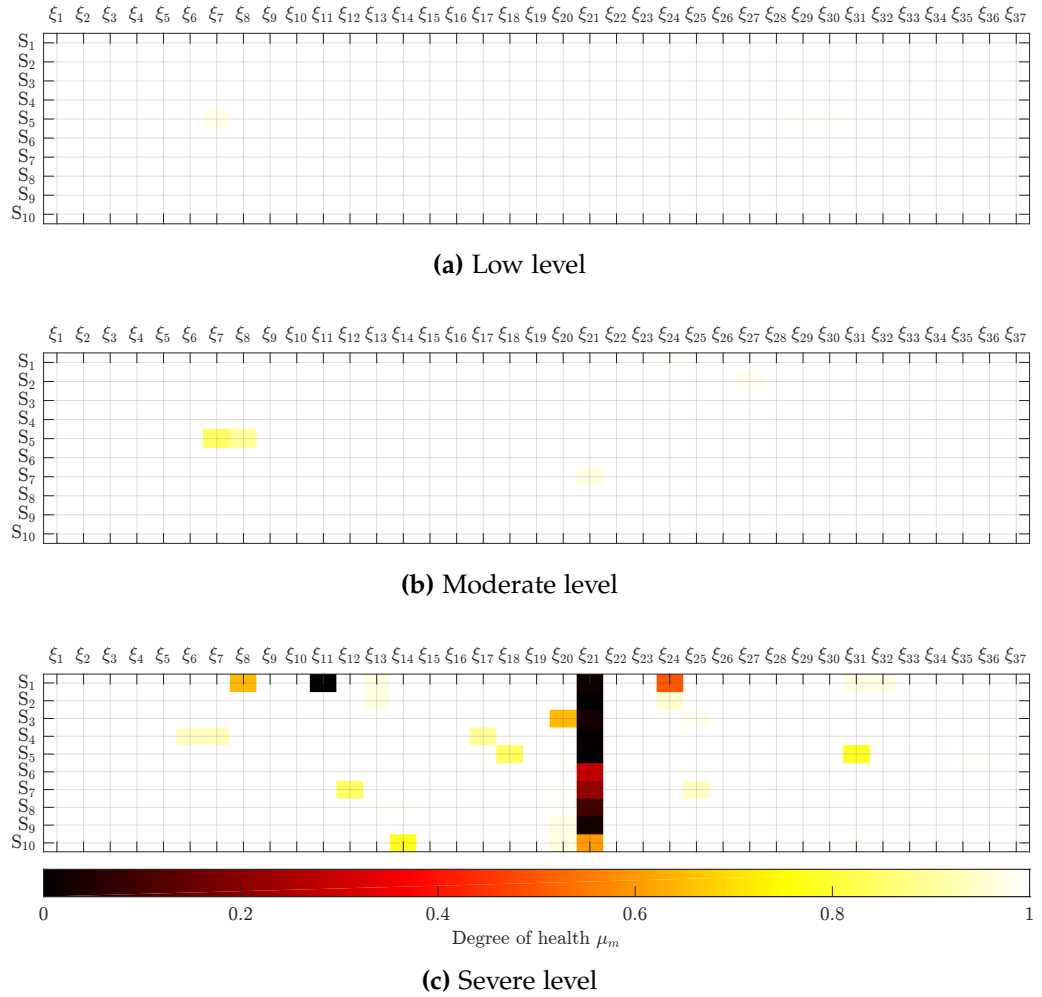
Figure 5.10: DoH matrices for beamforming data obtained for the aluminium plate with a hole as damage mode in three consecutive damage states.

additional coloured elements start showing an incipient degradation with respect to the pristine condition. Lastly, when the hole was opened through the plate, a significant number of elements of the matrix appears as different from one, depicting a more severe damage scenario in the structure, which enables its detection.

The DoH matrices obtained for the beamforming data are depicted in Figure 5.10. Note that an analogous behaviour is identified between beamforming and round-robin data. Low and moderate damage levels show only small variations with respect to the pristine state of the plate. The third level shows a more severe damage scenario where some elements go close to zero. Note that the identification of the direction where the damage is located was obtained at $\vec{\xi}_{21} = 100°$ from the centre of the phased-array. This angle corresponds to the real direction of the hole in the plate with respect to phased-array. Given the particular working mode of beamforming (refer to Section 5.2.2), in this case it allows both detection and localisation of damage.

5.4.2 Edge crack in aluminium plate

In this case, two damage scenarios corresponding to two cracks on an edge of the plate of two lengths over a $1003 \times 503 \times 1$ mm^3 aluminium plate were assessed. The length of the crack in the first scenario was 1cm, while in the second stage the crack was increased up to 2cm using a hacksaw, as shown in Table 5.1. The same configuration for the phased array, experimental modes, and characteristics of the fuzzy sets as the ones described in Section 5.4.1 were used in these experiments.

Figure 5.11 show the results from the round-robin data. In case of the 1 cm edge crack (see Figure 5.11a), the fuzzy logic based approach is able to detect a significant variation in most of the signals acquired. Note that in this particular case, the connection of the tenth PZT in the phased-array to PAMELA® failed, leading to noise signals and therefore to zero values in the tenth column and row. Note that in Figure 5.11a there are a black column

and a black row corresponding to the data from that PZT. Thus, the proposed method is able to identify the malfunction of a PZT in the phased array. In case of the 2cm edge crack (Figure 5.11b), the DoH matrix shows several cells with values close to zero, which indicate a more severe damage.

On the other hand, DoH matrices stemming from beamforming data are shown in Figure 5.12. In the first damage state, the DoH matrix (see Figure 5.12a) already shows a significant number of cells with values close to zero. Note that, in contrast to what the results for the hole showed, the damage position cannot be identified from the DoH results. This phenomenon can

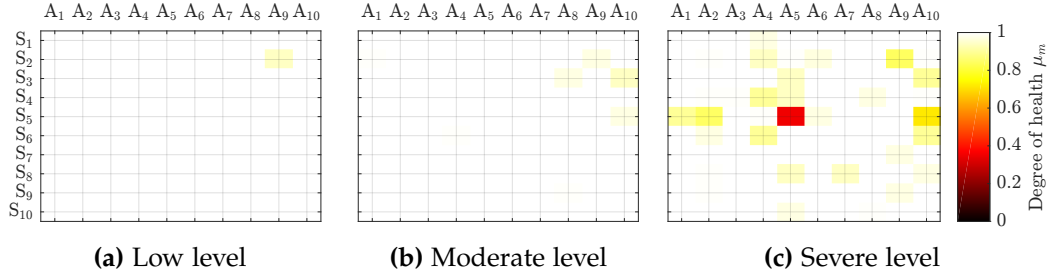**(a)** 1 cm crack length **(b)** 2 cm crack length
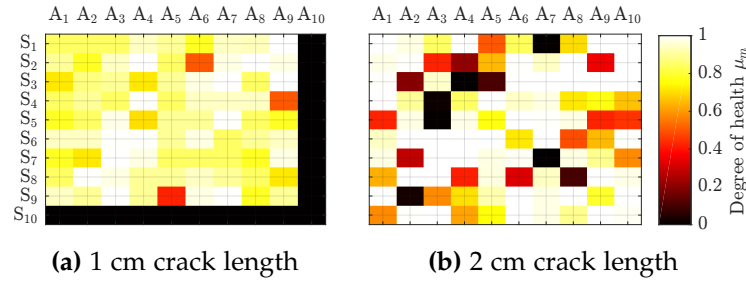
Figure 5.11: DoH matrices for round-robin data obtained for the aluminium plate with an edge crack as damage mode in two consecutive damage states.

(a) 1 cm crack length

(b) 2 cm crack length
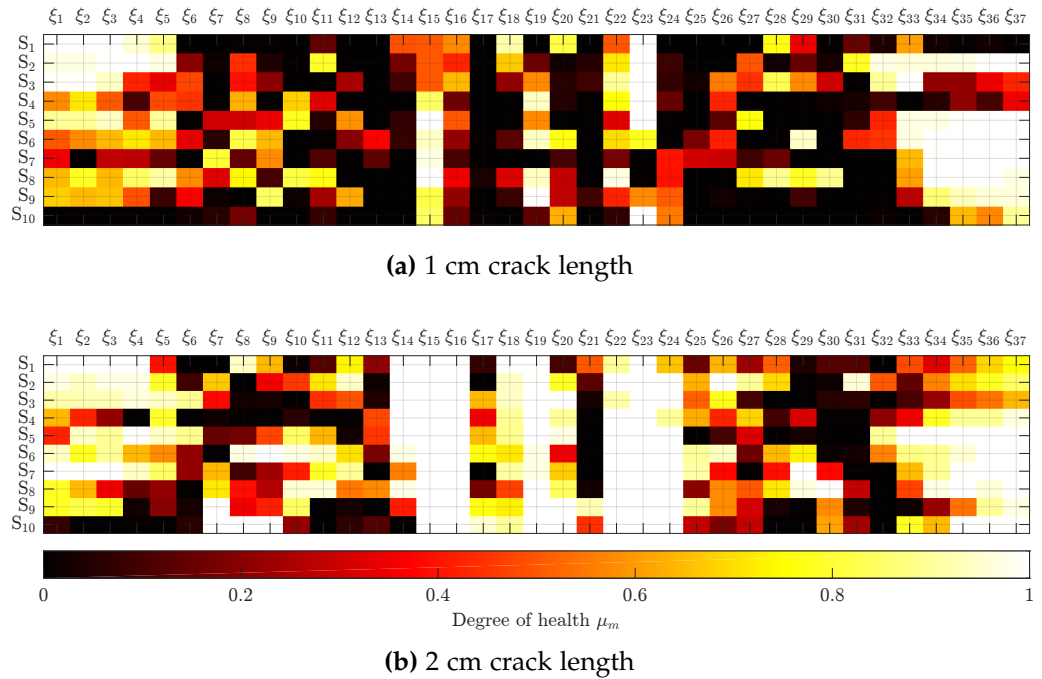
Figure 5.12: DoH matrices for beamforming data obtained for the aluminium plate with an edge crack as damage mode in two consecutive damage states.

be explained given the relative position of the damage in the plate. While the hole was close to the centre of the plate, the crack has been applied to an edge. This position causes the different waves to interact with the damage before arriving back at the phased array, even if the main beam is not directed towards the direction where the damage is located. In the second stage, corresponding to a 2cm crack length, the DoH matrix shown in Figure 5.12b still provides a high number of cells with values close to zero. Observe, however, that in this case the DoH matrix looks healthier than the one provided for the first damage state although the damage is more severe. Such behaviour can be explained because of the different trajectories that the guided-waves follow after intersecting with the boundaries of the plate and the crack. Note also that the real damage direction can be enclosed between $\vec{\zeta}_{25}$ and $\vec{\zeta}_{32}$, i.e. between 120° and 155°. This may be seen as an additional complexity for damage localisation, but in general the main purpose of the proposed approach, i.e. damage detection, is successfully covered by the DoH matrices in both cases.

5.4.3 Tool fall on composite plate

This case study tries to emulate the real damage caused by a tool fall in a composite structure during maintenance actions. In this context, a hammer was let fall onto a $803 \times 403 \times 1.8$ mm^3 composite panel from two different heights (see Table 5.1): (1) from 40cm and (2) from 80cm. Note that the heights are measured with respect to the metallic part of the hammer. The hammer impacted in the same area both times, so a more severe damage was expected to appear. Equivalently to the aluminium plate, a 10 PZT phased array was attached to the structure, according to the design provided in Figure 5.8a. Here, however, only the round-robin experimental mode was used for damage detection, given that the complexity of the cross-ply laminate and the lack of mechanical properties made the calculation of the delays for beamforming not feasible.

Figure 5.13 depicts the DoH matrices obtained for both damage scenarios caused by the hammer fall from two heights. In both cases, the damage

is identified in the matrix given that there are some elements which differs significantly from one. Additionally, the second scenario, where a second impact from double height was performed, provides at least two elements of the matrix with values close to zero. This indicates a relatively severe degree of damage to the structure.

5.4.4 Lightning strike on composite plate

Damage stemming from a lightning strike was recreated in the laboratory by creating a 60V electrical discharge using a 22mF capacitor, as can be observed in Table 5.1. A composite plate (described in Section 5.3.2) was used in this case in order to study the effect of this scenario, whereby matrix degradation occurs and it causes changes in the mechanical properties. As described above for the tool fall scenario, only round-robin experiments are carried out. Two electrical discharges are applied to the the same composite structure.

Figure 5.14 shows the DoH matrices for the two states with one and two

(a) First height   **(b)** Second height
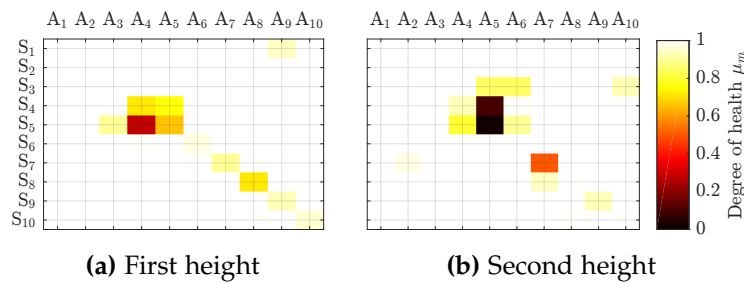
Figure 5.13: DoH matrices for round-robin data obtained for the composite plate with damage created by two tool falls at different heights.

(a) First discharge   **(b)** Second discharge
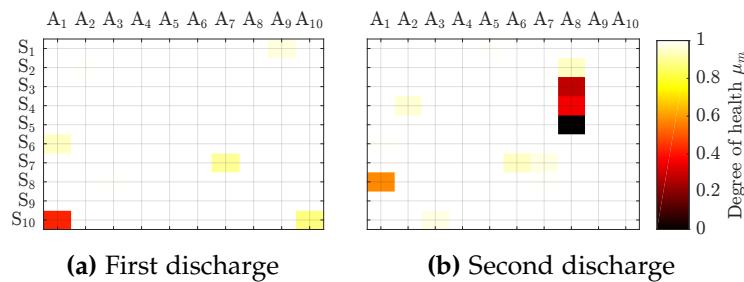
Figure 5.14: DoH matrices for round-robin data obtained for the composite plate with damage created by two tool falls at different heights.

electrical discharges. It can be noted that in the first discharge some elements in the matrix are observed to be different from 1, thus indicating a certain degree of damage. When the second discharge is applied, more elements with lower numbers arise, therefore suggesting that a more severe damage is present in the structure.

(a) Drawing and dimensions of the specimen

(b) Plate & testing machine

(c) Cracks at 100 000 cycles
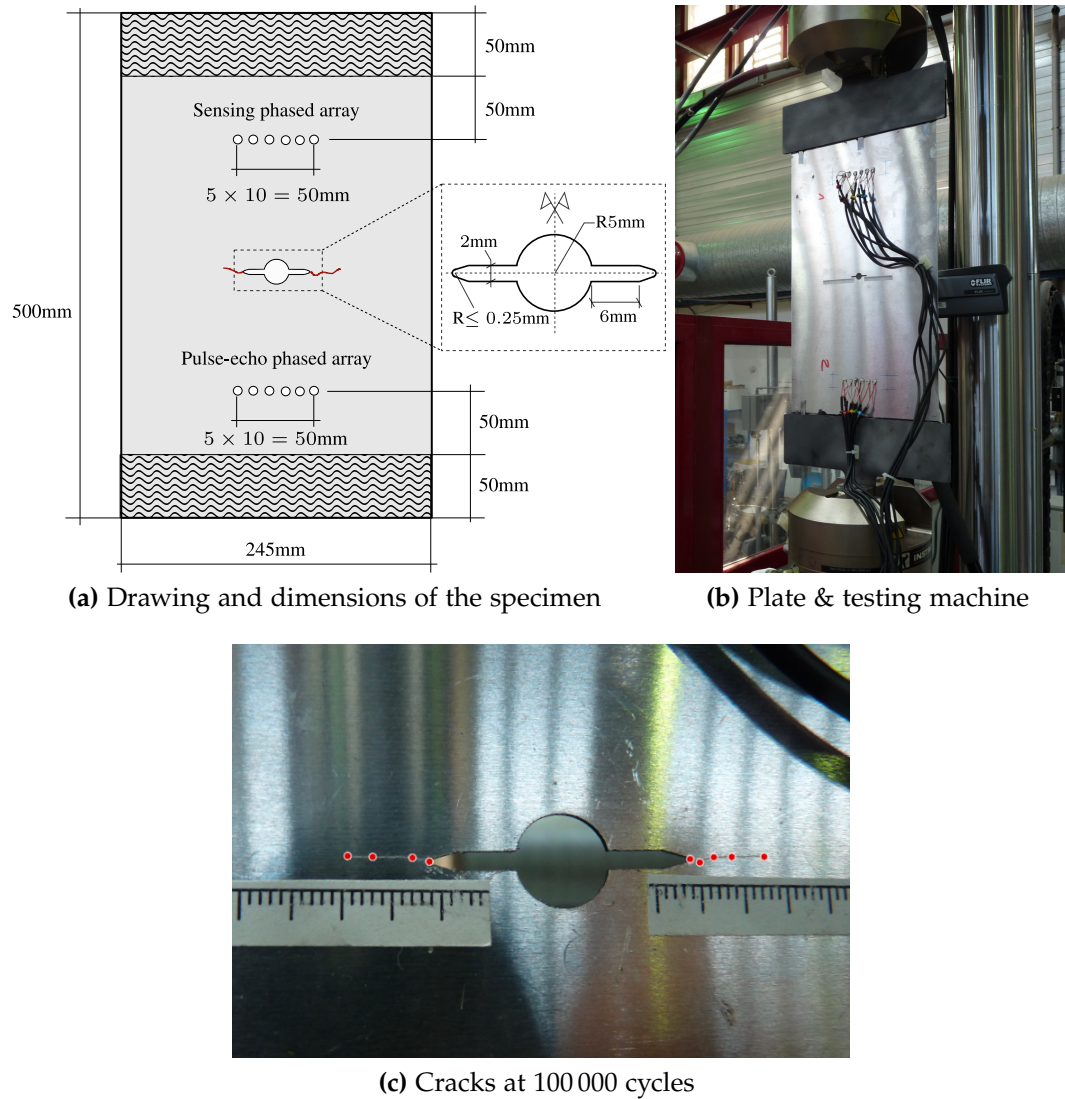
Figure 5.15: Drawing of the plate used for the fatigue test in (a) along with a photo in (b) of the specimen mounted into the fatigue testing machine. Finally, in panel (c), a zoomed picture used to measure the crack length at 100,000 cycles.

5.4.5 Fatigue test in aluminium plate

The last case study shows the results obtained during a fatigue test in a $500 \times 245 \times 1 \text{mm}^3$ aluminium plate (refer to Section 5.3.2 for material properties and Table 5.1 for fatigue testing properties). The test was stopped every 1 000 cycles in order to carry out guided-wave experiments and take photographs to measure the cracks length, therefore the same loading conditions were ensured for all measurements. Note that two cracks appear at every tip of the central notch. The plate was monitored with PAMELA$^{\circledR}$ and 12 PZT transducers as shown in Figures 5.15a and 5.15b. The bottom phased-array was used in pulse-echo mode, while the upper one was used for sensing only. Round-robin and beamforming experimental modes were adopted to check the capabilities of the proposed approach in detecting and monitoring damage along the different loading cycles. The crack length was measured from the photographs taken during the experiment at several cycles (every 10 000 cycles). The photographs were digitised and, using the attached scale rulers, scaled into real dimensions, as shown in Figure 5.15c.

Figure 5.16 shows the results obtained from the proposed damage detection approach along with the crack lengths measurements. It is worth mentioning that in this case study, the 6×6 (i.e. 6 emitters and 6 receivers) DoH matrices are reduced to a unique number which is given by the mean of all the
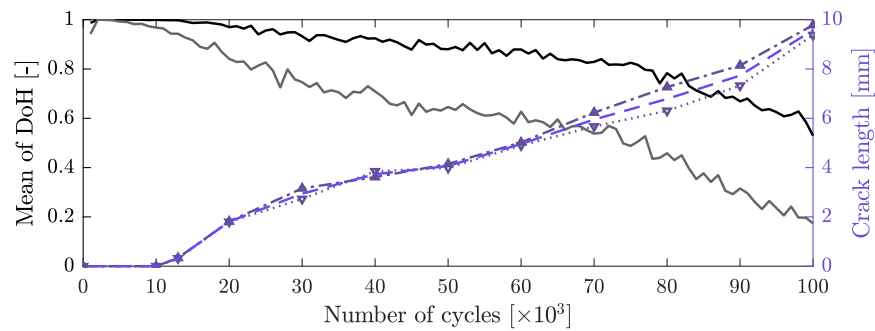
Figure 5.16: Mean of DoH matrices for round-robin test results from the pulse-echo phased array (black line) and the sensing one (grey line). In the right vertical axis, digitised crack lengths from the left (blue dash-dotted line with up triangle) and right (blue dotted line with downwards triangles) cracks. The average of both crack lengths is represented as a blue dashed line.

numbers in a DoH matrix, given the high amount of matrices obtained (one for each phased array and for every 1 000 cycles). Thus, both black and grey lines in Figure 5.16 represent the mean of the DoH matrices for the pulse-echo and the sensing phased arrays, respectively. Note that they start providing information about damage at around 10, 000 cycles, which matches with the approximate crack onset in the plate (see the blue lines in Figure 5.16). However, there is a significant variation between the data from the pulse-echo and the sensing phased arrays. This can be explained since the data from the pulse-echo mode have a significant less amplitude than the sensing data and the same level of threshold is applied to reduce the influence from noise. This causes the data from the sensing array to have a higher sensitivity to changes in the ToF of the ultrasonic signal than the data from the pulse-echo array, thus providing an earlier and more severe damage estimation. Nevertheless, the trend of both lines and the detection of initial damage are relatively similar between both datasets. Note also that the sensing array has a higher sensitivity to initial states of damage, even when no crack can be measured from the photos.

Equivalently, the results from the beamforming DoH matrices are summarised in Figure 5.17. These matrices are reduced to a single number by taking the average of all the degree of membership values for every direction. Since the DoH matrices have 37×6 elements (37 directions, i.e. $0°, 5°, \ldots, 180°$, and 6 receivers), more information is considered in this case. Similarly to the
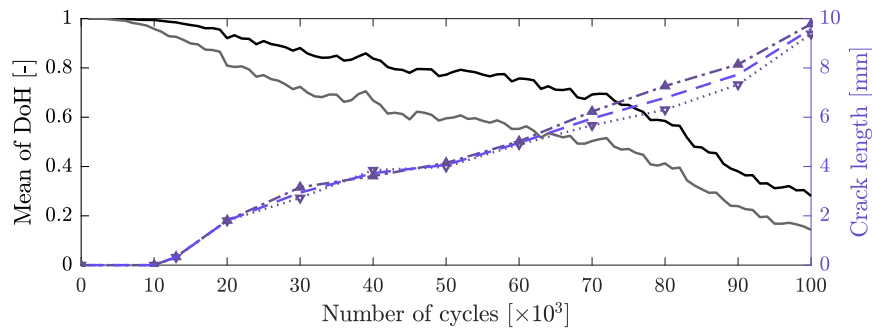
Figure 5.17: Mean of DoH matrices for transmission beamforming test results from the pulse-echo phased array (black line) and the sensing one (grey line). In the right vertical axis, digitised crack lengths from the left (blue dash-dotted line with up triangle) and right (blue dotted line with downwards triangles) cracks. The average of both crack lengths is represented as a blue dashed line.

data form the round-robin tests, Figure 5.17 shows a similar decreasing trend of the structural DoH when the fatigue cycles increase. Note, however, that both lines from the pulse-echo and the sensing data are closer to each other compared to the round-robin test results. This might be caused by the higher amplitude created by the transmission beamforming technique, whereby six PZT are actuated synchronously. These higher amplitudes make the sensitivity of the DoH similar in both phased arrays (i.e. pulse-echo and sensing ones), given that the noise contamination is lower than in the case of using one PZT for the actuation. It is also worth highlighting that the DoH-related lines are smoother than the ones obtained from round-robin data, which indicates a more robust damage assessment, given that a higher number of signals are used to obtain the average of the DoH matrices.

5.5 Discussion

5.5.1 On the results

The proposed fuzzy logic based damage detection methodology based on ultrasonic guided-waves has been illustrated in five different damage scenarios. Note that this approach uses only the membership functions from the fuzzy sets theory (see Appendix B), and that the degree of membership value is used as the QoI for the evaluation of the structural condition. Therefore, no further fuzzy logic operations and defuzzication need to be applied. In particular, this damage assessment is carried out by establishing fuzzy sets on the ToF of maximum and minimum points of the ultrasonic signal obtained in the pristine state of a structure. A new signal, measured during the operation of the structural system, is then evaluated in these fuzzy sets and the mismatch of the ToF is assessed. A degree of membership μ_m for the m-th signal is finally obtained as a damage index. This process is applied to all the signals obtained in two different experimental modes: (1) round-robin fashion; and (2) transmission beamforming. As a result, DoH matrices are obtained which provides

information about the healthy condition of a structure.

It is noticeable that in the four sudden damage scenarios (except the fatigue test) an indication of damage is provided by the proposed approach. Both round-robin and beamforming data provide a clear assessment of the damage in aluminium and composite plate-like structures. However, the DoH matrices are complex in nature and therefore their interpretation might be complex. This is particularly revealed in the beamforming data, where for the case of the hole in the aluminium plate both the detection and even the localisation in terms of direction with respect to the phased array was obtained (Figure 5.10). Note also that in the case of the edge crack only the damage existence could be detected (Figure 5.12). Here, the damage in the edge of the plate causes that a large number of signals, even when the main beam is not directed towards its location, interact with the crack and make the identification of the direction of the damage not possible. This may be seen as a limitation of the method, but considering that the proposed approach focuses on the detection of damage, the main research objective is still achieved.

The proposed methodology has also been tested to monitor the degradation of an aluminium sheet in a fatigue test. Two phased arrays were installed in the structure so that one of them worked in pulse-echo mode and the other only in sensing mode. The main objective of installing these two sets of transducers was to have redundant data and thus validate that the pulse-echo mode is enough to monitor and detect damage. The results obtained from both round-robin and beamforming testing modes (Figures 5.16 and 5.17, respectively) suggest that the pulse-echo mode is able to monitor accurately the degradation of the structure, which was measured as crack length with the number of cycles. In this context, a desirable future work would be to carry out additional tests in different specimens of the same material in order to use the data to obtain a fast degradation model (e.g. using hidden Markov models [222]) that relates the average of the DoH matrix with a crack length. Therefore, fast and on-board oriented SHM for prognosis of the remaining useful life of a structure would be supported.

5.5.2   On the experimental modes

Transmission beamforming experiments using ultrasonic guided-waves had been typically restricted to a few transducers, given the high complexity of the hardware needed to carry it out. Here, PAMELA® version 4 was used as it allows a practical implementation of round-robin and transmission beamforming experimental modes. The latter is able to provide higher amplitudes (energy) and therefore the damage is generally better identified. However, it is a complex technique that requires the calculation of time delays in order to obtain a main beam at different directions. This aspect may be seen as a limitation in cases where the material is anisotropic such as in the composite laminates, as the calculation of the skew angle and delays is not straightforward. In such cases, a round-robin test might be enough as seen in the damage scenarios provided above, however if the structure is larger, attenuation would cause the quality of the DoH to deteriorate and become more sensitive to noise. Therefore, the study and implementation of these delays in more complex materials would be a natural future extension of this research work.

Additionally, the time required for the excitation, measurement, and writing process of the data generated in the beamforming mode at 37 different directions (i.e. $0°, 5°, \ldots, 180°$) is less than 24 seconds. Furthermore, the evaluation of a new signal in the fuzzy sets takes between 10 to 50 seconds, which provides a total amount of time, between experiment realisation and damage assessment, of 1 minute approximately. This encourages the use of the proposed approach for an online and on-board SHM system.

Note that the loading conditions, and therefore, the stress state of the plate-like structures, must be similar between measurements, so that the damage assessment is not contaminated by other factors. This stress state might be influenced by external loading conditions such as the temperature variation during day and night or, in the context of aerospace industry, for the different locations where an aeroplane may land. Therefore, another desirable future work would be to investigate the influence of environmental changes (e.g. tem-

perature or humidity) in the definition of the fuzzy sets, so that a more robust damage detection can be carried out.

5.6 Conclusions and future work

A damage detection approach for ultrasonic guided-wave based SHM is proposed in this chapter. The methodology is based on fuzzy logic principles to allow a fast, yet robust, damage assessment. Besides, this approach uses a damage index that quantifies the ToF mismatch of maximum and minimum points of an ultrasonic signal. The efficiency and effectiveness of the damage detection method have been illustrated using five different damage scenarios with different damage modes and materials. The following conclusions are drawn from this chapter:

- The proposed fuzzy logic based method provides a fast and robust framework for damage detection for an on-board SHM system, which accounts for noise variance.

- Sudden damage scenarios has been successfully detected in composite laminates and aluminium structures using the proposed approach.

- Damage onset and growth in an aluminium structure subjected to fatigue loading conditions have been detected and monitored remarkably well.

Further research work has been proposed to further improve the robustness and usability of the fuzzy logic based method on the following lines: (1) to develop models that relate DoH measurements with damage features (e.g. crack length) so that they can be used to assess the remaining useful life of the structure; (2) to investigate and implement time delays to perform transmission beamforming tests in anisotropic materials (e.g. composite laminates) using PAMELA®; and (3) to study the influence of environmental factors such as temperature variations in the definition of the fuzzy sets.

<div style="text-align: right; font-size: 4em; color: #999;">6</div>

Robust Bayesian damage localisation

This chapter proposes a multi-level Bayesian framework to rigorously account for the overall uncertainty in the problem of ultrasound guided-wave based damage localisation. The main novelty of this chapter is that it provides a unified methodology to rationally address the problem of damage localisation using ultrasounds from probabilistic Bayesian principles: first, the problem of TF model selection is addressed for a given experimental configuration based on *posterior probabilities* that assess the relative degree of belief [34] of a particular model over a set of candidates; then, the problem of damage localisation is addressed using a BIP based on signal features adopting a *hyper-robust* TF model resulted from the first assessment level. To this end, once the raw data have been acquired, two BIPs are hierarchically formulated for each PZT sensor so that the outcome of the model selection problem is used as input for damage localisation, as shown in Figure 6.1. In this framework, uncertainties coming from (1) the mechanical properties of the material; (2) measurement errors; and (3) epistemic uncertainty in the TF model due to the Heisenberg principle [162, 172], are taken into account. The proposed approach relies on rigorous *probability-logic* assumptions (whereby conditional probabilities are interpreted as degree of plausibility for a given condition) for model class selection [32] and as such, it avoids experience-based decisions about the optimal post-processing technique. Here, probability is interpreted as a multi-valued

<div style="text-align: center;">120</div>

logic that expresses the degree of belief of a proposition conditioned on the given information [28, 32]. The methodology is applied in two case studies using aluminium plates with one and two damaged areas, respectively. For the particular problem of damage localisation, the AIMS [51, 52] algorithm is adopted to solve the resulting Bayesian inverse problem, showing high efficiency in dealing with damage multi-modality. In general, the results show the efficiency of the proposed methodology in reconstructing the damage position in plate-like structures using guided-waves, while rigorously accounting for the modelling uncertainties in the reconstruction.
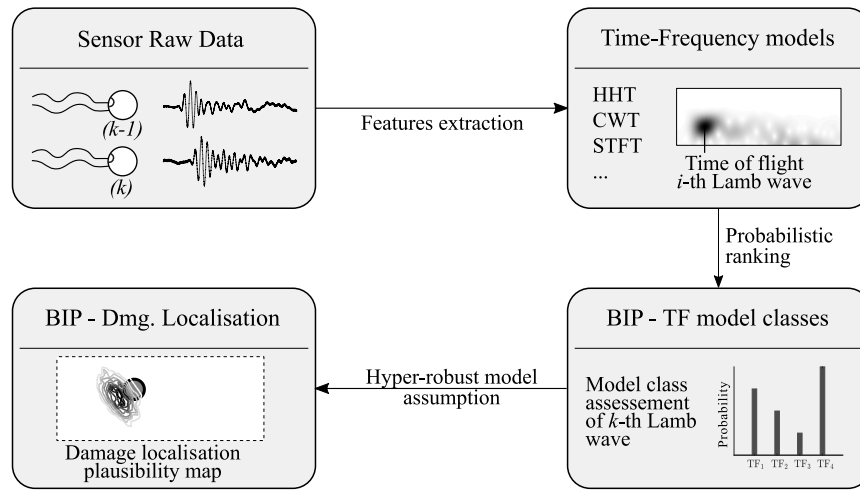
Figure 6.1: General workflow proposed to address the challenge of damage localisation. Note that the signal data can be obtained by numerical (e.g. finite element analysis) or experimental methods (e.g. using PZT transducers, a signal generator, and an oscilloscope).

The remainder of the chapter is organised as follows. Section 6.1 shows the TF models used in the proposed model selection problem. Section 6.2 comprises the probabilistic methodology used to obtain the robust estimate of the ToF for each sensor. The BIP principles used to obtain the damage localisation are presented in Section 6.3. In Section 6.4, the proposed framework is applied in two case studies to serve as example. Section 6.5 discusses the robustness of the proposed methodology. Finally, Section 6.6 provides concluding remarks.

6.1 Time-frequency models

Out of the most widely-used TF models in the literature, four models are selected in this chapter to be assessed and ranked using the proposed Bayesian methodology for each sensor, independently; namely the HHT, CWT, STFT, and WVD. The main formulations of these TF representation techniques are shown in the following subsections.

6.1.1 Hilbert-Huang transform

The HHT is obtained from the sum of intrinsic mode functions (IMF) whereby the spectrum is defined after performing the Hilbert transform over each IMF component [163, 168], as follows:

$$g_1(t) = \sum_{j=1}^{n_{imf}} \kappa_j(t) \exp\left(i \int \omega_j(t) \, dt\right) \qquad (6.1)$$

where $\kappa_j(t)$ is the magnitude of the analytic signal which is typically considered as the envelope of the input time series or directly the signal acquired by the sensor, n_{imf} is the number of IMF components, and $\omega_j(t)$ is the instantaneous frequency. Equation (6.1) represents the amplitude and instantaneous frequency as function of time.

6.1.2 Continuous wavelet transform

TF wavelets are used in the CWT to obtain the TF representation of the assessed signal, by:

$$g_2(b, a) = \frac{1}{\sqrt{a}} \int_{-\infty}^{\infty} X(t) \overline{\Psi\left(\frac{t-b}{a}\right)} \, dt \qquad (6.2)$$

where $X(t)$ represents the time series of the signal, $\Psi(t)$ denotes the analysing wavelet, $a > 0$ is the scale factor, b is the time-shift variable, and the overline denotes the complex conjugate [164, 223]. Remarkable time and frequency

resolution are obtained using this model.

6.1.3 Short-time Fourier transform

Alternatively, the TF representation can be obtained by applying a STFT, which performs Fourier transforms within a moving window in the assessed signal [162, 224], as follows:

$$g_3(\omega, t) = \frac{1}{2\pi} \int_{-\infty}^{\infty} e^{-i\omega\tau} X(\tau) \mathfrak{h}(\tau - t) d\tau \tag{6.3}$$

where $X(t)$ is the time series, $\mathfrak{h}(t)$ is a window function, and ω denotes the angular frequency. The energy spectrum of an STFT is known as a spectrogram.

6.1.4 Wigner-Ville distribution

The WVD can be interpreted as a measure of the signal's local TF energy [224], and it is defined as follows:

$$g_4(\omega, t) = \int_{-\infty}^{\infty} X\left(t + \frac{\tau}{2}\right) \overline{X\left(t - \frac{\tau}{2}\right)} e^{-i\omega\tau} d\tau \tag{6.4}$$

where $X(t)$ is the time series and the overline denotes the complex conjugate. This technique is highly effective in detecting and localising Dirac impulses and sinusoids [162, 224].

6.1.5 Summary of time-frequency models

The TF models in this section are just different alternatives based on a number of simplifying hypotheses and modelling assumptions to represent the same reality. For a particular model, the validity of such simplifying assumptions depends on the adopted values of certain model parameters (e.g. the dispersion parameter). Thus, to simultaneously identify both the plausibility of each TF model and the values of the model parameters that better suit the information coming from the raw ultrasonic data, a BIP is proposed here. Given a plate-like

structure monitored through a set of PZT sensors, the BIP is addressed independently for each PZT sensor due to potential differences between sensors, such as different working environments or manufacturing defects.

6.2 Bayesian model class ranking

6.2.1 Stochastic embedding of TF models

Let $g_j : \mathbb{R}^n \to \mathbb{R}$ be a candidate TF model defined by the relationship between a discrete signal $\mathcal{D}^{(k)} \in \mathbb{R}^n$ acting as input and the model output $g_j \in \mathbb{R}$, where k denotes the k-th sensor in the structure. Next, let $\hat{d}_j^{(k)} \in \mathbb{R}$ be the first energy peak observed in the scattered ultrasound signal, so that $\hat{d}_j^{(k)} = g_j(\mathcal{D}^{(k)})$. Under the assumption that g_j is only a candidate model over a set of alternatives [32] (e.g. like those described in Section 6.1), then the measured first peak, denoted here as $\tilde{d}^{(k)}$, would be more rigorously represented as an uncertain variable, as follows:

$$\tilde{d}^{(k)} = g_j\left(\mathcal{D}^{(k)}\right) + \epsilon \tag{6.5}$$

where ϵ is an uncertain prediction error term which accounts for the discrepancy between $\hat{d}_j^{(k)}$ and $\tilde{d}^{(k)}$, namely the modelled and measured values for the first energy peak, respectively. Following the principle of maximum information entropy (PMIE) [28, 32], this error can be conservatively assumed to be modelled as a zero-mean Gaussian distribution with standard deviation σ_ϵ, i.e., $\epsilon \sim \mathcal{N}(0, \sigma_\epsilon)$. The PMIE enables a rational way to establish a probability model for the model error term such that it produces the largest uncertainty (largest Shannon entropy); the selection of any other probability model would lead to an unjustified reduction in such uncertainty [32]. Thus, following Equation (6.5), a probabilistic description of the TF model can be obtained as:

$$p\left(\tilde{d}^{(k)} | \mathcal{M}_j^{(k)}, \sigma_\epsilon\right) = \left(2\pi\sigma_\epsilon^2\right)^{-\frac{1}{2}} \exp\left(-\frac{1}{2}\left(\frac{\tilde{d}^{(k)} - g_j^{-1}\left(\mathcal{D}^{(k)}\right)}{\sigma_\epsilon}\right)^2\right) \tag{6.6}$$

where $\mathcal{M}_j^{(k)}$ denotes the j-th candidate *model class* within a set of N_m available TF models $\mathbf{M} = \{\mathcal{M}_1^{(k)}, \ldots, \mathcal{M}_j^{(k)}, \ldots, \mathcal{M}_{N_m}^{(k)}\}$. Each model class is defined by the stochastic TF model given by Equation (6.6) along with the *prior* PDF of the model parameter σ_ϵ, $p(\sigma_\epsilon | \mathcal{M}_j^{(k)})$. This prior PDF represents the initial degree of belief of the values of σ_ϵ within a set of possible values $\Theta \subseteq \mathbb{R}$ before the information from measurements is incorporated through Bayesian updating, as explained further below. For all the sensors in the structure, the stochastic model is defined independently, thus accounting for different potential sources of errors and uncertainties.

6.2.2   Model parameters estimation

Before obtaining the model parameter updating from measurements, a preliminary assessment of the influence of the dispersion parameter σ_ϵ in the model class assessment and ranking was carried out, which showed a relatively high sensitivity of the resulting model class assessment to the value of this parameter. Thus, a first stage of the BIP is conceived to obtain the set of most plausible values for σ_ϵ given a set of data $\hat{\mathbf{d}}^{(k)} = \{\hat{d}_1^{(k)}, \ldots, \hat{d}_{N_m}^{(k)}\}$, which corresponds to a set of N_m values obtained by adopting each TF model class. To this end, the posterior PDF $p(\sigma_\epsilon | \hat{\mathbf{d}}^{(k)}, \mathcal{M}_j^{(k)})$ of the dispersion parameter σ_ϵ given the j-th TF model class ($\mathcal{M}_j^{(k)}$), is required. Thus, by using Bayes' theorem, this posterior PDF is given by:

$$p\left(\sigma_\epsilon | \hat{\mathbf{d}}^{(k)}, \mathcal{M}_j^{(k)}\right) = c^{-1} p\left(\hat{\mathbf{d}}^{(k)} | \sigma_\epsilon, \mathcal{M}_j^{(k)}\right) p\left(\sigma_\epsilon | \mathcal{M}_j^{(k)}\right) \tag{6.7}$$

where c is a normalising constant, so that:

$$\int_\Theta p\left(\sigma_\epsilon | \hat{\mathbf{d}}^{(k)}, \mathcal{M}_j^{(k)}\right) d\sigma_\epsilon = \int_\Theta c^{-1} p\left(\hat{\mathbf{d}}^{(k)} | \sigma_\epsilon, \mathcal{M}_j^{(k)}\right) p\left(\sigma_\epsilon | \mathcal{M}_j^{(k)}\right) d\sigma_\epsilon = 1 \tag{6.8}$$

In Equation (6.7), $p\left(\hat{\mathbf{d}}^{(k)} | \sigma_\epsilon, \mathcal{M}_j^{(k)}\right)$ is the likelihood function, which expresses how likely the data $\hat{\mathbf{d}}^{(k)}$ are reproduced by the stochastic model in Equation (6.6) if model class $\mathcal{M}_j^{(k)}$ is adopted, as shown in Figure 6.2. This

likelihood function can be obtained by substitution of the values of $\hat{\mathbf{d}}^{(k)}$ as the output of the stochastic model, as follows:

$$p\left(\hat{\mathbf{d}}^{(k)}|\sigma_\epsilon, \mathcal{M}_j^{(k)}\right) = \prod_{\ell=1}^{N_m} p\left(\hat{d}_\ell^{(k)}|\sigma_\epsilon, \mathcal{M}_j^{(k)}\right) \tag{6.9}$$
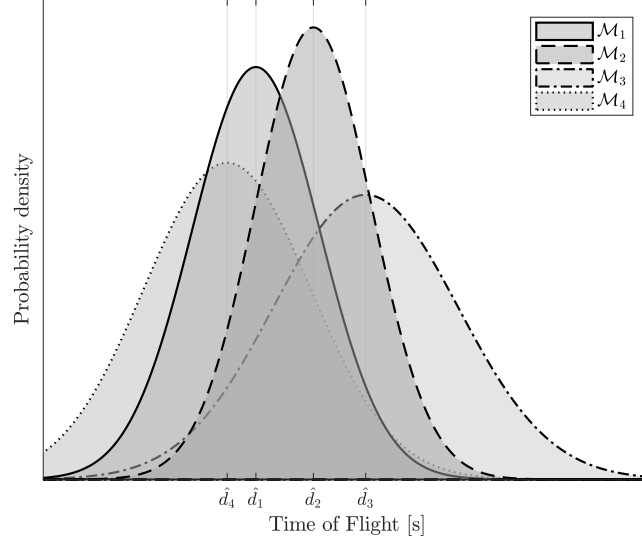
Figure 6.2: Likelihood functions derived from each time of flight $(\hat{d}_j^{(k)})$. The standard deviation provided by *level I* of the proposed model ranking is expected to have different values in each model-class. The time of flight data are then substituted in the likelihood function $p(\hat{\mathbf{d}}^{(k)}|\sigma_\epsilon, \mathcal{M}_j^{(k)})$. $\mathcal{M}_1$: HHT; $\mathcal{M}_2$: CWT; $\mathcal{M}_3$: STFT; $\mathcal{M}_4$: WVD.

Therefore, Equation (6.7) rewrites as:

$$p\left(\sigma_\epsilon|\hat{\mathbf{d}}^{(k)}, \mathcal{M}_j^{(k)}\right) \propto \left\{\prod_{\ell=1}^{N_m} p\left(\hat{d}_\ell^{(k)}|\sigma_\epsilon, \mathcal{M}_j^{(k)}\right)\right\} p\left(\sigma_\epsilon|\mathcal{M}_j^{(k)}\right) \tag{6.10}$$

Furthermore, it is observed that the evaluation of the normalising constant c in Equation (6.7) cannot usually be evaluated analytically except for special cases based upon linear models and Gaussian uncertainties [225]. However, stochastic simulation based on MCMC methods [188, 189] can be used to obtain samples from the posterior avoiding the evaluation of c, as shown in the next section.

6.2.3 Model class assessment

The probabilistic approach for model class assessment is motivated by the uncertainty about the TF model based on the assumed hypotheses and simplifications adopted for its formulation [28, 32]. Once the posterior $p(\sigma_\epsilon | \hat{\mathbf{d}}^{(k)}, \mathcal{M}_j^{(k)})$ is obtained, the plausibility of the model class $\mathcal{M}_j^{(k)}$ can be obtained by applying the total probability theorem as:

$$
\begin{aligned}
P\left(\mathcal{M}_j^{(k)} | \hat{\mathbf{d}}^{(k)}\right) &= \int_{\Theta} P\left(\mathcal{M}_j^{(k)} | \hat{\mathbf{d}}^{(k)}, \sigma_\epsilon\right) p\left(\sigma_\epsilon | \hat{\mathbf{d}}^{(k)}\right) d\sigma_\epsilon \\
&= \int_{\Theta} \frac{p\left(\hat{\mathbf{d}}^{(k)} | \mathcal{M}_j^{(k)}, \sigma_\epsilon\right) P\left(\mathcal{M}_j^{(k)} | \mathbf{M}\right)}{\sum_{\ell=1}^{N_m} p\left(\hat{\mathbf{d}}^{(k)} | \mathcal{M}_\ell^{(k)}, \sigma_\epsilon\right) P\left(\mathcal{M}_\ell^{(k)} | \mathbf{M}\right)} p\left(\sigma_\epsilon | \hat{\mathbf{d}}^{(k)}\right) d\sigma_\epsilon
\end{aligned}
$$

$$(6.11)$$

where $p\left(\sigma_\epsilon | \hat{\mathbf{d}}^{(k)}\right)$ denotes the posterior PDF obtained by Equation (6.10). Equation (6.11) can be simplified by applying the asymptotic Laplace's approximation [32] as follows:

$$
P\left(\mathcal{M}_j^{(k)} | \hat{\mathbf{d}}^{(k)}\right) \approx \frac{p\left(\hat{\mathbf{d}}^{(k)} | \mathcal{M}_j^{(k)}, \sigma_{M_j}\right) P\left(\mathcal{M}_j^{(k)}\right)}{\sum_{\ell=1}^{N_m} p\left(\hat{\mathbf{d}}^{(k)} | \mathcal{M}_\ell^{(k)}, \sigma_{M_j}\right) P\left(\mathcal{M}_\ell^{(k)}\right)}
$$

$$(6.12)$$

where the conditioning on $\mathbf{M}$ has been suppressed for simplicity and σ_{M_j} is the MAP value of the posterior PDF $p(\sigma_\epsilon | \hat{\mathbf{d}}^{(k)}, \mathcal{M}_j^{(k)})$, i.e.:

$$
\sigma_M = \arg\max_{\sigma_\epsilon} p(\sigma_\epsilon | \hat{\mathbf{d}}^{(k)}, \mathcal{M}_j^{(k)})
$$

$$(6.13)$$

6.2.4 Hyper-robust model estimation

The probability-based ranking of the model classes $\mathcal{M}_j^{(k)}$ obtained above provides information about the degree of belief of the j-th TF model class for each sensor. However, a *hyper-robust* model [32] is proposed to account for the

uncertainties held by all the model classes, thus providing a rigorous tool to address the model class selection. The hyper-robust model for a specific sensor k is defined as a weighted average of each TF model as follows:

$$
\begin{aligned}
p\left(\tilde{d}^{(k)}|\mathbf{M}\right) &= \sum_{\ell=1}^{N_m} p\left(\tilde{d}^{(k)}|\mathcal{M}_\ell^{(k)}, \sigma_{M_\ell}\right) P\left(\mathcal{M}_\ell^{(k)}|\hat{\mathbf{d}}^{(k)}\right) \\
&\cong \mathcal{N}\left(\sum_{\ell=1}^{N_m} \mathfrak{w}_\ell^{(k)} \hat{d}_\ell^{(k)}, \sum_{\ell=1}^{N_m} \left(\mathfrak{w}_\ell^{(k)} \sigma_{M_\ell}\right)^2\right)
\end{aligned}
\tag{6.14}
$$

where $\tilde{d}^{(k)}$ are the possible ToF values and $\mathfrak{w}_\ell^{(k)} = P(\mathcal{M}_\ell^{(k)}|\hat{\mathbf{d}}^{(k)})$ are the weights given by the posterior probabilities of the ℓ-th model class. Given that each stochastic model is assumed to be distributed as a Gaussian function, a simplified expression for the hyper-robust Gaussian distribution is also provided in Equation (6.14). However, to address the damage localisation problem, the use of a stochastic model as the input data would require excessive computational effort. Instead, the mean value of the hyper-robust model in the k-th sensor, denoted as $D^{(k)}$, is adopted.

6.3 Bayesian damage localisation

The localisation of damage is addressed in this chapter by using the same ToF model based BIP already described in Sections 3.1.2 and 4.1.3 under the assumptions of isotropic material properties and a concentrated patch damage within a bounded area. However, the model prediction error is considered here as an additional uncertain variable, which would need to be updated in the BIP as well as the damage position and wave propagation velocity variables. Therefore, the vector of uncertain model parameters is defined here as $\boldsymbol{\theta} = \{X_d, Y_d, V, \sigma_e\} \in \boldsymbol{\Theta}$. Given the likelihood function in Equation (3.12), one can obtain the posterior PDF of the model parameters given the ToF data $\mathbf{D} = \{D^{(1)}, \ldots, D^{(n)}\}$, where n is the number of sensors by applying the well-

known Bayes' theorem as:

$$p(\boldsymbol{\theta}|\mathbf{D}) = \frac{p(\mathbf{D}|\boldsymbol{\theta})p(\boldsymbol{\theta})}{p(\mathbf{D})} \qquad (6.15)$$

where $p(\boldsymbol{\theta})$ is the prior PDF of the model parameters, and $p(\mathbf{D}|\boldsymbol{\theta})$ is the likelihood function for the set of data $\mathbf{D}$. Given the stochastic independence of the measurements, the likelihood can be expressed as $p(\mathbf{D}|\boldsymbol{\theta}) = \prod_{k=1}^{N} p(D^{(k)}|\boldsymbol{\theta})$, where each factor $p(D^{(k)}|\boldsymbol{\theta})$ is given by Equation (3.12). Finally, $p(\mathbf{D})$ is the evidence of the data under the model specified by $\boldsymbol{\theta}$. This term, which acts as a normalising factor within Bayes' theorem, can be bypassed through sampling, e.g. using MCMC methods [199]. Thus, Equation (6.15) can be rewritten as:

$$p(\boldsymbol{\theta}|\mathbf{D}) \propto \left\{ \prod_{k=1}^{n} p\left(D^{(k)}|\boldsymbol{\theta}\right) \right\} p(\boldsymbol{\theta}) \qquad (6.16)$$

6.3.1 Asymptotic independence Markov sampling algorithm

In practice, the presence of multiple damage locations in plate-like structures is possible, thus the updating algorithm used to obtain the posterior PDF of the locations of such potential damage should be able to provide samples of a multimodal PDF. In the literature, the majority of available MCMC algorithms can identify multimodal posterior PDFs at the cost of increasing the computational burden, which can be exacerbated if large dimensional parameter spaces are explored, or by introducing *ad-hoc* algorithmic modifications [226]. To overcome this drawback, the AIMS algorithm [51] is used here due to its efficiency in providing samples from multi-modal posterior PDFs. In the AIMS algorithm, a posterior PDF $p(\cdot|\mathbf{D})$ is approximated using a combination of three well-known stochastic simulation methods. To this end, *simulated annealing* is used to obtain the target distribution $p(\cdot)$ from the prior distribution by sampling intermediate distributions $p_j(\cdot)$ through a *random walk M-H*. The intermediate distributions $p_j(\cdot)$ are approximated by using *importance sampling*. A pseudo-code implementation of AIMS method is provided as Algorithm 6.1.

Algorithm 6.1: Pseudo-code implementation of AIMS algorithm.

```
   /*        Preamble                                               */
 1 Define γ ∈ ℝ ;        // threshold for the essential sampling size
                             (ESS)
 2 Define {N_j^A}_{j=0}^m ;   // total number of samples in each annealing
                             level j
 3 Define {q_j(·|θ)}_{j=0}^m ; // proposal distributions at each annealing
                             level j
   /*        Algorithm                                              */
 4 j = 0 ;                 // first annealing level
```

5 Sample $\{\theta_0^{(i)}\}_{i=1}^{N_0^A} \sim p(\boldsymbol{\theta})$;

```
 6 Obtain the ESS ;         // measure of the similarity between p_0(·) and
                             the target distribution p(·)
```

7 **while** *ESS*/*N_j* < γ **do**

8   Obtain the normalised importance weights as a measure of the relative importance of the likelihood function in annealing levels $j + 1$ and j [51];

9   Run the M-H algorithm to generate N states of a Markov chain with target distribution $p_{j+1}(\cdot)$: Generate a Markov chain $\theta_{j+1}^{(1)} \ldots \theta_{j+1}^{(N_{j+1}^A)}$ with target distribution $p_{j+1}(\cdot)$ [51];

10   Calculate the ESS as a measure of the similarity between $p_{j+1}(\cdot)$ and the target $p(\cdot)$;

11      $j \leftarrow j + 1$;

12 **end**

```
13 Set m = j + 1 ;          // total number of steps in the annealing
                             approach
```

14 Generate a Markov chain $\theta_m^{(1)} \ldots \theta_m^{(N_m^A)}$ with distribution $p_m(\cdot) = p(\cdot)$ at annealing level *m*;

6.4   Case studies

In this section, two case studies are presented to validate the proposed model class selection methodology using a set of guided-waves synthetically generated by FEM. The methodology is applied to two cases of damage detection and localisation considering one and two damaged areas, respectively.

6.4.1   Synthetic signal generation

To numerically generate the input signals, Lamb waves are modelled using Abaqus® [196] for the simulations. The waves are generated over a thin plate made of aluminium-based alloy 2024-T351 with dimensions 0.5 m × 0.25 m,
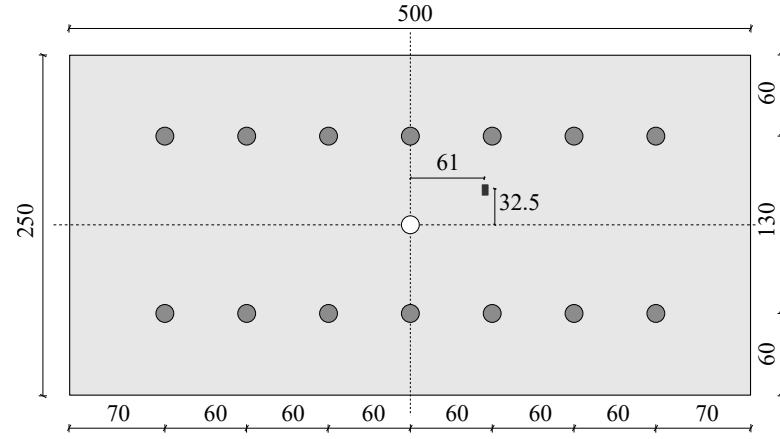
(a) Case study 1 considering one damage locations and 14 sensors.
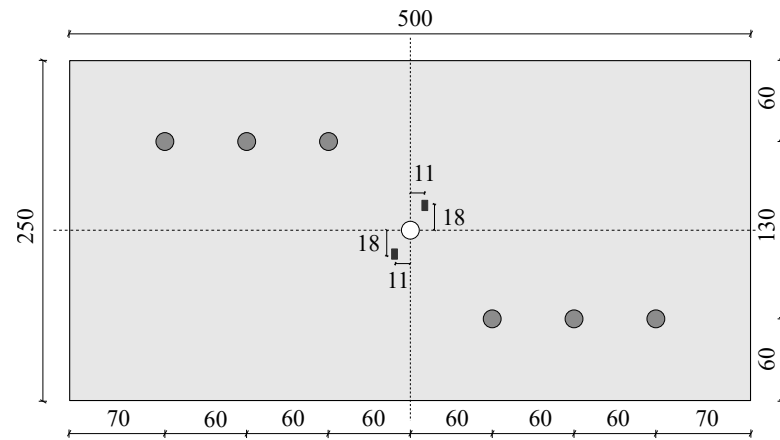
(b) Case study 2 considering two damage locations and 6 sensors.

Figure 6.3: Representation of the aluminium plates considered in both case studies along with the position and layout of the sensors (dimensions expressed in millimetres). The white circle represents the actuator, which is positioned in the centre of the plate. Damage is represented using dark rectangles.

as depicted in Figure 6.3 (see further properties about the aluminium alloy 2024-T351 [227] in Table 6.1). In Figure 6.3a, sensor numbering is established starting from S1 for the left-most upper sensor to S14 for the right-most down sensor. In panel (b), which corresponds to the case of two damage locations, sensors are analogously arranged starting from S1 to S6. For the ToF calculations, the Abaqus/Explicit® module is used in this work for its effectiveness in simulating the transient behaviour of the ultrasonic guided-waves.

A 4-node, quadrilateral, stress-displacement shell element with reduced integration and a large-strain formulation, referred to as the S4R element [196], is

Table 6.1: Material and structural properties (aluminium alloy 2024-T351) used in the Abaqus® model.

Young's modulus [GPa]	Poisson's ratio [-]	Density [kg/m^3]	Thickness [mm]
73.1	0.33	2780	1.5

used for the plate model, which is uniformly meshed using square elements of 1 mm size. The element size is determined by the smallest wavelength λ_{min} of the guided-wave mode represented. A minimum of 10 nodes per wavelength is normally required to ensure the avoidance of spatial aliasing [202]. The signal excitation is modelled as a perpendicular point force generated as a sine tone-burst of 5 cycles centred at a frequency $f = 100$ kHz. This frequency is selected to avoid extra complexity in the signal post-processing due to the appearance of possible higher order guided-waves modes. When the frequency is maintained at relatively low values, only two modes, namely the first anti-symmetric mode (A0) and the first symmetric mode (S0), are excited [202]. Given that the wave propagation velocity of the mode[1] captured by the model is around $V = 1950$ m/s, the maximum element size would be $\lambda/10 = (V/f)/10 = 1.95$ mm. However, note that the selected element size (1 mm) is nearly half of the maximum value. Next, the damage is modelled as a rectangular hole of dimension 2 mm × 4 mm for both case studies considered in this chapter. Free boundary conditions are considered in both cases. The ultrasonic signals are then received by the sensors in both undamaged and damaged cases. Afterwards, signals from both states are subtracted, thus the scattered information from the damage is obtained.

6.4.2 Model selection results

As previously mentioned, the simulated response of the plate to Lamb waves is used as data within the Bayesian framework. First, the standard deviation parameter σ_ϵ is defined as $\sigma_\epsilon = \rho \cdot \hat{d}_j^{(k)}$, where $\hat{d}_j^{(k)}$ is the time of arrival at the k-

---

[1]The referred mode is the anti-symmetric mode (A0) since only the bending mode can be captured with shell elements.

th sensor using the j-th TF model, and ρ is a factor defined within a sufficiently large interval, which in this example is taken as $(0, 0.5]$. Therefore, the prior PDF of σ_ϵ can be expressed as a uniform distribution over the referred interval, i.e. $p(\sigma_\epsilon) = \mathcal{U}(0, 0.5 \cdot \hat{d}_j^{(k)})$. The posterior PDF $p(\sigma_\epsilon | \hat{\mathbf{d}}^{(k)}, \mathcal{M}_j^{(k)})$ is obtained through samples using the M-H algorithm (see a pseudo-code implementation in Appendix A) with $T_s = 40000$ and a Gaussian *proposal distribution*, i.e., $q(\theta' | \theta) = \mathcal{N}(\theta, \sigma)$, where σ is the standard deviation of the M-H random walk which is selected such that the acceptance rate r lies within the interval $[0.2, 0.4]$ [203–205]. The MAP parameter is then computed and introduced as an input for the model class selection problem, as explained in Section 6.2.3.

(a) $P(\mathcal{M}_i | \hat{\mathbf{d}})$ for case study 1

(b) $P(\mathcal{M}_i | \hat{\mathbf{d}})$ for case study 2
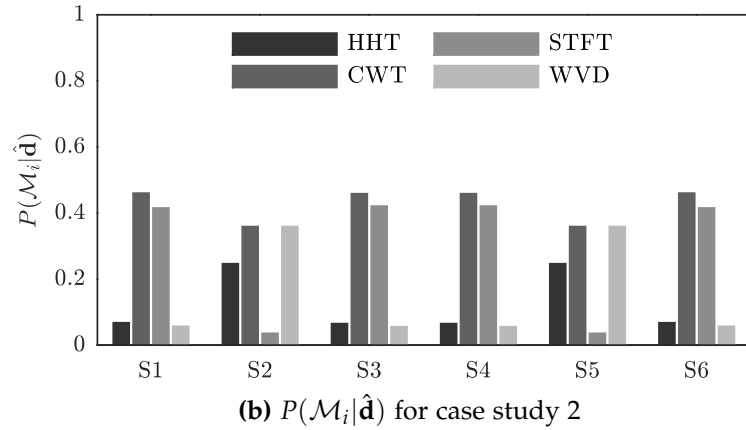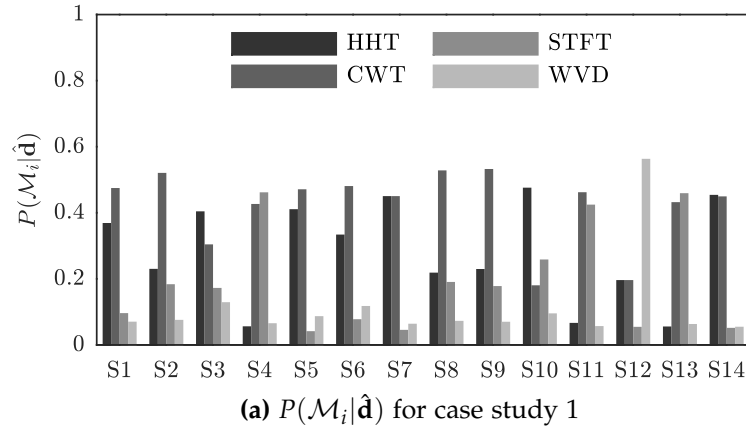
Figure 6.4: Posterior probability $P(\mathcal{M}_i | \hat{\mathbf{d}})$.

The resulting posterior probabilities from Equation (6.12) are subsequently used to rank the candidate TF models for each of the sensors, as shown in Figures 6.4a and 6.4b for case study 1 and 2, respectively. Observe from these results that there is not a particularly predominating TF model for all the sen-

Table 6.2: Time of arrival ($D^{(k)}$) obtained as the mean of the hyper-robust models given by Equation (6.14).

	Sensor	Time $D^{(k)}$ [μs]	Sensor	Time $D^{(k)}$ [μs]
Case study 1	S1	157.53	S8	163.33
	S2	125.29	S9	136.23
	S3	98.125	S10	114.66
	S4	71.539	S11	94.115
	S5	49.164	S12	83.664
	S6	70.242	S13	96.235
	S7	98.500	S14	116.35
Case study 2	S1	109.96	S4	54.577
	S2	81.214	S5	81.214
	S3	54.577	S6	109.96

sors. Nonetheless, the CWT model emerges as the most plausible one for a considerable majority of sensors, i.e., 8 out of 14 sensors for the case study 1, and 4 out of 6, for case study 2. Therefore, if a single TF model had to be selected for damage identification, a rational selection based on these results would be to choose the CWT model, since the better representation of the given data for the majority of sensors is provided by this choice. This output is in agreement with most of the authors in the literature who select CWT model to obtain the ToF from the scattered signals [50, 166]. Notwithstanding, a hyper-robust model can be obtained by applying Equation (6.14) using the posterior probabilities of each model class. The ToFs in this case are obtained by a model average from the probabilistic model from each sensor, as shown in Table 6.2. These values are subsequently used to reconstruct the damage in the BIP of damage localisation, which is shown next.

6.4.3 Damage localisation and reconstruction

Once the TF models are ranked and the hyper-robust TF model is obtained, the mean values of each hyper-robust model for each sensor are used as ToF data **D** within the BIP of damage localisation, described in Section 6.3. The prior information of the model parameters has been defined as a uniform distribu-

tion for the damage position and dispersion parameter ($X \sim \mathcal{U}(-0.25, 0.25)$m, $Y \sim \mathcal{U}(-0.125, 0.125)$m, and $\sigma_e \sim \mathcal{U}(0, 10^{-4})$), and a Gaussian PDF for the velocity $V \sim \mathcal{N}(v, \sigma_v)$, where $v = 1950$m/s and $\sigma_v = 40$m/s. The posterior PDF of model parameters $\boldsymbol{\theta}$ is obtained in this case using the AIMS algorithm, with a threshold value $\gamma = 1/2$, 10^5 samples per annealing level, and a Gaussian PDF as the proposal distribution, i.e. $q(\theta'|\theta) = \mathcal{N}(\theta, \sigma)$, where σ is the standard deviation of the M-H random walk which is again selected such that the acceptance rate r lies within the interval $[0.2, 0.4]$. Figure 6.5 shows the inferred damage position for the aluminium plates of case study 1 and 2, respectively, using the hyper-robust TF model obtained by Equation (6.14). The hyper-robust model is obtained for each sensor by model averaging weighted using the posterior plausibilities of the TF models, shown in Figure 6.4. It is observed that the damage position is efficiently reconstructed with the BIP methodology presented in this chapter. The results also show that, for the particular case study 2, the multi-modality due to dual damage position is well addressed using the AIMS algorithm.

The marginal posterior distributions of the other two parameters used by the BIP of damage localisation, namely the standard deviation factor of the likelihood function σ_e and the wave propagation velocity V, are depicted in Figure 6.6. In case study 1, a lower level of dispersion in both parameters, σ_e and V, is observed, whereas in case study 2, a higher dispersion is obtained.

6.5   Discussion

The proposed Bayesian methodology for damage localisation has been demonstrated using two case studies presented in Section 6.4. For each of the sensors, a Bayesian model class assessment framework is proposed to rank the candidate TF models, according to relative plausibilities that measure the relative degree of belief of the candidate model class in interpreting the raw signal acquired by the sensor. These relative plausibilities are then used to obtain a hyper-robust TF model for each sensor, which provides a higher level of ro-
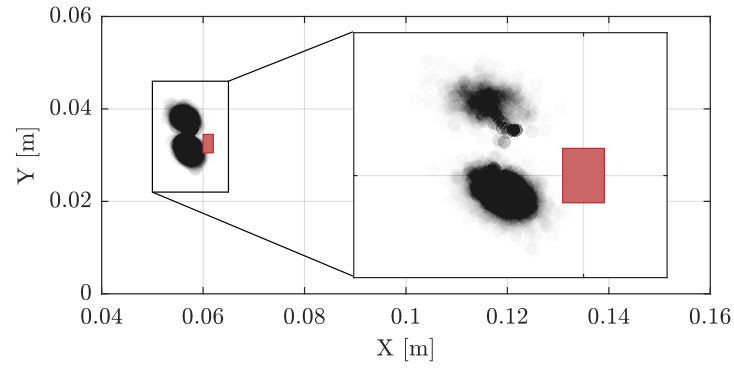
(a) Estimated and actual damage position $(X - Y)$ for case study 1
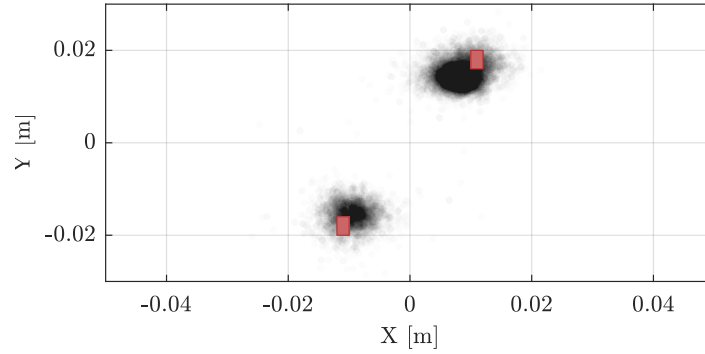
(b) Estimated and actual damage position $(X - Y)$ for case study 2

Figure 6.5: Damage location estimation for the plate of case study 1 and 2. The actual position of the centre of the damage is depicted using red rectangles which are represented in actual dimensions.

bustness to damage localisation than just taking the most plausible TF model among the candidate set. This robustness is clearly manifested in Figure 6.5a, where the damage position is identified in two plausible regions close to the actual damage position; an unjustified TF model choice would lead to a biased localisation due to unconsidered model uncertainty. The same behaviour can be also observed in Figure 6.6b for the reconstruction of the wave propagation velocity parameter. Note that the ultrasonic data used in both case studies are synthetically obtained through FEM, although the methodology is entirely applicable to real ultrasonic signals. However, for real ultrasonic data,
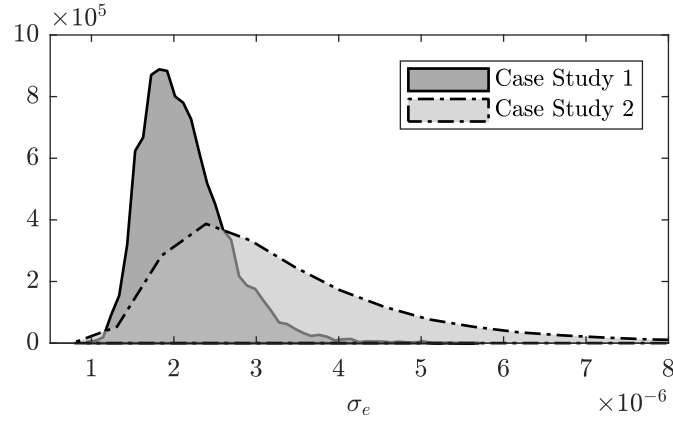
(a) Dispersion parameter (σ_e).
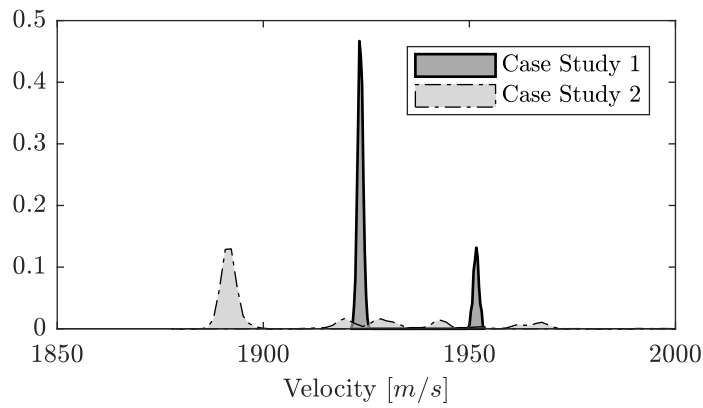
(b) Wave propagation velocity (V).

Figure 6.6: Posterior PDFs of the σ_e and V parameters for both case study 1 and 2.

the uncertainty in the damage localisation would be higher due to electronic noise or other measurement errors coming from, for instance, imperfect sensor bonding.

Then, a damage localisation BIP using an ellipse-based model is applied to reconstruct the damage position using the AIMS algorithm as the Bayesian updating algorithm. The data **D** are obtained by using the mean of the hyper-robust model, given by Equation (6.14) for each sensor independently. The damage location has been inferred remarkably well in both case studies. However, a higher dispersion in the $X - Y$ parameters (larger localisation uncertainty) has been found in case study 2 compared to case study 1, as can be observed in Figure 6.5. In addition, a higher dispersion is identified in the marginal distribution of the standard deviation parameter σ_e in case study 2.

This could be explained by the nature of the likelihood function from Equation (3.12), which is a Gaussian distribution. In order to properly identify the two damage positions in this case study, the posterior values of σ_e (which is an updatable parameter) need to increase, hence leading to a higher dispersion in the damage localisation as well as in the velocity parameter reconstruction, as observed in Figure 6.6. This points out a limitation of the proposed methodology when dealing with multiple damage locations. In this context, a desirable further work would be the exploration of optimal likelihood functions to deal with damage multi-modality.

The robustness of the proposed methodology can then be observed by comparing the Bayesian identification results against those obtained using a deterministic approach. A well-known method to address inverse problems efficiently, but deterministically, is by the use of GA [228]. GA are used to find the value of the parameters that minimises a *cost function*, which in this case can be defined as $\|\text{ToF}_{\mathcal{D}}^{(a-s)} - \text{ToF}_{M}^{(a-s)}(\boldsymbol{\theta}')\|_2^2$, a L_2-norm of the residual time of flight between the model and the data. Figure 6.7 depicts the comparison between the damage identification results obtained using the proposed Bayesian methodology and a deterministic GA-based inverse problem. To better highlight the robustness of the proposed Bayesian damage identification methodology in the presence of uncertainties, a bias is artificially introduced in the velocity term as a 5% of deviation in the value obtained through Abaqus® (from 1950 m/s to 1850 m/s). Note that even with this small deviation, the damage localisation results given by the GA become biased, whereas the results using Bayesian methodology are virtually immune to such variation. This simple example demonstrates the superiority of the proposed methodology in reconstructing the position of damage from guided-waves data, regardless of potential input errors.
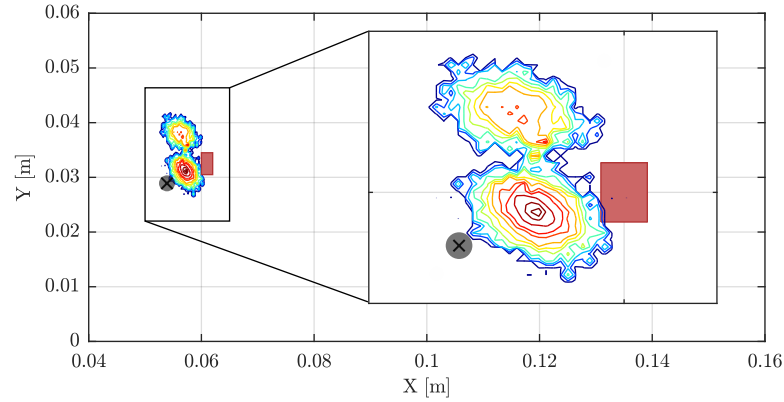
Figure 6.7: Comparison between a deterministic damage localisation using GA (grey point) and the results obtained with the proposed Bayesian methodology.

6.6 Conclusions

A Bayesian methodology for damage location using guided-waves is presented in this chapter. This methodology makes it possible accounting for several sources of uncertainty, such as the epistemic uncertainty due to TF model selection, and the uncertainty coming from the measurement noise and variable material properties. The effectiveness of the method is shown through two case studies with one and two damaged areas, respectively. The following conclusions are drawn from this chapter:

- The damage position can be accurately reconstructed using ToFs proving the effectiveness of the proposed multi-level Bayesian inverse problem methodology;

- The use of a hyper-robust TF model as an input for the damage localisation Bayesian inverse problem leads to a more robust damage inference;

- The reconstruction of the two damage areas in case study 2 has been remarkably addressed by using the AIMS algorithm. However, under this scenario of damage, an important increase in the posterior uncertainty of the model parameters is obtained.

Further research work is under consideration with regards to: (1) the assessment of a suitable likelihood function to efficiently deal with multi-modal

damage scenarios, and (2) the influence of different types of damage in the performance of the proposed methodology.

7

Bayesian damage identification in beam composite structures

This chapter addresses the identification of damage from ultrasonic measurements acquired in beam composite structures while quantifying *aleatory* and *epistemic* uncertainties (refer to Section 2.7). To this end, a WFE based guided-wave model is used in a multi-level Bayesian framework, which allows the classification, quantification, and localisation of damage. Bayes' theorem is applied at two hierarchical levels: (1) to obtain the posterior information about the unknown model parameters of a particular damage hypothesis, e.g. a specific damage mode such as a delamination, and (2) to provide the relative degree of belief of different damage hypothesis within a set of candidate hypotheses (or model classes). Note that the first level addresses the quantification and localisation of damage in a beam structure, given that each damage hypotheses contains relevant damage-related parameters. The second level classifies the damage according to the plausibility of each candidate model classes and therefore the identification of damage mode is obtained. Numerical results show that the proposed Bayesian framework is able to localise and identify damage in multi-layered composite laminates while quantifying the uncertainty present in both the numerical data and the wave propagation model.

In contrast to the Bayesian approach proposed in Chapter 6, where the position of damage was the main objective, this chapter addresses the identification of damage, which involves determining its type and quantifying its severeness. In this context, Chapter 6 uses a simplified ellipse-based ToF model to localise the damage, while this chapter requires a physics-based model that provides time-domain ultrasonic signals carrying information about the damage type and extent. Furthermore, the Bayesian approaches are different as well: Chapter 6 uses two interconnected BIPs, whereby a hyper-robust ToF model is built using the asymptotic Laplace's approximation followed a BIP of damage localisation that uses the hyper-robust ToF estimation as input data. Conversely, this chapter addresses the identification of damage in a Bayesian model class selection framework by estimating the *evidence* of each class (i.e. damage hypothesis). Therefore, the main differences between this and the previous chapter lies in: (1) the diagnosis stage that is addressed, i.e. localisation against identification; (2) the Bayesian framework for model class selection, i.e. using asymptotic approximations or estimating the evidence; and (3) the type of the model used, i.e. ellipse-based against physics-based models.

The chapter is organised as follows: the WFE model for guided wave simulation is presented in Section 7.1; the Bayesian approach for damage identification is shown in Section 7.2; an algorithmic implementation of the proposed Bayesian framework is provided in Section 7.3; Section 7.4 illustrates the methodology in a numerical case study; finally, concluding remarks and a brief discussion are provided in Section 7.5.

7.1 Guided-wave propagation model

The transient ultrasonic guided-wave simulation model used in this chapter, based on the WFE scheme, is briefly introduced in this section. For further implementation and base theory details, please refer to [179]. This model, which works in the frequency domain, builds its computational efficiency on the use of three different sections of the modelled structure (see Figure 7.1), as

follows:

(i) a coupling section for arbitrary excitations,

(ii) a scatterer containing arbitrary damage, and

(iii) the rest of the waveguide.
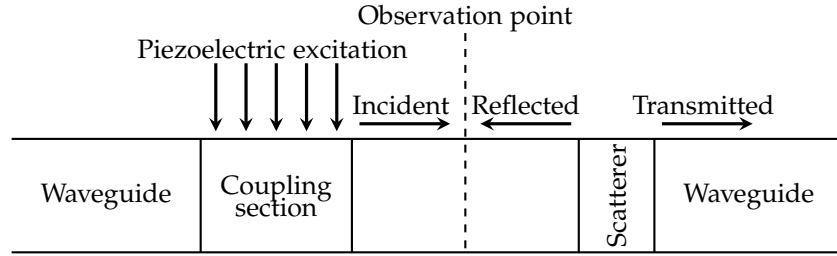
Figure 7.1: Wave propagation due to external excitation.

This wave propagation model combines the previous sections efficiently in a semi-analytical approach using *periodic structure theory* [229]. Besides, the WFE method is used to obtain the wave propagation characteristics by modelling a periodic section of the waveguide in a FEM software. Stiffness ($\mathbf{K}^b$), mass ($\mathbf{M}^b$) and damping ($\mathbf{C}^b$) matrices are obtained from such model of a beam. Then, these matrices are used to set up the dynamic equilibrium of the section as follows:

$$\mathbf{D}^b(\omega)\mathbf{u} = \mathfrak{f} \tag{7.1}$$

where, $\mathbf{D}^b(\omega) = \mathbf{K}^b + i\omega\mathbf{C}^b - \omega^2\mathbf{M}^b$ is the frequency dependent dynamic stiffness matrix, $\mathbf{u}$ is the vector of degrees of freedom, $\mathfrak{f}$ is the internal forces vector, and ω is the angular frequency. These vectors can be internally partitioned into left ($\mathbf{L}$) and right ($\mathbf{R}$) degrees of freedom with respect to direction of wave propagation. According to Bloch's theorem [230], the free wave propagation in a waveguide of length l_x has the propagation constant $\lambda = \mathrm{e}^{ikl_x}$, with k being the wave-number, which gives $\mathbf{u}_R = \lambda\mathbf{u}_L$ and $\mathfrak{f}_R = -\lambda\mathfrak{f}_L$. An eigenvalue problem for λ can then be formulated by substituting these expressions into

Equation (7.1), as follows:

$$\lambda \left\{ \begin{array}{c} \mathbf{u}_L \\ \mathfrak{f}_L \end{array} \right\} = \mathbf{T} \left\{ \begin{array}{c} \mathbf{u}_L \\ \mathfrak{f}_L \end{array} \right\} \tag{7.2}$$

where $\mathbf{T}$ is the transfer matrix and λ are the eigenvalues of $\mathbf{T}$. Note that the propagation constants λ exist in pairs for positive $(+)$ and negative $(-)$ travelling waves. Additionally, the eigenvectors $\boldsymbol{\phi}$ are the wavemodes as given below:

$$\boldsymbol{\phi} = \left\{ \begin{array}{c} \boldsymbol{\phi}_u \\ \boldsymbol{\phi}_{\mathfrak{f}} \end{array} \right\}, \quad \text{where } \boldsymbol{\phi}^+ = \left\{ \begin{array}{c} \boldsymbol{\phi}_u^+ \\ \boldsymbol{\phi}_{\mathfrak{f}}^+ \end{array} \right\}, \; \boldsymbol{\phi}^- = \left\{ \begin{array}{c} \boldsymbol{\phi}_u^- \\ \boldsymbol{\phi}_{\mathfrak{f}}^- \end{array} \right\} \tag{7.3}$$

The wavemodes are used here as basis functions to transform the problem into wave domain where the forces and displacements are represented by a linear combination of incoming $(\mathbf{a}^+)$ and outgoing amplitudes $(\mathbf{a}^-)$ as shown below:

$$\mathbf{u} = \boldsymbol{\phi}_u^+ \mathbf{a}^+ + \boldsymbol{\phi}_u^- \mathbf{a}^-, \quad \mathfrak{f} = \boldsymbol{\phi}_{\mathfrak{f}}^+ \mathbf{a}^+ + \boldsymbol{\phi}_{\mathfrak{f}}^- \mathbf{a}^- \tag{7.4}$$

Note that the piezoelectric excitation generates outgoing amplitudes $(\mathbf{a}^-)$ into the structure. These amplitudes are obtained by modelling the coupling section in FEM software and extracting matrices to set up the dynamic equilibrium similar to Equation (7.1). The interface between the waveguide and the coupling section must be consistent in order to satisfy the continuity and equilibrium conditions. Then the outgoing amplitudes can be obtained as follows:

$$\mathbf{a}^- = \left(\mathbf{D}_{\mathbf{cs}}^b \mathbf{R} \boldsymbol{\phi}_u^- - \mathbf{R} \boldsymbol{\phi}_{\mathfrak{f}}^- \right)^{-1} \mathfrak{f}_{\mathbf{cs}} \tag{7.5}$$

where, $\mathbf{D}_{\mathbf{cs}}$ is the dynamic stiffness matrix of the coupling section, $\mathbf{R}$ is the rotation matrix to transform from local degrees of freedom to global and $\mathfrak{f}_{\mathbf{cs}}$ is the frequency domain external excitation from the piezoelectric transducer. Then, the scattering coefficients for a damage are computed to reconstruct the transient response at the observation point. The procedure follows the same

steps of modelling the damaged section in FEM software and extracting the matrices. Then, the application of continuity and equilibrium at the interface of the scatterer and waveguide sections results in the scattering matrix, as follows:

$$\mathbf{S} = -\left[\mathbf{R}\boldsymbol{\phi}_{\mathfrak{f}}^{-} - \mathbf{D}_{J}^{b}\mathbf{R}\boldsymbol{\phi}_{u}^{-}\right]^{-1}\left[\mathbf{R}\boldsymbol{\phi}_{\mathfrak{f}}^{+} - \mathbf{D}_{J}^{b}\mathbf{R}\boldsymbol{\phi}_{u}^{+}\right] \tag{7.6}$$

where, $\mathbf{D}_{J}^{b}$ is the dynamic stiffness matrix of the scatterer and $\mathbf{S}$ denotes the scattering matrix. The scattered amplitudes ($\mathbf{a}_{s}$) can be obtained from the incident amplitudes ($\mathbf{a}_{i}$) by $\mathbf{a}_{s} = \mathbf{S}\mathbf{a}_{i}$. The transient response is obtained by summing up all amplitudes reaching the selected observation point in the desired time window expanding. Then, these amplitudes are expanded over the individual degrees of freedom using Equation (7.4) and an inverse discrete Fourier transform based on a fast Fourier transform algorithm [231] is performed.

It is worth highlighting that the model parameters that are related to the actual damage are (1) the location of the damage along the axis of the beam (i.e. X_d) and (2) the reflection and transmission coefficients (i.e. r and t, respectively), which are contained in the scattering matrix $\mathbf{S}$. The latter group of coefficients represent the energy part of each incident wave mode (e.g. bending or tensile/compressive) that is transmitted or reflected. For instance, if a pressure wave mode is incident in the damage, four coefficients will be involved in creating the scattered wave: (1) pressure-to-pressure reflection coefficient r_{pp}, (2) pressure-to-bending reflection coefficient r_{pb}, (3) pressure-to-pressure transmission coefficient t_{pp}, and (4) pressure-to-bending transmission coefficient t_{pb}. Note also that these coefficients will have different values for different damage modes (i.e. depending on the wave interaction with the damage), hence allowing the differentiation between them.

7.2   Bayesian approach for damage identification

A Bayesian model class assessment framework [32] is developed in this section for a rigorous and robust identification and localisation of damage. A set of

N_m candidate damage hypotheses or model classes $\mathbf{M} = \{\mathcal{M}_j\}_{j=1}^{N_m}$ are initially defined to this end, e.g. considering a crack or a delamination. These hypotheses are then ranked according to their posterior plausibilities, which rely on the information obtained from the ultrasonic data $\mathbf{q}_\mathcal{D} \in \mathbb{R}^{N_q}$. Note that these data carry information about the health condition of the structure. Additionally, we assume that a deterministic wave propagation model $\mathbf{q}_\mathcal{M}(\boldsymbol{\theta}) \in \mathbb{R}^{N_q}$, whose output can be directly comparable to the experimental measurement, is available. The model is defined as a function of a set of unknown model parameters $\boldsymbol{\theta} \in \boldsymbol{\Theta} \subset \mathbb{R}^{N^\theta}$. In this chapter, the wave propagation model based on the hybrid WFE model (refer to Section 7.1) is adopted. A probabilistic version of the wave propagation model can be defined by introducing an error term $\mathbf{e} \in \mathbb{R}^{N_q}$ that measures the discrepancy between the modelled $\mathbf{q}_\mathcal{M}(\boldsymbol{\theta})$ and experimental ultrasonic data $\mathbf{q}_\mathcal{D}$, as follows:

$$\mathbf{q}_\mathcal{D} = \mathbf{q}_\mathcal{M}(\boldsymbol{\theta}) + \mathbf{e} \tag{7.7}$$

Based on the Principle of Maximum Information Entropy [28, 32], a zero mean Gaussian distribution with standard deviation σ_e as $\mathcal{N}(0, \sigma_e)$ is adopted to model the error term $\mathbf{e}$ in order to produce the largest uncertainty. Thus, the stochastic version of the model is given by a Gaussian distribution, as:

$$p\left(\mathbf{q}_\mathcal{D}|\mathbf{q}_M, \boldsymbol{\theta}, \mathcal{M}_j\right) = \left(2\pi\sigma_e^2\right)^{-\frac{1}{2}} \exp\left(-\frac{1}{2\sigma_e^2} \mathcal{J}(\boldsymbol{\theta}, \mathcal{D})\right) \tag{7.8}$$

where $\mathcal{J}(\boldsymbol{\theta}, \mathcal{D})$ is the goodness-of-fit function which is selected to be the L_2-norm of the measured and modelled data, as: $\mathcal{J}(\boldsymbol{\theta}, \mathcal{D}) = \sum_{i=1}^{N_q}(q_{i,\mathcal{M}} - q_{i,\mathcal{D}})^2$, with $q_{i,\mathcal{M}}$ and $q_{i,\mathcal{M}}$ being the i-th element of the vectors $\mathbf{q}_\mathcal{M}$ and $\mathbf{q}_\mathcal{D}$, respectively. To completely define the model class $\mathcal{M}_j$, the prior distribution of the model parameters $p(\boldsymbol{\theta}|\mathcal{M}_j)$ also needs to be provided. Next, the posterior distribution of the model parameters $p\left(\boldsymbol{\theta}|\mathcal{D}, \mathcal{M}_j\right)$, given the data $\mathcal{D} \triangleq \mathbf{q}_\mathcal{D}$ and a specific model class $\mathcal{M}_j$, can be defined by applying the Bayes' theorem, as follows:

$$p\left(\boldsymbol{\theta}|\mathcal{D}, \mathcal{M}_j\right) = \frac{p\left(\mathcal{D}|\boldsymbol{\theta}, \mathcal{M}_j\right) p(\boldsymbol{\theta}|\mathcal{M}_j)}{p(\mathcal{D}|\mathcal{M}_j)} \tag{7.9}$$

where $p\left(\mathcal{D}|\boldsymbol{\theta}, \mathcal{M}_j\right)$ denotes the likelihood function in Equation (7.8) and $p(\mathcal{D}|\mathcal{M}_j)$ is the evidence of the model class $\mathcal{M}_j$ in representing the data $\mathcal{D}$. Note that the computation of Equation (7.9) requires addressing multidimensional integrals, which usually do not have an analytical expression. Thus, the M-H algorithm [188, 189] (see Appendix A) is adopted here as MCMC method to obtain samples from the posterior distribution $p\left(\boldsymbol{\theta}|\mathcal{D}, \mathcal{M}_j\right)$ avoiding the computation of the normalising factor.

Finally, the model classes (i.e. damage hypotheses) are ranked by using their posterior plausibilities $P(\mathcal{M}_j|\mathcal{D}, \mathbf{M})$ obtained through Bayes' theorem, as follows:

$$P\left(\mathcal{M}_j|\mathcal{D}, \mathbf{M}\right) = \frac{p\left(\mathcal{D}|\mathcal{M}_j\right) P\left(\mathcal{M}_j|\mathbf{M}\right)}{\Sigma_{l=1}^{N_m} p\left(D|\mathcal{M}_l\right) P\left(\mathcal{M}_l|\mathbf{M}\right)} \tag{7.10}$$

where $P\left(\mathcal{M}_j|\mathbf{M}\right)$ is the prior probability of the model class $\mathcal{M}_j$. Note that the posterior plausibilities are dependent on the evidence terms calculated for each model class. The calculation of the evidence is addressed in the section below. Therefore, both damage identification and the inference of model parameters are addressed by this hierarchical Bayesian approach.

7.2.1 Evidence of a model class

The evidence calculation is based on [232], where a logarithmic approximation of the evidence was proposed to provide a more reliable estimation of such quantity. Note that the evidence could be approximated by samples from the prior distribution using the total probability theorem as follows:

$$p(\mathcal{D}|\mathcal{M}_j) = \int p(\mathcal{D}|\boldsymbol{\theta}, \mathcal{M}_j) \underbrace{p(\boldsymbol{\theta}|\mathcal{M}_j)}_{\text{Prior PDF}} d\boldsymbol{\theta} \approx \frac{1}{N^\theta} \sum_{k=1}^{N^\theta} p(\mathcal{D}|\boldsymbol{\theta}^{(k)}, \mathcal{M}_j) \tag{7.11}$$

However, such an approximation involves the use of samples that are, in general, very different from the area of high probability of the likelihood function $p(\mathcal{D}|\boldsymbol{\theta}, \mathcal{M}_j)$, and therefore the accuracy of the approximation may be compromised. To overcome this issue, Cheung and Beck [232] proposed a stable

technique based on an analytical approximation of the posterior distribution. Thus, the log-evidence can be approximated by:

$$\log p(\mathcal{D}|\mathcal{M}_j) \approx \log p(\mathcal{D}|\boldsymbol{\theta}, \mathcal{M}_j) + \log p(\boldsymbol{\theta}|\mathcal{M}_j) - \underbrace{\log p(\boldsymbol{\theta}|\mathcal{D}, \mathcal{M}_j)}_{\text{Analytical approx.}} \quad (7.12)$$

Equation (7.12) can be obtained by applying logarithms to Bayes' theorem that defines the inverse problem in Equation (7.9). Implementation details of this method focused on the use of M-H as the MCMC algorithm to obtain samples from the posterior PDF are provided in Section 7.3.

Note that, in addition to the calculation of the evidence of a model class, the trade-off between data fitting and the information gained from the ultrasonic data is of interest. This allows to distinguish between over-fitting and robust to noise model classes. This additional information can be obtained from the evidence calculation from a information theoretic perspective [32, 217], as follows:

$$\log p(\mathcal{D}|\mathcal{M}_j) = \underbrace{\int_{\Theta} \big[\log p(\mathcal{D}|\boldsymbol{\theta}, \mathcal{M}_j) \big] p(\boldsymbol{\theta}|\mathcal{D}, \mathcal{M}_j) d\boldsymbol{\theta}}_{\text{Average goodness of fit}}$$
$$- \underbrace{\int_{\Theta} \log \left[\frac{p(\boldsymbol{\theta}|\mathcal{D}, \mathcal{M}_j)}{p(\boldsymbol{\theta}|\mathcal{M}_j)} \right] p(\boldsymbol{\theta}|\mathcal{D}, \mathcal{M}_j) d\boldsymbol{\theta}}_{\text{Expected information gain}} \quad (7.13)$$

where the averaged goodness-of-fit (AGF) measures the data fitting of the samples obtained from the posterior PDF and the expected information gain (EIG) quantifies the relative entropy between the posterior and prior PDFs of the model parameters. The EIG term measures the complexity of the model class, given that it tends to provide higher values for more complex damage hypotheses. Besides, it is a penalty term in the calculation of the log-evidence. Therefore, from this information theoretic point of view, the preferred model classes will be the ones which tend to provide a good representation of the data (i.e. high AGF), while remaining robust, hence gaining the minimum information from them (i.e. low EIG).

7.3   Algorithmic implementation

The proposed Bayesian framework for damage identification is described here at an algorithmic level. First, the posterior PDFs are built from samples obtained from the M-H algorithm (see Appendix A) for each model class, and then the evidence for each of them is calculated. Once the evidence terms of all the candidate model classes are obtained, the posterior plausibility of the model class is provided by Equation (7.10) and the most probable one is selected. A generic algorithmic implementation of the model class selection problem is provided in Algorithm 7.1.

Algorithm 7.1: Bayesian model class selection

---

1 Define $\triangleright$ $\mathbf{M} = \{\mathcal{M}_j\}$ with $j = 1, 2, \ldots, N_m$;   // Model classes
2 Define $\triangleright$ $\boldsymbol{\theta}$ and $p(\boldsymbol{\theta}|\mathcal{M}_j)$ $\forall \mathcal{M}_j \in \mathbf{M}$;   // Parameters and prior PDF
3 **for** $j = 1$ **to** N_m **do**
4 | Obtain $p(\boldsymbol{\theta}|\mathcal{D}, \mathcal{M}_j) \sim$ M-H algorithm (Appendix A) ;   // BIP
5 | Estimate $p(\mathcal{D}|\mathcal{M}_j) \sim$ Algorithm 7.2 ;   // Evidence
6 **end**
7 Obtain $P(\mathcal{M}_j|\mathcal{D}, \mathbf{M}) \sim$ Eq. (7.10);
8 Select the most plausible $\mathcal{M}^* = \arg\max P(\mathcal{M}_j|\mathcal{D}, \mathbf{M})$;

Additionally, the calculation of the evidence is detailed in Algorithm 7.2. Note that this algorithm is based on the M-H algorithm, and therefore some of the equations are referred to the Appendix A. This method is based on samples from the posterior PDF, which are used to build an analytical approximation of itself. After the log-evidence is calculated, the EIG term may be obtained by applying Equation (7.13) given that the AGF term is estimated based on the samples from the posterior.

7.4   Numerical case studies

In this section, two numerical case studies are presented using a layered carbon fibre composite beam with two different damage modes: (1) a delamination and (2) a crack, as shown in Figure 7.2. The delamination has a length of 5mm

---

Algorithm 7.2: Evidence calculation.

1 Take $\{\boldsymbol{\theta}^{(k)}\}_{k=1}^{N_1} \sim p(\boldsymbol{\theta}|\mathcal{D}, \mathcal{M}_j)$;   // Samples from the posterior PDF
2 Choose a model parameter vector $\boldsymbol{\theta} \in \boldsymbol{\Theta}$;
3 **for** $k = 1$ **to** N_1 **do**
4 $\quad$ Evaluate $q(\boldsymbol{\theta}|\boldsymbol{\theta}^{(k)})$;   // Proposal distribution
5 $\quad$ Evaluate $r(\boldsymbol{\theta}|\boldsymbol{\theta}^{(k)})$;   // Equation (A.1)
6 **end**
7 Take $\{\boldsymbol{\theta}^{(\ell)}\}_{\ell=1}^{N_2}$ samples from $q(\cdot|\boldsymbol{\theta})$;
8 **for** $\ell = 1$ **to** N_2 **do**
9 $\quad$ Evaluate $r(\boldsymbol{\theta}^{(\ell)}|\boldsymbol{\theta})$;   // Equation (A.1)
10 **end**
11 Obtain $p(\boldsymbol{\theta}|\mathcal{D}, \mathcal{M}_j) \approx \dfrac{\frac{1}{N_1}\sum_{k=1}^{N_1} q(\boldsymbol{\theta}|\boldsymbol{\theta}^{(k)})r(\boldsymbol{\theta}|\boldsymbol{\theta}^{(k)})}{\frac{1}{N_2}\sum_{\ell=1}^{N_2} r(\boldsymbol{\theta}^{(\ell)}|\boldsymbol{\theta})}$;
12 Evaluate $\log p(\mathcal{D}|\mathcal{M}_j)$;   // Equation (7.12)
13 Obtain the AGF and EIG terms ;   // Equation (7.13)

---

and it is located between the second and third layer, while the crack starts from the upper surface and has a depth of 1mm. The beam has a height of 3mm and width of 2mm and its stacking sequence is $[0_2/90]_s$. Each carbon fibre layer has a density of 1560 kg/m^3 and the stiffness matrix shown below:

$$C = \begin{bmatrix} 143.8 & 6.2 & 6.2 & 0 & 0 & 0 \\ 6.2 & 13.3 & 6.5 & 0 & 0 & 0 \\ 6.2 & 6.5 & 13.3 & 0 & 0 & 0 \\ 0 & 0 & 0 & 3.6 & 0 & 0 \\ 0 & 0 & 0 & 0 & 5.7 & 0 \\ 0 & 0 & 0 & 0 & 0 & 5.7 \end{bmatrix} \text{GPa} \qquad (7.14)$$

The numerical data $\mathcal{D}$ are generated by performing FEM simulations in Abaqus® [196] for each type of damage, which will be used as experimental data in these case studies. The first antisymmetric mode is selected for damage identification, given that it can detect both crack and delamination [11]. Thus, a Hanning windowed sinusoid with 6 cycles centred at a frequency of 100 kHz is applied as the excitation signal at one end of the beam in the vertical direction (see Figure 7.2). The in-plane response is then observed at 0.2m from the point of excitation for a time window of $720\mu s$. Note that the beam is assumed to be
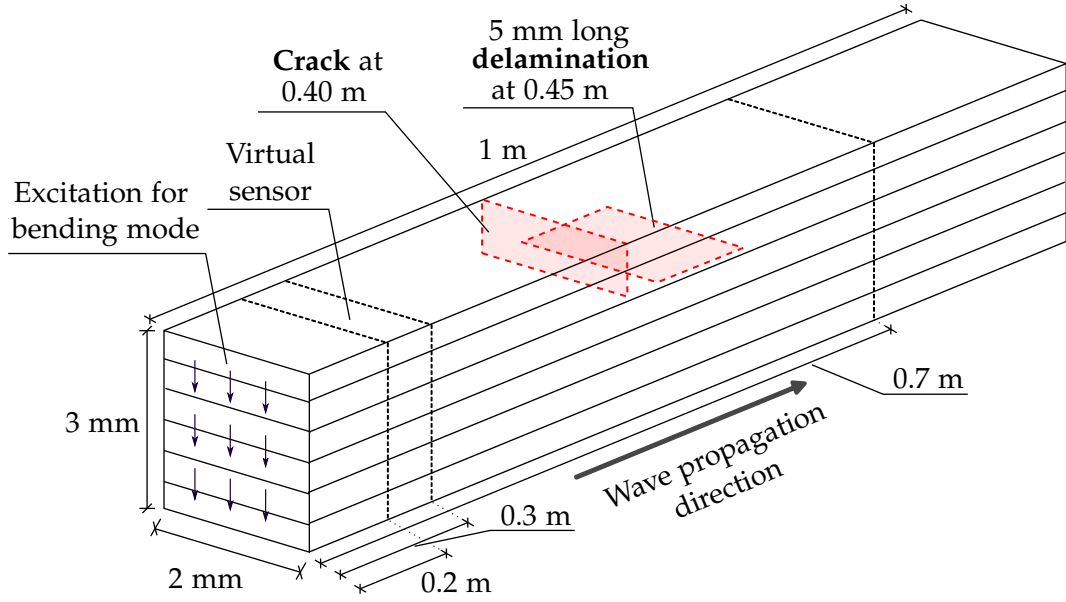
Figure 7.2: Schematic of both crack and delamination types of damage along with the geometry of beam under consideration.

sufficiently long that the reflections from the far end of the beam do not reach back to the observation point in the selected time window. The chosen damage modes are modelled by node duplication in both the Abaqus/Explicit® simulation and the WFE model. The mesh is comprised of solid elements (i.e. C3D8R) in Abaqus® with the following dimensions: 0.5mm thick, 0.5mm width, and 0.2mm long.

For illustration purposes of the proposed methodology, two damage hypotheses are assumed in the numerical case studies: (1) a crack damage mode (i.e. $\mathcal{M}_1$), and (2) a delamination damage mode (i.e. $\mathcal{M}_2$). Among this set of model classes, the Bayesian framework will identify the most probable one based on samples from the posterior PDF. Given the geometry of the selected beam and the location of the actuator and sensor, different parameterisations may be provided for each model class. The sets of unknown model parameters are comprised of several reflection coefficients and the damage location, as can be observed in Table 7.1. Note that the delamination model class $\mathcal{M}_2$ does not contain any reflection coefficient implying an incident pressure wave, i.e. r_{pp} and r_{pb}. This is a consequence of the assumption that the pressure wave is negligibly altered by a discontinuity parallel to the wave propagation direction. The prior PDFs of these unknown model parameters are also shown

in Table 7.1.

Table 7.1: Sets of model parameters for each damage hypothesis.

Model class	Damage hyp.	θ_1	θ_2	θ_3	θ_4	θ_5
$\mathcal{M}_1$	Crack	X_d	r_{pp}	r_{pb}	r_{bp}	r_{bb}
Prior PDF	$p(\boldsymbol{\theta}|\mathcal{M}_1)$	$\mathcal{U}(0.3,0.7)$	$\mathcal{U}(0,1)$	$\mathcal{U}(0,1)$	$\mathcal{U}(0,0.8)$	$\mathcal{U}(0,0.8)$
$\mathcal{M}_2$	Delamination	X_d	r_{bb}	r_{bp}		
Prior PDF	$p(\boldsymbol{\theta}|\mathcal{M}_2)$	$\mathcal{U}(0.3,0.7)$	$\mathcal{U}(0,1)$	$\mathcal{U}(0,1)$		

$X_d \rightarrow$ location of the damage.

$r_{pp} \rightarrow$ pressure-to-pressure reflection coefficient.

$r_{pb} \rightarrow$ pressure-to-bending reflection coefficient.

$r_{bp} \rightarrow$ bending-to-pressure reflection coefficient.

$r_{bb} \rightarrow$ bending-to-bending reflection coefficient.

7.4.1 Damage mode: crack

The data $\mathcal{D}$ obtained from the Abaqus$^{\circledR}$ model of the beam with a crack is assessed with the proposed Bayesian framework (see Section 7.2) in order to localise and identify its damage. Samples from the posterior PDFs of each set of model parameters are obtained through the M-H algorithm (refer to Appendix A) with $T_s = 400,000$ samples and a Gaussian proposal distribution. The standard deviation of the M-H random walk is selected such that the acceptance rate r lies in the interval $[0.2, 0.4]$ [204, 205]. The resulting posterior PDFs for each model class are depicted in Figure 7.3. It can be appreciated in Figure 7.3a that the location of the damage (i.e. 0.4m) is better inferred in the case of the first model class (i.e. assuming a crack in Figure 7.3a).

The classification of damage is addressed based on the posterior plausibility of each model class and, therefore, on their evidence. By applying Equation (7.10), these posterior probabilities are obtained and shown in Table 7.2. Note that the classification of the damage using the WFE model and the proposed Bayesian framework has provided a very accurate diagnosis. Additionally, the procedure used to calculate the evidence (see Section 7.2.1) makes it possible to provide a deeper insight into the reconstruction provided by each model class. Thus, it is observed that $\mathcal{M}_1$ provides a higher AGF term

(a) Posterior PDF $p(\boldsymbol{\theta}|\mathcal{D}, \mathcal{M}_1)$

(b) Posterior PDF $p(\boldsymbol{\theta}|\mathcal{D}, \mathcal{M}_2)$
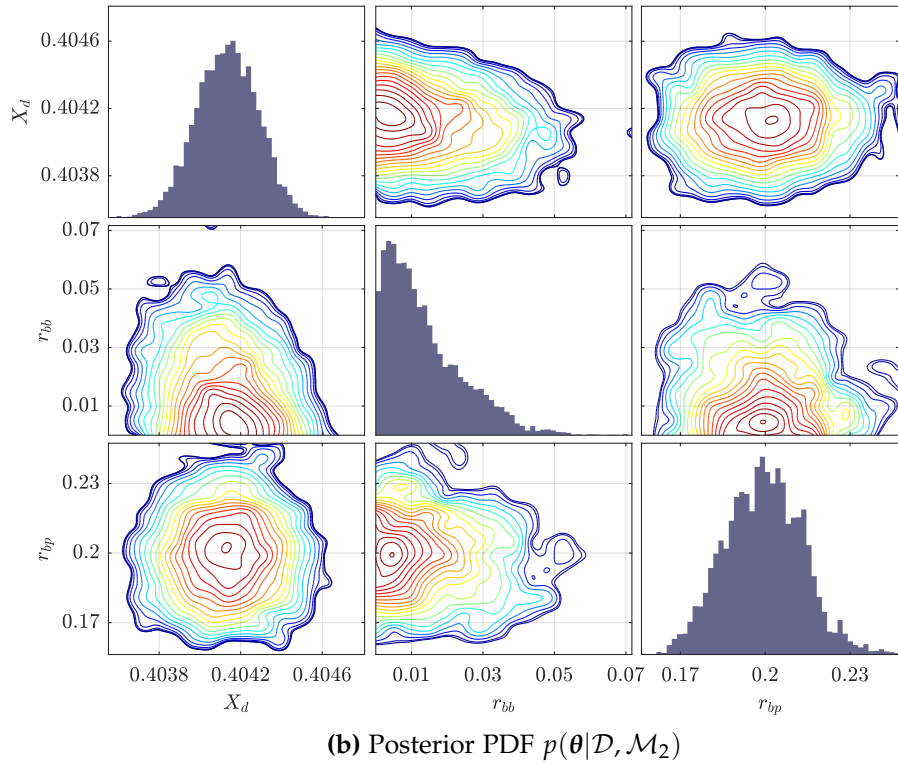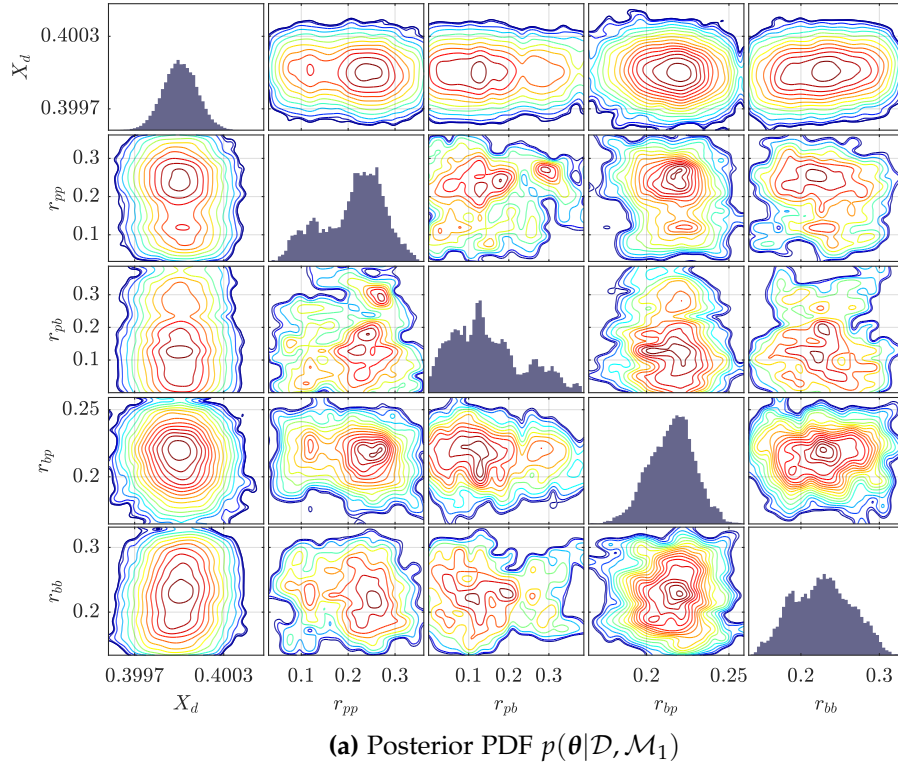
Figure 7.3: Posterior PDFs of the model parameters for damage hypothesis: crack in panel (a) and delamination in panel (b).

in Table 7.2 compared to $\mathcal{M}_2$. The large difference in AGF compensates for the inverse difference of EIG. Therefore, a higher evidence is provided by the

model class $\mathcal{M}_1$ even though such model class is more complex and therefore is more penalised.

Table 7.2: Bayesian model class selection result.

Model class	AGF	EIG	$\log p(\mathcal{D}|\mathcal{M}_j)$	$P(\mathcal{M}_j|\mathcal{D}, \mathbf{M})$
Crack - $\mathcal{M}_1$	-1.2488	7.5846	-8.8334	**99.99**%
Delamination - $\mathcal{M}_2$	-17.1338	5.4638	-22.5977	0.01%

(a) Reconstruction by $\mathcal{M}_1$ (b) Reconstruction by $\mathcal{M}_2$
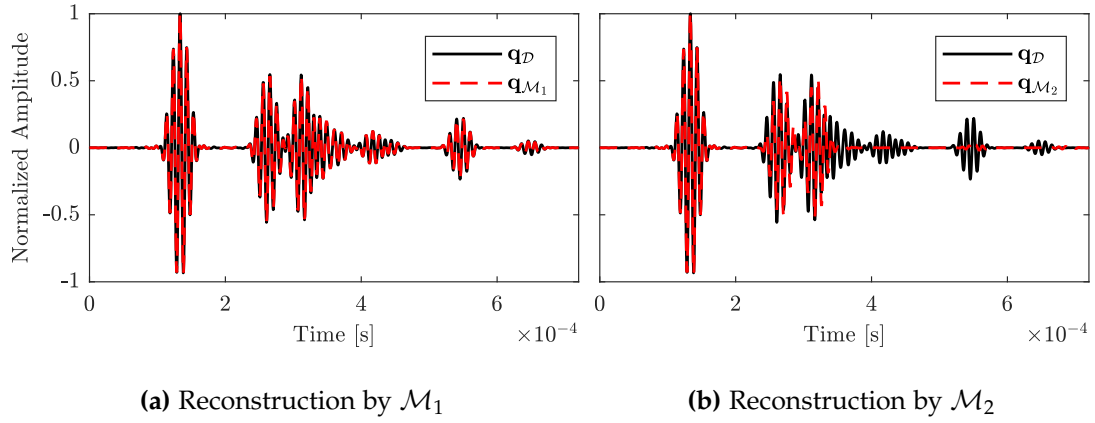
Figure 7.4: Reconstruction of the ultrasonic signal with the WFE model and the two model hypotheses: (a) crack and (b) delamination.

Furthermore, the reconstruction of the ultrasonic signal and its comparison with the numerical data is shown in Figure 7.4 for both model classes. It can be appreciated in Figure 7.4a that the model class representing a crack damage (i.e. $\mathcal{M}_1$) is able to provide a remarkable reconstruction of the numerical data $\mathbf{q}_\mathcal{D}$. $\mathcal{M}_2$, however, provides a less accurate reconstruction (see Figure 7.4b), thus supporting the previous classification of the damage hypotheses. It is worth mentioning that there are several wave packets that are not reconstructed in the case of $\mathcal{M}_2$, as shown in Figure 7.4b. This is caused by the adoption of a simpler set of model parameters than $\mathcal{M}_1$, which does not contain coefficients from an incident pressure wave mode (see Table 7.1). Therefore, $\mathcal{M}_2$ is unable to create the additional wave packets present in the ultrasonic data $\mathcal{D}$.

7.4.2 Damage mode: delamination

Similarly to the previous case study, here the identification and localisation of damage are carried out using the ultrasonic data obtained from the Abaqus® model with a delamination. The inference of the model parameters is carried out using the M-H algorithm configured in the same manner as for the previous case study. The posterior PDFs for both damage hypotheses are depicted in Figure 7.5. It is noticeable that the marginal distribution for the location of the damage X_d shows a bimodal shape in the case of the first model class (i.e. representing a crack) in Figure 7.5a. Moreover, none of its high probability areas falls within the actual damage location (i.e. 0.45m). Conversely, $p(\boldsymbol{\theta}|\mathcal{D},\mathcal{M}_2)$ provides a more accurate localisation of the damage (see Figure 7.5b). Note also that the posterior PDFs of the reflection parameters related to the incident pressure wave (i.e. r_{pp} and r_{pb} in Figure 7.5a) are very uncertain, with a similar probability density throughout almost the entire interval of their prior distributions (see Table 7.1).

Table 7.3: Bayesian model class selection result.

Model class	AGF	EIG	$\log p(\mathcal{D}|\mathcal{M}_j)$	$P(\mathcal{M}_j|\mathcal{D},\mathbf{M})$
Crack - $\mathcal{M}_1$	-1.5669	5.5424	-7.1093	15.98%
Delamination - $\mathcal{M}_2$	-0.7357	4.7135	-5.4493	**84.02**%

Nonetheless, the classification of the candidate model classes is carried out based on their evidence terms and posterior plausibilities. Table 7.3 summarises this classification along with relevant information about their evidences, such as the AGF and EIG. The delamination model class $\mathcal{M}_2$ is the most plausible one with a 84.02% of posterior probability. This higher probability is obtained due to a better fitness (i.e. higher AGF) and lower information gain, which leads to a model class that fits better with the data and is more robust against noise variations.

The comparison of the reconstructed ultrasonic data with the mean of the posterior PDFs is shown in Figure 7.6. In this case, it is shown that both candidate model classes provide a similar reconstruction. However, it is noticeable

(a) Posterior PDF $p(\boldsymbol{\theta}|\mathcal{D}, \mathcal{M}_1)$

(b) Posterior PDF $p(\boldsymbol{\theta}|\mathcal{D}, \mathcal{M}_2)$
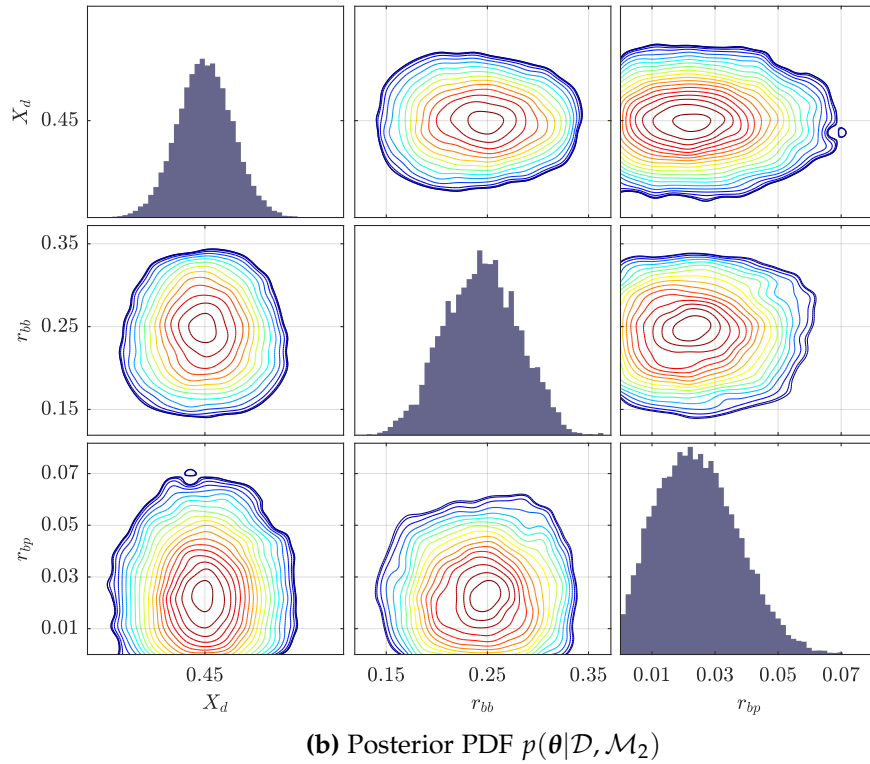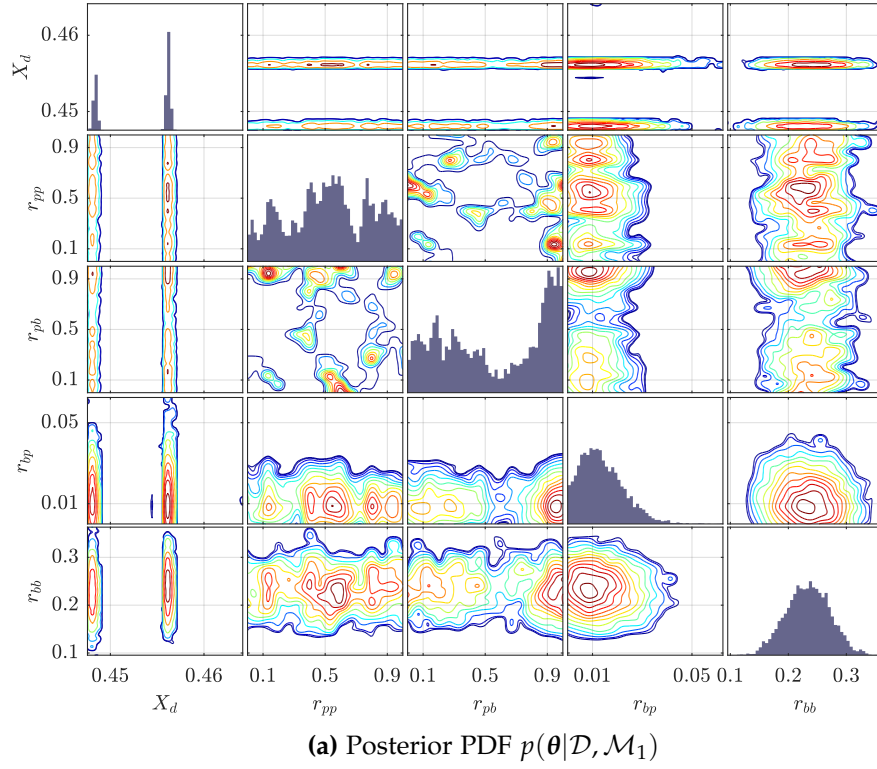
Figure 7.5: Posterior PDFs of the model parameters for each class: crack in panel (a) and delamination in panel (b).

that the reconstruction for $\mathcal{M}_1$ (i.e. crack damage in Figure 7.6a) shows a slight phase mismatch in all the wave packets except for the first one. This is

(a) Reconstruction by $\mathcal{M}_1$ **(b)** Reconstruction by $\mathcal{M}_2$
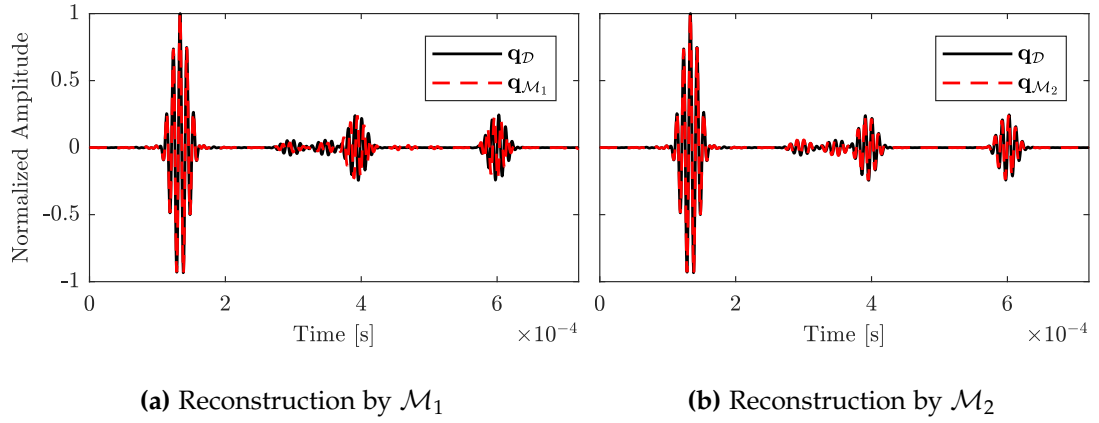
Figure 7.6: Reconstruction of the ultrasonic signal with the WFE model and the two model hypotheses: (a) crack and (b) delamination.

the main reason why this model class has a lower AGF than $\mathcal{M}_2$ (i.e. delamination damage). Figure 7.6b illustrates a better reconstruction of the ultrasonic data, hence the proposed Bayesian framework chose $\mathcal{M}_2$ as the most plausible one.

7.5   Conclusions and discussion

A comprehensive damage identification approach for composite beams using ultrasonic guided-wave measurements is presented in this chapter. As a key contribution of the proposed approach, the ultrasonic measurements are directly compared to the model predictions. This enables that no further post-processing techniques are applied to the measurements, hence reducing the sources of uncertainty. The methodology is based on a hierarchical BIP, which allows the inference of damage-related model parameters and ranking several candidate damage hypotheses. A guided-wave simulation model based on the hybrid WFE method is used in the proposed identification framework. This model is parameterisable in terms of its scatterer-related coefficients and the damage location, which allow the differentiation between different damage modes. Note that the appropriate definition of the damage hypotheses is crucial in this context, as they are the basis for identifying the type of damage.

Therefore, a profound knowledge of the interaction between wave and damage is required to set up the identification approach.

The methodology has been numerically illustrated using ultrasonic data stemming from Abaqus® simulations in two case studies. To this end, a single crack and a delamination crack have been modelled in a composite beam and the corresponding model classes have been defined. A remarkable level of accuracy in reconstructing the damage location and scattering coefficients along with the damage identification has been obtained. Notwithstanding this, there are certain limitations of the adopted damage hypotheses that could be encountered should several damage instances be present in the structure. The appropriate definition of such type of model classes along with its experimental validation comprise two required extensions of the proposed methodology.

Furthermore, the proposed methodology is able to reconstruct the damage efficiently in beam structures. However, the use of beam composite structures and its monitoring is very limited in real-world engineering scenarios. To provide a more practical damage identification framework, a guided-wave propagation model that represents the wave-damage interaction in two dimensional structures (e.g. plates) is essential. This also comprises another desirable extension of the current work, which in turn encompasses its respective numerical and experimental validation.

Further research effort is under consideration regarding: (1) the definition of additional damage modes, including the presence of multiple damages; (2) the experimental validation of the proposed approach using experimental data; and (3) the extension of the proposed approach from beam structures to plate-like ones.

Part III

CONCLUSIONS AND FUTURE WORK

8

Conclusions and future work

Addressing ultrasonic guided-wave based SHM for aerospace structures is a challenge given the intrinsic complexities associated with each of the diagnosis steps, which range from the optimal SHM design to the identification of damage with quantified uncertainty.

> ☞ In this doctoral thesis, *a holistic framework for SHM using ultrasonic guided-waves is provided by addressing its diagnosis stages from a probabilistic Bayesian perspective.*

Information theory, Bayesian inverse problem, and fuzzy logic fundamentals are the core methodological elements of the proposed frameworks. These have been illustrated using different case studies suited for each approach, which include a set of numerical and experimental scenarios. The general conclusions drawn from this thesis are described and their implications discussed in the following sections that go through the different stages of the diagnosis.

8.1   Optimal SHM design

A new sensor optimisation framework based on the value of information was developed in Chapter 3 to provide a globally identifiable optimal design point, which contains the optimal number and spatial distribution of sensors. This

methodology trades-off the amount of information that is acquired from a Bayesian damage localisation approach and the cost of the monitoring that includes hardware, maintenance, or post-processing related costs. Note that this approach supports research hypothesis 1 defined in Section 1.2.1 and therefore meets the first research objective. The key contribution was a mathematical formulation for sensor number and location optimisation using value of information fundamentals, hence accounting for the various sources of uncertainty. The methodology was tested using different case studies in the context of ultrasonic guided-waves and PZT sensors, which showed its effectiveness in providing optimal SHM designs. Additionally, it was shown that the value of information can be used as a tool to compare and rank different strategies in positioning the sensors, e.g., by adopting geometrically unrestricted sensor configurations or linearly-aligned phased-arrays. Overall, **the unrestricted configuration provided the most informative damage reconstruction with the lowest number of sensors**. A suitable and complete definition of the cost-related function was also found to be key for an unbiased optimal configuration, as it drives the selection of the optimal number of sensors to be used.

The methodology based on the value of information is mathematically rigorous, but it has shown some limitations stemming from the adoption of one fixed actuator. In the context of ultrasonic guided-waves, the optimisation of the actuators is almost equally important as that of the sensors. However, if the actuators were considered in the aforementioned optimisation approach, the computational cost could be exacerbated. Therefore, a novel optimisation framework based on both the Shannon's information entropy and a generic cost function was proposed in Chapter 4. This chapter addressed the second research hypothesis and its corresponding research objective established in Section 1.2.2. The entropy-based objective function is based on binary decision variables (i.e. $\{0,1\}$), which are relaxed into continuous variables in the interval $[0,1]$ and hence convexifying the objective function. This simple idea enables a drastic reduction of the computational time for the optimisation

problem, which ultimately provides a valuable guidance to the optimal layout of both sensors and actuators. The optimisation in this context can be viewed as finding the sensor and actuator configuration that provides the largest information gain about the damage. One of the major contributions here was the adoption of the actuators in addition to the sensors in a highly efficient optimisation scheme. This encourages the use of the proposed methodology in online and adaptive SHM systems, where the adoption of an optimal subset of sensors and/or actuators is crucial to maintain a healthy balance between information accuracy and complexity. The proposed methodology was illustrated by its application to ultrasonic guided-wave based SHM in structures with two different materials, i.e. aluminium and carbon fibre reinforced polymer. Overall, **the optimal sensor and actuator layouts were found to be coincident in both location and number**. Also, the optimal locations for the aluminium plates were those that are farthest from the area of possible damage occurrence. Besides, the proposed approach requires fewer sensors and actuators with higher uncertainty (entropy), which can be viewed as a disadvantage if poor quality transducers are to be used.

The above methodology based on the convexification of the entropy-based objective function relies on several simplifying assumptions, such as the Laplace asymptotic approximation or the reliance on a large amount of data. These provide this methodology with a high efficiency but it is at the cost of a small loss of accuracy. To overcome this issue, a desired extension of this methodology would be the consideration of the mutual information between data and model parameters as an objective function. This function comprises a computationally challenging scenario that requires from the evidence calculation of every data sample. Additionally, another future work under consideration is the use of a physics-based model in the proposed methodologies, rather than the ToF model, so that the wave interaction with different damage types as well as wave attenuation are taken into account.

8.2   Damage detection

Robustness and computational efficiency are two key characteristics for a damage detection approach to be applicable in real-life engineering scenarios. To meet the third research hypothesis and objective proposed in Section 1.2.3, a new damage detection approach for ultrasonic guided-wave measurements based on fuzzy logic principles was proposed in Chapter 5. This approach is based on fuzzy sets built from the ToFs of the ultrasonic signal peaks acquired in an undamaged state. The corresponding signal peaks for non-pristine conditions are then evaluated using the fuzzy sets, which gives an estimation of the structural health condition denoted as DoH (e.g., undamaged, damaged, or some degree of degradation in the interval $[0, 1]$). The robustness in the sense of high probability of detection of the proposed method builds on the use of a set of ultrasonic measurements (rather than a single one), which stem from two experimental procedures: (1) the round-robin configuration and (2) the transmission beamforming technique. Note that these complex experimental modes are easily implemented in practice thanks to the use of PAMELA® as SHM system. As a result, a matrix with a set of DoH values is obtained rather than a single value. Several experiments were conducted to illustrate the effectiveness of this approach with sudden and progressive damage scenarios. Overall, the results showed that **sudden damage scenarios are successfully detected** and that a **progressive damage scenario such as a fatigue crack can be detected and monitored**.

Based on the results, the use of transmission beamforming is preferred over the round-robin configuration since it leads to a better resolution due to the higher wave amplitude that is obtained without the need of further amplification. Although any structure benefits from the beamforming properties, carbon fibre laminates do more given that a higher wave attenuation is experimented. However, the calculation of the delays using the transmission beamforming technique depends on the slowness surface of the wave propagation in these materials, which is particularly challenging to obtain and is outside

the scope of this thesis. Therefore, they were not considered in the case studies and it comprises a future line of research.

Furthermore, the proposed damage index is also robust against measurement noise, which is accounted for in the definition of the fuzzy set through the repetition of several experiments. However, for this methodology to be applied in an industrial environment, further variations need to be taken into account. For instance, temperature and humidity variations are well-known features that affect the mechanical properties of different materials leading to variations of their nominal ultrasonic properties, and hence introducing another source or uncertainty. To address this additional complexity, another desirable extension of this damage index is the temperature and humidity compensation of the fuzzy sets.

It is worth highlighting that the results obtained from the fatigue test also showed a strong correlation with the measured crack length. These results encourage the future use of a ultrasonic guided-wave based monitoring technique for fatigue crack estimation, without the need for visual or perceptive inspection. Another future extension of this approach could be the application of data-driven stochastic models such as hidden Markov models to prognosticate the crack length and hence the remaining useful life of a component or structure.

8.3   Damage localisation

A novel Bayesian methodology was proposed in Chapter 6 to deal with the damage localisation using ultrasonic guided-waves, which in turn addresses the research hypothesis and the objective introduced in Section 1.2.4. This framework is comprised of two levels: first, a Bayesian TF model selection is carried out by assessing the relative degree of belief of a set of candidate model classes; and second, a BIP of damage localisation is set up considering as input data the outcome of the first level. This methodology accounts for several sources of uncertainty, ranging from the epistemic uncertainty due

to the TF model selection to the measurement noise. As a key contribution, the proposed framework provides a unified methodology for damage localisation using ultrasonic guided-waves based on rigorous probabilistic Bayesian principles. The methodology was numerically illustrated by reconstructing the damage position in two case studies, assuming one and two areas of damage simultaneously. The results confirmed **the effectiveness of the methodology in reconstructing the damage location in an accurate and robust manner**. In this context, the adoption of a hyper-robust TF model allowed the consideration of additional sources of uncertainty stemming from the heterogeneity of the candidate models. Hence, the choice of any particular TF model would lead to an unjustified uncertainty reduction along with a biased damage reconstruction. It is also worth highlighting the accurate reconstruction of the bimodal posterior PDF in the second case study, which was efficiently addressed by the chosen AIMS algorithm.

The efficiency of the proposed methodology relies on the adoption of the ToF model for the Bayesian damage localisation. This model represents the time of flight of a wave scatter taking place at the damage location. However, the methodology has certain limitations should the influence of different damage modes (e.g., microcracks or delamination) need to be assessed. A physics-based wave propagation model instead of a ToF model would be needed to this end, where the wave-damage interaction may be considered. Therefore, a desirable extension of this Bayesian framework would be the adoption of a physics-based wave propagation model to study the influence of different damage modes in the performance of the damage localisation.

Additionally, the case study with two damaged areas showed an increased uncertainty in the standard deviation of the model prediction error. The adoption of a unimodal distribution to represent the prediction model error showed an increase of entropy in the case of a multimodal posterior PDF. In this context, a natural extension of this work would be the exploration of an alternative definition of the likelihood function to better deal with damage multimodality.

8.4 Damage identificiation

The identification of damage in composite beams using ultrasonic guided-waves was addressed by proposing a Bayesian model class selection framework in Chapter 7. This methodology uses a hybrid WFE model that provides time-domain signals from beam composite structures that can be directly compared to the ultrasonic measurements. In fact, the ability to compare these signals in the time-domain comprises one of the major contributions of this framework, given that no additional post-processing techniques need to be applied to the raw data thus avoiding a possible source of uncertainty. The multi-level Bayesian framework allows: (1) the inference of damage-related parameters (e.g. reflection coefficients); (2) the localisation of damage; and (3) the ranking of several damage hypotheses. This methodology, which is based on the relative degree of belief of each candidate damage hypothesis, enables a robust identification of damage while accounting for different sources of uncertainty. This methodology was illustrated in a carbon fibre beam using two damage scenarios, namely a crack and a delamination. The results showed an **accurate identification of damage for each scenario**, provided that the parameterisation of each damage hypothesis is well defined. Thus, the fifth research hypothesis described in Section 1.2.5 was confirmed. However, these data were obtained numerically, as the base data was computed using an Abaqus FE model. Therefore, a natural extension of this work would be to test the proposed methodology using experimental data. Note that guided-wave experiments in beams are particularly challenging due to the geometrical limitations stemming from the reduced dimensions of the specimen. Additionally, the chosen wave propagation model simulates the excitation of a single wave mode. Therefore, experiments should be designed so that only one wave mode is excited, which also comprises another significant difficulty.

Furthermore, the methodology has been illustrated using two damage hypotheses, a crack and a delamination. In this context, a more realistic approach would require the consideration of additional damage modes in multiple lo-

cations. This parameterisation work needs to be addressed with a profound knowledge of the wave-damage interaction, which may establish the adoption of different model parameters or different prior information about them. Therefore, this work package comprises another desirable piece of future work.

Nevertheless, the use of composite beam structures in engineering applications is limited; this limits the usefulness of monitoring such structures. A more practical approach should consider wave propagation in thin-walled plate structures, which are widely used in industries such as aerospace. To this end, the development and implementation of a two (or three) dimensional wave propagation model is required and comprises a future line of research. In this context, the Bayesian methodology for damage identification would not change in essence, apart from the derivation of different damage hypotheses for each damage mode.

Bibliography

[1] Louis Cartz. *Nondestructive testing*. ASM International, United States, 1995.

[2] Steven W Smith. *The scientist and engineer's guide to digital signal processing*. California Technical Pub., San Diego, CA, USA, 1997.

[3] Robert MH Knotts. Civil aircraft maintenance and support Fault diagnosis from a business perspective. *Journal of Quality in Maintenance Engineering*, 5(4):335–348, 1999.

[4] Fiona C Saunders, Andrew W Gale, and Andrew H Sherry. Conceptualising uncertainty in safety-critical projects: A practitioner perspective. *International Journal of Project Management*, 33(2):467–478, 2015.

[5] Mike Gerdes, Dieter Scholz, and Diego Galar. Effects of condition-based maintenance on costs caused by unscheduled maintenance of aircraft. *Journal of Quality in Maintenance Engineering*, 22(4):394–417, 2016.

[6] Jong-Ho Shin and Hong-Bae Jun. On condition based maintenance policy. *Journal of Computational Design and Engineering*, 2(2):119–127, 2015.

[7] Enrico Zio. The future of risk assessment. *Reliability Engineering & System Safety*, 177:176–190, 2018.

[8] Swagato Das, P Saha, and SK Patro. Vibration-based damage detection techniques used for health monitoring of structures: a review. *Journal of Civil Structural Health Monitoring*, 6(3):477–507, 2016.

[9] D Goyal and BS Pabla. The vibration monitoring methods and signal processing techniques for structural health monitoring: a review. *Archives of Computational Methods in Engineering*, 23(4):585–594, 2016.

[10] Damien Kinet, Patrice Mégret, Keith W Goossen, Liang Qiu, Dirk Heider, and Christophe Caucheteur. Fiber bragg grating sensors toward structural health monitoring in composite materials: Challenges and solutions. *Sensors*, 14(4):7394–7419, 2014.

[11] Zhongqing Su, Lin Ye, and Ye Lu. Guided Lamb waves for identification of damage in composite structures: A review. *Journal of Sound and Vibration*, 295(3-5):753–780, 2006.

[12] G Aranguren, PM Monje, Valerijan Cokonaj, Eduardo Barrera, and Mariano Ruiz. Ultrasonic wave-based structural health monitoring embedded instrument. *Review of Scientific Instruments*, 84(12):125106, 2013.

[13] Pedro María Monje, Luciano Casado, Gerardo Aranguren, Valerijan Cokonaj, Eduardo Barrera, and Mariano Ruiz. Integrated electronic system for ultrasonic structural health monitoring. In *European Workshop on Structural Health Monitoring*, pages 1–8, 2012.

[14] Angel Alcaide, Eduardo Barrera, Mariano Ruiz, and Gerardo Aranguren. Damage detection on Aerospace structures using PAMELA SHM System. In *6th International Symposium on NDT in Aerospace, Madrid*, 2014.

[15] LE Mujica, M Ruiz, F Pozo, J Rodellar, and A Güemes. A structural damage detection indicator based on principal component analysis and statistical hypothesis testing. *Smart Materials and Structures*, 23(2):025014, 2013.

[16] Wieslaw Ostachowicz, Rohan Soman, and Pawel Malinowski. Optimization of sensor placement for structural health monitoring: a review. *Structural Health Monitoring*, page 1475921719825601, 2019.

[17] Ronald A Howard. Information value theory. *IEEE Transactions on Systems Science and Cybernetics*, 2(1):22–26, 1966.

[18] Robert Schlaifer and Howard Raiffa. *Applied Statistical Decision Theory*. MIT Press, 1961.

[19] Andreas Krause, Carlos Guestrin, Anupam Gupta, and Jon Kleinberg. Near-optimal sensor placements: Maximizing information while minimizing communication cost. In *Proceedings of the 5th International Conference on Information Processing in Sensor Networks*, pages 2–10. ACM, 2006.

[20] Dennis V Lindley. On a measure of the information provided by an experiment. *The Annals of Mathematical Statistics*, pages 986–1005, 1956.

[21] Hwanjeong Cho and Cliff J Lissenden. Structural health monitoring of fatigue crack growth in plate structures with ultrasonic guided waves. *Structural Health Monitoring*, 11(4):393–404, 2012.

[22] J.D. Achenbach. *Wave Propagation in Elastic Solids*. North-Holland Publishing Company/American Elsevier, 1973.

[23] Juan Chiachío, Nicolas Bochud, Manuel Chiachío, Sergio Cantero, and Guillermo Rus. A multilevel Bayesian method for ultrasound-based damage identification in composite laminates. *Mechanical Systems and Signal Processing*, 88:462–477, 2017.

[24] Sergio Cantero-Chinchilla, Juan Chiachío, Manuel Chiachío, Dimitrios Chronopoulos, and Arthur Jones. A robust Bayesian methodology for damage localization in plate-like structures using ultrasonic guided-waves. *Mechanical Systems and Signal Processing*, 122:192–205, 2019.

[25] EWC Wilkins. Cumulative damage in fatigue. In *Colloquium on Fatigue/Colloque de Fatigue/Kolloquium über Ermüdungsfestigkeit*, pages 321–332. Springer, 1956.

[26] Ramesh Talreja and Chandra Veer Singh. *Damage and failure of composite materials*. Cambridge University Press, 2012.

[27] Raul Yondo, Esther Andrés, and Eusebio Valero. A review on design of experiments and surrogate models in aircraft real-time and many-query aerodynamic analyses. *Progress in Aerospace Sciences*, 96:23–61, 2018.

[28] Edwin T Jaynes. Information theory and statistical mechanics. *Physical Review*, 106(4):620, 1957.

[29] L.A. Zadeh. Fuzzy sets. *Information and Control*, 8(3):338 − 353, 1965.

[30] John Yen and Reza Langari. *Fuzzy logic: intelligence, control, and information*, volume 1. Prentice Hall Upper Saddle River, NJ, 1999.

[31] Edwin T Jaynes. *Probability theory: The logic of science*. Cambridge University Press, 2003.

[32] James L Beck. Bayesian system identification based on probability logic. *Structural Control and Health Monitoring*, 17(7):825–847, 2010.

[33] Albert Tarantola. *Inverse problem theory and methods for model parameter estimation*, volume 89. SIAM, 2005.

[34] G Rus, J Chiachío, and M Chiachío. Logical inference for inverse problems. *Inverse Problems in Science and Engineering*, 24(3):448–464, 2016.

[35] Huidong Gao and JL Rose. Ultrasonic sensor placement optimization in structural health monitoring using evolutionary strategy. In *AIP Conference Proceedings*, volume 820, pages 1687–1693. AIP, 2006.

[36] Johannes FC Markmiller and Fu-Kuo Chang. Sensor network optimization for a passive sensing impact detection technique. *Structural Health Monitoring*, 9(1):25–39, 2010.

[37] Marco Thiene, Z Sharif-Khodaei, and MH Aliabadi. Optimal sensor placement for damage detection based on ultrasonic guided wave. In *Key Engineering Materials*, volume 665, pages 269–272. Trans Tech Publ, 2016.

[38] M Thiene, Z Sharif Khodaei, and MH Aliabadi. Optimal sensor placement for maximum area coverage (MAC) for damage localization in composite structures. *Smart Materials and Structures*, 25(9):095037, 2016.

[39] Xun Huan and Youssef M Marzouk. Simulation-based optimal Bayesian experimental design for nonlinear systems. *Journal of Computational Physics*, 232(1):288–317, 2013.

[40] Costas Argyris, Costas Papadimitriou, and Panagiotis Panetsos. Bayesian optimal sensor placement for modal identification of civil infrastructures. *Journal of Smart Cities*, 2(2):69–86, 2017.

[41] Jin Zheng, Md Zakirul Alam Bhuiyan, Shaohua Liang, Xiaofei Xing, and Guojun Wang. Auction-based adaptive sensor activation algorithm for target tracking in wireless sensor networks. *Future Generation Computer Systems*, 39:88–99, 2014.

[42] Md Zakirul Alam Bhuiyan, Jie Wu, Guojun Wang, Tian Wang, and Mohammad Mehedi Hassan. e-sampling: Event-sensitive autonomous adaptive sensing and low-cost monitoring in networked sensing systems. *ACM Transactions on Autonomous and Adaptive Systems (TAAS)*, 12(1):1, 2017.

[43] Stephen Boyd and Lieven Vandenberghe. *Convex optimization*. Cambridge University Press, 2004.

[44] Siddharth Joshi and Stephen Boyd. Sensor selection via convex optimization. *IEEE Transactions on Signal Processing*, 57(2):451–462, 2009.

[45] Pinaky Bhattacharyya and James L Beck. Exploiting convexification for bayesian optimal sensor placement by maximization of mutual information. *arXiv preprint arXiv:1906.05953*, 2019.

[46] Mira Mitra and S Gopalakrishnan. Guided wave based structural health monitoring: A review. *Smart Materials and Structures*, 25(5):053001, 2016.

[47] Jeong-Beom Ihn and Fu-Kuo Chang. Detection and monitoring of hidden fatigue crack growth using a built-in piezoelectric sensor/actuator network: I. Diagnostics. *Smart Materials and Structures*, 13(3):609, 2004.

[48] Liang Si and Qian Wang. Rapid multi-damage identification for health monitoring of laminated composites using piezoelectric wafer sensor arrays. *Sensors*, 16(5):638, 2016.

[49] Chun H Wang, James T Rose, and Fu-Kuo Chang. A synthetic time-reversal imaging method for structural health monitoring. *Smart Materials and Structures*, 13(2):415, 2004.

[50] Gang Yan. A Bayesian approach for damage localization in plate-like structures using Lamb waves. *Smart Materials and Structures*, 22(3):035012, 2013.

[51] James L Beck and Konstantin M Zuev. Asymptotically independent Markov sampling: a new Markov chain Monte Carlo scheme for Bayesian inference. *International Journal for Uncertainty Quantification*, 3(5), 2013.

[52] Konstantin M Zuev and James L Beck. Global optimization using the asymptotically independent Markov sampling method. *Computers & Structures*, 126:107–119, 2013.

[53] Shuai He and Ching-Tai Ng. Guided wave-based identification of multiple cracks in beams using a Bayesian approach. *Mechanical Systems and Signal Processing*, 84:324–345, 2017.

[54] Ching-Tai Ng. Bayesian model updating approach for experimental identification of damage in beams using guided waves. *Structural Health Monitoring*, 13(4):359–373, 2014.

[55] Brian R Mace and Elisabetta Manconi. Modelling wave propagation in two-dimensional structures using finite element analysis. *Journal of Sound and Vibration*, 318(4-5):884–902, 2008.

[56] S Gholizadeh. A review of non-destructive testing methods of composite materials. *Procedia Structural Integrity*, 1:50–57, 2016.

[57] Mark R Jolly, Arun Prabhakar, Bogdan Sturzu, K Hollstein, R Singh, S Thomas, Peter Foote, and Andy Shaw. Review of non-destructive testing (ndt) techniques and their applicability to thick walled composites. *Procedia CIRP*, 38:129–136, 2015.

[58] Ruizhen Yang and Yunze He. Optically and non-optically excited thermography for composites: A review. *Infrared Physics & Technology*, 75:26–50, 2016.

[59] Clemente Ibarra-Castanedo and Xavier PV Maldague. Infrared thermography. In *Handbook of technical diagnostics*, pages 175–220. Springer, 2013.

[60] A Sophian, GY Tian, D Taylor, and J Rudlin. Electromagnetic and eddy current ndt: a review. *Insight*, 43(5):302–306, 2001.

[61] Baldev Raj and B Venkatraman. Overview of diagnostics and monitoring methods and techniques. In *Handbook of Technical Diagnostics*, pages 43–68. Springer, 2013.

[62] F Lam and J Szilard. Pulse compression techniques in ultrasonic non-destructive testing. *Ultrasonics*, 14(3):111–114, 1976.

[63] Nicolas Bochud et al. *Signal processing-based identification of pathology using ultrasonics*. PhD thesis, University of Granada, Granada (Spain), 2014.

[64] Douglas Adams. *Health monitoring of structural materials and components: methods with applications*. John Wiley & Sons, 2007.

[65] Roberto Rocchetta, Matteo Broggi, Quentin Huchet, and Edoardo Patelli. On-line bayesian model updating for structural health monitoring. *Mechanical Systems and Signal Processing*, 103:174–195, 2018.

[66] James MW Brownjohn, Alessandro De Stefano, You-Lin Xu, Helmut Wenzel, and A Emin Aktan. Vibration-based monitoring of civil infrastructure: challenges and successes. *Journal of Civil Structural Health Monitoring*, 1(3-4):79–95, 2011.

[67] Basuraj Bhowmik, Tapas Tripura, Budhaditya Hazra, and Vikram Pakrashi. First-order eigen-perturbation techniques for real-time damage detection of vibrating systems: theory and applications. *Applied Mechanics Reviews*, 71(6), 2019.

[68] Mousumi Majumder, Tarun Kumar Gangopadhyay, Ashim Kumar Chakraborty, Kamal Dasgupta, and Dipak Kumar Bhattacharya. Fibre bragg gratings in structural health monitoring—present status and applications. *Sensors and Actuators A: Physical*, 147(1):150–164, 2008.

[69] Daniel Balageas, Claus-Peter Fritzen, and Alfredo Güemes. *Structural health monitoring*, volume 90. John Wiley & Sons, 2010.

[70] Ye Qiu, Quan-bao Wang, Hai-tao Zhao, Ji-an Chen, and Yue-ying Wang. Review on composite structural health monitoring based on fiber bragg grating sensing principle. *Journal of Shanghai Jiaotong University (Science)*, 18(2):129–139, 2013.

[71] Victor Giurgiutiu. *Structural health monitoring: with piezoelectric wafer active sensors*. Elsevier, 2007.

[72] Joseph L Rose. *Ultrasonic guided waves in solid media*. Cambridge university press, 2014.

[73] T Wandowski, PH Malinowski, and WM Ostachowicz. Circular sensing networks for guided waves based structural health monitoring. *Mechanical Systems and Signal Processing*, 66:248–267, 2016.

[74] Victor Giurgiutiu. Chapter 9 - Impact and Acoustic Emission Monitoring for Aerospace Composites SHM. In Victor Giurgiutiu, editor, *Structural Health Monitoring of Aerospace Composites*, pages 317 – 394. Academic Press, Oxford, 2016.

[75] Acous Tobias. Acoustic-emission source location in two dimensions by an array of three sensors. *Non-destructive Testing*, 9(1):9–12, 1976.

[76] Jonghyun Park and Fu-Kuo Chang. System identification method for monitoring impact events. In *Smart Structures and Materials 2005: Smart Sensor Technology and Measurement Systems*, volume 5758, pages 189–201. International Society for Optics and Photonics, 2005.

[77] Luis Eduardo Mujica, Josep Vehí, Wieslaw Staszewski, and Keith Worden. Impact damage detection in aircraft composites using knowledge-based reasoning. *Structural Health Monitoring*, 7(3):215–230, 2008.

[78] Heming Fu, Chi-Man Vong, Pak-Kin Wong, and Zhixin Yang. Fast detection of impact location using kernel extreme learning machine. *Neural Computing and Applications*, 27(1):121–130, 2016.

[79] Lei Wang and FG Yuan. Active damage localization technique based on energy propagation of Lamb waves. *Smart Structures and Systems*, 3(2):201–217, 2007.

[80] Wieslaw J Staszewski, Keith Worden, R Wardle, and Geof R Tomlinson. Fail-safe sensor distributions for impact detection in composite materials. *Smart Materials and Structures*, 9(3):298, 2000.

[81] K Worden and WJ Staszewski. Impact location and quantification on a composite panel using neural networks and a genetic algorithm. *Strain*, 36(2):61–68, 2000.

[82] Keith Worden and AP Burrows. Optimal sensor placement for fault detection. *Engineering Structures*, 23(8):885–901, 2001.

[83] V Mallardo, MH Aliabadi, and Z Sharif Khodaei. Optimal sensor positioning for impact localization in smart composite panels. *Journal of Intelligent Material Systems and Structures*, 24(5):559–573, 2013.

[84] Maria De Stefano, Marco Gherlone, M Mattone, Marco Di Sciuva, and K Worden. Optimum sensor placement for impact location using trilateration. *Strain*, 51(2):89–100, 2015.

[85] HY Guo, L Zhang, LL Zhang, and JX Zhou. Optimal placement of sensors for structural health monitoring using improved genetic algorithms. *Smart Materials and Structures*, 13(3):528, 2004.

[86] Frank YS Lin and Pei-Ling Chiu. A near-optimal sensor placement algorithm to achieve complete coverage-discrimination in sensor networks. *IEEE Communications Letters*, 9(1):43–45, 2005.

[87] Philippe Blanloeuil, Nur AE Nurhazli, and Martin Veidt. Particle swarm optimization for optimal sensor placement in ultrasonic SHM systems. In *Nondestructive Characterization and Monitoring of Advanced Materials, Aerospace, and Civil Infrastructure 2016*, volume 9804, pages 9804 – 9804 – 11. International Society for Optics and Photonics, 2016.

[88] M Azarbayejani, AI El-Osery, KK Choi, and MM Reda Taha. A probabilistic approach for optimal sensor allocation in structural health monitoring. *Smart Materials and Structures*, 17(5):055019, 2008.

[89] Zahra Sharif Khodaei and MH Aliabadi. An optimization strategy for best sensor placement for damage detection and localization in complex composite structures. In *8th European Workshop On Structural Health Monitoring (EWSHM 2016)*, pages 5–8, 2016.

[90] MS Salmanpour, Z Sharif Khodaei, and MH Aliabadi. Transducer placement optimisation scheme for a delay and sum damage detection algorithm. *Structural Control and Health Monitoring*, 24(4), 2017.

[91] Hussein Tarhini, Rafic Itani, Mohammad Ali Fakih, and Samir Mustapha. Optimization of piezoelectric wafer placement for structural health-monitoring applications. *Journal of Intelligent Material Systems and Structures*, page 1045389X18799204, 2018.

[92] James L Beck, Costas Papadimitriou, Siu-Kui Au, and Michael W Vanik. Entropy-based optimal sensor location for structural damage detection. In *Smart Structures and Materials 1998: Smart Systems for Bridges, Struc-*

tures, and Highways, volume 3325, pages 161–173. International Society for Optics and Photonics, 1998.

[93] Costas Papadimitriou, James L Beck, and Siu-Kui Au. Entropy-based optimal sensor location for structural model updating. *Journal of Vibration and Control*, 6(5):781–800, 2000.

[94] Costas Papadimitriou. Optimal sensor placement methodology for parametric identification of structural systems. *Journal of Sound and Vibration*, 278(4-5):923–947, 2004.

[95] Jie Zhang, Kristof Maes, Guido De Roeck, Edwin Reynders, Costas Papadimitriou, and Geert Lombaert. Optimal sensor placement for multi-setup modal analysis of structures. *Journal of Sound and Vibration*, 401:214–232, 2017.

[96] Costas Papadimitriou and Geert Lombaert. The effect of prediction error correlation on optimal sensor placement in structural dynamics. *Mechanical Systems and Signal Processing*, 28:105–127, 2012.

[97] Costas Argyris, Sharmistha Chowdhury, Volkmar Zabel, and Costas Papadimitriou. Bayesian optimal sensor placement for crack identification in structures using strain measurements. *Structural Control and Health Monitoring*, 25(5):e2137, 2018.

[98] Giovanni Capellari, Eleni Chatzi, and Stefano Mariani. Optimal sensor placement through Bayesian experimental design: effect of measurement noise and number of sensors. In *Multidisciplinary Digital Publishing Institute Proceedings*, volume 1, page 41, 2017.

[99] Giovanni Capellari, Eleni Chatzi, and Stefano Mariani. Cost–benefit optimization of structural health monitoring sensor networks. *Sensors*, 18(7):2174, 2018.

[100] Wan M Said and Wieslaw J Staszewski. Optimal sensor location for damage detection using mutual information. *Signal Processing and Composites*, pages 428–435, 2001.

[101] Pinaky Bhattacharyya. *Optimal sensor placement for Bayesian parametric identification of structures*. PhD thesis, California Institute of Technology, 2017.

[102] Giovanni Capellari, Eleni Chatzi, and Stefano Mariani. Structural health monitoring sensor network optimization through Bayesian experimental design. *ASCE-ASME Journal of Risk and Uncertainty in Engineering Systems, Part A: Civil Engineering*, 4(2):04018016, 2018.

[103] Kathryn Chaloner and Isabella Verdinelli. Bayesian experimental design: A review. *Statistical Science*, pages 273–304, 1995.

[104] Matteo Pozzi and Armen Der Kiureghian. Assessing the value of information for long-term structural health monitoring. In *Health monitoring of structural and biological systems 2011*, volume 7984, page 79842W. International Society for Optics and Photonics, 2011.

[105] Athena Zitrou, Tim Bedford, and Alireza Daneshkhah. Robustness of maintenance decisions: Uncertainty modelling and value of information. *Reliability Engineering & System Safety*, 120:60–71, 2013.

[106] Daniele Zonta, Branko Glisic, and Sigrid Adriaenssens. Value of information: impact of monitoring on decision-making. *Structural Control and Health Monitoring*, 21(7):1043–1056, 2014.

[107] Katerina Konakli, Bruno Sudret, and Michael H Faber. Numerical investigations into the value of information in lifecycle analysis of structural systems. *ASCE-ASME Journal of Risk and Uncertainty in Engineering Systems, Part A: Civil Engineering*, 2(3):B4015007, 2015.

[108] Daniel Straub. Value of information analysis with structural reliability methods. *Structural Safety*, 49:75–85, 2014.

[109] Daniel Straub, Eleni Chatzi, Elizabeth Bismut, Wim Courage, Michael Döhler, Michael Havbro Faber, Jochen Köhler, Geert Lombaert, Piotr Omenzetter, Matteo Pozzi, et al. Value of information: A roadmap to

quantifying the benefit of structural health monitoring. In *ICOSSAR-12th International Conference on Structural Safety & Reliability*, 2017.

[110] S Thöns and Michael Havbro Faber. Assessing the value of structural health monitoring. In *11th International Conference on Structural Safety and Reliability*, pages 2543–2550. Balkema Publishers, AA/Taylor & Francis The Netherlands, 2013.

[111] Sebastian Thöns, Ronald Schneider, and Michael H Faber. Quantification of the value of structural health monitoring information for fatigue deteriorating structural systems. In *12th International Conference on Applications of Statistics and Probability in Civil Engineering (ICASP12)*, pages 1–8, 2015.

[112] Jianjun Qin, Sebastian Thöns, and Michael H Faber. On the value of SHM in the context of service life integrity management. In *12th International Conference on Applications of Statistics and Probability in Civil Engineering (ICASP12)*, pages 1–8, 2015.

[113] Sebastian Thöns. On the Value of Monitoring Information for the Structural Integrity and Risk Management. *Computer-Aided Civil and Infrastructure Engineering*, 33(1):79–94, 2018.

[114] Carl Malings and Matteo Pozzi. Value of information for spatially distributed systems: Application to sensor placement. *Reliability Engineering & System Safety*, 154:219–233, 2016.

[115] C Malings and M Pozzi. Submodularity issues in value-of-information-based sensor placement. *Reliability Engineering & System Safety*, 183:93–103, 2019.

[116] Michael A Demetriou. A numerical algorithm for the optimal placement of actuators and sensors for flexible structures. In *Proceedings of the 2000 American Control Conference. ACC (IEEE Cat. No. 00CH36334)*, volume 4, pages 2290–2294. IEEE, 2000.

[117] Rex K Kincaid and Sharon L Padula. D-optimal designs for sensor and actuator locations. *Computers & Operations Research*, 29(6):701–713, 2002.

[118] K Ramesh Kumar and S Narayanan. Active vibration control of beams with optimal placement of piezoelectric sensor/actuator pairs. *Smart Materials and Structures*, 17(5):055008, 2008.

[119] Yunlong Li, Xiaojun Wang, Ren Huang, and Zhiping Qiu. Actuator placement robust optimization for vibration control system with interval parameters. *Aerospace Science and Technology*, 45:88–98, 2015.

[120] Isabelle Bruant, Laurent Gallimard, and Shahram Nikoukar. Optimal piezoelectric actuator and sensor location for active vibration control, using genetic algorithm. *Journal of Sound and Vibration*, 329(10):1615–1635, 2010.

[121] Vivek Gupta, Manu Sharma, and Nagesh Thakur. Optimization criteria for optimal placement of piezoelectric sensors and actuators on a smart structure: a technical review. *Journal of Intelligent Material Systems and Structures*, 21(12):1227–1243, 2010.

[122] Joshua A Taylor, Natchanon Luangsomboon, and Dariush Fooladivanda. Allocating sensors and actuators via optimal estimation and control. *IEEE Transactions on Control Systems Technology*, 25(3):1060–1067, 2017.

[123] Armin Zare, Neil K Dhingra, Mihailo R Jovanović, and Tryphon T Georgiou. Proximal algorithms for large-scale statistical modeling and optimal sensor/actuator selection. *arXiv preprint arXiv:1807.01739*, 2018.

[124] Ahron Ben-Tal and Arkadi Nemirovski. *Lectures on modern convex optimization: analysis, algorithms, and engineering applications*, volume 2. Siam, 2001.

[125] Dimitri P Bertsekas and Athena Scientific. *Convex optimization algorithms*. Athena Scientific Belmont, 2015.

[126] Victor Giurgiutiu. Chapter 6 - piezoelectric wafer active sensors. In Victor Giurgiutiu, editor, *Structural Health Monitoring of Aerospace Composites*, pages 177 – 248. Academic Press, Oxford, 2016.

[127] Steven E Olson, Martin P DeSimio, and Mark M Derriso. Beam forming of Lamb waves for structural health monitoring. *Journal of Vibration and Acoustics*, 129(6):730–738, 2007.

[128] Kai E Thomenius. Evolution of ultrasound beamformers. In *1996 IEEE Ultrasonics Symposium. Proceedings*, volume 2, pages 1615–1622. IEEE, 1996.

[129] Guillaume David, Jean-luc Robert, Bo Zhang, and Andrew F Laine. Time domain compressive beam forming of ultrasound signals. *The Journal of the Acoustical Society of America*, 137(5):2773–2784, 2015.

[130] Victor Giurgiutiu and JingJing Bao. Embedded-ultrasonics structural radar for in situ structural health monitoring of thin-wall structures. *Structural Health Monitoring*, 3(2):121–140, 2004.

[131] Hwee Kwon Jung, Gyuhae Park, and Jun Young Jeon. Development of an asymmetric sensor array with beamforming. In *EWSHM-9th European Workshop on Structural Health Monitoring*. 2018.

[132] Giola B Santoni, Lingyu Yu, Buli Xu, and Victor Giurgiutiu. Lamb wave-mode tuning of piezoelectric wafer active sensors for structural health monitoring. *Journal of Vibration and Acoustics*, 129(6):752–762, 2007.

[133] Lingyu Yu and Victor Giurgiutiu. In situ 2-D piezoelectric wafer active sensors arrays for guided wave damage detection. *Ultrasonics*, 48(2):117–134, 2008.

[134] Fucai Li, Haikuo Peng, and Guang Meng. Quantitative damage image construction in plate structures using a circular PZT array and lamb waves. *Sensors and Actuators A: Physical*, 214:66–73, 2014.

[135] Lassaad Mhamdi and Thomas Schumacher. A Comparison Between Time-of-Arrival and Novel Phased Array Approaches to Estimate Acoustic Emission Source Locations in a Steel Plate. *Journal of Nondestructive Evaluation*, 34(4):38, 2015.

[136] Lingyu Yu and Zhenhua Tian. Guided wave phased array beamforming and imaging in composite plates. *Ultrasonics*, 68:43–53, 2016.

[137] Zhenhua Tian, Lingyu Yu, and Cara Leckey. Rapid guided wave delamination detection and quantification in composites using global-local sensing. *Smart Materials and Structures*, 25(8):085042, 2016.

[138] Zhenhua Tian, Stephen Howden, Zhaoyun Ma, Wenfeng Xiao, and Lingyu Yu. Pulsed laser-scanning laser Doppler vibrometer (PL-SLDV) phased arrays for damage detection in aluminum plates. *Mechanical Systems and Signal Processing*, 121:158–170, 2019.

[139] Shankar Sundararaman, Douglas E Adams, and Elias J Rigas. Structural damage identification in homogeneous and heterogeneous structures using beamforming. *Structural Health Monitoring*, 4(2):171–190, 2005.

[140] James S Hall and Jennifer E Michaels. Minimum variance ultrasonic imaging applied to an in situ sparse guided wave array. *IEEE Transactions on Ultrasonics, Ferroelectrics, and Frequency Control*, 57(10):2311–2323, 2010.

[141] James S Hall and Jennifer E Michaels. Adaptive dispersion compensation for guided wave imaging. In *AIP Conference Proceedings*, volume 1430, pages 623–630. 2012.

[142] James S Hall and Jennifer E Michaels. Multipath ultrasonic guided wave imaging in complex structures. *Structural Health Monitoring*, 14(4):345–358, 2015.

[143] Sang Jun Lee, Navneet Gandhi, James S Hall, Jennifer E Michaels, Buli Xu, Thomas E Michaels, and Massimo Ruzzene. Baseline-free guided wave imaging via adaptive source removal. *Structural Health Monitoring*, 11(4):472–481, 2012.

[144] Chris Adams, Sevan Harput, David Cowell, Thomas M Carpenter, David M Charutz, and Steven Freear. An adaptive array excitation scheme for the unidirectional enhancement of guided waves. *IEEE Transactions on Ultrasonics, Ferroelectrics, and Frequency Control*, 64(2):441–451, 2017.

[145] WAK Deutsch, A Cheng, and Jan Drewes Achenbach. Self-focusing of Rayleigh waves and Lamb waves with a linear phased array. *Journal of Research in Nondestructive Evaluation*, 9(2):81–95, 1997.

[146] Arthur C Clay, Shi-Chang Wooh, Lawrence Azar, and Ji-Yong Wang. Experimental study of phased array beam steering characteristics. *Journal of Nondestructive Evaluation*, 18(2):59–71, 1999.

[147] Emmanuel Moulin, Nicolas Bourasseau, Jamal Assaad, and Christophe Delebarre. Lamb-wave beam-steering for integrated health monitoring applications. In *Nondestructive Evaluation and Health Monitoring of Aerospace Materials and Composites II*, volume 5046, pages 124–132. 2003.

[148] Volkan Y Senyurek, Amin Baghalian, Shervin Tashakori, Dwayne McDaniel, and Ibrahim N Tansel. Localization of multiple defects using the compact phased array (CPA) method. *Journal of Sound and Vibration*, 413:383–394, 2018.

[149] Zhenhua Tian and Lingyu Yu. Elastic phased diffraction gratings for manipulation of ultrasonic guided waves in solids. *Physical Review Applied*, 11(2):024052, 2019.

[150] Seunghee Park, Chung-Bang Yun, Yongrae Roh, and Jong-Jae Lee. PZT-based active damage detection techniques for steel bridge components. *Smart Materials and Structures*, 15(4):957, 2006.

[151] WH Leong, WJ Staszewski, BC Lee, and F Scarpa. Structural health monitoring using scanning laser vibrometry: III. Lamb waves for fatigue crack detection. *Smart Materials and Structures*, 14(6):1387, 2005.

[152] BC Lee and WJ Staszewski. Lamb wave propagation modelling for damage detection: II. Damage monitoring strategy. *Smart Materials and Structures*, 16(2):260, 2007.

[153] Lei Qiu, Shenfang Yuan, and Christian Boller. An adaptive guided wave-Gaussian mixture model for damage monitoring under time-varying conditions: Validation in a full-scale aircraft fatigue test. *Structural Health Monitoring*, 16(5):501–517, 2017.

[154] Jinsong Yang, Jingjing He, Xuefei Guan, Dengjiang Wang, Huipeng Chen, Weifang Zhang, and Yongming Liu. A probabilistic crack size quantification method using in-situ Lamb wave test and Bayesian updating. *Mechanical Systems and Signal Processing*, 78:118–133, 2016.

[155] Prashant M Pawar and Ranjan Ganguli. *Structural health monitoring using genetic fuzzy systems*. Springer Science & Business Media, 2011.

[156] Zhiye Zhao and Chuanyu Chen. A fuzzy system for concrete bridge damage diagnosis. *Computers & Structures*, 80(7-8):629–641, 2002.

[157] MM Reda Taha and J Lucero. Damage identification for structural health monitoring using fuzzy pattern recognition. *Engineering Structures*, 27(12):1774–1783, 2005.

[158] A Mojtahedi, MA Lotfollahi Yaghin, Y Hassanzadeh, MM Ettefagh, MH Aminfar, and AB Aghdam. Developing a robust SHM method for offshore jacket platform using model updating and fuzzy logic system. *Applied Ocean Research*, 33(4):398–411, 2011.

[159] Haran Pragalath, Sankarasrinivasan Seshathiri, Harsh Rathod, Balasubramanian Esakki, and Rishi Gupta. Deterioration assessment of infrastructure using fuzzy logic and image processing algorithm. *Journal of Performance of Constructed Facilities*, 32(2):04018009, 2018.

[160] Jennifer E Michaels and Thomas E Michaels. Guided wave signal processing and image fusion for in situ damage localization in plates. *Wave Motion*, 44(6):482–492, 2007.

[161] Jennifer E Michaels, Anthony J Croxford, and Paul D Wilcox. Imaging algorithms for locating damage via in situ ultrasonic sensors. In *Sensors Applications Symposium, 2008. SAS 2008. IEEE*, pages 63–67. IEEE, 2008.

[162] Leon Cohen. *Time-frequency Analysis: Theory and Applications*. Prentice-Hall, Inc., Upper Saddle River, NJ, USA, 1995.

[163] Norden E Huang, Zheng Shen, Steven R Long, Manli C Wu, Hsing H Shih, Quanan Zheng, Nai-Chyuan Yen, Chi Chao Tung, and Henry H Liu. The empirical mode decomposition and the Hilbert spectrum for nonlinear and non-stationary time series analysis. In *Proceedings of the Royal Society of London A: mathematical, physical and engineering sciences*, volume 454, pages 903–995. The Royal Society, 1998.

[164] Charles K. Chui. *An Introduction to Wavelets*. Academic Press Professional, Inc., San Diego, CA, USA, 1992.

[165] Chunxiao Bao, Hong Hao, Zhong-Xian Li, and Xinqun Zhu. Time-varying system identification using a newly improved HHT algorithm. *Computers & Structures*, 87(23-24):1611–1623, 2009.

[166] Claude Fendzi, Nazih Mechbal, Marc Rebillat, Mikhail Guskov, and G Coffignal. A general Bayesian framework for ellipse-based and hyperbola-based damage localization in anisotropic composite plates. *Journal of Intelligent Material Systems and Structures*, 27(3):350–374, 2016.

[167] Mohammad Saleh Salmanpour, Zahra Sharif Khodaei, and MH Aliabadi. Impact damage localisation with piezoelectric sensors under operational and environmental conditions. *Sensors*, 17(5):1178, 2017.

[168] Buli Xu, Lingyu Yu, and Victor Giurgiutiu. Advanced methods for time-of-flight estimation with application to lamb wave structural health monitoring. In *Proc. International Workshop on SHM*, pages 1202–1209, 2009.

[169] L Peralta, X Cai, P Laugier, and Q Grimal. A critical assessment of the in-vitro measurement of cortical bone stiffness with ultrasound. *Ultrasonics*, 80:119–126, 2017.

[170] Eric B Flynn, Michael D Todd, Paul D Wilcox, Bruce W Drinkwater, and Anthony J Croxford. Maximum-likelihood estimation of damage location in guided-wave structural health monitoring. In *Proceedings of the Royal Society of London A: Mathematical, Physical and Engineering Sciences*, volume 467, pages 2575–2596. The Royal Society, 2011.

[171] Long Yu and Zhongqing Su. Application of kernel density estimation in Lamb wave-based damage detection. *Mathematical Problems in Engineering*, 2012, 2012.

[172] E Dehghan Niri and S Salamone. A probabilistic framework for acoustic emission source localization in plate-like structures. *Smart Materials and Structures*, 21(3):035009, 2012.

[173] Ivan Bartoli, Alessandro Marzani, Francesco Lanza di Scalea, and Erasmo Viola. Modeling wave propagation in damped waveguides of arbitrary cross-section. *Journal of Sound and Vibration*, 295(3-5):685–707, 2006.

[174] Takahiro Hayashi, Koichiro Kawashima, and Joseph L Rose. Calculation for guided waves in pipes and rails. In *Key Engineering Materials*, volume 270, pages 410–415. Trans Tech Publ, 2004.

[175] Christian Willberg, Sascha Duczek, Juan Miguel Vivar-Perez, and ZAB Ahmad. Simulation methods for guided wave-based structural health monitoring: a review. *Applied Mechanics Reviews*, 67(1), 2015.

[176] Hauke Gravenkamp, Carolin Birk, and Chongmin Song. Simulation of elastic guided waves interacting with defects in arbitrarily long structures using the scaled boundary finite element method. *Journal of Computational Physics*, 295:438–455, 2015.

[177] Wenbo Duan and Ray Kirby. Guided wave propagation in buried and immersed fluid-filled pipes: Application of the semi analytic finite element method. *Computers & Structures*, 212:236–247, 2019.

[178] Yanfeng Shen. *Structural health monitoring using linear and nonlinear ultrasonic guided waves*. PhD thesis, University of South Carolina, 2014.

[179] Muhammad Khalid Malik, Dimitrios Chronopoulos, and Gregor Tanner. Transient ultrasonic guided wave simulation in layered composite structures using a hybrid wave and finite element scheme. *Composite Structures*, page 112376, 2020.

[180] James F. Doyle. *Wave Propagation in Structures - Spectral Analysis Using Fast Discrete Fourier Transforms*. Springer, New York, USA, 2nd edition, 1997.

[181] Wang-Ji Yan, Dimitrios Chronopoulos, Costas Papadimitriou, Sergio Cantero-Chinchilla, and Guo-Shu Zhu. Bayesian inference for damage identification based on analytical probabilistic model of scattering coefficient estimators and ultrafast wave scattering simulation scheme. *Journal of Sound and Vibration*, 468:115083, 2020.

[182] William L Oberkampf, Jon C Helton, Cliff A Joslyn, Steven F Wojtkiewicz, and Scott Ferson. Challenge problems: uncertainty in system response given uncertain parameters. *Reliability Engineering & System Safety*, 85(1-3):11–19, 2004.

[183] Edoardo Patelli. *COSSAN: A Multidisciplinary Software Suite for Uncertainty Quantification and Risk Management*, pages 1909–1977. Springer International Publishing, 2017.

[184] Achintya Haldar and Sankaran Mahadevan. *Probability, reliability, and statistical methods in engineering design*. J. Wiley & Sons, Incorporated, 2000.

[185] Lotfi Asker Zadeh. Fuzzy sets as a basis for a theory of possibility. *Fuzzy sets and systems*, 1(1):3–28, 1978.

[186] M Beer, FA DiazDelaO, E Patelli, and SK Au. Conceptual comparison of bayesian approaches and imprecise probabilities. *Computational Technology Reviews*, 9:1–29, 2014.

[187] Radford M Neal. *Probabilistic inference using Markov chain Monte Carlo methods*. Department of Computer Science, University of Toronto Toronto, Ontario, Canada, 1993.

[188] Nicholas Metropolis, Arianna W Rosenbluth, Marshall N Rosenbluth, Augusta H Teller, and Edward Teller. Equation of state calculations by fast computing machines. *The Journal of Chemical Physics*, 21(6):1087–1092, 1953.

[189] W Keith Hastings. Monte Carlo sampling methods using Markov chains and their applications. *Biometrika*, 57(1):97–109, 1970.

[190] Siu-Kui Au and James L Beck. Estimation of small failure probabilities in high dimensions by subset simulation. *Probabilistic engineering mechanics*, 16(4):263–277, 2001.

[191] Stuart Geman and Donald Geman. Stochastic relaxation, gibbs distributions, and the bayesian restoration of images. *IEEE Transactions on pattern analysis and machine intelligence*, (6):721–741, 1984.

[192] George Casella and Edward I George. Explaining the gibbs sampler. *The American Statistician*, 46(3):167–174, 1992.

[193] Radford M Neal. Slice sampling. *Annals of statistics*, pages 705–741, 2003.

[194] Peter J Green. Reversible jump markov chain monte carlo computation and bayesian model determination. *Biometrika*, 82(4):711–732, 1995.

[195] Jianye Ching and Yi-Chu Chen. Transitional markov chain monte carlo method for bayesian model updating, model class selection, and model averaging. *Journal of engineering mechanics*, 133(7):816–832, 2007.

[196] ABAQUS. *Abaqus Documentation*. Dassault Systèmes, Providence, RI, USA, 2016.

[197] Kenneth J Ryan. Estimating expected information gains for experimental designs with application to the random fatigue-limit model. *Journal of Computational and Graphical Statistics*, 12(3):585–603, 2003.

[198] Jeong-Beom Ihn and Fu-Kuo Chang. Pitch-catch active sensing methods in structural health monitoring for aircraft structures. *Structural Health Monitoring*, 7(1):5–19, 2008.

[199] F. Liang, C. Liu, and J. Chuanhai. *Advanced Markov Chain Monte Carlo Methods*. Wiley Online Library, 2010.

[200] Andreas Krause, Ajit Singh, and Carlos Guestrin. Near-optimal sensor placements in gaussian processes: Theory, efficient algorithms and empirical studies. *Journal of Machine Learning Research*, 9(Feb):235–284, 2008.

[201] Ting-Hua Yi and Hong-Nan Li. Methodology developments in sensor placement for health monitoring of civil infrastructures. *International Journal of Distributed Sensor Networks*, 8(8):612726, 2012.

[202] D Alleyne and Peter Cawley. A two-dimensional Fourier transform method for the measurement of propagating multimode signals. *The Journal of the Acoustical Society of America*, 89(3):1159–1168, 1991.

[203] Manuel Chiachío, Juan Chiachío, Guillermo Rus, and James L. Beck. Predicting fatigue damage in composites: A Bayesian framework. *Structural Safety*, 51:57 – 68, 2014.

[204] A. Gelman, G. Roberts, and W. Gilks. Efficient Metropolis jumping rules. *Bayesian Statistics*, 5:599–608, 1996.

[205] G.O. Roberts and J.S. Rosenthal. Optimal scaling for various Metropolis-Hastings algorithms. *Statistical Science*, 16(4):351–367, 2001.

[206] Frederick N Fritsch and Ralph E Carlson. Monotone piecewise cubic interpolation. *SIAM Journal on Numerical Analysis*, 17(2):238–246, 1980.

[207] Brian R Mace and Elisabetta Manconi. Modelling wave propagation in two-dimensional structures using finite element analysis. *Journal of Sound and Vibration*, 318(4-5):884–902, 2008.

[208] Anthony Giunta and Layne Watson. A comparison of approximation modeling techniques-Polynomial versus interpolating models. In *7th*

AIAA/USAF/NASA/ISSMO Symposium on Multidisciplinary Analysis and Optimization, page 4758, 1998.

[209] Jerome Sacks, William J Welch, Toby J Mitchell, and Henry P Wynn. Design and analysis of computer experiments. *Statistical Science*, pages 409–423, 1989.

[210] Roger G. Ghanem and Pol D. Spanos. *Stochastic finite elements: a spectral approach*. Springer-Verlag, New York, 1991.

[211] Norbert Wiener. The homogeneous chaos. *American Journal of Mathematics*, 60(4):897–936, 1938.

[212] James L Beck and Lambros S Katafygiotis. Updating models and their uncertainties. I: Bayesian statistical framework. *Journal of Engineering Mechanics*, 124(4):455–461, 1998.

[213] Armin Huber. *Dispersion Calculator User's Manual*. German Aerospace Center (DLR), Augsburg, Germany, 2019.

[214] Youssef M Marzouk and Habib N Najm. Dimensionality reduction and polynomial chaos acceleration of Bayesian inference in inverse problems. *Journal of Computational Physics*, 228(6):1862–1902, 2009.

[215] Sergio Cantero-Chinchilla, Juan Chiachío, Manuel Chiachío, Dimitrios Chronopoulos, and Arthur Jones. Optimal sensor configuration for ultrasonic guided-wave inspection based on value of information. *Mechanical Systems and Signal Processing*, 135:106377, 2020.

[216] Weisong Shi, Jie Cao, Quan Zhang, Youhuizi Li, and Lanyu Xu. Edge computing: Vision and challenges. *IEEE Internet of Things Journal*, 3(5):637–646, 2016.

[217] Matthew Muto and James L Beck. Bayesian updating and model class selection for hysteretic structural models using stochastic simulation. *Journal of Vibration and Control*, 14(1-2):7–34, 2008.

[218] Don H Johnson and Dan E Dudgeon. *Array signal processing: concepts and techniques.* Englewood Cliffs: PTR Prentice Hall, 1993.

[219] Lingyu Yu and Victor Giurgiutiu. Improvement of Damage Detection with the Embedded Ultrasonics Structural Radar for Structural Health Monitoring. In *Proceedings of 5th International Workshop on Structural Health Monitoring, Stanford University, Stanford, CA.* 2005.

[220] Gerardo Aranguren, Josu Etxaniz, Eduardo Barrera, Mariano Ruiz, Mikel A Olivares, Imara Taboada, Aitor Urrutia, and Raúl Melendez. Structural Health Monitoring Ultrasound System. In *EWSHM-8th European Workshop on Structural Health Monitoring.* 2016.

[221] Barry D Van Veen and Kevin M Buckley. Beamforming: A versatile approach to spatial filtering. *IEEE ASSP Magazine*, 5(2):4–24, 1988.

[222] Lloyd R Welch. Hidden markov models and the baum-welch algorithm. *IEEE Information Theory Society Newsletter*, 53(4):10–13, 2003.

[223] Hyunjo Jeong and Young-Su Jang. Wavelet analysis of plate wave propagation in composite laminates. *Composite Structures*, 49(4):443–450, 2000.

[224] Marc Niethammer, Laurence J Jacobs, Jianmin Qu, and Jacek Jarzynski. Time-frequency representations of Lamb waves. *The Journal of the Acoustical Society of America*, 109(5):1841–1847, 2001.

[225] M Sanjeev Arulampalam, Simon Maskell, Neil Gordon, and Tim Clapp. A tutorial on particle filters for online nonlinear/non-Gaussian Bayesian tracking. *IEEE Transactions on Signal Processing*, 50(2):174–188, 2002.

[226] Julian Besag and Peter J Green. Spatial statistics and Bayesian computation. *Journal of the Royal Statistical Society. Series B (Methodological)*, pages 25–37, 1993.

[227] Tolga Dursun and Costas Soutis. Recent developments in advanced aircraft aluminium alloys. *Materials & Design (1980-2015)*, 56:862–871, 2014.

[228] Mitsuo Gen and Runwei Cheng. *Genetic algorithms and engineering optimization*, volume 7. John Wiley & Sons, 2000.

[229] DM Mead. Wave propagation in continuous periodic structures: research contributions from Southampton, 1964–1995. *Journal of Sound and Vibration*, 190(3):495–524, 1996.

[230] Leon Brillouin. *Wave propagation in periodic structures: electric filters and crystal lattices*. McGraw-Hill Publishing Company, New York, USA, 1953.

[231] Matteo Frigo and Steven G Johnson. Fftw: An adaptive software architecture for the fft. In *Proceedings of the 1998 IEEE International Conference on Acoustics, Speech and Signal Processing, ICASSP'98 (Cat. No. 98CH36181)*, volume 3, pages 1381–1384. IEEE, 1998.

[232] Sai Hung Cheung and James L Beck. Calculation of posterior probabilities for Bayesian model class assessment and averaging from posterior samples based on dynamic system data. *Computer-Aided Civil and Infrastructure Engineering*, 25(5):304–321, 2010.

[233] George Klir and Bo Yuan. *Fuzzy sets and fuzzy logic*, volume 4. Prentice hall New Jersey, 1995.

A

<div align="right">

Metropolis-Hastings simulation for

Bayesian updating

</div>

The M-H algorithm generates samples from a specially constructed Markov chain whose stationary distribution is the required posterior PDF $p(\boldsymbol{\theta}|\hat{\mathbf{d}}, \mathcal{M})$. By sampling a candidate model parameter $\boldsymbol{\theta}'$ from a *proposal distribution* $q(\boldsymbol{\theta}'|\boldsymbol{\theta}^{\zeta})$, the M-H obtains the state of the chain at $\zeta + 1$, given the state at ζ, specified by $\boldsymbol{\theta}^{\zeta}$. The candidate parameter $\boldsymbol{\theta}'$ is accepted (i.e., $\boldsymbol{\theta}^{\zeta+1} = \boldsymbol{\theta}'$) with probability $\min\{1, r\}$, and rejected (i.e., $\boldsymbol{\theta}^{\zeta+1} = \boldsymbol{\theta}^{\zeta}$) with the remaining probability $1 - \min\{1, r\}$, where:

$$r = \frac{p(\hat{\mathbf{d}}|\boldsymbol{\theta}', \mathcal{M})p(\boldsymbol{\theta}'|\mathcal{M})q(\boldsymbol{\theta}^{\zeta-1}|\boldsymbol{\theta}')}{p(\hat{\mathbf{d}}|\boldsymbol{\theta}^{\zeta-1}, \mathcal{M})p(\boldsymbol{\theta}^{\zeta-1}|\mathcal{M})q(\boldsymbol{\theta}'|\boldsymbol{\theta}^{\zeta-1})} \tag{A.1}$$

Algorithm A.1: M-H algorithm

---

1   Initialise $\boldsymbol{\theta}^{\zeta=0}$ by sampling from the prior PDF: $\boldsymbol{\theta}^0 \sim p(\boldsymbol{\theta}|\mathcal{M})$;

2   **for** $\zeta = 1$ **to** T_s **do**

3   Sample from the proposal: $\boldsymbol{\theta}' \sim q(\boldsymbol{\theta}'|\boldsymbol{\theta}^{\zeta-1})$;

4   Compute r from Eq. (A.1);

5   Generate a uniform random number: $\alpha \sim \mathcal{U}[0, 1]$;

6   **if** $r \geqslant \alpha$ **then**

7   Set $\boldsymbol{\theta}^{\zeta} = \boldsymbol{\theta}'$;

8   **else**

9   Set $\boldsymbol{\theta}^{\zeta} = \boldsymbol{\theta}^{\zeta-1}$;

10   **end**

11 **end**

The process is repeated until T_s samples have been generated so that the monitored acceptance rate (ratio between accepted M-H samples over total amount of samples) reaches an asymptotic behaviour. A pseudo-code description of this method is provided below as Algorithm A.1.

B

Fuzzy sets: concepts for damage detection

Fuzzy sets are mathematical artefacts that represent qualitative information, which can be expressed in linguistic terms [233]. A typical example is the classification of people's height in three sets: *small*, *normal*, and *tall*. It is clear that an adult with a height of 2.0m can be classified within the *tall* set, or that someone of 1.40m belongs to the *small* group. However, intermediate heights such as 1.80m may be arguably categorised as both *normal* and *tall*, based on subjectivity. Given the lack of exact numbers that separate these sets, a gradual transition can be established between them through different *membership functions* as shown in Figure B.1, which in turn form the fuzzy sets. In this context, a 1.80m person that does not entirely fall within any set could be classified with a 0.2 membership value for belonging to the *normal* set and 0.8 for the *tall* set.
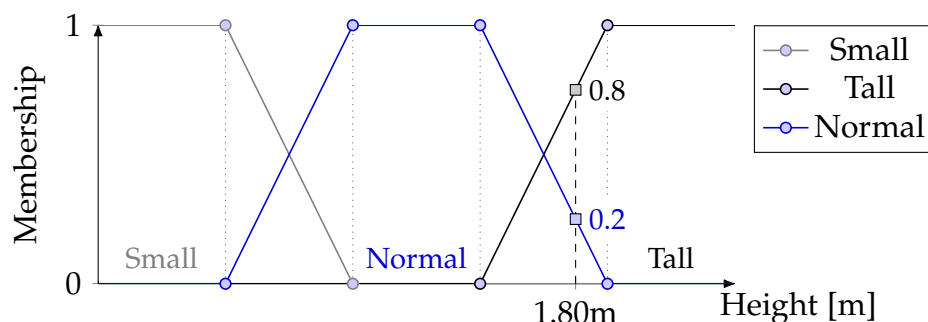

Figure B.1: Fuzzy sets for the classification of people's height.

In the context of damage detection using ultrasonic guided-waves, three trapezoidal fuzzy sets (or linguistic concepts) are defined so that the ToF mismatch between two measurements can be classified into the following: *advanced*, *on time*, and *delayed*. Figure B.2 shows these fuzzy sets around the ToF^i of the i-th peak of an ultrasonic measurement. The points that define the sets (i.e. A^i, B^i, C^i, and D^i) are given by the measurement uncertainty captured by the range between the maximum and minimum values of the N_t repetitions of ToF^i. Additional separation between the defining points is established proportional to the frequency of excitation f so that $\overline{\text{ToF}, \text{D}} = \overline{\text{A}, \text{ToF}} \in \left(0, 1/(4f)\right]$. The maximum distance of $1/(4f)$ is established so that there is no overlapping between the *on time* fuzzy sets of adjacent signal peaks. Note that these fuzzy sets are defined in the time domain relative to the ultrasonic measurement, so the space of the ToF variable will range from 0 (start of the experiment) to ∞. This *fuzzification* process is applied to all the peaks obtained from the ultrasonic signals. The corresponding peaks from new signals are then evaluated in their fuzzy sets so that the membership value is obtained.
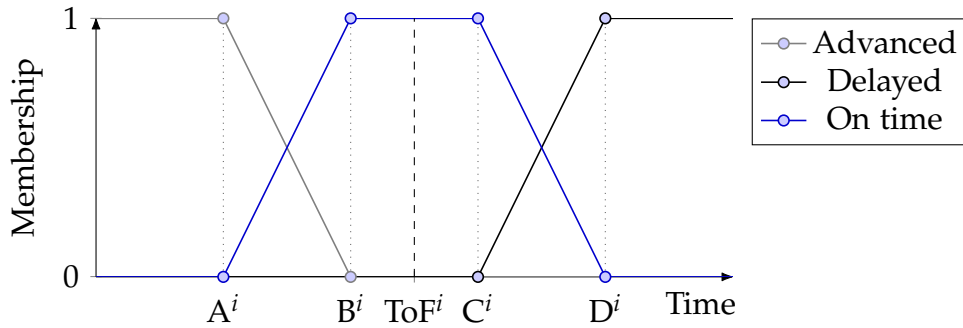

Figure B.2: Fuzzy sets used for the classification of the ToF mismatch for the i-th peak of an ultrasonic signal.

Observe that the fuzzy sets in Figure B.2 are symmetric in the intervals $[A^i, B^i]$ and $[C^i, D^i]$. From this standpoint, the *on time* set can be defined by the complement of the union of the sets *advanced* and *delayed*, as shown in Figure B.3. Note also that *on time* can then be defined as the multiplication of a ZMF and a SMF, which can be identified as the complement membership functions of the *delayed* and *advanced* sets, respectively.
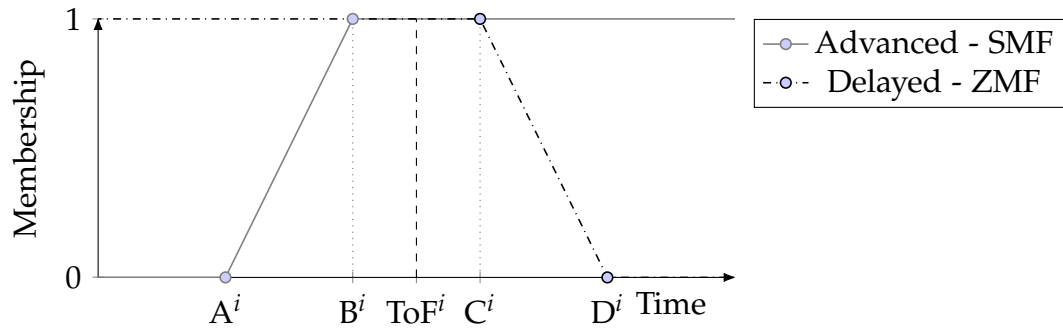
Figure B.3: *On time* fuzzy set as a complement of the union of *advanced* and *delayed* fuzzy sets.

The use of fuzzy sets in this context provides a practical method for managing irreducible measurement uncertainties, while evaluating a continuous damage index. This index can be used not only for the binary decision of damage detection, but also to provide a continuous index relative to the severeness of the damage.

Note that the detection of damage is assessed by the degree of membership of a new peak pertaining to the *on time* fuzzy set alone. Therefore, no further fuzzy logic operations and defuzzification need to be carried out.